Spray-ILGAR® deposition of controllable ZnS nanodots and application as passivation/point contact at the In_2S_3/$Cu(In,Ga)(S,Se)_2$ junction in thin film solar cells

Dissertation
to obtain the academic degree
Doctor rerum naturalium (Dr. rer. nat.)

Submitted to the Department of
Biology, Chemistry and Pharmacy
of Freie Universität Berlin

by

Yanpeng Fu

from Fujian, China

March, 2012

HZB Helmholtz Zentrum Berlin

This work has been carried out at Helmholtz Zentrum Berlin für Materialien und Energie during the period from December 2008 to March 2012.

1st Referee: Prof. Dr. Christian-Herbert Fischer

2nd Referee: Prof. Dr. Ulrich Abram

Date of Defense: May 15th, 2012

Acknowledgement

First and foremost, I would like to express my greatest gratitude to my supervisor, Prof. Dr. Christian-Herbert Fischer for his supervision, guidance with his knowledge and experience, good questions and discussions, lots of patience during this journey. Without those, this thesis would not have been possible. His devotion and my thanks to him cannot be expressed in words.

I would like to thank Prof. Dr. Ulrich Abram, for agreeing to be the 2nd supervisor for this thesis, as well as for his interest in this work and for helpful discussions.

I would also like to thank Prof. Dr. Martha Ch. Lux-Steiner for giving me the opportunity to realize this thesis in her department at Helmholtz-Zentrum Berlin, providing precious comments and discussions during every Montalk.

Special thanks go to Dr. Rodrigo Sáez Araoz for many discussions and advices in the field of photovoltaics and a lot of proof- reading.

Many thanks also to Dr. Sophie Gledhill for her assistance with the many machines at HZB especially at the beginning of my work.

I would also like to thank all the current and former members of the ILGAR-group for all the discussions, the help in the lab and the very nice working atmosphere, particularly: Tristan Köhler, Martin Krüger, Susanna Harndt, Anton Zykov and Johanna Krammer.

Further thanks go to CISSY-group, Dr. Iver Lauermann, for helping me with XPS and AES measurement and the corresponding discussions, and Alexander Grimm for the XPS and AES measurements.

I am very thankful to Dr. Thomas Dittrich for the introduction to the SPV measurements, the many discussions in the interpretation of the SPV measurement results.

I would also like to thank Dr. Jie Chen for introducing me to the ILGAR group at HZB.

Thanks also go to the electron microscope team at HZB, Dr. Daniel Abou-Ras for many discussions about SEM, EDX and TEM sample preparation and measurements, Ulli Bloeck for her TEM sample preparation and measurements, and Jürgen Bundesmann for his introduction of the SEM measurement. Additionally, I want to thank Christel Dieker, Prof. Dr.Wolfgang Jäger in Christian-Albrechts-Universität zu Kiel for the TEM cross section measurement.

Special thanks also go to Carola Kelch and Michael Kirsch for doing the CdS-deposition, sputtering of ZnO, as well as for grid deposition.

It is a great pleasure here to acknowledge the support from China Scholarship Council for the sponsoring my study in Helmholtz Zentrum Berlin.

Of course, also special thanks go to all my colleagues in E-I 2 and the rest of the HZB, who helped me to complete this thesis and to enjoy the time I spent at the HZB.

Last but not least, I also want to express my deepest gratitude to my parents who always supported me in my life. My deepest thanks go to my husband, Changbao Zhu, who supported me through all three years of this thesis with his love and encouragement, however my mood was.

Content

Kurzreferat

Mit dem Sprüh-ILGAR Verfahren können kompakte, homogene Metall Chalkogenid Filme hergestellt werden. Mit diesen Filmen als Pufferschicht werden hohe Wirkungsgrade in Dünnschichtsolarzellen erzielt.

Die große Herausforderung der Doktorarbeit bestand darin, mit dem Sprüh-ILGAR Verfahren gezielt nano-dot Filme herzustellen.

Qualitativ hochwertige, monodisperse und gut haftende Sub-Nanometer große Partikel konnten im Rahmen der Arbeit hergestellt werden. Die Dichte und zum Teil auch die Größe der Nanopartikel ist kontrollierbar. Wegen der Anwendung in Solarzellen sind die Anforderungen an den ILGAR Prozess niedrige Prozesstemperaturen. Der sequentielle und zyklische ILGAR Prozess lässt sich zudem für industrielle Anwendungen hochskalieren und erlaubt eine in-line Produktion.

Es war so möglich, strukturierte Pufferschichten für Dünnschichtsolarzellen herzustellen. Diese bestehen aus Zinksulfid (ZnS) nano-Partikeln, die mit einem kompakten Indium Sulfid (In_2S_3) Film bedeckt sind. Die ZnS Partikel dienen der Defekt-Passivierung an der Grenzfläche Absorber/Puffer, der In_2S_3 Film zur Punktkontaktierung, d.h. zum Ladungsträgertransport, nötig wegen der schlechten Leitfähigkeit von ZnS.

Um die ZnS Nanopartikel mit dem Sprüh-ILGAR Verfahren herzustellen, muss zunächst eine wässrige Zinkacetylacetonat Lösung vernebelt und auf das geheizte Substrat geleitet werden. Die gebildeten Zinkoxid nano-dots werden mit Schwefelwasserstoffgas in ZnS umgewandelt. Diese einzigartige Herstellungsmethode erlaubt die kontrollierte Bildung von hochwertigen Nanopartikeln. Durch Wahl geeigneter Prozessparameter (Lösungsmittel, Temperatur, Konzentration) kann die Dichte und zum Teil auch die Größe der Partikel kontrolliert werden. Die Partikel sind sehr homogen in der Zusammensetzung, der Form und der Größe. Sie bilden sich mit möglichst großem Abstand zueinander. Verglichen damit weisen Partikel die im Sprüh-CVD (chemical vapour deposition) Prozess entstehen, eine unregelmäßige, größere Form mit Zinkoxid Einschlüssen auf.

Der Mechanismus der Bildung der Nanopartikel wurde auf zwei Wegen untersucht. Mit in-situ Massenspektrometrie wurde die Thermolyse des Ausgangsproduktes Zinkacetylacetonat untersucht. Mit Hilfe der Raster- und der Transmissionselektronenmikroskopie war es möglich, das selbst limitierte Wachstum der Sprüh-ILGAR und der Sprüh-CVD Nanopartikel zu verstehen.

Die charakteristischen Eigenschaften wie Kristallstruktur, Morphologie, Bandlückenenergie und chemische Zusammensetzung der Sprüh-ILGAR und der Sprüh-CVD Nanopartikel, wurden mit folgenden Methoden untersucht: Röntgenbeugung, Transmissionselektronenmikroskopie, UV-VIS Spektroskopie und Photoelektronenspektroskopie.

Im zweiten Teil der Arbeit wurden die Nanopartikel hinsichtlich der Anwendung in Dünnschichtsolarzellen untersucht. Eine Passivierungsschicht/Punktkontaktschicht wird mit dem Sprüh-ILGAR Verfahren hergestellt, bestehend aus den ZnS Nanopartikeln bedeckt mit einem In_2S_3 Film. Die ZnS Nanopartikel reduzieren die Rekombination von Ladungsträgern an der Absorber/Puffer Grenzfläche, eine entscheidende Ursache für Effizienzverlust in Chalkopyrit Solarzellen. Der In_2S_3 Film ist wichtig für den Ladungsträgertransport, da die ZnS Nanopartikel eine niedrige Leitfähigkeit aufweisen. Die optimale Dichte der ZnS Nanopartikel, die In_2S_3 Dicke und die Prozesstemperatur wurden erforscht. Des Weiteren wurden die zwei Indiumsalze Indiumchlorid und Indiumacetylacetonat als Ausgangsmaterialien untersucht. Die Herstellungsverfahren, Sprüh-ILGAR und Sprüh-CVD, für die Nanopartikel wurden miteinander verglichen.

Die Photoelektronenspektroskopie deutet darauf hin, dass Zink aus den ZnS Nanopartikeln in den Absorber $Cu(In,Ga)(S,Se)_2$ diffundiert. Dies führt zu einer Typ Konvertierung des Halbleiters und wirkt sich vorteilhaft auf den Wirkungsgrad aus.

Die elektronischen Eigenschaften und die Ladungstrennung von den einzelnen Schichten und von der Kombination aus Absorber, ZnS Nanopartikeln und In_2S_3 Schicht wurden mittels Oberflächenphotospannung in der „Kelvin Probe“ Anordnung untersucht. Es hat sich gezeigt, dass tatsächlich die ILGAR ZnS Nanopartikel die Passivierung des Absorbers deutlich verbessern. Außerdem konnte gezeigt werden, dass sich Defekte bilden, wenn das In_2S_3 aus Indiumchlorid hergestellt wird, die bei der Verwendung von Indiumacetylacetonat nicht entstehen. Eine Interpretation dieser Defektbildung an der Grenzfläche konnte durch chemisches Ätzen mit dem Nebenprodukt HCl geliefert werden.

Vergleicht man das Ergebnis einer Solarzelle mit dem Passivierungs-/Punktkontaktt Puffer mit einer aus reinem In_2S_3, so konnte der Wirkungsgrad von Zellen mit der neuen ZnS/ In_2S_3 Pufferschicht um 1% absolut bis auf 15.7 % verbessert werden.

Abstract

The spray ion layer gas reaction (Spray-ILGAR) technique produces homogeneous compact metal chalcogenide films used as buffer layers for thin film solar cells with high efficiencies. It was a great challenge to elaborate this method for the deposition of nanodots. This thesis shows that high quality, uncoated, monodisperse and sub 10 nm ZnS nanodots with controllable dot density and size (to some extend) can be prepared at the requisite low temperature by this sequential, cyclic and low cost method which can be scaled up for industrial in-line production. In addition, by this Spray-ILGAR technique, a structured buffer layer, composed of ZnS nanodots covered by a closed In_2S_3 film, has been introduced as a defect passivation / point contact layer at the $Cu(In,Ga)(S,Se)_2$ (CIGSSe) absorber interface.

The ZnS nanodots are deposited starting from nebulizing an aqueous Zn acetylacetonate ($Zn(acac)_2$) solution followed by H_2S sulfurization. The unique sequential process allows the formation of the nanodot film with good properties. The choice of the process parameters (e.g. solvent, temperature, concentration) allows the control of particle density and partly also of particle size. These nanodots are rather homogeneous in size, shape and composition, and tend to keep maximum distance from each other. In contrast, ZnS nanodots deposited by a continuous spray chemical vapor deposition (Spray-CVD) are irregular in shape with inclusions of ZnO.

The mechanism behind the ZnS nanodots formation is studied in two ways. On one hand, the decomposition mechanism of $Zn(acac)_2$ on the hot substrate in the spray based processes is studied by means of in-situ mass spectroscopy. On the other hand, by interpretation of the scanning electron microscopy (SEM), energy filtered transmission electron microscopy results (EF-TEM), it is possible to elucidate the self-limiting growth of ZnS nanodots in the Spray-ILGAR and Spray-CVD processes.

The fundamental properties of the nanodots from these two processes, i.e. crystal structure, morphology, energy band gap and chemical composition, are comprehensively analyzed before their application as passivation buffer layers in the thin film solar cells by X-ray diffraction (XRD), transmission electron microscopy (TEM), ultraviolet-visible spectroscopy (UV-Vis), and x-ray photoelectron spectroscopy (XPS) respectively.

In the second part, the nanodot films dedicated for the application in the thin film solar cells are described. A passivation layer / point contact buffer composed of the ZnS nanodots covered by a homogenous In_2S_3 layer is produced consecutively by the Spray-ILGAR process. The ZnS reduces the recombination of the charge carriers at the absorber / buffer heterointerface which is one important position for performance loss in the chalcopyrite cells. The In_2S_3 in-between and on top of the ZnS dots is necessary for the charge carrier transport as ZnS has a poor conductivity. The optimal ZnS dot density, In_2S_3 thickness and process temperature are investigated. Moreover, the In precursor salt solutions, indium chloride ($InCl_3$) and indium acetylacetonate ($In(acac)_3$) and the ZnS nanodot deposition methods, Spray-ILGAR and Spray-CVD are varied and investigated.

The XPS study hints for a Zn diffusion from the ZnS layer into the $Cu(In,Ga)(S,Se)_2$ absorber, which leads to kinds of type conversion and is beneficial for the cell performance. Finally, the electronic properties and charge separation of the single layers and combined layer systems of $Cu(In,Ga)(S,Se)_2$, In_2S_3 and ZnS-nanodot layers are investigated by surface photovoltage (SPV) spectroscopy in the Kelvin probe arrangement. This shows that ZnS nanodots deposited by ILGAR improve significantly the passivation of CIGSSe absorbers. Moreover, the In_2S_3 deposition from $InCl_3$ is accompanied by defect generation at the interface, which can be avoided by In_2S_3 deposited from $In(acac)_3$. An interpretation of the formation of interface defects is given by the chemical etching with HCl byproduct.

Finally, the solar cell efficiency with ZnS / In_2S_3 buffer layer could be improved by about 1% absolutely as compared to a pure In_2S_3 buffered cell.

Chapter 1

Introduction

By 2050, 30% of the world's energy will need to come from solar, wind, and other renewable resource. British Petroleum and Royal Dutch Shell, two of the world's largest oil companies say that. The threat of global warming, population growth and the gradual depletion of petroleum supplies mean that renewables will need to play a bigger role in the future than they do today. As the most abundant energy source available on earth, solar energy has the largest potential to satisfy the future global need for renewable energy sources.

At present, crystalline silicon solar cells accounted for approximately 90% of the market. Due to its indirect band gap, silicon has lower optical absorption than comparable direct semiconductors. Therefore, the use of direct semiconductors allows replacing the 200 μm thick silicon absorbers by direct semiconductor thin films of about 2 μm in so-called thin film or second generation photovoltaic cells. For the thin film solar cells, they are usually categorized according to the photovoltaic material used, including amorphous silicon (a-Si) and other thin-film silicon, cadmium telluride (CdTe), chalcopyrite family $Cu(In_x,Ga_{1-x})(S_y,Se_{1-y})_2$, dye-sensitized solar cells (DSC) and other organic solar cells. In this thesis, the focus is put on the investigation of chalcopyrite based thin film solar cells.

In the standard configuration of the chalcopyrite solar cells, it requires a so called buffer layer between the p-type absorber and the n-type transparent front contact for an optimal p-n junction formation. In practice, today nearly all industrial concepts use chemical bath deposition (CBD) of cadmium sulfide (CdS) as buffer layer. Due to the highly toxicity of Cadmium and the not ideal batch process of CBD, an alternative material deposited by a technique compatible with in-line processing of the other cell components is highly desirable. Spray ion layer gas reaction (ILGAR) indium sulfide (In_2S_3) is one of the most promising candidates, which show comparable cell efficiency to the CBD CdS. However, despite the increased photocurrent, the open circuit voltage is slightly reduced in cells with Spray-ILGAR In_2S_3 (deposition from an $InCl_3$ solution). It remains a great challenge to find an optimum alternative buffer layer for these thin film heterojunction solar cells, which are often limited by interface recombination at the active heterointerface. The aim of the applied part of this thesis is to engineer the heterojunction interface with a combination of ZnS nanodots passivation layer plus the Spray-ILGAR In_2S_3 in a point contact structure to overcome this limitation. The spray-ILGAR technique produces homogeneous compact metal chalcogenide films used as buffer layers for thin film solar cells with high efficiencies. To realize this structured buffer layer, the challenge is to develop a low-cost deposition method for the controlled preparation of ZnS nanodots, which allows the achievement of the nanodots at low temperature (≤ 250 °C, which is the prerequisite of the chalcopyrite solar cells) and the flexible distance of the nanodots in the order of tens to hundreds of nanometers. Hence, to elaborate a method for the deposition of ZnS nanodots including the understanding of the chemistry and growth mechanism as well as the material properties, and to develop a point contact structured buffer layer with the as-prepared ZnS nanodots are the two main topics of this work.

In the following, a brief description of the structure of this dissertation and the contents of the individual chapters are given.

Chapter 2 starts with a brief discussion of the material properties and the application of ZnS. Furthermore, an introduction of the state of the art of chalcopyrite solar cells is presented. This includes the structure of the standard $Cu(In,Ga)(S,Se)_2$ solar cells and the current voltage characteristics. It is followed by the introduction of the role and requirement of the buffer layer and a short overview of the common deposition processes for the buffer layer. At the end of the chapter, the current status of the Spray-ILGAR process is reviewed.

Chapter 3 describes the implementation of two processes Spray-ILGAR and Spray-CVD for the preparation of ZnS nanodots. By the choice of appropriate precursors, zinc containing compound and solvent, the deposition of ZnS nanodots could be realized by the Spray-ILGAR process. In particular, the influences of the process parameters on the growth mechanism, morphology and coverage of the surface are analyzed in detail. Afterwards, a continuous Spray-CVD method, which combines the two sequential Spray-ILGAR steps (spray and sulfurization) in a simultaneous process, is introduced to prepare the ZnS nanodots. The similarities and differences of the nanodots obtained from these two processes are investigated and explained.

In Chapter 4, the thermochemical behavior of $Zn(acac)_2{\cdot}H_2O$ on the hot substrate surface is studied by in-situ mass spectrometry. A decomposition route of $Zn(acac)_2$ is proposed, which explains the formation of the observed phases and the influences of H_2S, H_2O and acid. Afterwards, real time mass spectrometry tracking of various masses in the Spray-ILGAR and Spray-CVD process are investigated. Following the thermal decomposition of $Zn(acac)_2{\cdot}H_2O$, the self-limiting growth of the ZnS nanodots is investigated. Firstly, the compositions of the nanodots obtained by Spray-ILGAR and Spray-CVD are analyzed and compared by energy filtered transmission electron microscopy (EF-TEM). In a second approach, different nucleation behaviors which lead to the self-limiting growth of the nanodots within the two processes are investigated and elucidated in detail.

Chapter 5 presents the fundamental properties of the nanodots prepared by the Spray-ILGAR and Spray-CVD processes, including the chemical composition, crystal structure, optical band gap and morphology.

Chapter 6 reports on the photovoltaic performance of $Cu(In,Ga)(S,Se)_2$ thin film solar cells prepared with the passivation / point contact bilayer buffer. The chapter begins with the introduction of the concept of the passivation / point contact buffer layer, in which the Spray-ILGAR ZnS nanodots serve as passivation layer, while the Spray-ILGAR In_2S_3 film works as point contact layer. This is followed by the comparison of the solar cell performances with the bilayer buffer, without any buffer layer and with different pure buffer layers, i.e. ZnS nanodots, In_2S_3 and the standard CdS. The important issues such as the optimal ZnS dot density, In_2S_3 thickness, process temperature, the different In precursor salt solutions for In_2S_3 preparation and the two kinds of ZnS nanodots deposition methods will be discussed. To investigate the reasons of the improved performance, the information about the potential interface diffusion at the buffer / absorber interface and its chemistry are studied by means of x-ray photoelectron spectroscopy (XPS). Furthermore, the electronic properties and charge separation of the single layers and combined layer systems of $Cu(In,Ga)(S,Se)_2$, In_2S_3 and ZnS nanodot layers are investigated by surface photovoltage (SPV) spectroscopy in the Kelvin probe arrangement and compared with the open circuit voltage (V_{OC}) of the corresponding solar cells.

A short description of the analysis techniques which are applied in this thesis is given in Appendix A.

The work is completed with a summary of the presented results in chapter 7.

Chapter 2

Material properties and chalcopyrite solar cells

Chapter 2 starts with a brief overview on ZnS fundamental properties and the corresponding application. Afterwards, the fundamental concepts of chalcopyrite based thin film solar cells are presented. The structure of the standard Cu(In,Ga)$(S,Se)_2$ solar cells device and the function of each of the layers in the devices are depicted. It is followed by the introduction of the current voltage characteristics, the role and requirement of the buffer layer and a short overview of common deposition processes for the buffer layer deposition. This review will be kept as short as possible and the reader is referred to the vast number of existing textbooks [1-4], for more details and a more complete derivation. At the end of the chapter, the current status of the Spray-ILGAR process and the background of this thesis are introduced.

2.1 Material properties and application

Zinc sulfide (ZnS) is one of the first semiconductors discovered [5], which belongs to the group of II–VI wide band gap semiconductors. This section gives a brief overview on fundamental properties of ZnS and the corresponding applications.

2.1.1 Fundamental properties of ZnS

ZnS is a semiconductor that has been extensively studied. In nature, ZnS is a white- to yellow-colored powder or crystal. It has two commonly available allotropes: one with cubic (sphalerite or zincblende) structure and another with hexagonal (wurtzite) structure. The hexagonal form is a thermodynamically metastable phase which is usually stable at very high temperature, while the cubic form is more thermodynamically stable phase at low temperature. It has been reported earlier that sphalerite to wurtzite transition occurs at temperatures of 1020 °C at atmospheric pressure [6]. However there are some reports stating the sphalerite to wurtzite transition temperature as a function of both growth temperature and sulfur fugacity. For instance, ZnS films with hexagonal structure were prepared at 425–500 ºC by atomic layer deposition (ALD) [7, 8] and at 400 ºC by physical vapor deposition (PVD) [9].

Figure 2.1 shows these two structures. The minute difference in atomic arrangement leads to large difference in properties [10], e.g. electronic structures and band [11] gap. The cubic form has a band gap of 3.54–3.6 eV, whereas the band gap of hexagonal form is higher being 3.74–3.87 eV [12-14]. ZnS exhibits high transparency over a wide spectrum region between 380 nm and 25 nm. The electrical resistivity is in the order of 10^4 Ω·cm with n type electrical conductivity. It can be doped as both n– and p–type semiconductor, which is unusual for the II–VI semiconductors.

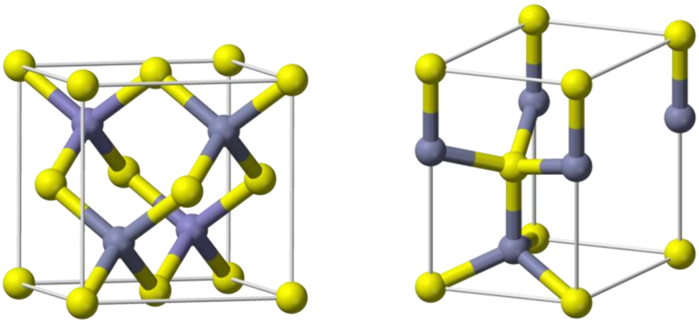

Figure 2: The zinc blende (left) and wurtzite (right) crystal structures of ZnS. S atoms are shown as yellow spheres and Zn atoms are gray spheres [15].

2.1.2 Application of ZnS

Zinc sulfide (ZnS), a well-known direct band gap II–VI semiconductor, is a promising material for fabricating photonic, optical, and electronic devices. It is considered as one of the most suitable candidates for field emitters [16-18], and field effect transistors (FETs) [19]; an ideal object for fabrication of high-performance sensors [20-23] due to their excellent fluorescence properties and nontoxicity; and important for applications in infrared windows [24] and lasers [25, 26].

In addition, a diverse range of solar device applications exists for ZnS thin films, including filters, anti–reflection coatings in silicon based solar cells and buffer layers in chalcopyrite semiconductor–based solar cells [27]. The band gap of ZnS (3.5–3.8 eV) is higher than that of CdS (2.4 eV) which should improve the solar cell device efficiency by eliminating absorption loss in the short wavelength region [28]. Recently thin film solar cells based on chemical bath deposition ZnS(O,OH) buffer layer have achieved an efficiency of 18.6% [29] which makes it a highly competitive alternative to the conventional CdS buffer layer.

2.2 Chalcopyrite based thin film solar cells

Conventional solar cells are made of semiconductor materials that form a p-n junction. When light shines on the solar cells, it excites electrons across the energy band gap of the semiconductor and generates a photovoltage. The history, physics and operational principles of solar cells can be found in the dedicated books [4, 30].

2.2.1 Fabrication of chalcopyrite based solar cells

A highest efficiency of above 20% is achieved in the laboratory scale with chalcopyrite based solar cells using CdS buffer layers deposited by chemical bath deposition (CBD) [31]. The structure of these chalcopyrite based thin film solar cells generally is based on a layer stack constituted by various compounds. A schematic sketch of the cross section of a typical $Cu(In,Ga)(S,Se)_2$ thin film solar cells is depicted in Figure 2.2. The constituting elements are shown as following:

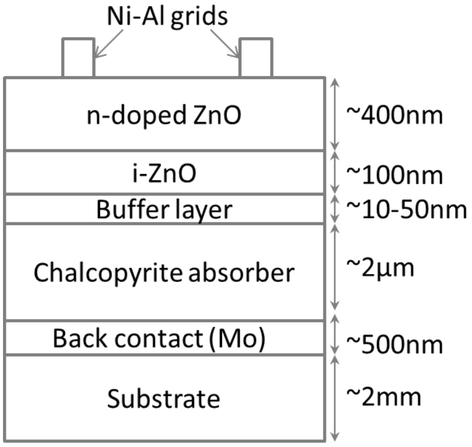

Figure 2.2: Schematic diagram of the layer sequence in a chalcopyrite based thin film solar cells. The approximate thicknesses of the different layers are also indicated.

Soda lime glass (SLG) substrate

The thickness of the SLG substrate is 1-3 mm. For the fabrication of flexible solar cells, other substrates such as titanium foil [32] or polyimide [33], can be chosen.

Molybdenum metal back contact

Molybdenum (Mo), coated on glass by DC-magnetron sputtering or by electron-beam evaporation, is commonly served as back contact for the $Cu(In,Ga)(S,Se)_2$ solar cells.

Absorber layer

The alloy $Cu(In,Ga)(S,Se)_2$ is a group I-III-VI p-type semiconductor, where most of the solar energy is absorbed. The energy band gap E_g is adjustable by changing the ratio of the group III elements In and Ga from 1.01eV ($CuInSe_2$) to 1.68 eV ($CuGaSe_2$). Moreover, the band gap can also be engineered by varying the ratio of the group VI elements S and Se from 1.01eV ($CuInSe_2$) to 1.53 eV ($CuInS_2$) or from 1.68 eV ($CuGaSe_2$) to 2.43 eV ($CuGaS_2$) [34]. In this work, $Cu(In,Ga)(S,Se)_2$ absorbers have been used, which are delivered by AVANCIS GmbH & Co. KG [35]. The absorbers, with energy band gaps about 1.1 eV, are prepared in a SEL-RTP (stacked elemental layer, rapid thermal process) line [36]. Due to the high absorption coefficient of the chalcopyrite compound (in the order of 10^5 cm^{-1}), a layer thickness of 1.5-2 µm is sufficient for photovoltaic (PV) application.

Buffer layer

State of the art thin film devices contain a thin layer (~50 nm) of CBD-CdS serving as buffer layer. The role of the buffer layer will be discussed in section 2.2.3.

Transparent front contact

The n^+ heterojunction partner is provided by ac-sputtering of a double layer of ZnO (see Figure 2.2) acting as a window layer, i.e. permitting the visible light to pass through with minor absorption losses and to reach the underlying absorber film. This double ZnO layer consists of an intrinsically doped ZnO (i-ZnO) layer and highly doped Al:ZnO layer. The i-ZnO layer prevents Al-diffusion into the buffer and reduces those losses associated to shunts in the p-n structure [37]. On the other hand, the Al: ZnO ensures that the band bending associated to the p-n junction takes place to a large extent within the absorber for an optimal collection of photogenerated carriers [38].

Metal front contact grid Ni/Al

To increase current collection and reduce contact resistance to the measurement probes, a thin Ni/Al grid is deposited on top of the ZnO:Al layer in the case of single cells. The purpose of Ni is to prevent the formation of a resistive Al_2O_3 barrier which is the result of the rapid oxidation of Al.

2.2.2 I-V characteristic of a solar cell and the equivalent circuit

As a consequence of the p-n junction, the current-voltage of a solar cell, which is considered as an electrical device, can be modeled by an equivalent circuit. The one diode model, introduced and depicted in Figure 2.2, is routinely used to characterize the chalcopyrite based solar cells [39].

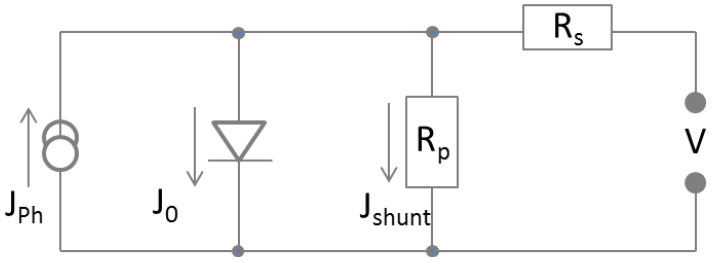

Figure 2.3: Equivalent circuit of the single diode model. The photogenerated current density J_{Ph} is indicated by a current source. In parallel to the current source but with inverted direction there is the saturation current density of the diode J_0 and the leakage current density J_{shunt} represented by a resistor R_p. The resistor R_s represents the resistive losses in the device.

The equivalent circuit consists of the diode which models the p-n junction, a parallel or shunt resistance R_p, a series resistance R_s and an additional parallel current density, which is opposed to the diode current density. In this so called one diode model, the current flowing through the device is therefore the sum of three parts, the diode current density, the current density flowing through the shunt and the photogenerated current density, which can be written as following:

$$J(V)=J_0\left(e^{\frac{q(V-JR_S)}{AkT}}-1\right)+\frac{V-JR_s}{R_p}-J_{Ph} \qquad \text{Eq.2.1}$$

Here, $q \approx 1.602 \cdot 10^{-19}$ C is the elementary charge. J_0 is the saturation and J_{Ph} is the photogenerated current density. The expression kT is the thermal energy, where $k \approx 1.38 \cdot 10^{-23}$ J/K is the Boltzmann constant and T is the absolute temperature. The diode quality factor A, the series resistance R_s and parallel resistance R_p illustrate non-ideal behavior of the device. For an ideal solar cell, R_s is zero, R_p is infinite and A=1. In a first approximation, J_{Ph}, the photogenerated current density, can be assumed to be independent of the voltage V.

The most important parameter to classify solar cells is the power conversion efficiency η, which is defined as the ratio of electric power output P_{out} to the incoming irradiative power P_{in}.

$$\eta = \frac{P_{out}}{P_{in}} \qquad \text{Eq.2.2}$$

The power output of the solar cells can be directly extracted from measuring the current flowing through the device as a function of the applied bias voltage, which is called I-V curve or J-V curve, depending if it is related to the current I (expressed in mA), or the current density J (expressed in $mA\cdot cm^{-2}$). The typical current-voltage characteristics as obtained in the dark and standardized AM 1.5 illumination of a CIGSSe based solar cell are shown in Figure 2.4. The power output is described in the following:

$$P_{out} = V \cdot I \qquad \text{Eq.2.3}$$

which is equivalent to the area of the rectangle enclosed by the corresponding point in the I-V curve and the axes.

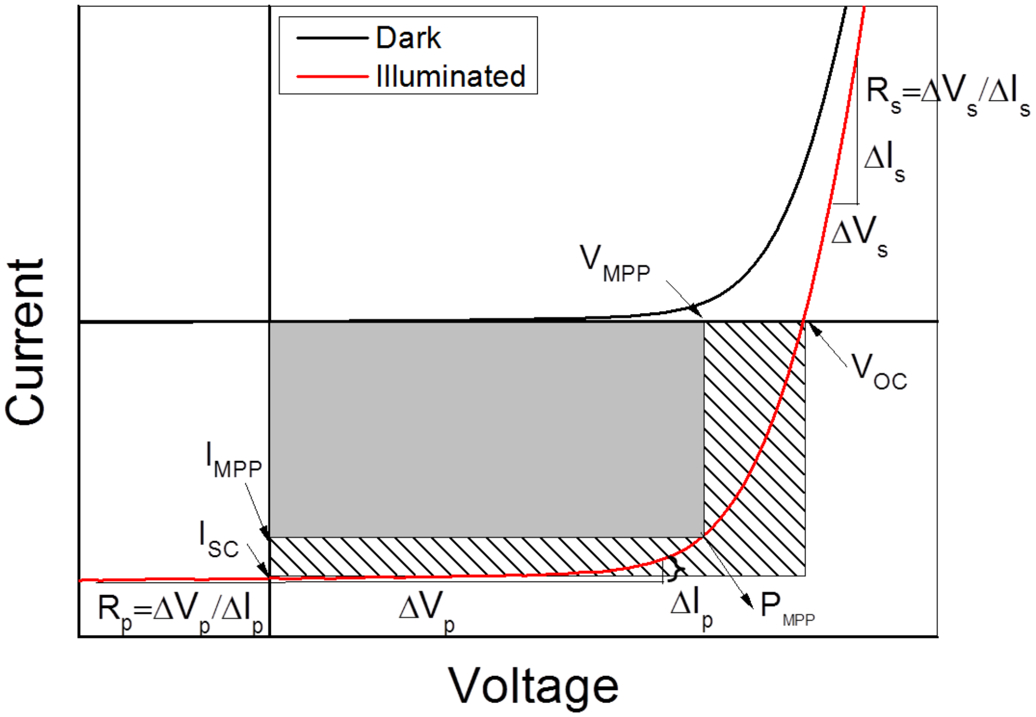

Figure 2.4: Current voltage characteristics of a CIGSSe solar cell in the dark (black) and under AM 1.5 illuminations (red). The electrical parameter indicated in Figure 2.4 are the series resistance R_s, the parallel resistance R_p, the voltage and current at the maximum power point (V_{MPP} and I_{MPP}) as well as the open circuit voltage (V_{OC}) and the short circuit current (I_{SC}). Also indicated is the maximum power point of the device. The maximum power point (P_{MPP}) is derived by curve sketching of the function $P(V)=I\cdot V$.

From the I-V curve, several fundamental parameters could be extracted, which are described below:

- Open circuit voltage V_{OC}: The voltage for which no current is flowing through the device ($V_{OC}=V\,(I=0A)$), which is the maximum voltage obtainable from the device.

- Short circuit current I_{SC}: The current at zero bias voltage, I_{SC}= I (V=0V), represents the photocurrent contribution to the electronic transport.
- Fill factor FF: It describes the squareness of the I-V curve and is defined as

$$FF = \frac{P_{MPP}}{V_{OC} I_{SC}} = \frac{V_{MPP} I_{MPP}}{V_{OC} I_{SC}} \qquad \text{Eq.2.4}$$

where P_{MPP} corresponds to the power at its maximum (Maximum Power Point), and is given by V_{MPP} and I_{MPP}. The fill factor FF can be graphically understood as the ratio between two rectangles: the one enclosed by the point of maximum power of the I-V curve and the two axes and the other defined by V_{OC}, I_{SC} and the two axes. Green found an empirical formula for the fill factor, which is defined [30]:

$$FF_0 = \frac{v_{oc} - \ln(v_{oc} + 0.72)}{v_{oc} + 1} \qquad \text{Eq.2.5}$$

where v_{oc} is given by the equation, $v_{oc}=qV_{oc}/AkT$, as a function of the ideality factor A. Including the series and the parallel resistances this expression is given [40]:

$$FF = FF_0 (1 - r_S) \left(1 - \frac{(v_{oc} + 0.7)}{v_{oc}} \frac{FF_0 (1 - r_S)}{r_P} \right) \qquad \text{Eq.2.6}$$

where r_s and r_p are normalized by the equation, $r_{s(p)}=R_{s(p)}\,J_{sc}/V_{oc}$. The fill factor depends on the series and parallel resistances as well as on the diode ideality factor. These dependencies are shown in figure 2.5 [41].

Finally, the energy conversion efficiency can be calculated according to Eq. 2.7:

$$\eta = \frac{P_{MPP}}{P_{in}} = \frac{V_{OC} I_{SC} FF}{P_{in}} \qquad \text{Eq.2.7}$$

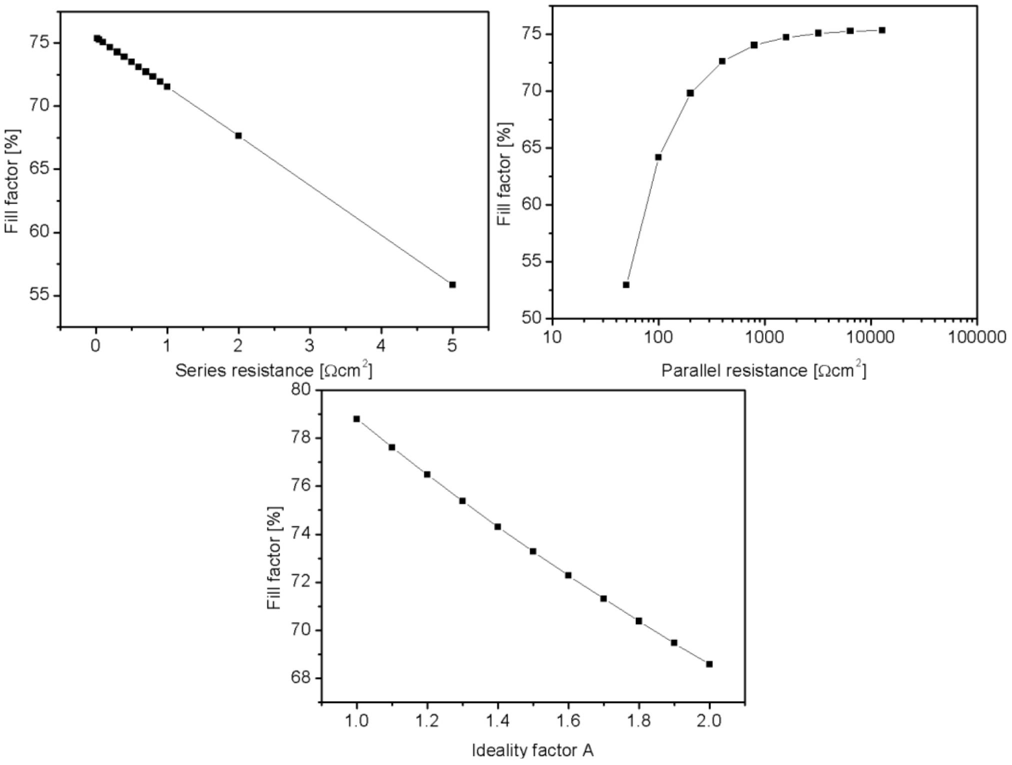

Figure 2.5: Dependence of the fill factor on the series resistance (a), parallel resistance (b), and ideality factor (c) as derived from Eq.2.6 [41].

2.2.3 Role of buffer layer

The role of buffer layer is still under controversial discussion. The primary function of a buffer layer in a heterojunction is to form a junction with the absorber layer while admitting a maximum amount of light to the junction region and absorber layer [42]. Chalcopyrite solar cells without a buffer layer achieve efficiency from 2-8%. It is essential to use a buffer layer to raise the cell efficiencies of the solar cell. The beneficial effects of the buffer layer ranges from modifying the absorber surface chemistry to protecting the sensitive interface during the subsequent window deposition [43]. The absorber film becomes better suited for air exposure when protected by a buffer layer. In addition, the energy band gap alignment maybe influenced by the buffer and or its deposition process. The crystal mismatch between the absorber and buffer should be as minimal as possible.

Although the highest efficiency of chalcopyrite based solar cell is achieved with CBD-CdS buffer layer, there are several reasons to substitute this material. Due to the environmental reasons and a relatively low energy band gap (2.4 eV) of CdS, which limits the levels of the optimum performance of the cells in the low wavelengths region (<520 nm), the development of the Cd-free alternative buffer layers is required. Most promising materials are In_2S_3, Zn(S,O) and (Zn,Mg)O. Table 2.1 shows a selection of such alternative buffers on $Cu(In,Ga)Se_2$ and $Cu(In,Ga)(S,Se)_2$ absorber layers.

Table 1.1: Selection of buffer layer materials for Cu(In,Ga)Se2 and Cu(In,Ga)(S,Se)2 thin film solar cells. A more detailed summary can be found in a review reported by Naghavi et al. [44]. Efficiency values with * correspond to cells with MgF2 anti-reflection coating.

Buffer layer	Deposition method	Absober	Efficiency %
CdS	CBD	$Cu(In,Ga)Se_2$	20.3 [31]
Zn(S,O)	CBD		18.5
	ALD		18.5*
(Zn,Mg)O	ALD		18.1*
In_2S_3	co-evaporation		13.3
	compound-evaporation		15.2
	reactive sputtered		11.1
	ceramic sputtered		13.3
	ALD		16.4
	USP		13.4
Zn(S,O)	CBD	$Cu(In,Ga)(S,Se)_2$	14.9
(Zn,Mg)O	Sputtered		13.1
In_2S_3	ILGAR		16.1 [1] [45]
	USP		12.4

---

[1] The new record was achieved with a modified In_2S_3 buffer after the end of this practical work. With the modified In_2S_3, it has not yet used in a combination with the ZnS nanodots as buffer layer.

The most important requirements for a good candidate of the alternative buffer material are listed in the following [46-48]:

- n-doping
- Sufficiently wide band gap in order to have minimum absorption losses. The band gap of the traditional CdS material is Eg=2.4 eV.
- A beneficial conduction band alignment to the absorber and the undoped ZnO
- Formation of no or only low defect density at the heterointerface to the absorber to reduce the recombination velocity
- Fermi level close to the conduction band to reach a high built in potential and high recombination barrier for holes at the interface
- High conductivity for efficient electron transport from the heterojunction to an external circuit

Finding an optimal Cd-free alternative buffer layer for chalcopyrite solar cells is still a great challenge. Due to the polycrystalline nature of the p- and n-type layers in the chalcopyrite thin film solar cell, defects at the interface are unavoidable. The defects at the junction originate from crystallographic point defects due to non-stoichiometry of the semiconductors at the interface [48]. These defects influence the potential distribution at the junction and can add additional transport paths for charge carrier tunneling and recombination [46]. Therefore, surface passivation of absorbers, which can keep excess charge carriers from recombining, is important for high energy conversion efficiencies of solar cells. In this thesis, a combination of ZnS nanodots passivation layer plus the Spray-ILGAR In_2S_3 in a point contact type structure is used to engineer the heterojunction interface and overcome this limitation.

2.2.4 Buffer layer deposition methods

The deposition methods for these alternative buffer layers are: chemical bath deposition (CBD), atomic layer deposition (ALD), ion layer gas reaction (ILGAR), physical vapor deposition (PVD) (sputtering and evaporation) and spray pyrolysis. In this section, a brief overview of methods for the deposition of the buffer layer is given. A special emphasis will be given to atomic layer deposition and spray pyrolysis, since both are related to the Spray-ILGAR process. These various techniques are reviewed by Siebentritt [49], Hariskos et al. [50] and more recently by Naghavi et al. [44]. Since the Spray-ILGAR is the main topic of this thesis, it is discussed separately in section 2.2.5.

As a general remark for the following reported cell efficiency, all components of the cell are important for the output, especially the absorber and the buffer layers.

Chemical bath deposition (CBD)

CBD is the most classical and frequently used process for the buffer layer deposition. Solar cells with CBD CdS as buffer layer yield the highest and most reproducible cell efficiencies so far. Among the alternative Cd-free buffers, the CBD-Zn(S,O) is one of the most popular candidates for replacing the CBD CdS. Efficiencies up to 18.6% have been obtained using CBD-ZnS as buffer layer in $Cu(In,Ga)Se_2$ (CIGS) based cells [29]. The record efficiency of 15.7% with CBD-In_2S_3 buffer layer was obtained in 1996 [51].

The CBD sulfide films involve the precipitation of a compound from a corresponding metal complex and sulfur precursor solution. A beneficial side effect of the CBD technique is the chemical cleaning of the absorber surface in the ammonia containing batch [52] and the recovery of the surface inversion [53]. However, CBD is a batch process, which is difficult to implement in an in-line production. Additionally, it is a wet chemical method, which requires substrate drying for the subsequent vacuum-based front contact deposition and generates a substantial quantity of liquid wastes. A substituting deposition technique compatible with in-line processing is highly required.

Atomic layer deposition (ALD)

ALD is also referred to as Atomic Layer Chemical Vapor Deposition (ALCVD) or Atomic Layer Epitaxy (ALE) when epitaxial crystalline substrates are used [54]. Several materials, Zn(O,S), (Zn,Mg)O, and In_2S_3 deposited by ALD technique have been successfully applied as buffer layer for the CIGS based solar cells, with the record efficiencies 18.5%, 18.1% and 16.4% respectively [55-57].

The ALD method, a modified CVD process, is a cyclic vacuum-based method for the deposition of semiconductor thin films, where the reactants are pulsed into the reactor sequentially and the film grows layer-by layer. For the deposition of sulfides, a monolayer of a metal-organic precursor compound is deposited onto the substrate in short pulses of 100-300 ms by a carrier gas. Subsequently, this layer is converted to metal sulfide by H_2S gas.

ALD produces the film with very conformal coverage, excellent thickness and compositional control for optimal band alignment. In addition, it is possible to integrate the buffer deposition in an in-line vacuum system. The main drawback of this technique is the slow deposition rate compared to other deposition methods. The reaction principle of the ALD process is very similar to the principle underlying the Spray-ILGAR process, which is the focus of this thesis.

Physical vapor deposition(PVD)

The PVD techniques (sputtering and evaporation) can be easily upscaled for industrial in-line production due to its vacuum processes. Furthermore, there is not any liquid waste produced. For evaporated In_2S_3 buffer layer, recently the record efficiency of 15.2% has been obtained on Cu(In,Ga)Se_2 absorber [58]. Two different approaches, co-evaporation of indium and sulfur and direct evaporation of In_2S_3 have been performed for the buffer deposition. The co-evaporation method, employed in the reported record cell, depends strongly on the quality of the In_2S_3 source which could vary over long deposition duration. The difference of these two methods is not yet fully investigated. An efficiency up to 16.1% has been reported with sputter Zn(Mg,O) buffer layer on Cu(In,Ga)Se_2 absorbers [59].

The problem with vacuum evaporation is the poor continuous coating of the CIGS films, while the sputter deposition leads to more conformal coverage [44]. However, due to the high evaporation temperatures and the high vacuum, such processes are rather expensive for producing buffer layer.

Spray pyrolysis

Spray pyrolysis is a low cost, non-vacuum and large-area scalable deposition technique, which has been used over the years for the production of simple oxide, mixed oxide and other chalcogenide films. The method was first described by Camberlin and Skarman in 1966 [60]. It can be categorized by the droplet formation method between the ultrasonic, pneumatic, or electrostatic spray pyrolysis methods. Spray pyrolysis is a process where a precursor solution, containing all the constituent elements of the compound, is nebulized in the form of tiny droplets onto the preheated substrate, where upon the thermal decomposition of the precursor an adherent film of a thermally more stable compound forms [61]. With spray pyrolysis In_2S_3, 12.4% cell efficiency has been obtained on $Cu(In,Ga)Se_2$ solar cell [62].

However, as every other method, even though the method of spray pyrolysis is well established, it has some disadvantages, main ones of them can be listed as follows: possible oxidation of sulfides when processed in air atmosphere and film quality may depend on the droplet size and spray nozzle.

2.2.5 Spray-ILGAR

Introduction

The spray ion layer gas reaction (Spray-ILGAR) method, which is the focus of the present work, is a modification of the ILGAR technique. The ILGAR process was developed and patented [63] at the Hahn-Meitner-Institut (now Helmholtz Zentrum für Materialien und Energie) in Berlin. Originally, the precursor solution was applied onto the substrate by dipping it into the metal precursor solution and then the remaining solid precursor film was converted to metal oxide or sulfide by wet ammonia or H_2S gas, respectively. This ILGAR technique is referred to as ''Dip-ILGAR'' [64, 65]. The corresponding process is shown in Fig.2.6 for the case of In_2S_3 deposition from an $InCl_3$ solution. It has been successfully used for the deposition of ZnO and ZnS buffer layers for chalcopyrite thin film solar cells [66].

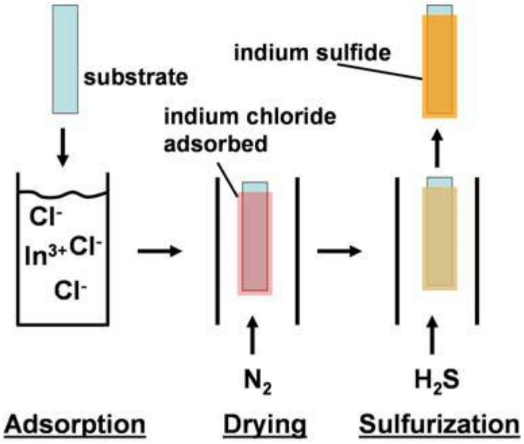

Fig. 2.6: Schematic sketch of the dip ILGAR setup for deposition of In_2S_3 from an $InCl_3$ solution [67].

Since the dipping cannot be integrated into an in-line process and the deposition rate in each cycle is limited by the adherence of the liquid film, the spray version of the ILGAR technique has been developed. At first, the solution was sprayed to the moderately heated substrate (below 100 °C) by a pneumatic nebulizer. The formed aerosol was transported by a N_2 carrier gas stream and arrived vertically at the substrate surface. Afterwards, the layer was converted by the corresponding gas as in the dip ILGAR process. Due to the moderate substrate temperature and the setup geometry, the deposition layer was not homogeneous even after post annealing. An optimization of the original Spray-ILGAR construction with the goal of a homogeneous coating led to the design shown in Figure 2.7, at which the aerosol flows under an angle of 45° over the heated substrate. In this case, the aerosol can pass the substrate and turbulences are reduced. Additionally, the pneumatic nebulizer was replaced by an ultrasonic source, which produces a much finer mist (around 2µm in average formed from EtOH), and substrate temperature was increased to about 200-250 °C, which results in a more complete evaporation of the aerosol droplets in the vicinity of the substrate surface. The layer quality was improved through these modifications. For a lab scale Spray-ILGAR deposition, the schematic sketch and a photograph of the setup are shown in Figure 2.7. This is now our standard Spray-ILGAR process. The ILGAR technique was awarded as German High Tech Champion in 2011 by Fraunhofer Society [68]. More details of this process are described in the following section.

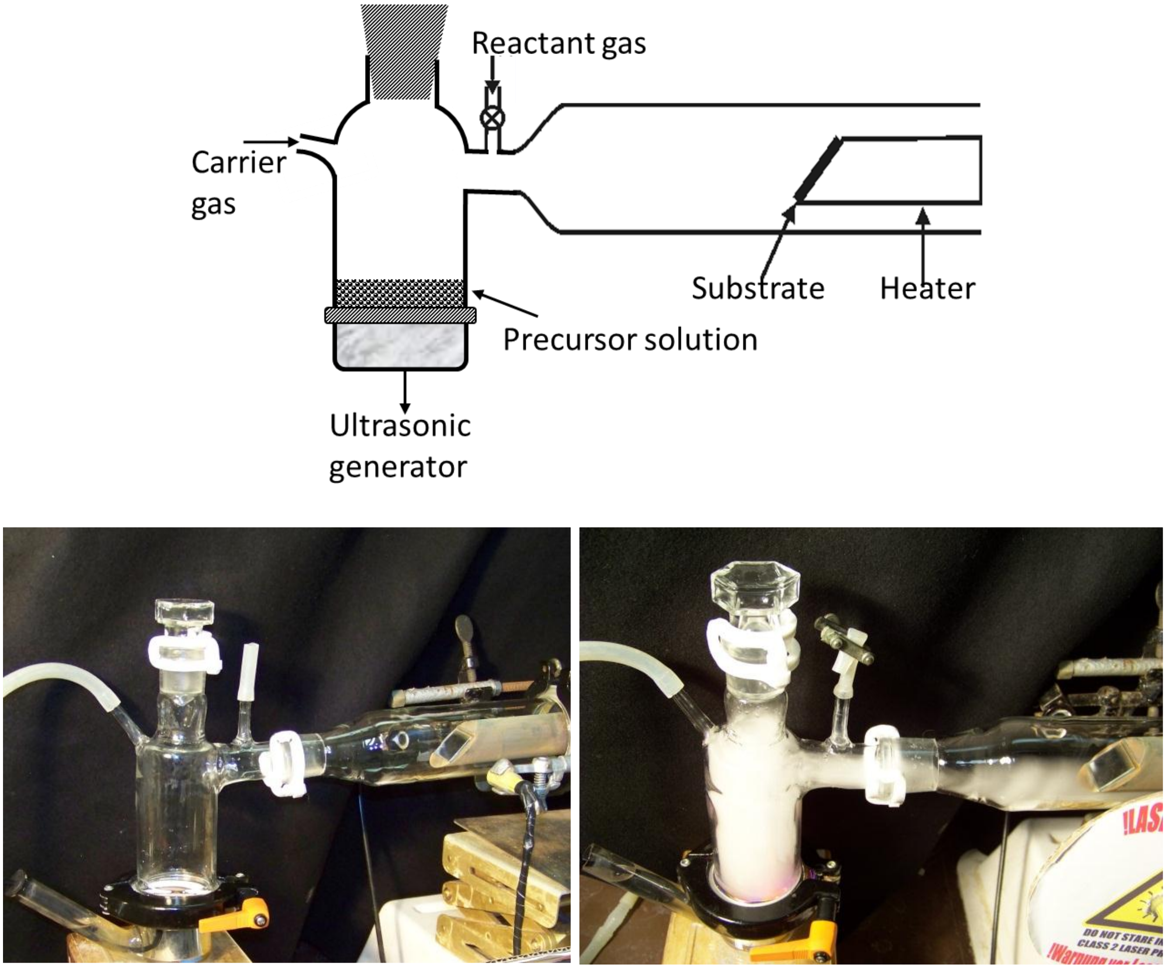

Figure 2.7: (a) Schematic sketch and (b) Photograph of the lab-scaled Spray-ILGAR deposition set up before and after switching on the ultrasonic generator.

Standard process

The Spray-ILGAR is a sequential and cyclic 2-step process. The standard process in the case of In_2S_3 is described below. In a first step, an alcoholic $InCl_3$ solution is nebulized by an ultrasonic atomizer which generates a fine mist of aerosol droplets above the surface of the solution. The aerosol droplets are then blown by a N_2 carrier gas to a heated substrate, where the droplets evaporate and decompose forming a precursor film $In(O_x,Cl_y,(OH)_z)$. In a standard process, this lasts for 1min. In the second step, H_2S gas is introduced for 20s to convert the precursor film into In_2S_3. These two steps are repeated sequentially until the desired film thickness is grown. As remark, between these two steps is a pause with 10s N_2 purging, which allows the aerosol or H_2S to be cleared from the chamber before the sequential step. The schematic diagram of this process is shown in Figure 2.8.

The duration of the single step in the Spray-ILGAR process and the experimental parameters for the In_2S_3 thin film deposition were found empirically by Allsop et al. to optimize the efficiency of the solar cells. These parameters are listed in Table 2.2. Full details of the method are published elsewhere [69]. With this standard process, Allsop et al. deposited In_2S_3 buffer layers for highly efficient $Cu(In,Ga)(S,Se)_2$ thin film solar cells. The In_2S_3 preparation in this thesis is based on this recipe described above. However, very recently, the process is modified by addition of a small amount of H_2O into the In precursor solution, which results in much better PV performance, which will be discussed in the following.

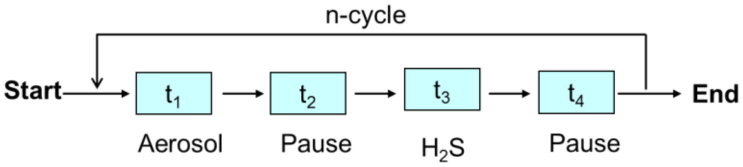

Figure 2.8: Schematic diagram of Spray-ILGAR process.

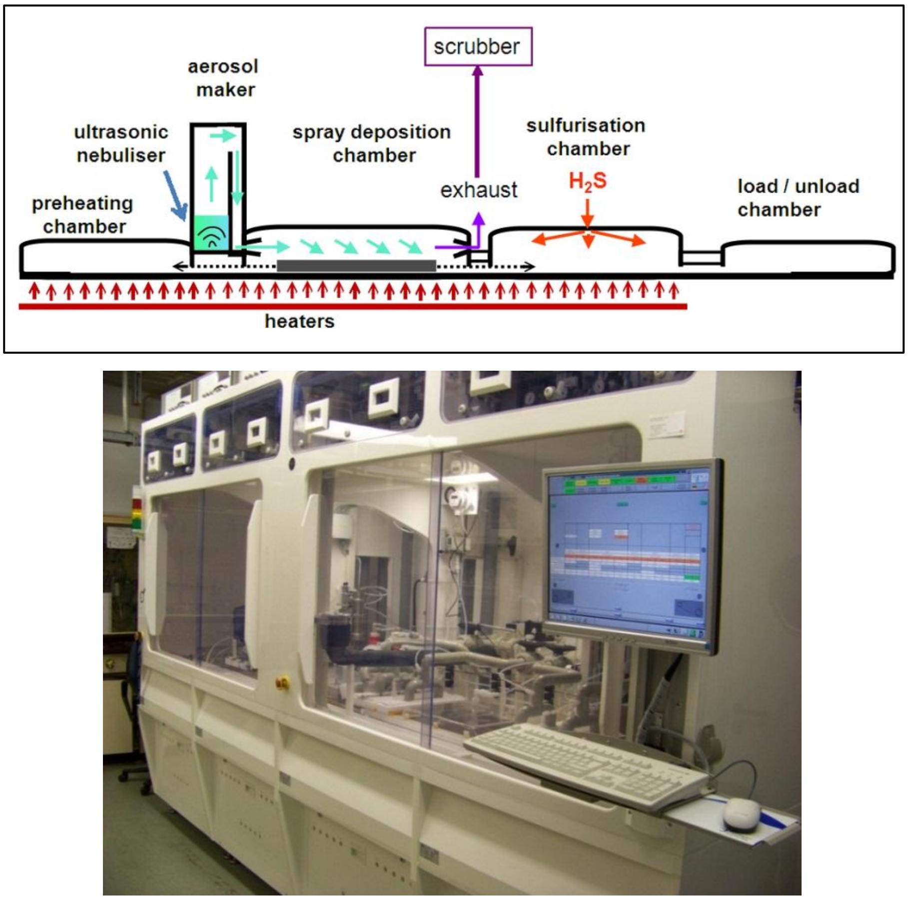

Figure 2.9: Schematic (top) and photograph (bottom) of an ILGAR in-line prototype coater for substrate up to 30x30 cm^2 designed by SINGULUS STANGL Solar in collaboration with Helmholtz Zentrum Berlin [70].

Table 2.2: Experimental parameters of the Spray-ILGAR process for the deposition of In_2S_3 film.

Carrier gas	4.5 L/min N_2
Reactive gas	1L/min H_2S
Precursor	$InCl_3$
Solvent	EtOH
Precursor concentration	25mM
Deposition Temperature	225 ºC
Spraying cycles	6

Up-scaling of the Spray-ILGAR process

While successfully working on the lab scale, the challenges faced when working on upscaling are different. An up scaling 10x10 cm^2 substrate size was developed first to demonstrate the performance of the Spray-ILGAR In_2S_3 buffer on mini-modules. Modules based on $Cu(In,Ga)(S,Se)_2$ abosorbers reached an efficiency of 12.4% [71]. Further development of the fully inline process to a moving 10 cm wide tape has shown that the In_2S_3 layers could be produced with an In yield better than 30% and a linear production speed of 1m/min [70]. Nowadays, an ILGAR in-line prototype coater for substrates up to 30x30 cm^2 designed by SINGULUS STANGL Solar in collaboration with Helmholtz Zentrum Berlin is being optimized. A schematic diagram and photograph of the prototype are shown in Figure 2.9. The sample is first loaded in the load chamber and then goes to the preheating chamber where it is heated up until the desired temperature is reached. Then the ultrasonic nebulizers generate the aerosol which is deposited on the substrate in the deposition chamber. Later, the film is converted in the sulfurization chamber by H_2S. The process is repeated as many times as necessary. So far, the best cell efficiency based on CIGSSe modules from AVANCIS is 13.7% compared to 13.6 ± 0.2% for the CdS reference.

Characteristics and application

Spray-ILGAR, being a low cost, fast, quasi-dry and non-vacuum deposition technique, has been successfully applied for the production of semiconductor thin films, e.g. chalcopyrite absorber layers and buffer layers. A closed, smooth and adherent film could be deposited on almost any substrate, as long as the substrates do not react with the chemicals, which are basically a metal salt and a reactant gas such as H_2S. And of course, the substrates have to be stable at the working temperature. The ILGAR buffer process is robust, with a wide processing window in terms of layer composition, thickness and process temperature. It is also possible to grow films with composition gradients or multi layers.

The method of material delivery and the experimental setup in the Spray-ILGAR process are similar to the ones of spray pyrolysis although the chemical reaction is different. The spray step for the In_2S_3 deposition is an aerosol assisted chemical vapor deposition (AACVD) process with a complex chemical mechanism which is discussed by Gledhill et al [72]. Spray-ILGAR can be regarded as a further developed process of spray pyrolysis, where there is one further step to convert the precursor film to the corresponding chalcogenide with a reactant gas. In contrast, the cyclic processing and the resulting growth mechanism are more similar to ALD.

The Spray-ILGAR and spray pyrolysis process have been successfully used for the deposition of various materials in our group, such as In_2S_3, Sb_2S_3, ZnS, MnS, ZnO, Al_2O_3,

VO_2, TiO_2 or $CuInS_2$. So far, the main application is in thin film photovoltaics. This technology can be successfully used for deposition of different layers within a solar cell: Cd-free buffer layer [73, 74], chalcopyrite absorber [75] as well as the intrinsic ZnO window layer [76] and Al_2O_3 barrier layer [77]. So far, the best cell efficiency with ILGAR In_2S_3 buffer on an industrial $Cu(In,Ga)(S,Se)_2$ absorber (AVANCIS) was 14.7% (certified by ISE, Freiburg) [73], while very recently, with modified ILGAR In_2S_3 buffer layer, the cell based on industrial absorber reaches 16.1% (certified by ISE, Freiburg) [45]. The sprayed i-ZnO window layer gives comparable solar cell results as rf-sputtered i-ZnO [78]. With ILGAR $CuInS_2$ absorber, the solar cells reach efficiencies of up to 4.1 % and thus just have proved the applicability of this method for the solar cell absorber deposition. The spray Al_2O_3 [77] works successfully as barrier layer for the solar cells on steel substrates to block Fe diffusion to the chalcopyrite absorber layer, which is devastating.

2.3 Background of this thesis

The Spray-ILGAR In_2S_3 buffers (deposition from $InCl_3$ solution) produce cells with a higher short circuit current and an equal or better fill factor compared to the CdS [69, 79]. However, the open circuit voltage is slightly reduced. Allsop et al. proposed a novel point contact buffer layer [80], which replaces the conventional CdS buffer material with a combination of a not closed ZnS passivation film plus an In_2S_3 layer both deposited by Spray-ILGAR. The first should reduce the detrimental charge carrier recombination at p-n junction; the latter is needed for the charge carrier transport because of the low conductivity of ZnS. A first test with such a buffer had improved the cell performance as compared to a single In_2S_3 buffer layer [74]. Moreover, in this reported paper, the photoluminescence of the three different buffers CdS, ZnS and In_2S_3 on $Cu(In,Ga)(S,Se)_2$ absorbers are compared, which shows a similar luminescence intensity for CdS and ZnS, but for In_2S_3 a clearly lower intensity. The open circuit voltage correlates with the photoluminescence intensity and is estimated using generalized Planck’s law, which is in good agreement with the measured values [30]. Therefore, ZnS is assumed to have a better interface to the absorber with less recombination than In_2S_3. Based on these first results as well as on the theoretical calculations, a controlled deposition of ZnS nanodot films has been developed and investigated in detail in this thesis.

For the fabrication of ZnS nanostructures, numerous methods have been investigated [81-85]. However, in view of the Spray–ILGAR preparation of In_2S_3, it is highly desirable to use a spray based method also for the synthesis of nanodot ZnS. Thus, a consecutive process with the same set-up had to be developed for the described double compound buffer. However, so far, only homogenous layers have been produced by the Spray-ILGAR technique. Ultrasonic spray process has been proven to be a versatile technique and been revived by several research groups as a generalized synthetic method for the preparation of nanostructure materials [86-89]. Nevertheless, in prior reports, the particle size is relatively large, up to micron size regime (0.2-2μm) [88, 90], coated with an organic ligand shell [86], or the process temperature is relatively high [87], all of which are not suitable for the application as buffer layers in chalcopyrite solar cells. Therefore, it remains a serious challenge to elaborate a method to produce high quality and uncoated semiconductor nanodots with a narrow size distribution at the requisite low temperature (≤ 250 °C).

The realization of nanodot ZnS films by the Spray-ILGAR process is the main topic of this thesis. In the 2nd part, these films are used, characterized and optimized for the development of the passivation / point contact bilayer buffer.

Chapter 3

ZnS nanodot preparation by Spray-ILGAR and Spray-CVD

This chapter describes the implementation of two processes Spray-ILGAR and Spray-CVD for the preparation of ZnS nanodots. In section 3.1, the development of the Spray-ILGAR process is described which is dedicated to the generation of ZnS nanodots and other semiconductor nanocrystals with controllable size to some extend and dot density. The influence of the process parameters (i.e. precursor concentration, pH value of the solution, number of process cycle, deposition temperature, solvent, precursor and H_2S) on the growth mechanism and therefore on the morphology and coverage of the surface is analyzed in detail. In section 3.2, a process which combines the two sequential Spray-ILGAR steps (spray and sulfurization) into a simultaneous and continuous step, called Spray-CVD, is introduced. The similarities and differences of the obtained nanodots from these two processes are investigated. Two kinds of reactant gas source are evaluated in the Spray-CVD process.

3.1 Spray-ILGAR deposition of ZnS nanodots

In the following section, the deposition of ZnS nanodots by Spray-ILGAR will be described. By the choice of appropriate precursors, zinc precursor compound and solvent, the deposition of ZnS nanodots could be realized (section 3.1.1). The detailed experimental description of the process is introduced in section 3.1.2. In particular, the influence of the process parameters on the preparation of the Spray-ILGAR nanodots is investigated (section 3.1.3).

3.1.1 Selection of chemical reagents as precursors

The first step in the development of a Spray-ILGAR process for the deposition of ZnS nanodot films is the choice of the appropriate zinc-containing precursor compound and solvent for the spray solution. Among the features of chemical species that are important to consider during aerosol processing are volatility, reactivity, solubility, wetting and polarity. The choice of the solute and solvent will determine the product or the process, which is the main topic of the following section.

3.1.1.1 Selection of a zinc-containing precursor compound

The first step of the Spray-ILGAR process is an aerosol assisted chemical vapor deposition (AACVD). The precursors are delivered to the surface via an aerosol which will evaporate before reaching the heated substrate surface leading to a deposition by thermal decomposition from the gas phase. Hence, the volatility of the zinc containing compound should be taken into account because it may determine the presence or absence of gas-phase reaction and the deposition rate. In the following, the arguments that lead to the choice of zinc acetylacetonate for the decomposition of ZnS are discussed. There are mainly three metal containing compounds can be considered:

- metal-inorganic compounds, such as metal nitrates, metal carbonates, metal sulfates: generally inexpensive, commercially available, but nonvolatile.
- metal-organic compounds, such as carboxylates, alkoxides, diketonates, amides: in particular, diketonates are frequently used as sources of metal for CVD.
- organometallic compounds: sufficiently volatile, but often toxic or explosive in nature

Zinc acetylacetonate (abbreviated as $Zn(acac)_2$ in the following) is a member of metal-diketonate family of compounds which are commonly used in metal-organic chemical vapor deposition (MOCVD) and atomic layer deposition (ALD) processes, especially where air stability and low process temperatures are required. This compound consists of metal-oxygen bonds which are weak and can be broken easily. It has successfully been used in hydrothermal processing, solution chemistry, MOCVD, laser-assisted technique, and spray pyrolysis for the production of nanostructure ZnO [91]. It has also some other advantages: no toxicity, free of pollution, ease of use, wide availability and no unwanted by-products to the target products. The molecular formula of $Zn(acac)_2 \cdot H_2O$ is $Zn(CH_3COCHCOCH_3)_2 \cdot H_2O$. The schematic molecular structure of $Zn(acac)_2$, is shown in Fig.3.1. Its structure is shown in Figure 3.1. A good "horse" with a good "saddle" wins success. An appropriate solvent to dissolve solute is also one of the prerequisites to obtain a nanodot film using the Spray-ILGAR process. Subsequently, the selection of solvent is discussed.

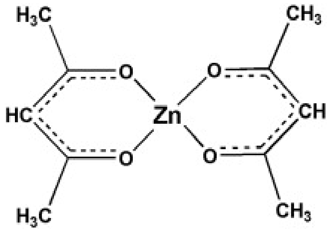

Figure 3.1: Structure of the metal-organic zinc compound zinc acetylacetonate [92].

3.1.1.2 Selection of solvent

The solubility of the solute in solvent is important in aerosol processes in which the solute is first dissolved in a solvent in order to deliver the solute to system using ultrasonic generator in this work. Solubility can affect particle morphology by different solubility of the reagent, compositional homogeneity during powders formation, and different transport rates during film deposition [93]. The effect of solubility on morphology and composition has been demonstrated [94-97].

Generally, “Like dissolves like” is a good rule of thumb in considering a solvent for the zinc-containing compound. Zn(acac)$_2$ is soluble in organic solvents, but poorly soluble in water. A compact ZnS film instead of a nanodot film was obtained by the Spray-ILGAR process when EtOH served as solvent to dissolve Zn(acac)$_2$ [74, 98]. An organic solvent doesn’t seem a good choice for the preparation of nanodots. See further discussion about the influence of solvent in section 3.1.3.5. A water-enhanced pyrolysis mechanism of Zn(acac)$_2$ is reported by Arri [99] and Fiddes et al [100]. Therefore, water is chosen as solvent for the precursor. In addition, a certain amount of acetic acid (HAc) is mixed to support dissolving Zn(acac)$_2$. Subsequently, the applicability of the zinc containing compound and solvent for the deposition of ZnS nanodots using Spray-ILGAR is discussed.

3.1.2 Deposition of Spray-ILGAR ZnS nanodots

In this section, the deposition of Spray-ILGAR ZnS nanodots is realized with the selected zinc containing compound Zn(acac)$_2$ and solvent H_2O. After deposition on a Si substrate, the surface is characterized by scanning electronic microscope (SEM). The experimental description and process parameters are described in detail.

ZnS nanodots were prepared by the Spray-ILGAR method using 25 mM aqueous Zn(acac)$_2$ solution with pH=4 adjusted by acetic acid as precursor and H_2S as reactant gas. This precursor solution was ultrasonically nebulized at 1.6 MHz into micro droplets for 1min. The produced dense mist was carried over the heated substrate (200 ºC) by N_2 stream (2.5 L/min), depositing a microscopically homogeneous ZnO precursor film. In the second step, the deposited precursor layer was converted to ZnS by H_2S gas. It should be noted that between these 2 steps is 10s N_2 purge which allows the aerosol or H_2S to clear the chamber before the sequential step. The spraying step, sulfurization step and 2 times purging consist a Spray-ILGAR cycle, which can be repeated to get the desired density of nanodots. The process and preparation parameters in this thesis are shown in Table 3.1 and Table3.2 respectively.

Table 3.1: Process parameters of the Spray-ILGAR process for the deposition of ZnS nanodot film.

Step	1	2	3	4
	Spray	Pause after spray step	H_2S sulfurization	Pause after H_2S step
Time (s)	60	10	30	10

Table 3.2: Preparation parameters of the Spray-ILGAR process for the deposition of ZnS nanodot film.

Carrier gas	2.5 L/min N_2
Reactant gas	1L/min H_2S
Precursor	Zn(acac)$_2$
Solvent	H_2O
Precursor concentration	25mM
pH value of Precursor	4

Deposition Temperature	200 ºC
Spraying cycles	20

When ZnS film is prepared at 200 ºC for 20 cycles on a Si substrate under the condition shown in Table 3.1 and 3.2, the SEM micrograph (Figure 3.2) clearly shows a rather homogenous size distribution of nanodots, in the range of 5-10nm. The density of the nanodots here is about 3×10^{11} cm^{-2} and the distance inbetween the nanodots is smaller than 100nm. However, the ZnS nanodot film could be tuned from a film with distributed nanodots to a compact film by the variable preparation parameters shown in Table 2.2. See the following discussions in section 3.1.3. It is worth mentioning that the distance inbetween the nanodots (<100 nm) is in the appropriate range for the later application as passivation layers (See Chapter 6). Another important point to be mentioned is that unlike other preparation methods, these nanodots are free of organic capping on their surface. The direct contact between the passivation and the absorber layer is desired for the application since the effect of the organic capping on the nanodots could be detrimental to the solar cell device. In addition, the process temperature is below 250 ºC, which is a prerequisite to avoid deterioration to the solar device. Therefore, the nanodots in our case without insulating surfactant ligands can serve as a good candidate for later application as passivation buffer layer in chalcopyrite thin film solar cells.

In the next section, the influence of the parameters to the preparation of the nanodots will be investigated. This will help to clarify the role of the different parameters on the nanodots formation.

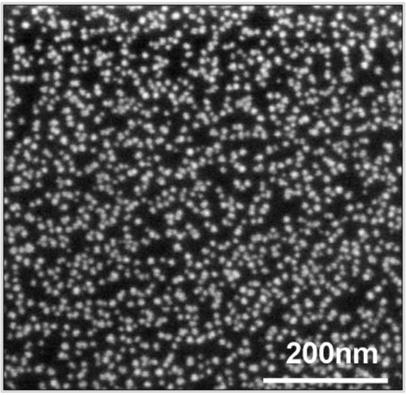

Figure 3.2: SEM image of ZnS nanodots obtained by Spray-ILGAR.

First tests with other semiconductor materials, such as indium and copper chalcogenide, result in similar nanodot films, as shown in Figure 3.3. Therefore, it is believed that Spray-ILGAR is a more general method to prepare semiconductor nanoparticle films, only volatile starting materials are required. This opens exciting opportunities for the incorporation of semiconductor nanoparticles in a variety of new applications.

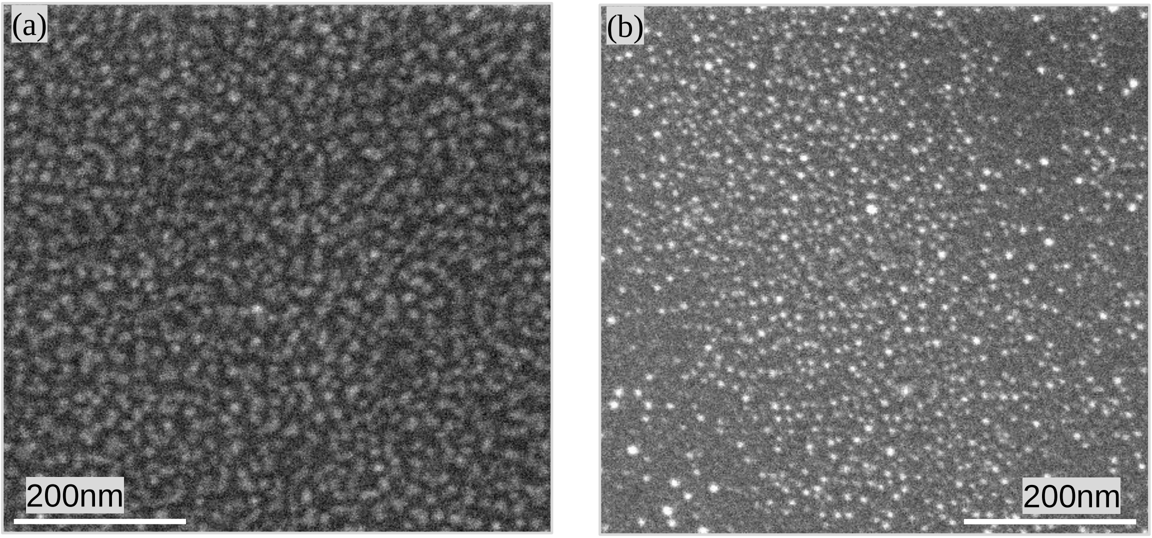

Figure 3.3: SEM images of a) In_2S_3, b) Cu chalcogenide, nanodots obtained by Spray-ILGAR.

3.1.3 Influence of the process parameter on the deposition process

Varying the process parameters has a direct impact on the growth mechanism and therefore on the morphology and coverage of the surface. A systematic study firstly aims to clarify the influence of the different conditions on the nanodots formation. Secondly, it provides information for the optimization of external parameters towards obtaining a homogeneous nanodot film. Thirdly, it gives hints for the further investigation of the growth mechanism.

The reference sample consists of ZnS nanodots obtained in 20 process cycles at 200 ºC, with the detailed description in section 3.1.2. In each set of examples, one of the variables was varied while all remaining variables were kept constant. The dependence of the deposition process on the parameters such as precursor concentration (section 3.1.3.1), solution pH value (section 3.1.3.2), number of process cycles (section 3.1.3.3), substrate temperature (section 3.1.3.4), solvent (section 3.1.3.5), zinc-containing compound (section 3.1.3.6), reactant gas (section 3.1.3.7) were analyzed in detail.

3.1.3.1 Precursor concentration

Precursor concentration is one of the most important parameters in the deposition of the ZnS nanodot film. For this experiment, precursor solutions of different concentrations were nebulized, keeping all other parameters constant as described in section 3.1.2. In all cases, the films were collected on the silicon substrate.

Figure 3.4 shows SEM pictures of the ZnS nanodots obtained with10mM, 25mM, and 50mM of aqueous $Zn(acac)_2$ solution on Si substrate, keeping all other process parameters as indicated in Table 3.2. Obviously, the density of the ZnS nanodots increases with the concentration of the starting precursor solution. The film grows from distribute nanodots gradually to almost a compact film. However, interestingly, the size of the nanodots remains the same instead of growing. The independence of the nanodot size on the precursor concentration suggests that Zn is transported via the vapor phase to the substrate and subsequently decompose, which is a CVD process. In the case that one aerosol droplet yields one produced particle, which would be actually a liquid to solid process, the size of the particle could be predicted in accordance with modification to the Lang equation (eq 3.1)[101], which describes the mean drop size of an aerosol produced by ultrasonic nebulization as a function of the frequency of the atomization frequency and the solution properties.

$$d_1 = 0.34\left(\frac{8\pi\sigma}{\rho f}\right)^{1/3} \qquad \text{Eq.3.1}$$

Here, d_1 is the droplet diameter, σ is the surface tension, ρ is the solution density and f is the atomization frequency.

When the properties of both the precursor solution and droplet diameter are known, the diameter of the product particle (assuming spherical particles) could be estimated by Eq 3.2.

$$d_2 = \left(\frac{M d_1^3 C}{1000\rho}\right)^{1/3} \qquad \text{Eq.3.2}$$

Here, d_2 is the produced particle diameter, M is molecular weight, C is the solution molar concentration, d_1 is the droplet diameter and ρ is the solution density.

If the droplets landed and dried on the substrate surface, the particle diameter should be proportional to the solution concentration. Obviously, this one to one relationship cannot be exploited to the nanodots preparation system under consideration. Hence, the process is a gas to solid conversion rather than a liquid to solid conversion.

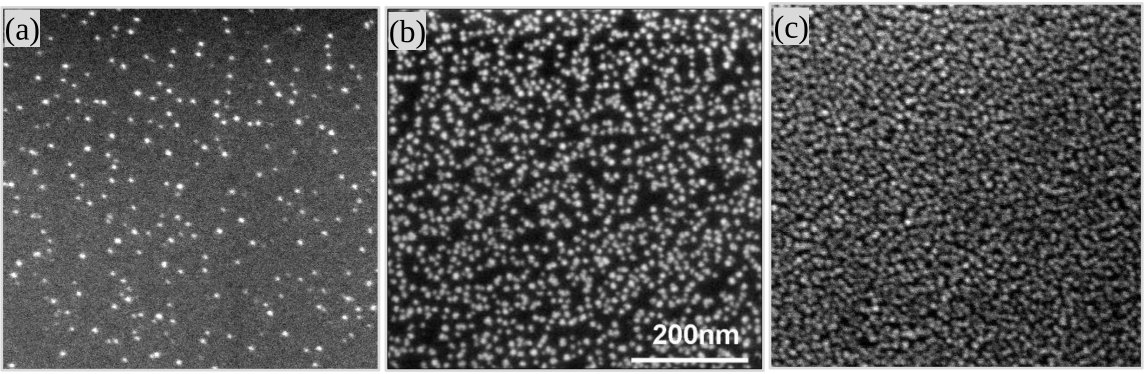

Figure 3.4: SEM images of ZnS nanodots obtained on Si substrate by Spray-ILGAR with different precursor concentrations a) 10mM, b) 25mM and c) 50mM.

3.1.3.2 pH value of the solution

According to the discussion in section 3.1.1.2, Zn(acac)$_2$ has poor solubility in H_2O. In order to dissolve it, small amount of HAc was added to form acidic solution. Therefore, the pH value of the solution could be tuned by different amounts of HAc. Further synthesis has been conducted by setting the pH value at 3, 4 and 5 to study the influence on the physical characteristics of the ZnS nanodots. In this pH range, the complex of acac-Zn complex is stable, whereas zinc acetato complexes are present when pH<2 [102].

As can be seen in Figure 3.5, the particle size remains constant (sub 10nm), without considerable agglomeration. For pH≥5, only a few nanodots are observed. When the pH value decreases to 4, the density of the nanodots increases by several times. The density was shown in section 3.1.2. The number of the nanodots further multiplies as the pH value goes down to 3. The nanodots are still monodispersed without agglomeration to bigger particles. They are arranged as one by one, side by side, with little space inbetween each other. Hence, we can draw the conclusion that HAc does not only help Zn(acac)$_2$ to dissolve in H_2O, but also remarkably increases the deposition rate. The role of H_2S will be further studied by means of mass spectrometer in section 4.2. The detailed explanations can be found there.

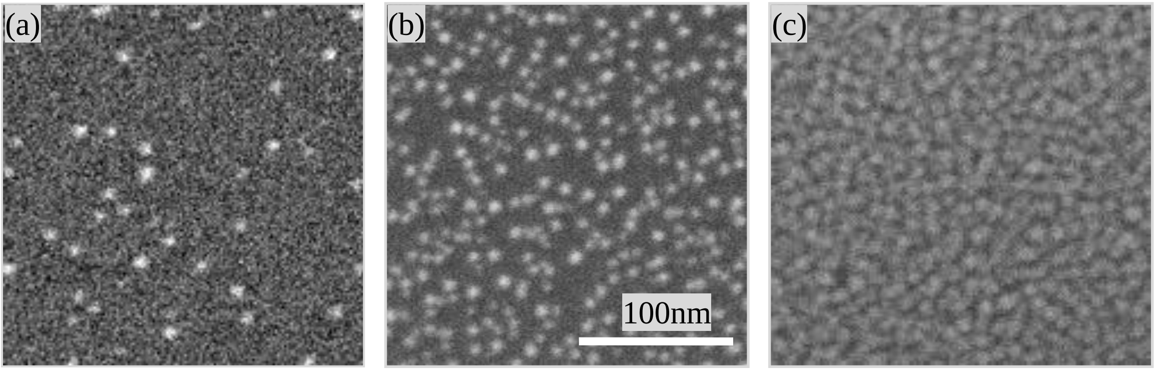

Figure 3.5: SEM images of ZnS nanodots obtained on Si substrate by Spray-ILGAR at different pH values: (a) pH=5, (b) pH=4 and (c) pH=3.

3.1.3.3 Number of process cycle

For this experiment, ZnS was deposited with different number of process cycles, keeping all other parameters constant.

In Figure 3.6, representative SEM images of the surfaces of the substrate after ZnS deposition after 20, 30, 50 and 100 spraying cycles are shown. As calculated in section 3.1.2, the density of the monodispersed nanodots obtained after 20 process cycles is about $3x10^{11}$ cm^{-2}. A comparison of Figure 3.6 (a), (b) and (c) indicates that the nanodots are getting denser at almost constant size after the more number of process cycles. The observed increase of the dots density with negligible increase of their sizes indicates that the precursor molecules nucleate mostly onto the gaps among the nanodots rather than onto the already formed nanodots as soon as they have reached a certain size (5-10 nm). This leads to a self-limiting growth and the obtained homogeneous dispersed sub 10 nm nanodots.

On the other hand, after 50 spraying cycles, the nanodots start touching each other although the discrete nature of the grains can still be distinguished. When the density increases to the maximum value, the touching nanodots start to coalescence, leading to a compact film of nanodots with variety of different sizes between 5 and 50 nm after 100 spraying cycles (Figure 3.6(d)). It can be seen that the larger nanodots are the aggregate of the small ones. This indicates that the increase in size is not obtained by formation of the residual precursor molecules nucleation onto the formed dots, which would lead to a somehow uniform increase of the size of each nanodot. However, it is obvious that the obtained nanodots in figure 3.6 (d) are inhomogeneous in size. Hence, the conclusion can be drawn that the coalescence is obtained by a fill in of the gaps among the existing dots. Once these newly formed dots are dense enough, they will touch each other and aggregate to form larger ones, leading to the coalescence almost in two dimensions. The influence of the number of process cycles to the deposition process in Spray-ILGAR is different to the one in Spray-CVD, which will further discussed in Section 3.2.1.2.

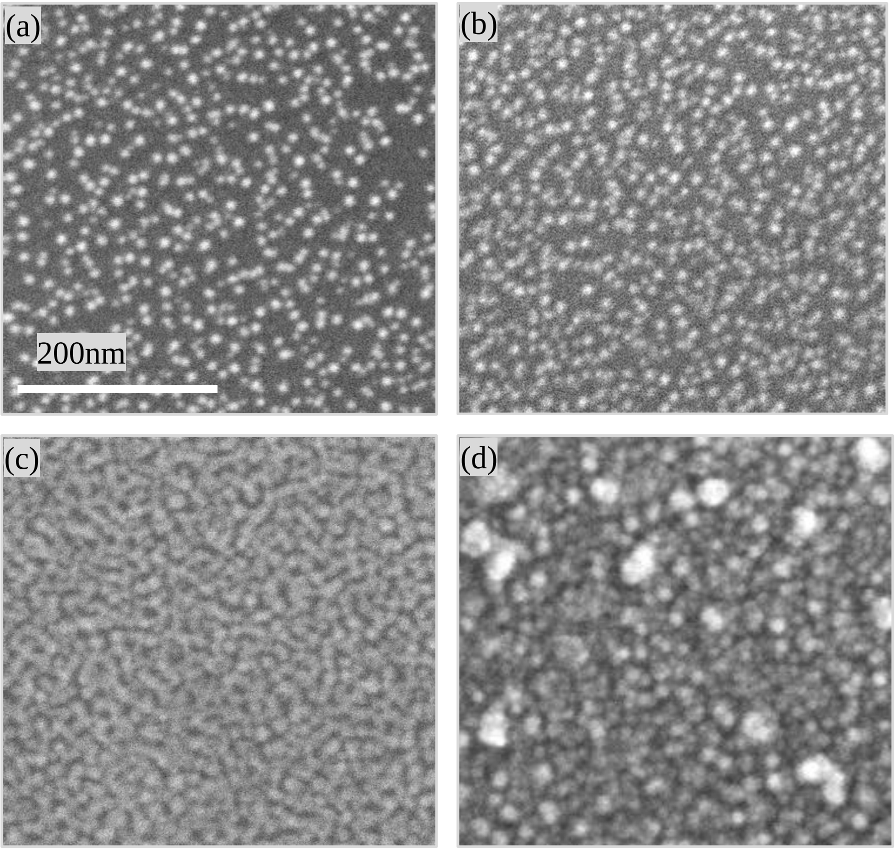

Figure 3.6: SEM images of ZnS nanodots obtained on Si substrate by Spray-ILGAR after different process cycles: a) 20, b) 30, c) 50 and (d) 100.

3.1.3.4 Substrate temperature

This set of experiments was carried out at different substrate temperature while keeping all other conditions constant as indicated in Table 3.2. The substrate temperatures given correspond to the substrate holder temperature. The actual value of the temperature of the substrate surface is a bit lower than the setting substrate holder temperature due to the cooling effect of carrier gas. Considering the application of these ZnS nanodots as passivation buffer layer in chalcopyrite solar cell, the nanodots should be prepared at temperature <250 ºC, which was successfully achieved as described in section 3.1.2. In this section, further investigation of the synthesis process at a wide temperature range, is conducted to study the influence of the temperature to the deposition. The selected temperature is from 175 to 400 ºC. The substrate holder temperature can be heated up to 450 ºC. No nanodot is detected at temperature <150 ºC.

Compared to the nanodots obtained at 175 ºC, the size achieved at 200 ºC increases by a negligible amount, but the rate of the increase in the dot density dominates over the rate of increase in the sizes (Figure 3.7 (a) and (b)). As the temperature keeps increasing, the nanodots grow bigger and become inhomogeneous. At 300 ºC, there are still some nanodots in the range of 10 nm, and some are about 20-25 nm which are quite monodispersed. The most interesting is that the 20-25 nm nanodots cluster into dimers and trimers at about 30-40 nm in their longest dimension. This phenomenon happens also at 400 ºC. The dimers and trimers grow even bigger to 50-60 nm. The dot density is not as high as the one at 200 ºC, which is the result of the increase of the nanodots size.

As the temperature increases, the chemical reaction occurs more rapidly, leading to a faster nucleation rate. This faster nucleation rate produces more particles. This fact explains that the density becomes higher from temperature 175 to 200 ºC. On the other hand, for the nanodots in figure 3.7 (a) and (b), they have almost the same average size and this indicates a kind of uniform nucleation of precursor molecules at these two temperatures.

A discretely different nucleation behavior of the precursor molecules is observed onto the heated substrate at temperature below and above 300 ºC. It is seen that the nanodots are homogeneous in size at 175 and 200 ºC, while they have a variety of different sizes at 300 and 400 ºC. As we discussed in section 3.1.3.3, the precursor molecules at 200 ºC nucleate mostly onto the gaps among the formed nanodots. Contradictory to the behavior observed at 200 ºC, the nucleation takes place both onto the gaps and the formed nanodots above 300 ºC , which leads to the variety of different sizes. These two different nucleation behaviors will be further discussed in Chapter 4.

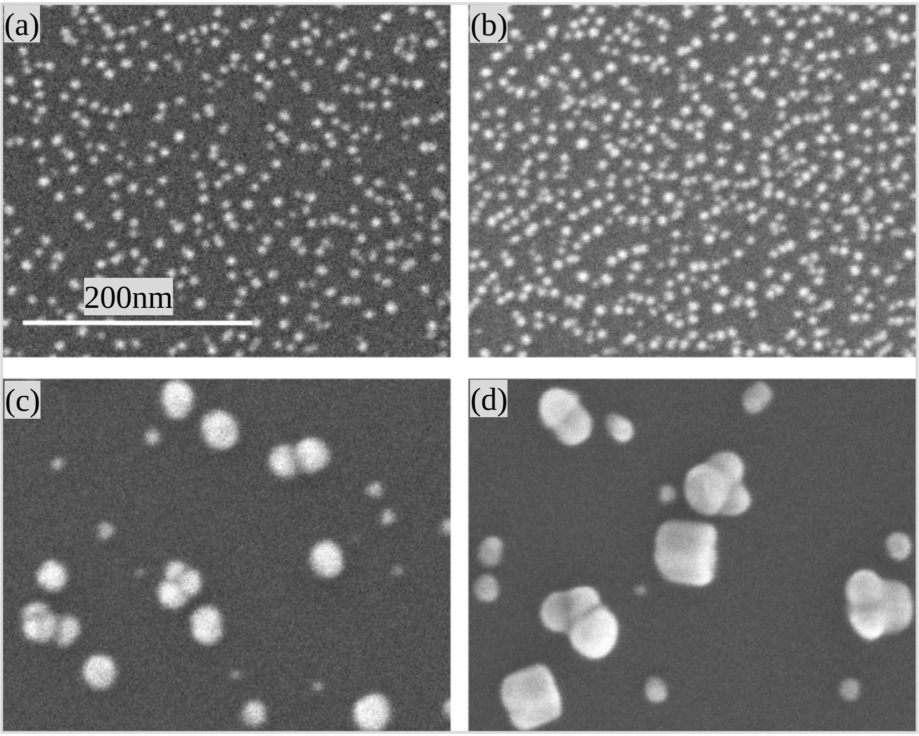

Figure 3.7: SEM images of ZnS nanodots obtained on Si substrate by Spray-ILGAR at different temperatures: a) 175 ºC, b) 200 ºC, c) 300 ºC and (d) 400 ºC.

3.1.3.5 Solvent

As mentioned in section 3.1.1.2, the films obtained from water and ethanol are completely different. Figure 3.8 shows the compact film, instead of a nanodot film, achieved by 25mM $Zn(acac)_2$ alcoholic solutions for 3 spraying cycles, while other parameters are kept the same as the nanodot film obtained after 20 process cycles spraying with aqueous solutions (Figure 3.2). Therefore, the deposition rate with alcoholic solution is much faster than aqueous solution, which could be partially explained in the following.

The quantity of the aerosol produced by ultrasonic nebulization at a constant power level of the ultrasonic source is a monotonically increasing function of the following ratio r [101]:

$$r = \frac{p}{\sigma \cdot \eta} \qquad \text{Eq.3.3}$$

Here, p is the saturated vapor pressure of the liquid, σ is the surface tension, and η is the dynamic viscosity. In table 3.3, these values are listed for some solvents, such as water, ispropanol, ethanol, acetonitrile, tetrahydrofuran and acetone.

Table 3.3 Saturated vapor pressure, surface tension, dynamic viscosity and ratio r (Eq. 3.3) of water, isopropanol, ethanol, acetonitrile, tetrahydrofuran and acetone [67].

Solvent	p [mmHg]	σ [mN/m]	η [cp]	Ration r
Water	24	72	1.00	0.3
Ispropanol	33	22	2.26	0.7
Ethanol	44	23	1.19	1.6
Actonitrile	73	29	0.39	6.4
Tetrahydrofuran	143	26	0.47	11.5
Acetone	185	24	0.32	24.3

The above table exhibits that, the ration r, which determines the nebulization rate and therefore also the deposition rate, is about 5 times stronger, if ethanol is used instead of water. There is one point to be mentioned, the values in Table 3.3 are valid for the pure solvents and change upon the addition of $Zn(acac)_2$. However, the experimental results, of which agree very well with the behavior expected from the trend in Table 3.3.

In addition, it is important to note that the solvent may participate in the chemistry of the reaction prior to or during the aerosol processing. As mentioned above, it was reported that water can enhance the pyrolysis of $Zn(acac)_2$. In chapter 4, by means of mass spectrometry, the role of solvent in the decomposition process is investigated in detail. The above discussion allows us to draw the conclusion that, the choice of the solvent is one of the key steps to prepare the nanodot film.

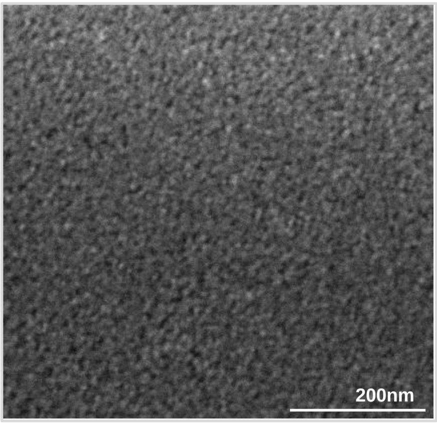

Figure 3.8: SEM image of ZnS film obtained after 3 spraying process cycles with 25mM $Zn(acac)_2$ alcohol solution by Spray-ILGAR.

3.1.3.6 Zinc-containing compound

As described in section 3.1.1.1, the choice of the appropriate zinc-containing compound is the first prerequisite for the deposition of the nanodot film by the Spray-ILGAR process. The choice of the solute will determine the product or the process. In the following, two zinc containing compounds, zinc acetate ($Zn(ac)_2$) and $Zn(acac)_2$, as the precursor are discussed.

Figure 3.9 (a) shows the product obtained with $Zn(ac)_2$, which consists of widely distributed submicron spherical particles, in the range of tens to hundreds of nanometers. A comparison of the figure 3.9 (a) and (b) shows that, the resulting particles achieved with $Zn(acac)_2$ are much denser and more uniform than those with $Zn(ac)_2$, although they were obtained under the same condition. More importantly, the more uniform particles in figure 3.9 (b) are sub 10 nm, which much smaller than those submicron particles in Figure 3.9 (a). These experimental results clearly suggest that different growth mechanisms may work for these two processes. The different feature of the chemical species, such as reactivity, volatility leads to different morphology of the obtained particles.

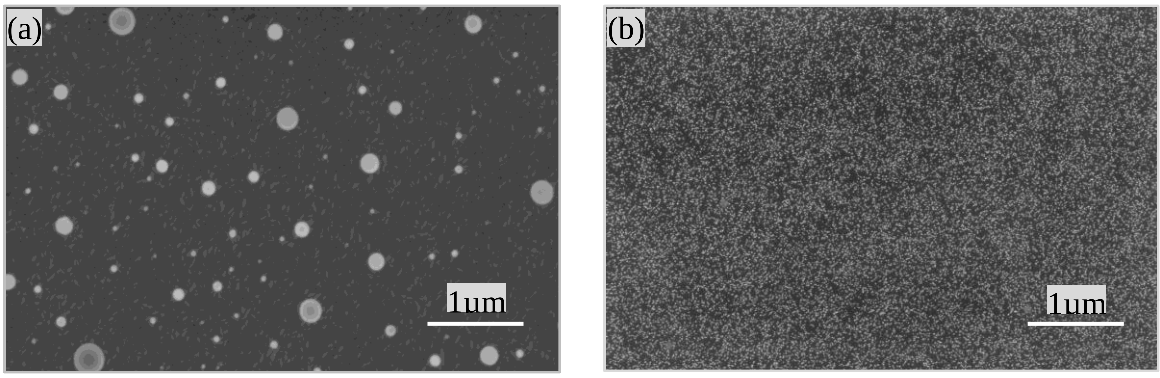

Figure 3.9: SEM images of ZnS particles obtained with different zinc-containing compound: (a) $Zn(ac)_2$ and (b) aqueous $Zn(acac)_2$ solution by Spray-ILGAR.

3.1.3.7 H_2S

One of the important reagents for the Spray-ILGAR process is H_2S which is introduced in the seconded step. The role of H_2S, as expected, is to convert the precursor film deposited in the first step to metal sulfide. In order to study the intermediate film and the role of H_2S in more detail, the zinc-containing precursor compounds were nebulized for a certain time, which is the 1st step in Figure 3.10. The obtained intermediate film was then characterized and later exposed to H_2S at 200 ºC to be converted to ZnS (2nd step in Figure 3.10). The film was prepared by nebulizing $Zn(acac)_2$ aqueous solution without any sulfurization. The spray step duration was in the range that was used for the deposition of Spray-ILGAR ZnS nanodot film. The spray steps were separated by 10s break, in order to avoid continuous cooling of the substrate. All other parameters were identical to those stated in Table 3.2.

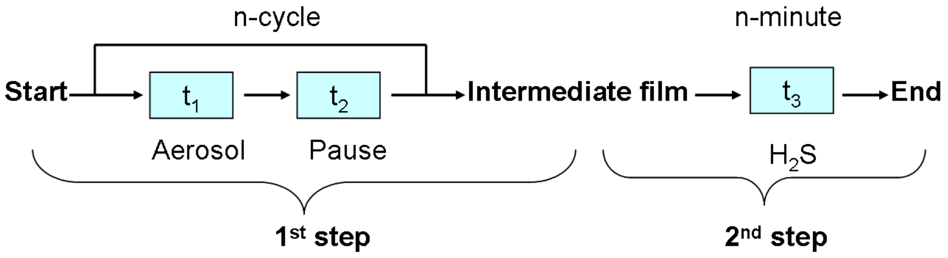

Figure 3.10: Schematic diagram showing the two individual steps of the Spray-ILGAR process: 1st step- nebulize the precursor solution for certain time without H_2S to obtain intermediate film; 2nd step- the intermediate film exposed to H_2S to be converted to ZnS.

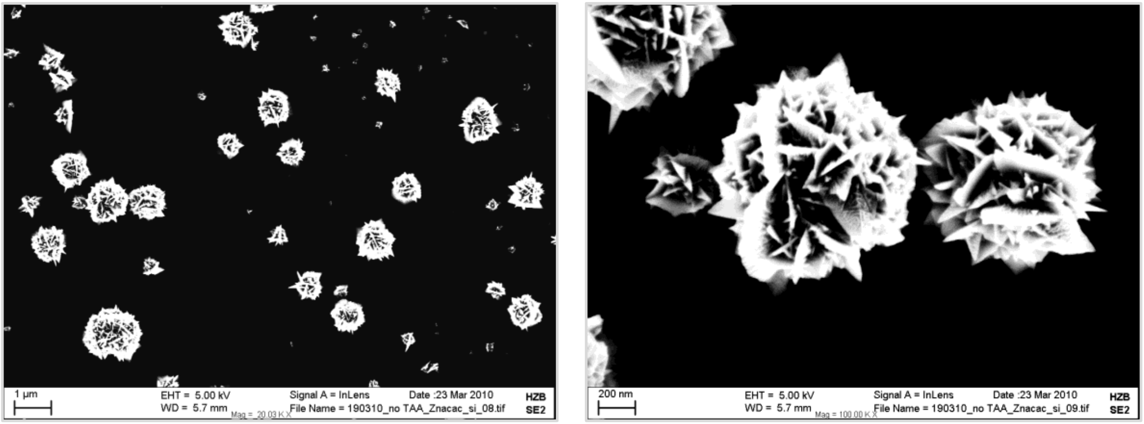

Figure 3.11: SEM images of the intermediate film obtained with 1st step of the Spray-ILGAR process at low (left) and high (right) magnification.

1st step of the Spray-ILGAR process

According to the results presented in section 3.1.2, it was anticipated that a homogeneous sub 10nm ZnO or $Zn(OH)_2$ nanodot film would be the intermediate deposition film in the first step, which will subsequently react with H_2S to form the well distributed ZnS nanodot film shown in Figure 3.1.1. However, as it turns out, the obtained intermediate film, as clearly shown in Figure 3.11, is wide distributed “stars”, in the range of several tens of nanometer to micrometer. The surface of the particles is quite rough whereas the surface of ZnS nanodots is smooth. Thus, a conclusion could be drawn from the above analysis that the homogenous ZnS nanodots in Figure 3.2 are not the direct sulfurization product from the intermediate film. However, will these microns “stars” be changed to a nanodot film when introducing H_2S?

Prior to the second sulfurization step, the composition of the intermediate film deposited at the spray step of the Spray-ILGAR process is studied. Figure 3.12 a-d show the SEM image and the EDX elemental intensity maps of the O-K, Si-K, Zn-L X-ray lines. The brightness within the maps represents the intensity of the EDX signal of the corresponding elements: bright indicates high and black low intensity. The signal of Si comes from the substrate. The places where show no signal from substrate Si, are found to have strong signals of Zn and O. This proves that the intermediate film from the first step is ZnO. The result agrees well with the EDX spectrum in Figure 3.12 (c).

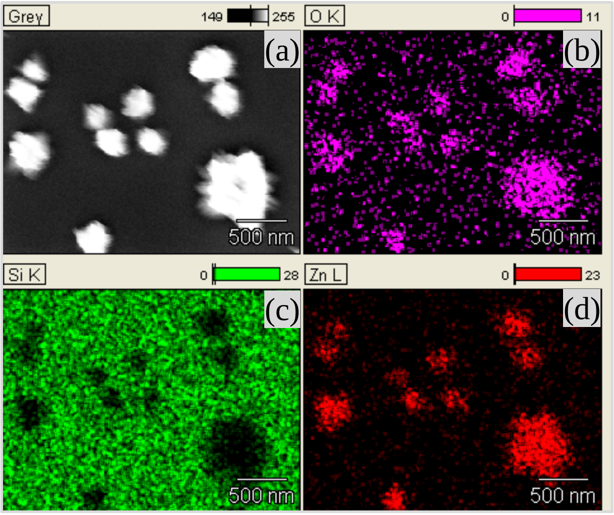

Figure 3.12: a) Plan-view SEM image of the intermediate film and EDX elemental intensity maps of the O-K (b), Si-K (c), and Zn-L (d) X-ray lines.

2nd step of Spray-ILGAR process

The previously discussed intermediate micron “stars” were deposited without sulfurizing. In the following, the processes occurring during the sulfurization process are focused. The as grown intermediate microns “stars” were then exposed to H_2S at 200ºC. As shown in Figure 3.13 (a) and (b), the morphology of the particles does not change before and after exposure to H_2S. However, the appearance of a small S peak is found in the EDX spectrum after the sulfurization (Figure 3.13(d)), which means that H_2S in the second step of Spray-ILGAR will only sulfurize the intermediate film, but no other reaction will occur to transform the microns “stars” to nanodots. Thereby, in order to form the nanodot ZnS film, nanodot ZnO should be first deposited at the first step of the Spray-ILGAR. However, what we obtained from the first step are these micron “stars” as shown Figure 3.11. How could the nanodot formed at the spray step?

Could the micron particles grow gradually from small nanodots during the several spraying cycles? However, the particles achieved with fewer process cycles are not found to be smaller than those in Figure 3.11. Compared this two-individual-step process to the sequential 2-step Spray-ILGAR process, the main difference is that the spray step in Spray-ILGAR is interrupted by introducing H_2S from time to time, whereas in the two-individual-step process the spray step is a continuous process without being interrupted. Although H_2S is expected to be cleared from the chamber by 10s N_2 purging in Spray-ILGAR, small amount of H_2S is still detectable by mass spectrometer (See chapter 4). This means that this small amount of H_2S exists in the tube and makes a critical difference in the first spray step of the Spray-ILGAR process. Therefore, it is assumed that H_2S does not only sulfurize the intermediate film to metal sulfide, but also play an important role in the first step, which will help to deposit a homogenous intermediate nanodot film. In order to further check this hypothesis, a small amount of H_2S is introduced simultaneously with the nebulizing aerosol in the spraying step, but without the second sulfurization step. This is actually a spray pyrolysis process or is called Spray chemical vapor deposition (Spray-CVD) by our group. Whether nanodots could be achieved by this Spray-CVD process, it will be the topic of section 3.2.

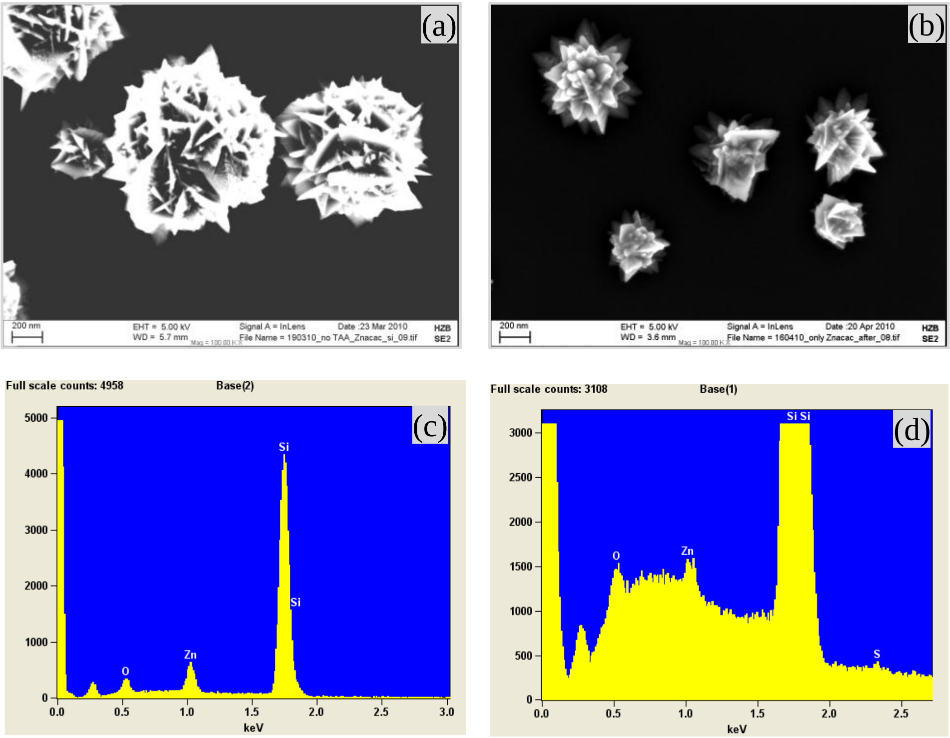

Figure 3.13: SEM images and EDX spectra of the intermediate film obtained on Si substrate before (a), (c) and after (b), (d) H_2S exposure.

3.2 Spray-CVD

In this section, a new process called Spray-CVD is developed to deposit nanodots. The main distinction between the Spray-CVD and “conventional” CVD is the method by which the precursors are delivered to the substrate. In the conventional CVD, the precursor is generally evaporated from a bubbler or entrained in a gas stream. For Spray-CVD, the delivery of the precursors is via an aerosol which vaporizes into a gas phase. The Spray-CVD process schematic diagram is shown in Figure 3.14. Different from the Spray-ILGAR process, in which H_2S is fed in sequentially after the aerosol is switched off, in Spray-CVD process, the nebulized aerosol and H_2S gas are simultaneously introduced into the chamber. Compared to Spray-ILGAR, Spray-CVD will omit the sulfurization and two purge steps, which can save almost half of the process time. Additionally, the deposition rate could be accelerated by varying the process parameters.

In this section, two kinds of reactant gas sources are used and evaluated for the Spray-CVD process. One is the commercial compressed H_2S gas used in the Spray-ILGAR process (section 3.2.1). The other is in-situ generating H_2S using thioacetamide (TAA) as the sulfur source (section 3.2.2).

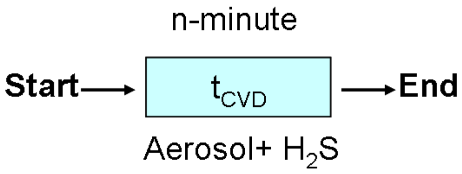

Figure 3.14: Schematic diagram of Spray-CVD process: H_2S are simultaneously present in the chamber with the nebulized aerosol.

3.2.1 Compressed H_2S gas

H_2S is a colorless, very poisonous, flammable gas with the characteristic foul odor of rotten eggs. Hydrogen sulfide reacts with metal ions to form metal sulfides, which is widely used as reactant for many material systems such as ZnS, CdS [103-105].

In the following, the dependence of the deposition on the H_2S concentration rate in the Spray-CVD process is investigated (section 3.2.1.1). Different H_2S flow rates are introduced simultaneously with the nebulized aerosol, keeping other process parameters identical to the ones in the Spray-ILGAR process. Furthermore, the influence of the spraying time on the Spray-CVD process is discussed and compared to one in the Spray-ILGAR process (section 3.2.1.1).

3.2.1.1 Influence of H_2S concentration in the Spray-CVD process

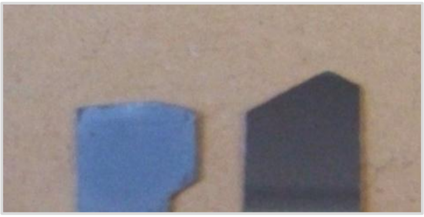

Figure 3.15: Photograph of the powdery film on Si substrate (left) and the bare Si wafer (right).

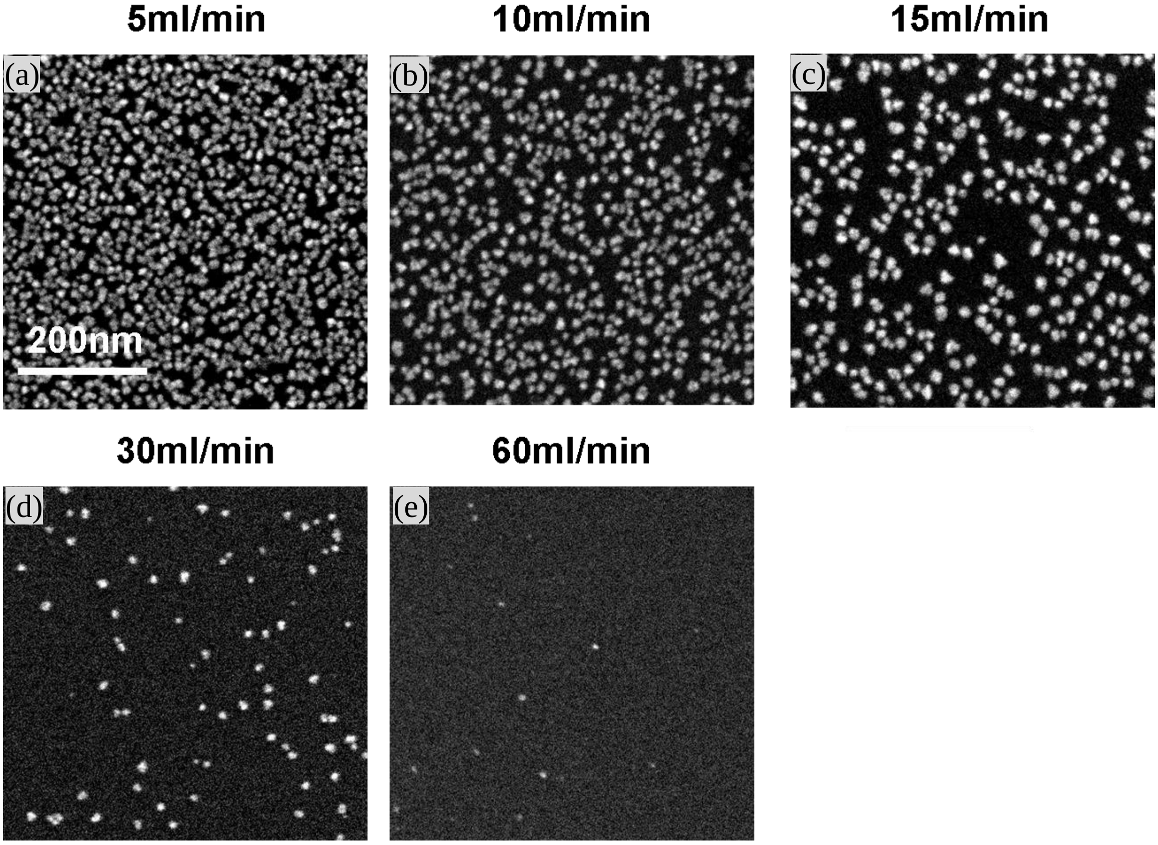

Figure 3.16: SEM images of the nanodots achieved at different H_2S concentrations in the Spray-CVD process (a) 5 ml/min, (b) 10 ml/min, (c) 15 ml/min, (d) 30 ml/min and (e) 60 ml/min.

In the Spray-CVD process, 5% H_2S (H_2S in Ar) instead of 100% is used. When 1L/min 100% H_2S (C_{H2S} is 18%), the same amount as in the Spray-ILGAR process, is used, white powdery film was obtained which could be easily scratched away, as shown in figure 3.15. Five different flow rates of 5% H_2S were chosen, 5 ml/min, 10 ml/min, 15 ml/min, 30ml/min, and 60 ml/min, and the corresponding concentration of H_2S was 0.01%, 0.02%, 0.03%,0.06% and 0.12% respectively. From Figure 3.16, it is obvious that ZnS nanodots[2], similar to the ones achieved by Spray-ILGAR, are indeed successfully achieved by Spray-CVD. Compared to the micron particles in Figure 3.13, the conclusion can be drawn that H_2S in the spraying step strongly affect the morphology of the obtained nanodots. This observation supports the assumption in section 3.1.3.7 that H_2S does not only sulfurize the intermediate film to metal sulfide, but also play an important role in the first step, which will help to deposit a homogenous intermediate nanodot film. On the other hand, the concentration of H_2S does not affect the size of the nanodots, which keeps constant at around 15-20 nm. However, a fast decrease of the dot density is observed with the increase of the H_2S concentration. The relationship between the dot density and the H_2S concentration is shown in Figure 3.17. For comparison, the dot density in the Spray-ILGAR process is also given in the figure. As calculated from Figure 3.17, the dot density decreases from 3.8×10^{11} cm^{-2} with 5 ml/min H_2S to 2.3×10^{11} cm^{-2} with 10 ml/min H_2S, 9.4×10^{10} cm^{-2} with 15ml/min H_2S, 2.8×10^{10} cm^{-2} with 30ml/min H_2S, and 4.4×10^{9} cm^{-2} with 60ml/min H_2S, Whereas the value for the Spray-ILGAR process is 3×10^{11} $cm^{-}{}_{2}$. Thereby, the deposition rate for the Spray-CVD with 5ml/min H_2S is faster than the Spray-ILGAR process.

In addition, it is observed from Figure 3.18 that the size of the nanodots in the Spray-CVD process is around two times larger than the one in the Spray-ILGAR process after the same spraying time (20 min). The reason for the larger nanodots in the Spray-CVD process will be further discussed in chapter 4.

The reason why the dot density drops off as the H_2S concentration increases is because particle formation occurs before the precursors reach the substrate. In the general CVD process, the volatile precursors are delivered to the hot substrate, above which they are absorbed and undergo gas phase reaction or decomposition to form a coating. However, in some cases, before reaching the hot substrate instead of above it, the precursors will react with other reactants or decompose and form solid particles. The solid particles will hardly deposit on the substrate, while they will be blew away and carried out by N_2 to the exhaust. The particle formation will lead to a reduction in the precursor concentration and therefore a reduction in the deposition rate. In the Spray-CVD process, the precursor and H_2S are introduced simultaneously. Although H_2S could help the $Zn(acac)_2$ precursor to decompose to homogenous nanodots (as discussed in section 3.1.3.7). Only a small amount of H_2S is necessary to help homogeneous decomposition, which will be further discussed in Chapter 4, excess H_2S will react with the precursor and form solid ZnS particles as well. Hence, as the concentration of H_2S increases, the reaction with $Zn(acac)_2$ precursor will gradually become dominant. Simultaneously, the concentration of $Zn(acac)_2$ which will later decompose above the hot substrate will decrease and lead to the reduce in the obtained dot density.

---

[2] Until the composition of the Spray-CVD nanodots is determined, it will be considered as ZnS.

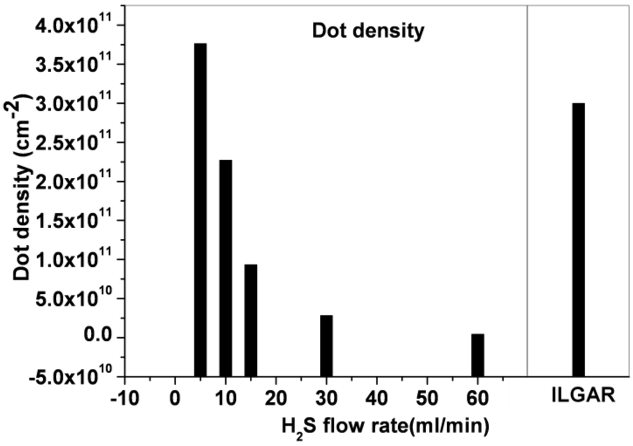

Figure 3.17: Dot density as function of the H_2S flow rate in the Spray-CVD and Spray-ILGAR process. The flow rate of the carrier gas N_2 is 2.5 L/min.

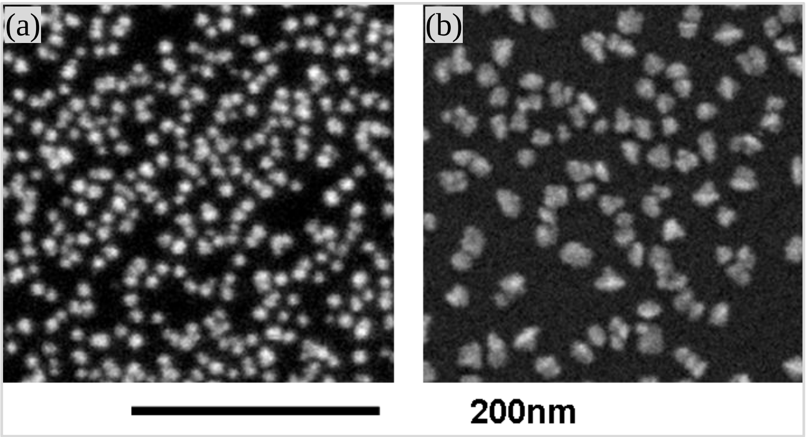

Figure 3.18: SEM images of the nanodots obtained by a) Spray-ILGAR, b) Spray-CVD process.

3.2.1.2 Influence of spraying time in the Spray-CVD process

As previously pointed out in section 3.1.3.3, the number of process cycle plays an important role in the Spray-ILGAR process. In the following, the influence of spraying time in the Spray-CVD process, which is corresponding to number of process cycles in Spray-ILGAR, is discussed.

Contrary to Spray-ILGAR, the nanodots are getting larger in size with the increasing spraying time, rather than form a layer-like film (Figure 3.19). It allow us to draw the conclusion about the nucleation behavior of ZnS onto the Si substrate surface: the nucleation takes place following the so-called island or Volmer-Weber growth model [106], where the nanodots are nucleated directly onto the surface and then grow into islands of the condensed phase. In addition, the nanodots in each image are homogeneous in size, which distinct from the variety of different sizes obtained after many process cycles in the Spray-ILGAR process. This means the uniform increase of the size of each nanodot. Therefore it is concluded that this coalescence is obtained by the formation of the precursor molecules nucleation onto the formed dots, rather than by newly formed nuclei. In other words, coalescence is obtained by the increase of the size of already formed dots in three dimensions. The reason leads to the different nucleation behavior as the increasing spraying time in Spray-ILGAR and CVD will be further discussed in chapter 4.

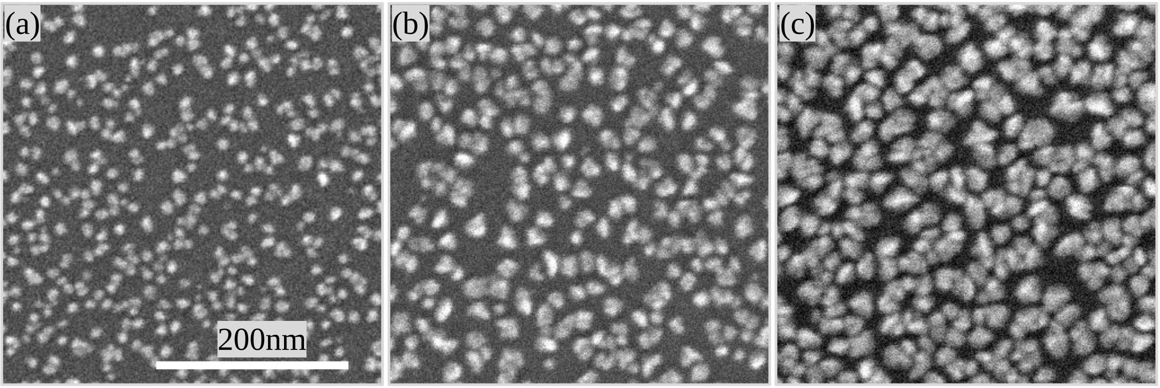

Figure 3.19: SEM image of ZnS nanodots obtained on Si substrate by Spray-CVD at different spraying time: (a) 10, (b) 20 and (c) 50 min.

3.2.2 In-situ generating H_2S with Thioacetamide

H_2S gas used in the Spray-ILGAR and Spray-CVD process (in section 3.2.1) is typically purchased from a supplier as a compressed gas. In this section, a process for in-situ generating H_2S using TAA as the sulfur source is discussed. Compared to H_2S gas, TAA is less hazardous than H_2S (its hazardous materials identification system rating for health, flammability, and reactivity rating is 1/1/1 compared to 4/4/0 for pure H_2S), and it decreases the risk of exposure to toxic and flammable compressed gas [107].TAA has previously been used to generate H_2S in the presence of acid for several different applications, for example, pharmaceutical testing, deposition of metal sulfide by CBD [108-110]. Thermal decomposition of TAA in acidic solution is known to proceed as follows [111]:

$$CH_3C(S)NH_2 \xrightarrow{H_3O^+} CH_3C(O)NH_2 + H_2S \qquad \text{Eq.3.4}$$

Spray-CVD with in-situ generating H_2S

For this experiment, the process is actually similar to the one in section 3.2.1, which is shown in Figure 3.14. The only difference is to substitute H_2S with 0.02M TAA aqueous solution, keeping all other parameters constant as described in section 2.1.2. The mixture precursor of 25 mM $Zn(acac)_2$ and 0.2 M aqueous TAA acidic solution will be nebulized, carried by N_2 to the hot substrate surface, where they undergo pyrolysis and deposit a film.

The product obtained by the in-situ generating H_2S, as shown in Figure 3.20, reveals a nanodot film homogeneous in size, similar to the one achieved after 10 min with the compressed H_2S gas in the Spray-CVD process (Figure 3.19 (a)). The diameters of the nanodots are below 10nm. According to the discussion in section 3.2.1, it would be reasonable to expect different dot density by varying the process parameters to control the H_2S release rate, which is not the focus of this thesis. In summary, in-situ H_2S generation using TAA as the sulfur source provides a method applicable to the spray pyrolysis process. The release rate of H_2S depends on different parameters, such as pH value of the solution, and temperature [112], which makes the whole process complicate since the concentration of H_2S is essential to the deposition rate as we discussed in section 3.1.3.7. Therefore, in our thesis, we will use the compressed H_2S as the sulfur source. Spray-ILGAR and Spray-CVD is the focus method in our following discussion and application.

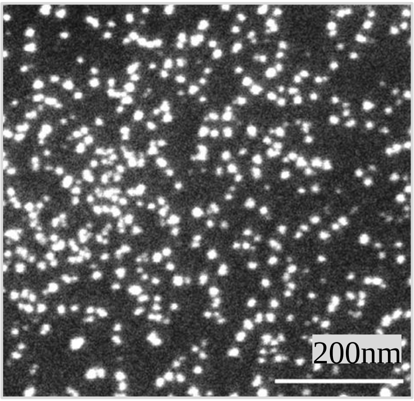

Figure 3.20: SEM image of ZnS nanodots obtained with in-situ generating H_2S.

Colloid chemistry technique with in-situ generating H_2S

Base on the above experiment, the $Zn(acac)_2$ and TAA precursor solutions were applied as the reactants in colloid chemistry technique to synthesize nanoparticles. Therefore, the advantage and disadvantage of the spray based method and the colloid chemistry technique can be compared. 0.05M $Zn(acac)_2$ and 0.4M aqueous TAA acidic solution were mixed and placed in a 80ºC water bath. The reaction time was fixed at 30min, after which the solution was terminated by rapidly cooling in an ice bath. The precipitates were centrifuged and washed for several times. The recovered precipitates were then dispersed in tetrahydrofuran (THF) with ultrasonicator to form the colloid solution. A Si substrate was successively dipped in the colloid solution and subsequently in an 80 ºC oven to evaporate the solvent. This cycle was repeated several times till a film was coated layer by layer on the substrate surface.

Figure 3.21 (a)-(e) show the low magnification view of the coated film at an increase dipping cycles from 10 to 160 times. As it can be seen, uniform ZnS nanoparticles are obtained and the number of coated nanoparticles gradually increases with the dipping cycle. The thickness of the coated particle films, which corresponds to the particles number, was measured by X-ray fluorescence (XRF). Nonlinear increase in the coated particles number with the dipping cycles is observed. If the magnification is increased (Figure 3.22), it is possible to find that the obtained ZnS are 150 nm uniform spherical particles, and with a narrow size distribution. As the dipping cycle increases, they are more and more particles covered on the substrate surface. However, they are stacked layer by layer, instead of self-assemble into an ordered 2D array. This is not optimizing for the further application as passivation buffer layer which requires a thin layer covering most of the absorber surface. Although the reactants are the same for these two techniques, different reaction mechanisms lead to the completely different results.

In conclusion, with the same start precursor solutions, ZnS nanoparticles have been both achieved for both the Spray-CVD method and the colloid chemistry technique. The particles obtained by the colloid method are around 10 times larger than the ones by Spray-CVD. Additionally, compared to the Spray-CVD method, the colloid method has many and miscellaneous steps which are more complicate and need longer time for the preparation. Last but not least, the stack colloid layer is not appropriate for the application as a passivation buffer layer, which is the second aim of our thesis. However, both methods are good choices for the preparation of nanoparticles.

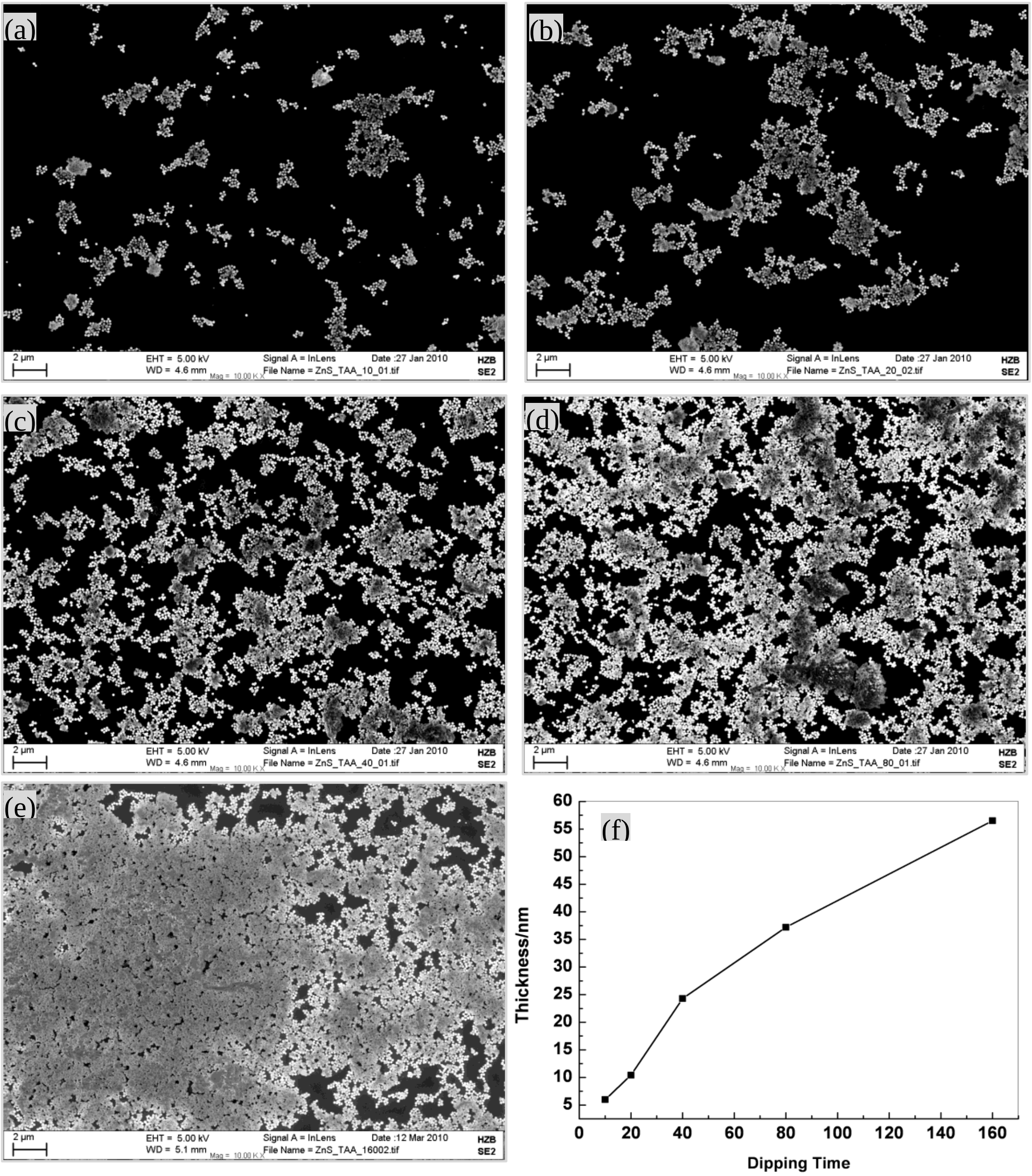

Figure 3.21: Low-magnification view of the coated films after different dipping times (a) 10, (b) 20, (c) 40, (d) 80, (e) 160, and (f) the obtained film thickness as a function of the dipping time.

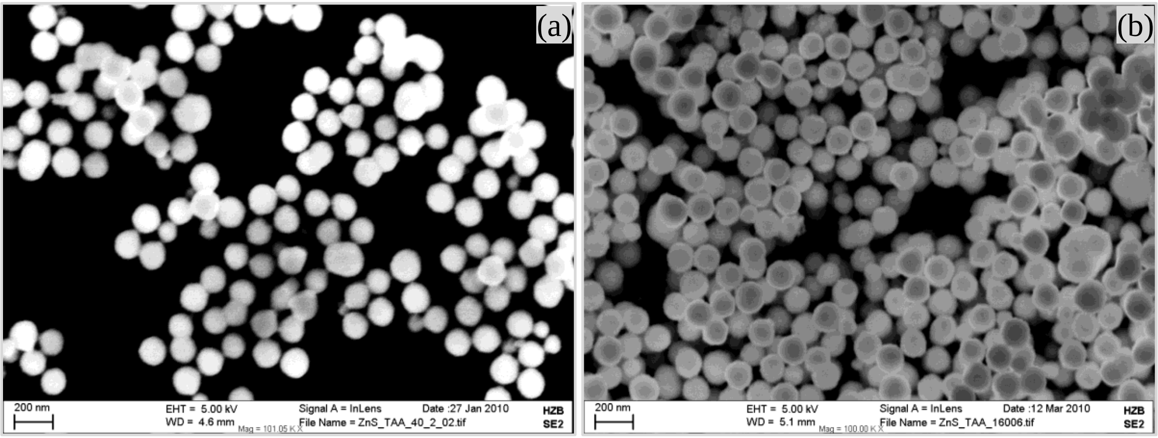

Figure 3.22: High-magnification view of the coated films at (a) 80, (b) 160 dipping times.

3.3 Summary

In this chapter, the development of two processes for the deposition of ZnS nanodots, Spray-ILGAR and Spray-CVD are described.

Using Spray-ILGAR method, high quality sub 10 nm ZnS nanodots without insulating surfactant ligands are produced at 200 °C with rather homogeneous size distribution, which are desirable for further application as a passivation buffer layer in chalcopyrite thin film solar cell. This is done by choosing an appropriate zinc containing compound ($Zn(acac)_2$) and solvent (H_2O). The choices of different zinc containing compound and solvent lead to products with different morphologies. Inhomogeneous submicron particles are obtained with $Zn(ac)_2$ as precursor, while an almost compact film is achieved within short time when use EtOH as solvent. The size and dot density is controllable by varying the process parameters such as precursor concentration, pH value of the solution, number of process cycle, substrate temperature, solvent, zinc-containing compound, and reactant gas. The details are shown as following:

- The nanodots could be tuned from sparse scattering to dense arrangement, even to a compact film, while keep constant in size, by increasing the precursor concentration, the deposition temperature (175< T <300 °C), the number of process cycle (<50 cycles) or decreasing the pH value of the solution. The increase of the dot density with negligible increase of their size is explained by the self-limiting growth mechanism in chapter 4. Briefly, the precursor molecules nucleate onto the gaps among the nanodots rather than onto the existing dots.
- The density of the nanodots reaches the maximum value at about 50 process cycles. Afterwards, with more and more newly formed small nanodots, the distributed nanodots start touching each other due to the limited space, which leads to the aggregation of the nanodots. Afterwards, the aggregation of the touching nanodots leads to larger nanodots, while the newly formed small nanodots keep filling the gaps among existing dots. Finally, a compact nanodot film with variety of different sizes is obtained when keep increasing the number of process cycle.
- As the temperature enhanced above 300 °C, the obtained nanodots are bigger than below 300 °C and they cluster into dimers and trimers with the size from several nanometer to tens of nanometer. The variety of the different sizes indicates a

different nucleation behavior to the one at 200 ºC. The nucleation takes place both onto the gaps and the formed dots.

- H_2S is not only to sulfurize the intermediate film to ZnS, but also help the precursor film decompose to homogeneous nanodot.

The same zinc containing compound and solvent as in the Spray-ILGAR process are chosen for the Spray-CVD process, while two different sources of reactant gases, compressed H_2S gas and in-situ generating H_2S with TAA are used and compared. Homogeneous nanodots are both obtained for these two conditions.

For the Spray-CVD process with the compressed H_2S gas, the investigation reveals that:

- Compared to the Spray-ILGAR process, the nanodots obtained by Spray-CVD are also homogeneous in size, but larger in size. By choosing the appropriate parameter, the deposition rate is faster than the Spray-ILGAR process. In addition, Spray-CVD save half of the process time by omitting the sulfurization and two purge steps in Spray-ILGAR.
- The deposition rate drops off remarkably as the H_2S concentration goes up. Particle formation through the reaction of $Zn(acac)_2$ and H_2S before reaching the substrate leads to the reduction in the obtained dot density.
- The nanodots, which nucleate following the island or Volmer-Weber growth model, get larger in size even before forming a compact layer as the spraying time prolongs. Nucleation occurs mostly on the already formed nanodots which results in the uniform increase of the size in three dimensions.

For the Spray-CVD process with in-situ generating H_2S, ZnS nanodots could be obtained. However, the release rate of H_2S by the decomposition of TAA makes the process more complicate for the application.

Colloid chemistry technique with the same reactants $Zn(acac)_2$ and TAA as in Spray-CVD is undertaken to compare to the aerosol technique for the preparation of nanodots. Uniform spherical particles with 150 nm in diameter are obtained though colloid chemistry technique. However, the process is time consuming and the obtained stacked layer is not suitable for further application as passivation buffer layer.

In the following chapter, the mechanisms that govern the growths of the Spray-ILGAR and Spray-CVD ZnS nanodots will be investigated.

Chapter 4

Thermolysis mechanism of $Zn(acac)_2$ and self-limiting growth of ZnS nanodots

The decomposition mechanism of $Zn(acac)_2$ on the hot substrate surface and the self-limiting growth of ZnS nanodots in the Spray-ILGAR and Spray-CVD processes are discussed in this chapter.

As a basis for the following section, section 4.1 briefly introduces the chemical vapor deposition (CVD), including the difference and advantages of AACVD, five key steps of CVD and the limited growth rate steps during CVD process.

In section 4.2, mass spectrometry is applied to elucidate the mechanism of the thermal decomposition of $Zn(acac)_2$ on the hot substrate surface. In-situ mass spectrometry studies on the thermal behavior of $Zn(acac)_2$ powder under different atmospheres, are investigated and compared in the presence and absence of H_2S. Then, the gases produced during the Spray-ILGAR nanodot preparation with $Zn(acac)_2$ alcoholic and aqueous solutions are characterized with the in-situ mass spectrometry. Last but not least, a thermal decomposition route of $Zn(acac)_2$ is proposed which allows adequate interpretation of the present results and the influence of H_2S, H_2O and acid as well. Finally, real time intensity tracking of various masses by mass spectrometry in the Spray-ILGAR and Spray-CVD process are investigated.

The self-limiting growth of the ZnS nanodots is discussed in section 4.3. To start with, the composition of the nanodots obtained from Spray-ILGAR and Spray-CVD are analyzed and compared by energy filtered transmission electron microscope (EF-TEM). Afterwards, the different nucleation behaviors which lead to the self-limiting growth of the nanodots within the two processes are investigated and elucidated in detail.

4.1 Chemical vapor deposition

The origin of chemical vapor deposition (CVD) can be traced back to the early work in the production of carbon filaments for the incandescent lamp industry [113]. Since then, CVD technique has been developed as one of the major methods of synthesizing films, coating, powder, composites, nanostructured materials, etc., for a wide range of application. Chemical vapor deposition is a process in which chemical precursors are transported in the vapor phase to decompose on a heated substrate to form a film.

In conventional CVD techniques, the problems of selection and delivery of chemical precursors are often considerable, especially for multicomponent products[93]. Except for the conventional thermally activated CVD, a number of groups are developing methods to initiate CVD reaction by different energy sources. This has given rise to variant CVD methods such plasma enhanced CVD (PECVD), photo-assisted CVD (PACVD), Atomic Layer Deposition (ALD), metalorganic CVD (MOCVD), aerosol assisted CVD (AACVD), flame vapor assisted deposition (FAVD), electrochemical vapor deposition (EVD), and chemical vapor infiltration (CVI). For more details, the reader is referred to the vast number of existing dedicated books [93, 114-116].

The first step of the Spray-ILGAR method is an aerosol assisted CVD process, which uses aerosol droplets to transport the precursors with the aid of inert carrier gases towards the hot substrate. AACVD has many advantages [93]:

- Deposition of multicomponent films
- Controlled stoichiometry
- Simplicity
- Wide variety of materials
- Oriented or epitaxial films
- High deposition rate
- Many choices for precursors
- Extended range of thermal stability for volatile precursors
- Possibility of doping
- Conformal coverage
- Reproducible, constant delivery rates for multicomponent systems

As a result of the aerosol transport of the precursor and the associated CVD deposition mechanism, AACVD can combine the advantages of both conventional CVD and spray pyrolysis.

In general, the key steps involved in a CVD process are shown as following:

(1) Transport of reactant to the reactor
(2) Diffusion and absorption of reactant to the surface of the substrate
(3) Surface reaction
(4) Desorption of gaseous by-products
(5) Transport of gaseous by-products

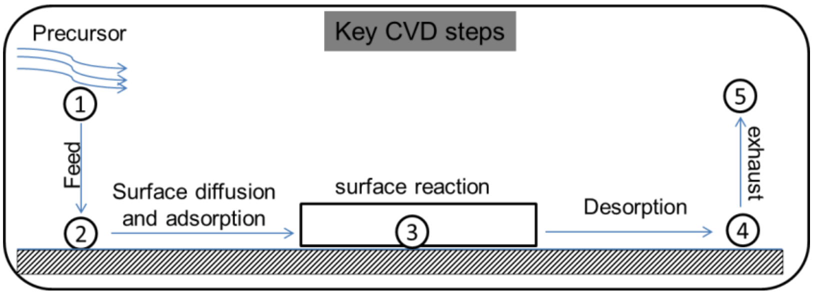

Figure 4.1: Key steps involved in chemical vapor deposition.

The growth rate of the film in the CVD process is limited by either (a) the feed rate of the precursor, (b) mass transport (diffusion) of precursor to the substrate, or (c) surface reaction kinetics. Since these three steps are in series, the slowest step will limit the overall rate. The deposition rate is often determined by (a), when the precursor has low vapor pressure, otherwise determined by (b) or (c) for precursors with high vapor pressure. In most CVD processes, abundant reactants near the substrate are available, as in our case, to ensure the deposition of uniform films. Therefore, the deposition rate is often limited by (b) or (c). CVD may be performed in the mass transfer controlled regime when high deposition rate is needed. This situation is often obtained at high pressure and temperature, where the reaction rate is sufficiently high that it does not limit the deposition rate. On the other hand, the deposition rate is limited by the rate of surface reaction with high precursor throughputs at low pressures and low temperatures.

In the following, without limitations imposed by the feed-rate, the qualitative dependence of the deposition rate on the relevant parameters is described. The analysis assumes a first-order surface reaction written in terms of the gas phase concentration of the reactant at the surface. It also assumes diffusion through a concentration boundary layer of known thickness. The whole process consists of two steps in series, diffusion to the surface and surface reaction. The more detail description can be found in reference [114, 116] .

The deposition rate is given by Eq 4.1-4.3.

$$r = \frac{C_r v}{1/k + L/D} \qquad \text{Eq.4.1}$$

$$r = kC_r v = k_0 v\left[P_r / RT\right]\exp\left(-\frac{E_A}{RT}\right) \qquad \text{for k<< D/L} \qquad \text{Eq.4.2}$$

$$r = \frac{vDC_r}{L} = \left(\frac{VD_0}{L}\right)\left(\frac{P_0}{P}\right)\left(\frac{T}{T_0}\right)^{3/2}\left(\frac{P_r}{RT}\right) \qquad \text{for k>> D/L} \qquad \text{Eq.4.3}$$

$$D = D_0\left(\frac{P_0}{P}\right)\left(\frac{T}{T_0}\right)^{3/2} \qquad \text{Eq.4.4}$$

Here C_r the reactant concentration outside the concentration boundary layer (a thin layer close to the substrate surface), *v* the volume of depositing precursor species, k the surface reaction rate constant, L the thickness of the concentration boundary layer, D the diffusion coefficient, D_0 the diffusion coefficient at reference conditions, k_0 pre-exponential constant, E_A the activation energy, and R the gas constant P the total pressure, P_0 total pressure at reference conditions, P_r reactant partial pressure outside the concentration boundary, T the temperature of gas above the substrate, T_0 the reference temperature for gas above the substrate.

For large k (k >> D/L), the surface reaction is rapid and the rate is given by vDC_r/L, corresponding to a diffusion limited process. This expression corresponds to the rate of diffusion of the reactant through the concentration boundary layer. For a slow reaction rate (k << D/L) or rapid diffusion in the gas phase (large D or small L), the rate is $kC_r v$, which is simply the rate of the surface reaction corresponding to surface-reaction-limited deposition.

A plot of logarithm of growth rate versus reciprocal temperature, known as an Arrhenius plot, can be used to determine the rate limiting step of a reaction (Figure 4.2).

At low temperature, the deposition rate increases rapidly in exponential manner on temperature, which matches with the Eq.4.2. This indicates that the rate-limiting mechanism is surface chemical kinetics. From the slop, the activation energy can be determined.

At higher temperature, the surface reactions become so fast that the deposition rate is limited by the diffusion of the precursor to the substrate surface. It is therefore the mass-transport limited process. The deposition rate depends only weakly on the temperature which is roughly $T^{3/2}$(See Eq.4.3). This behavior illustrates that the growth transits from surface reaction control at low temperatures to diffusion control at high temperatures.

At even higher temperatures, the gas phase particle formation, which cannot deposit on the substrate, may occur and lead to the depletion of the reactant concentration in the gas phase and reduces the rate [117]. Other possible reasons might be a thermodynamic limitation of reactant conversion or rapid adsorptions of the precursor from the surface before reaction occur [116].

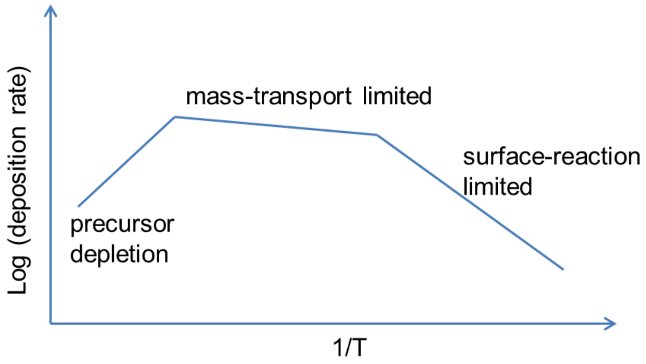

Figure 4.2: Schematic showing dependence of deposition rate on temperature.

4.2 Mass spectrometric study of the gas-phase chemistry during spray deposition of ZnS nanodots

In the Spray-CVD process and the first step of Spray-ILGAR, the generated $Zn(acac)_2$ aerosol droplets will evaporate before reaching the heated substrate surface leading to a deposition by thermal decomposition from the gas phase, which is an AACVD process. Hence, it is expected to detect two processes in theses spray-based techniques: evaporation and thermal decomposition of $Zn(acac)_2$. In this section, mass spectrometry is carried out to provide more insight into the mechanism of $Zn(acac)_2$ decomposition which occurs in both techniques. The mass spectrometer can be regarded as a kind of chemistry laboratory, especially designed to study ions in the gas phases [118, 119].

$Zn(acac)_2$ as one of the metal β-diketonates has been widely applied as a precursor to prepare films and coatings due to its high volatility and its ready availability. Turgambaeva et al. [120-122] have investigated the thermal stability and thermolysis of several β-diketonates using high temperature mass spectrometry, such as $Cu(acac)_2$, $Sc(acac)_3$, $Al(acac)_3$ and $Pb(acac)_2$. The thermolysis of $Zn(acac)_2$ has been studied by Ismail using thermogravimetry (TGA) and differential temperature analysis (DTA). IR-spectrometry and XRD have been used to analyze the products [123]. Arii et al. [99], also used sample-controlled thermogravimetry (SCTG), thermogravimetry combined with evolved gas analysis by mass spectrometry (TG-MS) and simultaneous differential scanning calorimetry and X-ray diffraction (DSC-XRD) to investigate the humidity controlled thermal decomposition of $Zn(acac)_2$.

In order to elucidate the mechanism of ZnS synthesis from aqueous $Zn(acac)_2$ solution and H_2S, mass spectrometry is applied, which permits to make relatively simple and fast identification of the gas phase. Firstly, in-situ mass spectrometry study on the thermal decomposition of the $Zn(acac)_2$ powder using different carrier gases are investigated in section 4.2.1. Secondly, an in-situ characterization of the gaseous side-and intermediate products during the Spray-ILGAR nanodot growth is described in section 4.2.2. By means of these studies, a decomposition route of $Zn(acac)_2$ on a hot substrate surface is proposed in section 4.2.3. Finally, the real time intensity tracking of various masses by mass spectrometry in the Spray-ILGAR and Spray-CVD process are investigated separately.

4.2.1 In-situ mass spectrometry study on the thermal analysis of $Zn(acac)_2$ powder using different carrier gases

The Spray-ILGAR formation of ZnS nanodots from aqueous $Zn(acac)_2$ solution is rather complex: many parameters, such as solvent, pH value of solution, temperature and so on, play important roles in the deposition process. Furthermore, the essential effect of H_2S on the formation of homogeneous intermediate films during the first Spray-ILGAR step (see section 3.1.3.7) was still unclear. The investigation on the thermal pyrolysis process of $Zn(acac)_2$ powder alone is helpful for the following studies of the dependence of the deposition process on the different parameters. In the following, $Zn(acac)_2$ powders are heated under different atmospheres in order to study the influence of solvent on the decomposition process.

The apparatus used to simulate the thermal decomposition of $Zn(acac)_2$ is sketched in Figure 4.3. In experiment “A”, the $Zn(acac)_2$ powder was heated in a glass tube which had N_2 carrying the gaseous products to an attached mass spectrometer. A wad of glass wool, subsequent to the $Zn(acac)_2$ powder, was utilized to ensure that only gases rather than particles reach the measurement chamber. Experiments “B” and “C” were carried out with the similar set-up but the N_2 gas was firstly bubbled through EtOH or H_2O respectively, which is to study the effect of solvent. Accurate temperature measurements were made by a thermocouple attached to the bottom of the glass tube containing $Zn(acac)_2$ powder. Thus, the gaseous products formed as a function of temperature were measured.

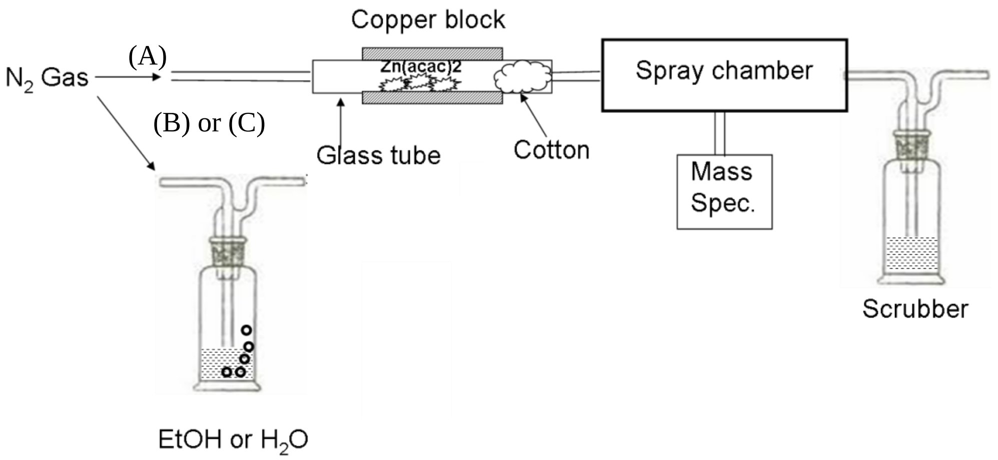

Figure 4.3: Scheme of the experimental setup for the in-situ mass spectrometry.

Arii [99] reported that the evolution of gaseous anhydrous $Zn(acac)_2$ and acetylacetone (Hacac), which are attributed to the evaporation and thermal decomposition process respectively, were detected during the thermal analysis of $Zn(acac)_2$ in dry atmosphere. However, the controlled humidity prevents the sublimation of $Zn(acac)_2$. According to the NIST-MS database [124, 125], and the mass spectra shown by Macdonald (metal acac), the mass spectrum of $Zn(acac)_2$ includes the fragment ions from anhydrous $Zn(acac)_2$, i.e. m/z 262,247,205,163, 64 and from Hacac, i.e. m/z 15, 29, 43, 58, 72, 85, 100. Therefore, the characteristic peak of anhydrous $Zn(acac)_2$ m/z 163 ($Znacac^+$) and acetylacetone m/z 100 ($Hacac^+$) are tracked as a function of the temperature, as well as the peak m/z 18 (H_2O^+) which could play an important role in the thermal decomposition process.

The thermolysis results of $Zn(acac)_2$ powder with three different carrier gases, i.e. dry N_2, N_2 saturated with EtOH and N_2 saturated with H_2O are presented in Figure 4.4 (a)-(c).

In order to assess the effect of H_2S on the deposition process, H_2S is introduced together with the above three different carrier gases in experiment “D”, “E” and “F”. The corresponding comparison results are demonstrated in Figure 4.4 (d)-(f).

It can be seen that, when $Zn(acac)_2$ powder is heated with dry N_2 as the carrier gas, weak signals of $Hacac^+$ and $Zn(acac)^+$ appear at around 170 °C (Figure 4.4 (a)). Afterwards, the $Hacac^+$ signal gradually increases as the temperature rises which indicates a slow decomposition process upon heating. In Figure 4.4 (b), the $Hacac^+$ and $Zn(acac)_2^+$ signals also show up at around 170 °C with the carrier gas of N_2 saturated with EtOH. The $Zn(acac)^+$ signal is as weak as the one for dry N_2 in Figure 4.4 (a), whereas the $Hacac^+$ signal is much stronger. Additionally, a second $Hacac^+$ peak appears at around 200 ± 10 °C. These twin peaks of $Hacac^+$ are present and become even stronger in Figure 4.4 (c), which indicates $Zn(acac)_2$ decomposes via a 2-step evolution of Hacac with the carrier gas of N_2 saturated with solvent H_2O or EtOH. However, the $Zn(acac)^+$ signal is not detected at all in Figure 4.4 (c) with N_2 saturated with H_2O as the carrier gas, which is consistent with the result reported by Arii, et al [99]. Therefore, it can be concluded that H_2O can prevent the sublimation of $Zn(acac)_2$, whereas it promotes the hydrolysis and decomposition process indicated by the strongest signal of $Hacac^+$ among these three experiments “A-C”.

When H_2S is introduced simultaneously with the carrier gas N_2, it is observed that both signals of $Znacac^+$ and $Hacac^+$ in Figure 4.4 (d)-(f) drastically increase compared to the ones in Figure 4.4 (a)-(c). It is worth mentioning that a strong $Znacac^+$ signal shows up when H_2S is present in the carrier gas of N_2 saturated with H_2O, while vice versa at the absence of H_2S. This indicates that a small amount of H_2S does help the sublimation of $Zn(acac)_2$ even in the aqueous atmosphere. This result explains and supports the previous assumption in section 3.1.3.7 that H_2S creates a different deposition mechanism in the first spray step of the Spray-ILGAR process, which leads to different morphologies of the obtained particles. It was shown that H_2S could not only sulfurize the intermediate film in the 2nd step, but also help $Zn(acac)_2$ to sublimate into gas phase and undergo CVD process instead of liquid to solid conversion in the 1st step. In the absence of H_2S (see Figure 4.4 (c)), the nebulized dissolved $Zn(acac)_2$ droplets decompose directly to ZnO solid particles without sublimation, which is a liquid to solid conversion process. One micron nebulized droplet yields one produced particle, which results in the submicron particles in Figure 3.11. However, the gaseous $Zn(acac)_2$ produced in the presence of H_2S (Figure 4.4 (f)) undergoes chemical vapor deposition and yields nanodots.

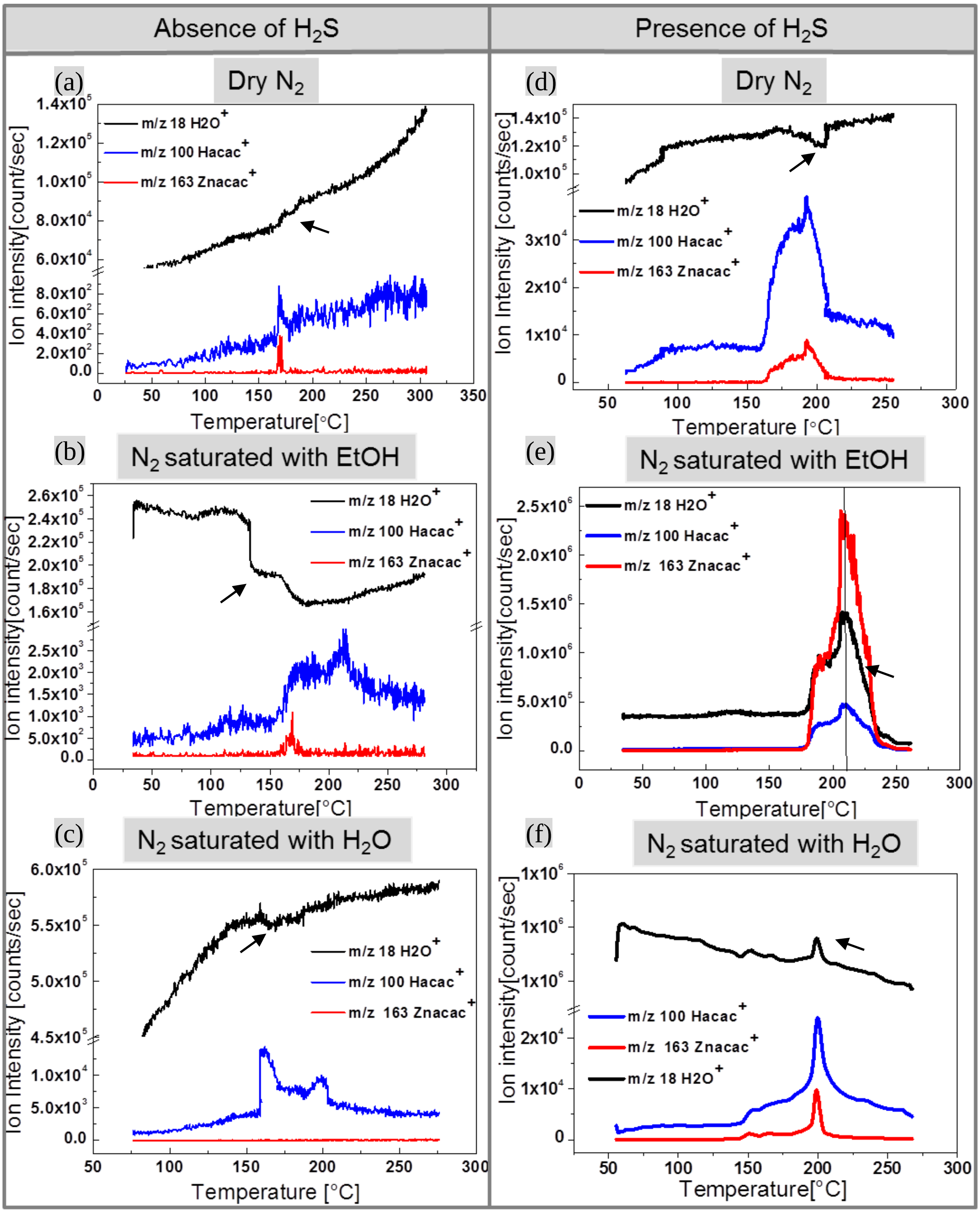

Figure 4.4: Mass spectra tracking ions m/z 163 ($Znacac^+$) (red line), m/z 100 ($Hacac^+$) (blue line) and m/z 18 (H_2O^+) (black line) as a function of temperature during the thermolysis of $Zn(acac)_2$ powder with different carrier gases. (a-c) in the absence of H_2S, (a) dry N_2, (b) N_2 saturated with EtOH, and (c) N_2 saturated with EtOH; (d-f) in the presence of H_2S, (d) dry N_2 and H_2S, (e) N_2 saturated with EtOH and H_2S, and (f) N_2 saturated with EtOH and H_2S.

Additionally, the H_2O^+ signals seem quite interesting in these six experiments “A-F”. In the absence of H_2S, negative H_2O^+ peaks (indicated with arrow in Figure 4.4 (a)-(f)) appear when the $Hacac^+$ signal peaks show up in Figure 4.4(a)-(c). This phenomenon is quite clear with the carrier gas of N_2 saturated with EtOH, where the deposition rate is faster than with the carrier gas of dry N_2 and therefore the system consumes more H_2O for hydrolysis, but the amount of H_2O in the carrier gas of N_2 saturated with EtOH is much less than N_2 saturated with H_2O. It happens also during the thermolysis of $Zn(acac)_2$ powder in the presence of H_2S with the carrier gas of dry N_2 (see Figure 4.4 (d)). These indicate that during the decomposition process, i.e. 2-step evolution of Hacac, $Zn(acac)_2$ first hydrolyzes with H_2O in the 1st step and then further thermally decomposes to ZnO. The water is consumed for hydrolysis according to the following equation:

$$Zn(acac)_2 + H_2O \xrightarrow{1^{st}} Zn(acac)(OH) + Hacac \xrightarrow{2^{nd}} ZnO + Hacac + H_2O \qquad \text{Eq.4.5}$$

This explains that ZnO formation from $Zn(acac)_2$ is enhanced at low temperatures by the addition of water in the reports [100, 126, 127].

In contrast, the H_2O^+ signal peak is positive during the thermolysis with the carrier gases of N_2 saturated with EtOH or H_2O in the presence of H_2S. The ZnO product from the decomposition of $Zn(acac)_2$, which consumes a certain amount of H_2O, will further react with the introduced H_2S and produce ZnS and H_2O. The generated H_2O could be one of the contributions to the positive H_2O^+ peaks signal peak. Probably, some other reactions also produce H_2O, which is still unknown. Based on these studies, the in-situ mass spectrometry study of the formation of spray ZnS nanodots preparation is described in the next section.

4.2.2 In-situ mass spectrometry study on the gas-phase species involved in the Spray-ILGAR and Spray-CVD processes

In-situ mass spectrometry is a promising technique for the detailed investigation of the mechanism of the decomposition. In this section, in-situ mass spectra recorded the gaseous products during the spray pyrolysis of $Zn(acac)_2$ alcoholic solution and aqueous solution are investigated.

Zn(acac)$_2$/EtOH solution

The $Zn(acac)_2$/EtOH solution was ultrasonically nebulized into micron size aerosol droplets, which were carried through a hot wall reactor by N_2 and then fed into the chamber connected to the mass spectrometer system. The reactor was set at 200° C, same as the substrate temperature in the deposition process. The resulting mass spectra are shown in Figure 4.5. Each mass spectrum is represented as a bar graph of abundance (vertical peak intensity) vs. mass (m). The lowest row in Figure 4.5 is the background measurement in the chamber before aerosol generation, which is the reference for comparison. The center and the top spectra are recorded during nebulizing in the presence and absence of H_2S, respectively. All the fragment ions and the corresponding assignment produced in the mass spectrum during the nebulization of $Zn(acac)_2$/EtOH solution are listed in Table 4.1.

By comparing with NIST database, the gases evolved are identified as a mixture of Hacac (m/z 72, 85, 100) and $Zn(acac)_2$ (m/z 64, 163, 205, 247, 262) when the aerosol is switched on without simultaneously introducing H_2S. The ion of m/z 262 ($(Zn(acac)_2)^+$) represents the molecular ion, which produces a series of abundant fragment ions, such as m/z 163 ($Zn(acac)^+$), m/z 64 (Zn^+). These two sets of ions suggest that $Zn(acac)_2$ does not only sublimate, but also concurrently thermal decompose, which support the fact that the

1st step of the Spray-ILGAR nanodot deposition is an AACVD process. However, as it can be seen in Figure 4.5 (center), the signal-to-noise ratio is not very good. The weak signals indicate that the decomposition and sublimation of Zn(acac)$_2$ in the absence of H_2S are slow processes.

When aerosol and H_2S are simultaneously introduced into the chamber, the intensities of these two sets of ions are several tens of time higher than in the absence of H_2S. This result is in good agreement with the one observed upon heating Zn(acac)$_2$ powder with the carrier gas of N_2 saturated with EtOH in Figure 4.4 (b) and (e). Additionally, the intensity of m/z 163 (Zn(acac)$^+$) ions is higher than the molecular ion m/z 262 (Zn(acac)$_2$)$^+$), which is expected to be the most abundant ions among the fragments of Zn(acac)$_2$ reported by Macdonald [128].This fact could be explained by the consumption of the molecular ions caused by the thermal decomposition of Zn(acac)$_2$. Simultaneously, some new ions at m/z 116, 145, 155 and 220 appear, as compared to the spectrum when no H_2S is present in the chamber. These new ions could be the products when the oxygen atom of the fragments is substituted by sulfur at the attack of H_2S. The ions m/z 116 and 220 are attributed to $C_5H_8OS^+$ (HacacS$^+$), and $C_7H_8OSZn^+$ (Zn(acac)S) $^+$), which are the substitutes for $C_5H_8O_2^+$ (Hacac$^+$), and $C_7H_8O_2Zn^+$ (Zn(acac)$^+$) and supposed to be the intermediate products during the decomposition process. These masses show clearly that H_2S is involved in the decomposition process of Zn(acac). An example showing how H_2S attacks the ions $C_5H_8O_2^+$ is represented in Figure 4.6.

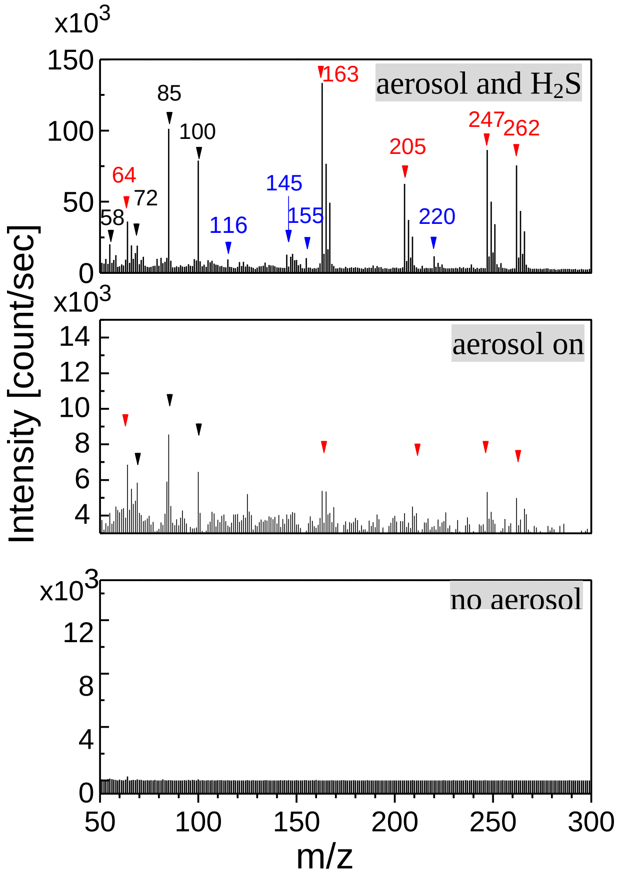

Figure 4.5: Mass spectra of the Zn(acac)$_2$/EtOH solution nebulized in the presence (top) and absence (center) of H_2S. The bottom is the background measurement in the chamber before aerosol generation. The red triangles

represent the set of ions corresponding to the fragments of $Zn(acac)_2$, the black ones corresponding to the fragments of Hacac and the blue ones corresponding to the new ions of the intermediate products.

Table 4.1: Fragment ions of Figure 4.5 produced in the mass spectra during nebulizing $Zn(acac)_2$ / EtOH solution and the corresponding assignment.

	m/z	Assignment
$Zn(acac)_2$	262	$C_{10}H_{14}O_4Zn^+$
	247	$C_9H_{11}O_4Zn^+$
	205	$C_7H_9O_3Zn^+$
	163	$C_5H_7O_2Zn^+$
	64	Zn^+
Hacac	100	$C_5H_8O_2^+$
	85	$C_4H_5O_2^+$
	72	$C_4H_8O^+$
	58	$C_2H_6CO^+$
New ions	220	$C_7H_8OSZn^+$
	155	fragment of m/z 205
	145	fragment of m/z 163
	116	$C_5H_8OS^+$

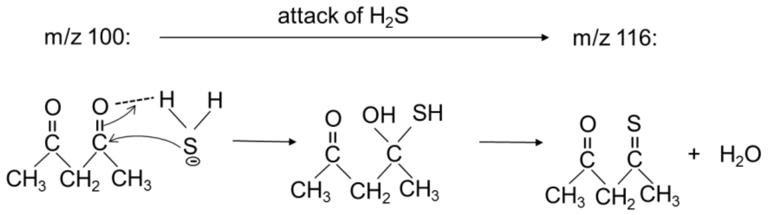

Figure 4.6: Schematic sketch showing H_2S attacks the ions $C_5H_8O_2^+$. The bond lengths and angles are not drawn to scale.

$Zn(acac)_2$ / H_2O solution

As mentioned in section 3.1.3.2, $Zn(acac)_2$ aqueous solutions with different pH values were used to prepare ZnS nanodots in the Spray-ILGAR process. The increase of H^+ concentration with the addition of HAc, will remarkably increase the deposition rate. In the following, the gas-phase species are recorded during nebulizing the aqueous $Zn(acac)_2$ solution at pH=3 in the presence or absence of H_2S respectively. In order to study the influence of pH value on the deposition process, the solution at pH=3 nebulized in the presence of H_2S is changed to pH=6. The background measurement is recorded as the reference for comparison. All the spectra are shown in Figure 4.7 A ((a)-(d)) with the corresponding SEM images of the obtained nanodots shown in Figure 4.7 B.

The fragment ions (except the ones shown already in Table 4.1) and the corresponding assignment are listed in Table 4.2. No zinc containing ions are detected or the signal is as weak as the noise when only aerosol is on, which means that no or only a little $Zn(acac)_2$ sublimates into gas phase without the presence of H_2S. The fact is in good agreement with the result upon heating $Zn(acac)_2$ powder with the carrier gas of N_2 saturated with H_2O in Figure 4.4 (c) and again demonstrates the importance of H_2S.

The ions observed in the mass spectrum when nebulizing $Zn(acac)_2$ aqueous solutions at pH=6 (Figure 4.7 (d)) is similar to the one when nebulizing $Zn(acac)_2$ / EtOH solution (Figure 4.5 (top)). However, the intensities are weaker, and some of the ions might be too weak to be detected, such as ions m/z 116, 145 and 155.

Some new ions are observed at pH=3 in Figure 4.7 (c), m/z 235-237, 256-258, and 285, which are attributed to the fragments of Zinc acetate ($Zn(ac)_2$) [129]. So far, it is still not clear whether these $Zn(ac)_2$ fragments are from the sublimation of $Zn(ac)_2$, which is the product of the reaction between $Zn(acac)_2$ and HAc, or the fragments stem from the rearrangement of $Zn(acac)_2$ by the interaction with H^+. It is reported by Vacassy et al. [102] that the zinc acetato complexes are present when pH<2. Additionally, no nanodots, but submicron particles were obtained with $Zn(ac)_2$ / H_2O solution (Figure 3.9), which indicates that $Zn(ac)_2$ does not sublimate into the gas phase to undergo a CVD process. Further study is necessary to figure out where the new ions stem from.

Compared to the spectrum obtained from pH=6 solution, the sum of the zinc containing ion intensities at pH=3 is much higher although the starting Zn precursor solution has the same concentration. This fact illustrates that the decomposition rate and therefore the deposition rate is much faster at the lower pH value, which is in good agreement with the experimental result in section 3.1.3.2, that the dot density obtained at pH=3 is higher than at pH=6. The acceleration of the decomposition rate by the H^+ ions will be further discussed in the following section 4.2.3.

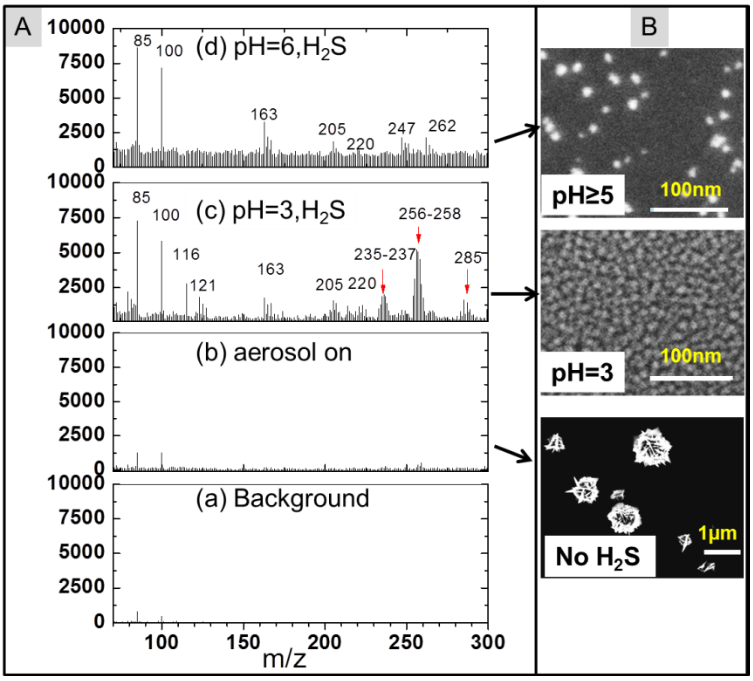

Figure 4.7: (A) Mass spectra of $Zn(acac)_2/H_2O$ solution nebulized in the presence and absence of H_2S. (a) Background measurement in the chamber before aerosol generation, (b) $Zn(acac)_2$ aqueous solution at pH=3 in the absence of H_2S, (c) $Zn(acac)_2$ aqueous solution at pH=3 in the presence of H_2S, and (d) $Zn(acac)_2$ aqueous solution at pH=6 in the presence of H_2S. The corresponding SEM images of the obtained nanodots. The red arrows correspond to the new ions compared to Figure 4.5, which are attributed to the fragments of Zinc acetate.

Table 4.2: Fragment ions of Figure 4.7 produced in the mass spectra during nebulizing $Zn(acac)_2$ / H_2O solution and the corresponding assignment. The ions have been listed in Table 4.1 are not shown below.

	m/z	Assignment
New ions	285	$[Zn_3(OCOCH_3)O_2]^+$
	256-258	$[Zn_4(OCOCH_3)_4O]^{2+}$
	235-237	$[Zn_4(OCOCH_3)_3(OH)O]^{2+}$

4.2.3 Decomposition route of $Zn(acac)_2{\cdot}H_2O$ on the hot substrate

In the following, the detailed description of the thermal decomposition of $Zn(acac)_2{\cdot}H_2O$ on the substrate surface is discussed. The influences of H_2S, H_2O and acid to the decomposition rate are taken into account as well. The proposed decomposition route of $Zn(acac)_2$ on the hot surface is described in Figure 4.8.

In the first step, $Zn(acac)_2{\cdot}H_2O$ transferred by the carrier gas to the reactor chamber, evaporates, diffuses and adsorbs on the hot surface, which will open the chelate cycles (Figure 4.8). Afterwards, $Zn(acac)_2{\cdot}H_2O$ hydrolyzes with the crystal H_2O with the evolution of Hacac and $Zn(acac)^+(OH)^-$ This is in good agreement with the first observed Hacac signal by mass spectrometry upon heating $Zn(acac)_2{\cdot}H_2O$ powder even with dry N_2 as the carrier gas (Figure 4.4 (a)).

In the second step, if there is no extra proton in the system, the $Zn(acac)^+(OH)^-$ group rearranges by migrating the proton from one methyl group (intramolecular H) (indicate in Figure 4.8) to the oxygen-metal bond (O-Zn group) with the evolution of a cumulene group and $Zn(OH)_2$, which further decompose to ZnO and H_2O. Although this reaction is not very probable due to the unstable cumulene, the driving force might be the further decomposition of $Zn(OH)_2$ with the formation of crystalline ZnO.

Otherwise, if there are extramolecular H in the system, which could stem from H_2O, H_2S or acid, the $Zn(acac)^+(OH)^-$ group prefers to react with these protons with the formation of Hacac (See Figure 4.8). Taking H_2O as an example, the $Zn(acac)^+(OH)^-$ further hydrolyzes with H_2O with the evolution of $Zn(OH)_2$ and Hacac. In the presence of the extramolecular H, $Zn(acac)_2{\cdot}H_2O$ decomposes by a 2-step evolution of Hacac, which agrees well with the observed two Hacac peaks in the mass spectra upon heating $Zn(acac)_2{\cdot}H_2O$ with the carrier gas of N_2 saturated with H_2O or alcohol as well as with addition of H_2S (See Figure 4.4 (b-f). The reaction with the extramolecular H gives an additional chance to the further decomposition of the $Zn(acac)^+(OH)^-$ group in comparison to the rearrangement by migrating the intramolecular H. Hence, the existence of H_2O, H_2S or acid will accelerate the decomposition of $Zn(acac)_2$ and the evolution of Hacac. This fact then explains the consumption of H_2O vapor upon $Zn(acac)_2{\cdot}H_2O$ powder heating in Figure 4.4 (a-d), and the increased intensity of Hacac and zinc containing fragments in the presence of H_2S compared to the absence of H_2S in Figure 4.4 (d-f) and Figure 4.5 (top) as well as the stronger Hacac fragment intensity with the solution of pH 3 than pH 6 in Figure 4.7 (c-d).

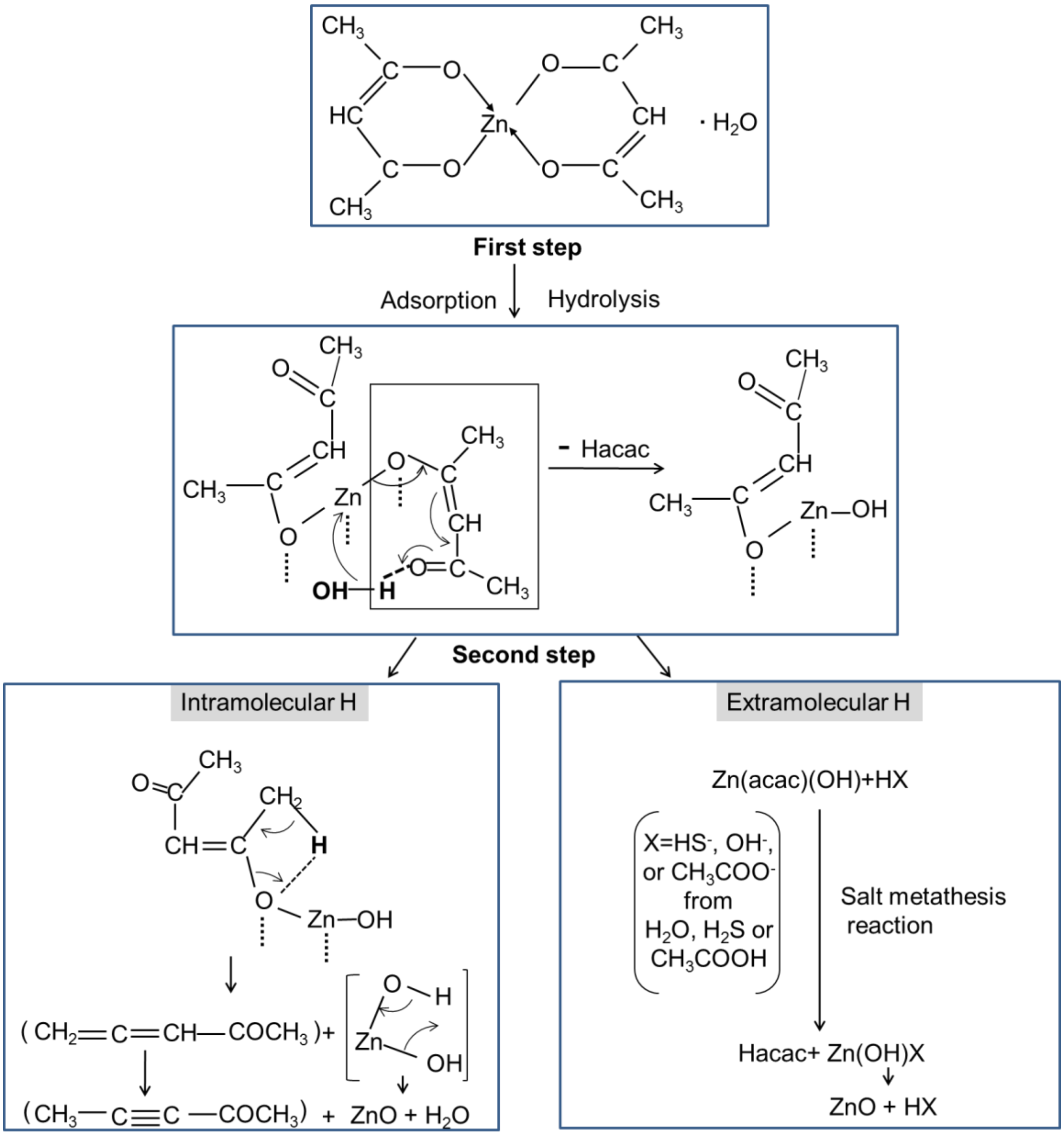

Figure 4.8: Scheme of thermal decomposition of Zn(acac)$_2$ on hot substrate
···· represents Van der Waals bonding to the substrate surface
The bond lengths and angles are not drawn to scale.

4.2.4 Real time tracking of various masses by mass spectrometry in the Spray-ILGAR and Spray-CVD processes

Real time mass spectrum tracking in the Spray-ILGAR process

In the following, the real time tracking of various masses by mass spectrometer in the Spray-ILGAR process is introduced. The most intensive Zn-containing ion m/z 163 (Zn(acac)$^+$) is chosen rather than a molecular ion m/z 262 (Zn(acac)$_2^+$) to describe the behavior of the complex during the spray process. In addition, the ion m/z 100 (Hacac$^+$), m/z 34 (H_2S) are also tracked as a function of time. Last but not least, the ions m/z 18 (H_2O) is detected as well, which could be reactant or product during the process.

Like the true ILGAR deposition process, between the spray and sulfurization step, there is a pause which allows N_2 to clear the aerosol or H_2S out of the chamber before the sequential step. Perpendicular lines in Figure 4.9 mark the switch to the next step. The gas is extracted from the ILGAR chamber which is heated to 200 °C.

Firstly, only N_2 is blown through the chamber (step marked as “0” in Figure 4.9 (a)), except N_2 and background H_2O detected by the mass spectrometer, there is a weak signal of H_2S, which is the residue from the previous cycle and important for the next step “1” as discussed in the section 4.2.2. Later, the nebulizer is switched on and the aerosol is generated and carried to the chamber (step indicated as “1” in Figure 4.9 (a)). The intensities of ions m/z 163 ($Zn(acac)^+$) and m/z 100 ($Hacac^+$) linearly increase with the time indicating the concurrent sublimation and decomposition of $Zn(acac)_2$ which correlates with the above discussion. There is a small anomalous step increase in mass 34. Since no H_2S is yet in the system this comes either from electrical noise interference from the nebulizer or from the reaction product between Hac and the ZnS on the reactor wall [72]. When the aerosol is switched off (step marked as “2” in Figure 4.9 (a)), the $Zn(acac)^+$, $Hacac^+$ signal exponentially decay to lower values. Once the H_2S is switched on (step marked as “3” in Figure 4.9 (a)), the signal intensity of H_2S^+, of course, increases remarkably. Simultaneously, the H_2O^+ signal increases. This fact, which agrees with the results in section 4.2.1 (see Figure 4.4 e-f), indicates that the sulfurization step produces H_2O due to the reaction between H_2S and the decomposition intermediate product ZnO, shown as follows,

$$ZnO + H_2S \rightarrow ZnS + H_2O$$

Step “4” in Figure 4.9 (a) is a pause time to clean the chamber for the subsequent spraying cycle, when both aerosol and H_2S are switched off. Although it is switched off, H_2S is still detectable after 40 s or even longer time. This result support the conclusion stated earlier that H_2S has not been completely cleared out of the spray chamber within the standard 10s purging time. This residual H_2S plays an important role in the whole nanodots deposition process, which was discussed in Chapter 3.

In order to exclude the influence of the water impurity in the system from H_2S gas, the ion m/z 18 (H_2O^+) is tracked while only H_2S and N_2 is introduced without aerosol. As seen in Figure 4.9 (b), the signal H_2O^+ increase with a negligible amount as the H_2S is switched on. The conclusion can be drawn that the increase in H_2O^+ signal in Figure 4.9 (a) is due to the produced H_2O in the sulfurization step.

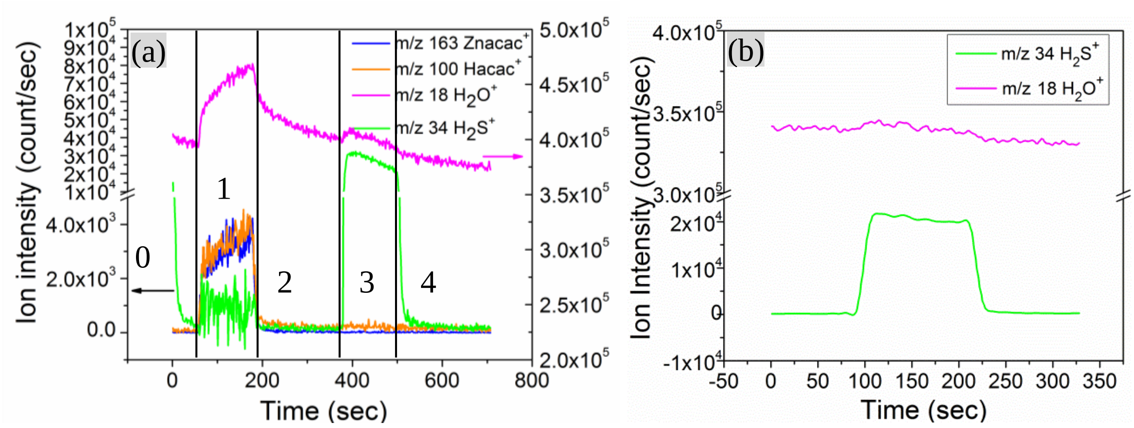

Figure 4.9: Real time mass spectra tracking of, (a) the mass fragments ion m/z 163 ($Znacac^+$), m/z 100 ($Hacac^+$), m/z 18 (H_2O^+) and m/z 34 (H_2S^+) in the Spray-ILGAR process, and (b) the mass fragment ions m/z 18 (H_2O^+) and m/z

34 (H_2S^+) when only H_2S is on. In figure 4.9 (a), Step "0"—only N_2 on; "1"—aerosol on; "2"—aerosol off; "3"—H_2S on; "4"—H_2S off.

Real time mass spectrum tracking in the Spray-CVD process

As mentioned above in section 4.2.2, $Zn(acac)_2$ could hardly to be detected without the presence of H_2S, especially for $Zn(acac)_2/H_2O$ solution. However, the deposition rate in the Spray-CVD process falls down remarkably as the H_2S concentration goes up as discussed in section 3.2.1.1. In the following, the influence of H_2S concentration in the Spray-CVD deposition process is studied by mass spectrometry. The ions m/z 100 $Hacac^+$, m/z 163 $Zn(acac)^+$, m/z 34 H_2S^+ are tracked as a function of H_2S flow rate, while the N_2 flow rate is kept constant at 2.5 mL/min.

To start with, only aerosol is introduced by the carrier gas N_2 into the chamber, when weak signals are detected in Figure4.10 (b). Once 5 ml/min 5% H_2S/Ar is simultaneously introduced into the chamber, the intensities of the ions m/z 100 $Hacac^+$, m/z 163 $Zn(acac)^+$ are significantly increased (Figure4.10 (c)). However, as the flow rate of 5% H_2S/Ar increases step by step, from 5 to 15, then to 30, and finally to 45 ml/min (H_2S flow rate is indicated in Figure 4.10 (d-f)), the intensities of the ions m/z 100 $Hacac^+$, m/z 163 $Zn(acac)^+$ gradually drop down, which is in agreement with the decreasing deposition rate detected in section 3.2.1.1. The SEM pictures of the nanodots obtained with the corresponding H_2S flow rates by Spray-CVD are shown at the bottom of the mass spectrum. The decline of these ion intensities is due to the particle formation as a result of the reaction between $Zn(acac)_2$ and H_2S before reaching the hot substrate.

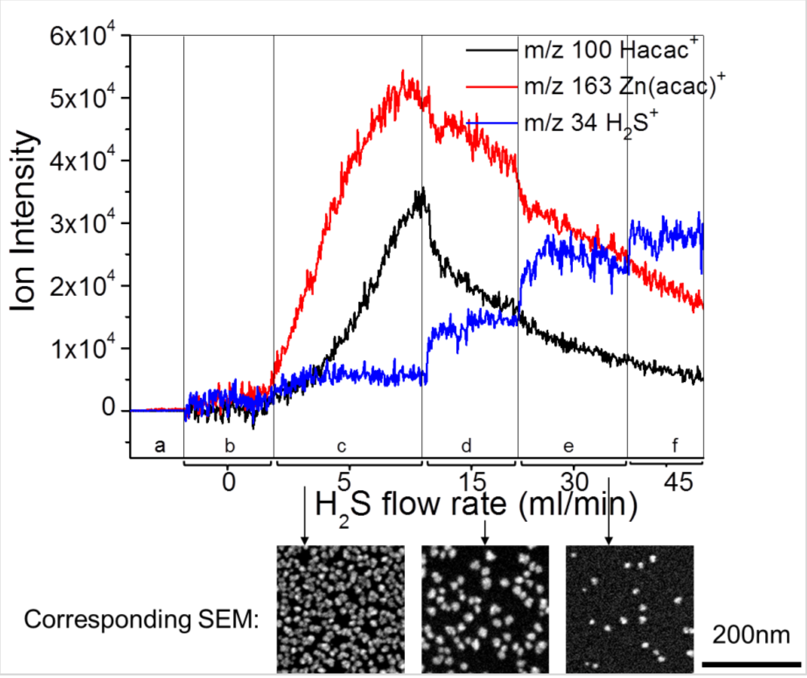

Figure 4.10: Real time mass spectrum tracking of mass fragment ions, m/z 163 ($Znacac^+$), m/z 100 ($Hacac^+$) and m/z 34 (H_2S^+) in the Spray-CVD process with different H_2S flow rate (a) no aerosol, (b) aerosol without H_2S, (c) aerosol with 5ml/min H_2S, (d) aerosol with 15ml/min H_2S, (e) aerosol with 30ml/min H_2S, and (f) aerosol with 45ml/min H_2S. The SEM figures of the nanodots obtained with the corresponding H_2S flow rates are shown at the bottom.

4.3 Self-limiting growth of ZnS nanodots

In this section, an overall model for the growth of the Spray-ILGAR and Spray-CVD nanodots is described. It would be interesting to know how coarsening of particle size, e.g., by Ostwald ripening or particle agglomeration, is efficiently suppressed.

Before the detailed discussion about the growth mechanism of the Spray-ILGAR and Spray-CVD nanodots in section 4.3.2, the composition difference between the nanodots obtained from these two processes is studied in section 4.3.1.

4.3.1 Composition difference between the Spray-ILGAR and Spray-CVD nanodots

The morphologies of the nanodots prepared by Spray-ILGAR and Spray-CVD are described in chapter 3, which are both quasi-sphere. The nanodots obtained by Spray-CVD are around two times larger in size than Spray-ILGAR. As the number of process cycles increases, the nanodots become denser with negligible increase in size in the Spray-ILGAR process, while in the Spray-CVD process, the nanodots get larger in size as the spraying time prolongs. In this section, the compositions of the achieved nanodots from these two processes are compared by the application of energy-filtered transmission electron microscope (EF-TEM) and the corresponding sulfur map.

Spray-ILGAR

As mentioned in 3.1.3.7, the intermediate film from the first step of the Spray-ILGAR is ZnO. Figure 4.11 (a) shows Zero-loss filtered TEM images of Spray-ILGAR nanodots. Zero-loss filtered TEM has better image contrast than standard TEM, due to the removal of the blurring effect of inelastic scattering by the Zero-loss filtering. Figure 4.11 (b) is the corresponding sulfur map. The brightness within the maps represents the intensity of the sulfur signal: bright indicates high and black low intensity. It can be seen obviously that, the places where show signal from the nanodots in Figure 4.11 (a), are found to have strong signal of S in Figure 4.11 (b). This indicates that in the Spray-ILGAR process the intermediate products ZnO are homogeneously converted to ZnS in the second step.

Spray-CVD

In contrary, the Zero-loss filtered TEM image of the Spray-CVD nanodots (Figure 4.12 (a)) and the corresponding sulfur map (Figure 4.12 (b)) look quite different from the ones of Spray-ILGAR. In Figure 4.12 (a), the particles achieved in the Spray-CVD process are irregular spheres with several bright dots. The bright dots in Figure 4.12 (a) have no corresponding S signal in Figure 4.12 (b), while the rest places in Figure 4.12(a) are found to have strong S signal. It is very probable that the ZnO intermediate film is only partially converted into ZnS. Hence, the obtained particles in the Spray-CVD process are actually Zn(S,O) instead of ZnS. The detailed ZnS and ZnO content will be studied in Chapter 5. The Zn(S,O) particle is not a core-shell structure, but O is randomly and separately distributed within one particle. This could be the result of partially sulfurization of the intermediate ZnO nanodot. Even though it is only partially sulfurized, it could be the product of the interdiffusion of sulfur and oxygen ions across a core-shell structure of ZnO / ZnS. The different compositions of the nanodots achieved from these two processes lead to different growth mechanisms, which will be the topic of the next section.

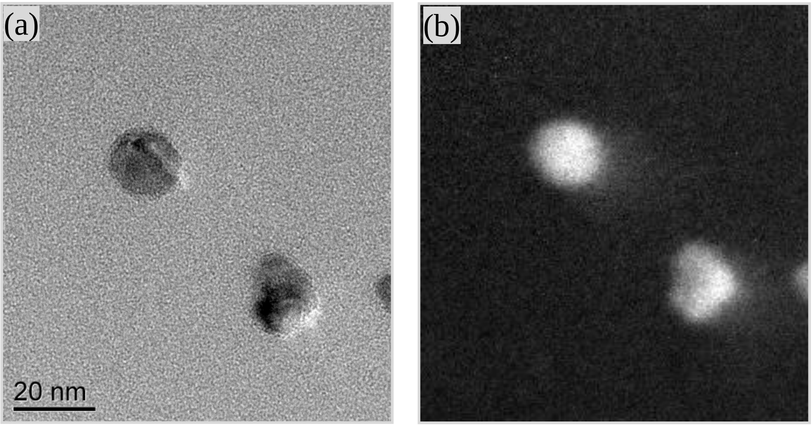

Figure 4.11: Zero-loss filtered TEM image of the Spray-ILGAR nanodots (a) and the corresponding sulfur map (b). Bright indicates high and black low intensity.

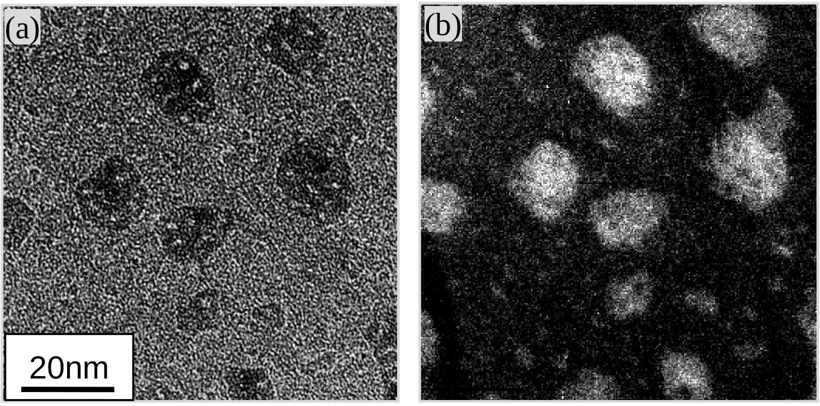

Figure 4.12: Zero-loss filtered TEM image of the Spray-CVD nanodots (a) and the corresponding sulfur map (b). Bright indicates high and black low intensity.

4.3.2 Self-limiting growth model in the Spray-ILGAR process

As mentioned above, Spray-ILGAR is a 2-step cyclic process, which consists of a CVD step with special precursor delivery manner and a H_2S sulfurization step. Hence, the growth mechanism of this spray-based nanodot method should follow the CVD growth model, while differentiate from the conventional CVD due to the effect of H_2S conversion step. The sulfurization of the nuclei in the H_2S step changes the surface composition and the structure of the formed nanocrystals. The lack of affinity between the nanocrystals before and after sulfurization plays an important role in the subsequent growth. Thus, it is necessary to take both CVD and sulfurization into account to understand the self-limiting growth of ZnS nanodots in the Spray-ILGAR process.

In common with other CVD experiments, the deposition rate can be limited by any of several steps which can be considered to occur in series (See Figure 4.1). As discussed in section 4.1, the growth rate is limited by either the feed rate of the precursors, mass transport (diffusion) of precursors to the substrate, or surface reaction kinetics.

For the feed-limited-deposition, the rate of the surface reaction is much faster than the delivery rate of the precursor to the surface. As a result, the delivery rate limits the overall deposition rate. However, as mentioned in section 4.1, abundant reactants near the substrate are available in most CVD processes to ensure the deposition of uniform films. Additionally, a key feature of the feed-rate-limited deposition is that the deposition rate does not depend on the substrate temperature as long as all other parameters remain constant [116]. Increasing the temperature can't increase the rate, which can be not faster than the rate of delivery the precursor to the surface. Contrary to this feed-rate-limited deposition, see discussion in section 3.1.3.4, the deposition rate and surface morphology change with the substrate temperature. Therefore, the observed growth behavior can be explained as mass transport- or surface-reaction-limited deposition.

These two kinds of limited depositions dominate at the two temperature regimes of the CVD process, which is shown in Figure 4.2. It is obvious that surface reaction kinetics dominates at low temperature, while mass transport limit occurs at high temperature. In the following section, the Spray-ILGAR nanodot growth behavior is understood by considering the two temperature regimes of the CVD process and the corresponding mechanisms which control the deposition.

4.3.2.1 Low temperature regime

In the low temperature region, defined as the substrate temperatures region below 300°C in this thesis, the process is within the kinetically controlled reaction regime. The deposition rate is under control by the reaction kinetics of the precursor absorbed on the surface. The growth mechanisms are depicted step by step in Figure 4.13 (a). The SEM pictures of the nanodots obtained after different process cycles are shown at the bottom of the corresponding process. These SEM pictures illustrating the growth of the nanodots step by step support the proposed growth mechanism.

As the temperature is low, the precursor molecules do not necessarily decompose instantly at the point of arrival. On the contrary, there is a finite time during which the molecules migrate (by diffusion) on the surface before decomposition. Due to the unique subsequent characteristic of the Spray-ILGAR method, the initial process could be different from the following step. The first process cycle and the subsequent ones will be discussed respectively in the following.

Initial nucleation and growth stage in the 1st process cycle

Before the discussion about the growth process, a typical Gibbs free energy curve as a function of the radius of the particle in the solution system, adapted from Ref. [130, 131] is shown in Figure 4.14. The graph displays both a critical state (maximum value of Gibbs free energy) and a stable state (minimum value of Gibbs free energy). The growth process is finished at the minimum value.

In the spraying step of the 1st cycle, once arrive on the hot substrate surface, the delivered precursor molecules may diffuse and be adsorbed to nucleation sites, where they decompose and form a large amount of nuclei. The nuclei greater than the critical state in Figure 4.14 begin to grow and stop at the final size particles, which is around 3-8 nm in this work, when the Gibbs free energy is at a minimum. It should be noted that the particles here mean the intermediate ZnO, which are converted into ZnS by H_2S in the following sulfurization step.

Compared to the colloid synthesis, additional considerations need to be taken into account during growth of heterogeneous nuclei in terms of film growth in the CVD process, which can determine the growth mode and final morphology of nanostructures. One key factor is the interaction strength, such as the wetting properties, between the adsorbed molecules and substrate surface, which could lead to three primary growth processes illustrated in Figure 4.15 (a-c): layer growth (Frank–van der Merwe (FM) growth) or island plus layer growth (Stranski-Krastanov growth), island growth (Volmer–Weber (VW) [106, 132]. This could be used to explain the obtained nanodots or compact films when using different solvents H_2O or alcohol, respectively.

It is obvious that in the first cycle of the Spray-ILGAR nanodot deposition, following the Volmer–Weber growth mode, the nuclei form on expense of the adsorbed precursor molecules on the substrate, grow into stable ZnO particles (3-8 nm) with a Gibbs free energy at minimum and are finally converted into ZnS particles.

In the traditional CVD process, subsequent growth in the island or Volmer–Weber growth mode occurs on the existing island site, which leads to the continuous growth of the existing particles. However, this is contradictory to the observation in section 3.3.1.3.3 that the nanodots keep constant in size with increasing number of process cycles (< 50 cycles) in the Spray-ILGAR process.

In colloid synthesis, the size and shape of particles can be controlled by both thermodynamic and kinetic factors, which are dictated by both the intrinsic structural properties and reaction systems such as, solvent, capping agent, and reducing agent [133]. Many chemicals including both organic and inorganic molecules as well as ions can be used to either passivate or activate particular surfaces and affect the natural growth habits of the particles. Other reaction conditions including concentration, time and temperature are also critical.

How the coarsening of the particles is efficiently suppressed in the Spray-ILGAR process will be discussed in the next section.

4.3.2.2 Nanodot growth in the subsequent process cycles

As mentioned above, there is a finite time during which the molecules migrate (by diffusion) on the surface before decomposition in the low temperature regime. At the very beginning of the deposition, due to the low dot density, the gaps among the originally formed dots might be much larger than the diffusion length of the molecules before decomposition. Hence, the precursor molecules $Zn(acac)_2$ even after diffusion decompose to ZnO before they find an already formed nanodot. This results in the new nuclei formation onto the gaps among the existing dots, leading to an increase of the dot density with a negligible increase of their sizes. In addition, due to the sulfurization by H_2S in the sulfurization step, the formed ZnO nanodots are converted to ZnS. The sulfurization of ZnO will prevent the further growth of the nanodots. This is due to the fact that the sulfurization changes the elemental composition and lattice distance of the dot material (see chapter 5). The ZnO, which is deposited in the following spray step, might grow on two pathways, either on an existing ZnS nanodot surface or the gaps between the formed ZnS nanodots. Since the composition and the crystal structure of both compounds are different (see chapter 5), the existing ZnS nanodots, like the stabilized organic capping agents, will not work as an effective decomposition site, but prevent the further growth. The subsequent ZnO is preferentially bound to the uncovered substrate, rather than the surface of the existing ZnS nanodots. Even if the precursor molecules arrive at the formed nanodots, they will preferentially diffuse to other preferential adsorption and decomposition sites. This leads to the formation of new nuclei and depress the further growth of the existing nanocrystals.

When the dot density is high enough, the distances among them become smaller than the diffusion length of the precursor molecules before decomposition. The new molecules have enough time to find an already existing nanodot. However, as mentioned above, the sulfurized surface of the existing nanodots does not work well as an adsorption and decomposition site, but serves as a barrier layer which limits further crystal growth even though the dot distance is smaller than the diffusion length. The precursor molecules keep decomposing on the uncovered substrate. Hence, the dots become denser and denser with a negligible increase in size, which is in good agreement with the experimental observation (Figure 3.6 (a-c)) and explains how the coarsening of the nanodots is efficiently suppressed.

When the density reaches the maximum value, the nanodots start touching each other (See figure 3.6 (c)). The substrate surface does not exist anymore. The subsequent ZnO must deposit on the existing ZnS nanodots. Hence, some dots aggregate to form larger ones. This results in the formation of nanodots with a variety of different sizes after many process cycles (See Figure 3.6 (d) and the last step of Figure 4.13 (a)).

4.3.2.2 High temperature regime

At substrate temperatures above 300 °C, the process is within the mass-transfer-limited regime, in which as quickly as the reactants encounter each other or an existing particle, they react. The deposition rate is under control by the rate of the arrival of the precursor molecules on the substrate or by the time of diffusion of molecules through the diffusion layer. As the temperature is high, the precursor molecules decompose instantly at the point of arrival without any migration. Hence, on one hand, the existing nanodots continue to grow. On the other hand, it produces also new nuclei among the existing dots, which is indicated in Figure 4.13 (c). This results in a variety of different sizes. The corresponding growth model is presented in Figure 4.13 (c).

4.3.3 Self-limiting growth model in the Spray-CVD process

At the very beginning, the Spray-CVD process also follows the Volmer–Weber growth mode, in which the nuclei form on the substrate, grow into ZnO particles and simultaneously converted into Zn(S,O) particles. The different degree of sulfurization in the Spray-ILGAR and Spray-CVD (see section 4.3.1) plays an important role in the following growth procedure.

In the low temperature regime, does the subsequent growth follow the mode in the Spray ILGAR process, where the formation of new nanodots occurs in the gap among the primary ones? Or does it still follow the Volmer–Weber growth mode, in which the precursor molecules diffuse to the existing nanodots and grow on them?

In the Spray-CVD process, the formed nanodots are Zn(S,O) instead of ZnS. Although it is reasonable to assume that the sulfurization of the intermediate ZnO nanodot film by H_2S preferentially takes place at surface, sulfur and oxygen ions will interdiffuse across the ZnO/ZnS interface. Therefore, the Zn(S,O) is not a core-shell structure, where the ZnS shell could act as a barrier layer to limit further crystal growth. In contrast, the Zn(S,O) is like a solid dispersion of oxide and sulfides regions containing S and O at the surface (see figure 4.12). The O-containing surfaces of the formed nanocrystals work as effective adsorption and decomposition sites for the subsequent ZnO growth in the following spraying step. Hence, the difference from the Spray-ILGAR process is that the precursor molecules decompose and nucleate on the existing nanodot, instead of searching for the uncovered substrate. This results in an increase of the size of the existing nanodots and more importantly an increase at the same rate for all nanodots. This growth model explains very well the experimental observation in section 3.2 (Figure 3.19), where the nanodots are homogeneous in size and grow larger as the spraying time increases. Last but not least, the nanodots will become irregular as the new ZnO from the subsequent cycle settles at the randomly distributed O-containing regions of the nanodots. This will be further discussed in Chapter 5. The corresponding growth model is presented in Figure 4.13 (b). In order to support the proposed growth mechanism, the SEM pictures of the nanodots obtained after different process cycles are shown as well at the bottom of the corresponding process.

At high temperature, the process is within the mass-transfer-limited regime, of which the growth behavior is the same as in the Spray-ILGAR process. The corresponding growth model is presented as well in Figure 4.13 (c).

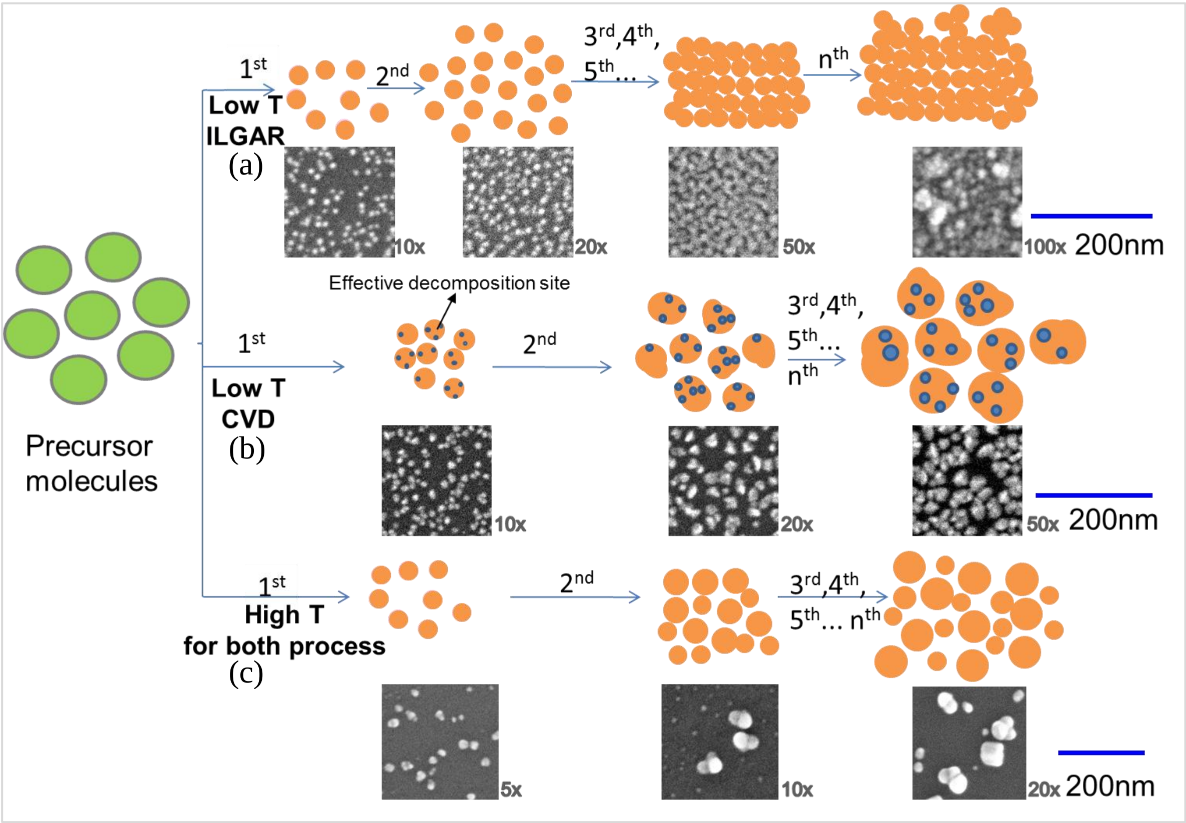

Figure 4.13: Growth model of the nanodots obtained at two different regimes. (a) Spray-ILGAR process at the low temperature regime, (b) Spray-CVD process at the low temperature regime and (c) Both process at the high temperature regime. To support the proposed growth model, SEM pictures of the nanodots obtained after different process cycles (indicated in the lower right corner) are shown at the bottom of the corresponding process.

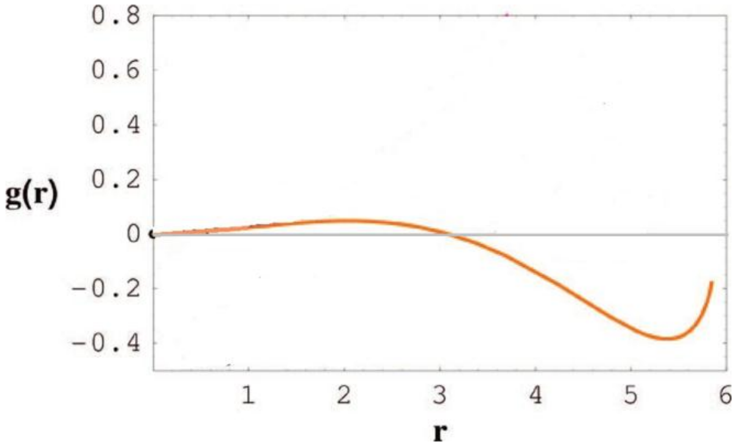

Figure 4.14: Gibbs free energy of a nanoparticle-solution system as a function of the radius of the particle. Adapted from Ref. [130, 131].

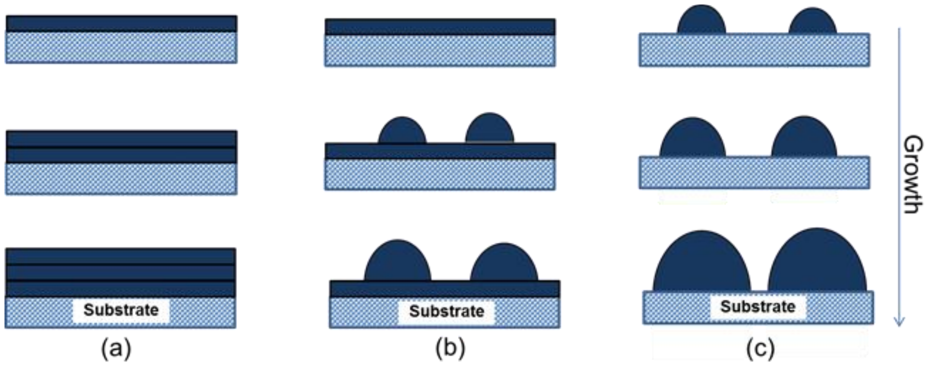

Figure 4.15: Chemical vapor deposition growth modes. (a) layer or Franck-van der Merwe growth, (b) layer plus island or Stranski-Krastanov growth, and (c) island or Volmer-Weber growth [106].

4.4 Summary

In chapter 4, the growth mechanism of ZnS nanodots including the thermal decomposition of Zn(acac)$_2$ followed by the nucleation and growth of the nanodots on the hot substrate surface is described in detail.

Section 4.2 deals mainly with the study of thermal behavior of Zn(acac)$_2$ by mass spectrometry (MS) in the Spray-ILGAR and Spray-CVD processes.

Upon heating the Zn(acac)$_2$ powder, the sublimation and decomposition processes of Zn(acac)$_2$ are faster with the carrier gas of N_2 saturated with EtOH than in dry N_2 atmosphere. On the other hand with N_2 saturated with H_2O, the sublimation process is suppressed, whilst the decomposition is promoted. Additionally, H_2S is found to drastically enhance the gas-phase thermal decomposition of Zn(acac)$_2$ powder.

In-situ MS study of the thermal decomposition from Zn(acac)$_2$ aerosol shows that H_2S is involved in the decomposition process. It does not only accelerate the sublimation and decomposition of Zn(acac)$_2$, but reacts with Zn(acac)$_2$ to produce intermediate compounds detected by mass spectrometry. Last but not least, the pH value of the precursor solution accelerates the deposition rate.

Based on the above discussions about the fragments detected by in-situ MS, the influence of the solvent, H_2S and pH value of the solution, a decomposition route of $Zn(acac)_2$ on hot surface is suggested. The molecules adsorbed on the surface, firstly, open the chelate ring, and hydrate with crystal H_2O with the evolution of Hacac and Zn(acac)(OH) group. Secondly, the Zn(acac)(OH) group could rearrange by migrating the intramolecular H to form $Zn(OH)_2$ or react with the extramolecular H from H_2O, H_2S and acid by the formation of second Hacac and the Zn containing intermediate product which could further decomposes to ZnO. The reaction with extramolecular H gives an additional chance to yield ZnO, which explains the influence of the solvents, H_2S and pH value of the precursor solution on the decomposition process.

Real time tracking of relevant masses by mass spectrometry in the Spray-ILGAR process reveals that the nebulized aerosol droplets evaporate before reaching the substrate surface leading to a gaseous deposition in the 1st step and then the H_2S gas converts the oxide into sulfide with H_2O as a byproduct in the 2nd step. In the Spray-CVD process, it is learned that H_2S at the low concentration helps $Zn(acac)_2$ to undergo gas-phase chemical decomposition, but an excess H_2S converts liquid $Zn(acac)_2$ aerosol droplets to ZnS solid particles before reaching the substrate and deplete the gas-phase $Zn(acac)_2$, and therefore the deposition rate on the substrate decreases.

In section 4.3, the self-limiting growth model of the nanodots obtained in the Spray-ILGAR and CVD process is discussed. The studies on zero-loss filtered TEM images and the corresponding sulfur maps reveal that the ZnS nanodots obtained by Spray-ILGAR are quasi spherical particles with homogeneous distribution of sulfur. In contrast, the ZnS particles achieved by Spray-CVD contain some unsulfurized ZnO regions, which are probably Zn(S,O) like compound, a product of incomplete sulfurization of oxide. The different compositions in these two processes account for the different growth mechanisms.

The self-limiting growth of the nanodots in these two processes is understood by taking into account both the mechanism of the two temperature regimes of the CVD process and the sulfurization of the nanodots.

In the low temperature region, the surface reaction kinetics controls this regime, where the precursor molecules have a finite time to diffuse and find the preferential nucleation site before decomposition.

- In the Spray-ILGAR process, the growth follows the Volmer-Weber mode in the 1st process cycle. The precursor molecules decompose and form a large amount of ZnO nuclei which grow into stable particles (3-8 nm) with a minimum Gibbs free energy and are subsequently converted to ZnS in the sulfurization step. In the following process cycle, the complete sulfurized surface of the existing nanodots, which are different from the subsequent decomposition product ZnO in the elemental composition and lattice distance, works like a barrier layers to limit the further growth of the existing nanodots. This leads to an increase of the dot density with a negligible increase of the size, which was observed in chapter 3. When the dots are dense enough, they start touching each other and they aggregate to larger nanodots. Hence, it results in the formation of nanodots with a variety of size.

- In the Spray-CVD process, the growth mechanism follows the Volmer-Weber mode. The precursor molecules prefer to nucleate on the formed nanodots, which are Zn(S,O) rather than ZnS. The oxygen rich sites on the surface of the existing Zn(S,O) nanodots, act as effective nucleation sites for the precursor molecules. Hence, this results in the irregular shape of the nanodots and an increase of the size of the existing nanodots at the same rate, which was observed in chapter 3 as well.

In the high temperature region, it is a regime dominated by the limit of the mass transfer where the decomposition rate is very fast. In both processes, the precursor molecules arriving on the substrate surface or on the existing nanodots decompose immediately without having time to diffuse to favored nucleation sites. Therefore, the old existing nanodots continue to grow while new nanodots form as well, which results in different sizes of the nanodots.

Chapter 5

Characterization of the nanodots obtained by Spray-ILGAR and Spray-CVD

Once the synthesis of the nanodots and the corresponding growth mechanisms have been studied in the previous two chapters, it is now time to investigate the properties of the as-prepared nanodots.

The crystal structure of the nanodots prepared by Spray-ILGAR and Spray-CVD process can be examined by using X-ray diffraction (XRD) (section 5.1) and Transmission electron microscopy (TEM) (section 5.2). The different morphologies between Spray-ILGAR and Spray-CVD nanodots are clearly observed by means of TEM (section 5.2). The ultraviolet-visible spectroscopy (UV-Vis) is performed for determination of the band gap in section 5.3. Additionally, the information about the chemical composition of the nanodot surface is acquired by using X-ray photoelectron spectroscopy (XPS) and X-ray excited Auger electron spectroscopy (AES) (section 5.4). A short description of structural, chemical and optical material analysis techniques that have been applied during the course of this work is given in Appendix A .The fundamental properties of the nanodots are analyzed before their application as passivation buffer layers in the thin film solar cells.

5.1 Crystal structure of the Spray-ILGAR and Spray-CVD nanodots

Crystalline ZnS is well known to exist in two crystallographic structures, cubic sphalerite (zinc blende) structure, and hexagonal wurtzite structure. Although the latter is a thermodynamically metastable phase below 1020 °C, the recent reports show that the phase transition temperature may be lower as nanocrystal size decreases [134-138]. And a theoretical prediction and subsequent experiment verification shows that zinc blende structure has surface energy higher than that of the wurtzite structure in the nanoscale regime [135, 136]. In the following, the crystal phases of the obtained nanodots by Spray-ILGAR and Spray-CVD are discussed. To identify the crystalline phases, the recorded X-ray diffraction patterns are compared to the references from the data base of the Joint Committee on Diffraction Standards (JCPDS). See more details in Appendix A.3.

5.1.1 Spray-ILGAR

Before the discussion about the structures of the nanodots obtained by Spray-ILGAR and Spray-CVD, the XRD pattern of the spray pyrolysis ZnO, which is produced by continuously spraying the same precursor solution as the above two processes, aqueous Zn(acac)$_2$ solution (pH=3) at 225 °C for 60 min, is shown in Figure 5.1. As discussed in section 4.2, in order to accelerate the deposition rate, N_2 saturated with H_2O is used as the carrier gas to transfer the nebulized Zn(acac)$_2$ precursor solution onto the hot substrate. All diffraction peaks can be indexed as the wurtzite phase ZnO (JCPDS No.36-1451).

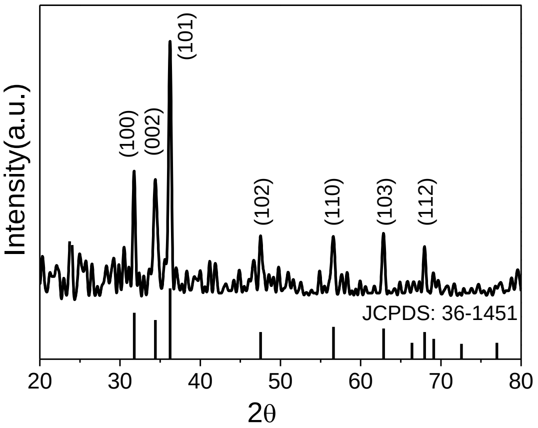

Figure 5.1: X-ray diffraction pattern of the spray pyrolysis ZnO film. (Vertical bars: randomly oriented wurtzite ZnO, JCPDS card No.36-1451).

Figure 5.2 shows the XRD patterns of the nanodots prepared by the Spray-ILGAR process for 100 cycles at different temperatures 175 (a), 225 (b), 300 (c), and 400 °C (d). Vertical bars indicate the standard peak positions of sphalerite ZnS JCPDS No. 05-0566 and wurtzite ZnS JCPDS No. 36-1450. The XRD peaks of the nanodots obtained at 175 °C could be attributed to sphalerite or wurtzite phase ZnS. As remark, due to the lower deposition rate at 175 °C, the XRD spectrum is quite noisy. However, the presence of a characteristic peak at around θ=27°, corresponding to $(100)_w$ (W=wurtzite), suggests that the nanodots obtained at 200 °C can be indexed as wurtzite-phase ZnS. It should be noted that from this XRD pattern, the existence of a cubic phase, of which the main characteristic XRD peaks overlap with hexagonal ZnS cannot be excluded. A similar result has been reported for a ZnS:Ni^{2+} film prepared by ultrasonic spray pyrolysis [139]. The XRD diffraction peaks are broadened as compared to those of bulk ZnS crystals, indicating the finite size of these crystallites. The average size of the nanodots could be estimated by Scherrer's formula, as shown in Eq. A.2.

The calculated values for all the samples are listed in the following Table 5.1. The estimated sizes of the nanodots obtained at 175 and 225 °C are larger than those observed from the SEM images, which could be explained by the influence of the process cycles on the Spray-ILGAR process at temperature < 300 °C. As discussed in section 3.1.3.3 and 4.3.2.1, the nanodots aggregate when the film is closed and the dots touch each other. Hence, the nanodots obtained at 100 process cycles, which are used for the XRD measurement, are expected to be larger than those obtained at 20 cycles for the SEM measurement. On the other hand, the calculated sizes of the nanodots achieved at 300 and

400 °C are close to those detected by the SEM images. The nanodots have a variety of sizes at any process cycles at temperature above 300 °C.

Table 5.1: Average sizes of the Spray-ILGAR nanodots obtained at different temperatures.

Temperature (°C)	175	225	300	400
Mean size (nm)	8	14	26	30

As compared to the polycrystalline pattern of randomly oriented ZnS (JCPSD card No.36-1450), the (002) peak in Figure 5.2 (a-d) is relatively much enhanced, indicating that the nanocrystals are preferentially oriented along the c-axis. The characteristic peaks of $(100)_W$, $(101)_W$, $(110)_W$, and $(112)_W$ peaks in Figure 5.2 (c) and (d) strongly indicate that the nanodots achieved at 300 and 400 °C are wurtzite-phase ZnS. The different preferential orientations of the nanodot films can be explained by the competition of the growth rate of the nuclei with various orientations at the corresponding temperature.

Compared to the XRD pattern of the spray pyrolysis ZnO, the ZnS nanodots obtained by the Spray-ILGAR process have the same wurtzite structure as ZnO, although the preferential orientation is different. This indicates the wurtzite structure is maintained during the conversion of the intermediate ZnO to the ZnS nanodots, which explains the achievement of the metastable wurtzite ZnS phase at such a low temperature (175-400 °C) by the Spray-ILGAR process. The detailed crystal phase of the Spray-CVD nanodots will be the focus of the following section.

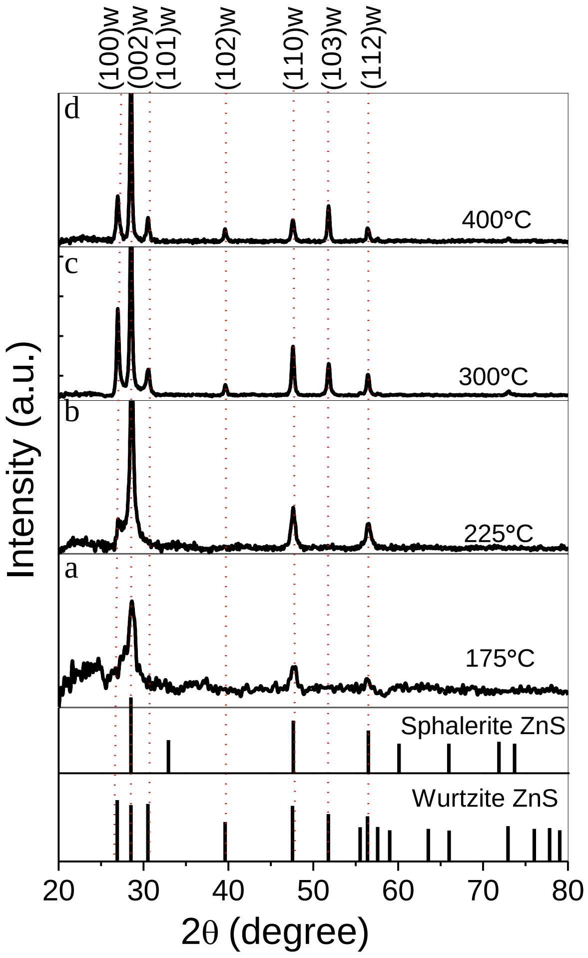

Figure 5.2: X-ray diffraction patterns of the nanodots obtained by Spray-ILGAR at different temperatures: (a) 175 °C, (b) 225 °C, (c) 300 °C and (d) 400 °C. (Vertical bars: randomly oriented wurtzite ZnS, JCPDS card No.36-1450 and sphalerite ZnS, JCPDS card No. 05-0566).

5.1.2 Spray-CVD

The XRD patterns of the nanodots achieved by Spray-CVD at 225 °C with different 5% H_2S/Ar flow rates are illustrated in Figure 5.3 (b-e), 30 ml/min (b), 15 ml/min (c), 10 ml/min (d), and 5 ml/min (e) 5% H_2S/Ar together with 2.5 L/min N_2. For comparison, the XRD pattern of Spray-ILGAR ZnS nanodots is shown in Figure 5.3 (a). The standard peak positions of sphalerite ZnS JCPDS No. 05-0566 and wurtzite ZnS JCPDS No. 36-1450 are indicated in vertical bars as well.

The average sizes of the Spray-CVD nanodots achieved with different H_2S flow rates are tabulated in Table 5.2, estimated using Scherrer's equation Eq. A.2. It is obvious that the size of the nanodots doesn't change with the H_2S flow rate, which supports the SEM observation in section 3.2.1.1. The values are close to those illustrated in the SEM images (Figure 3.16).

Table 5.2: Average sizes of the Spray-CVD nanodots with different H_2S flow rates at 225 °C. The calculated mean size of the Spray-ILGAR nanodots are shown as well for comparison.

H_2S flow rate (ml/min)	5	10	15	30	ILGAR
Mean size (nm)	22	23	22	20	14

It is obvious that all the nanodots achieved by the Spray-CVD process with different H_2S flow rates are wurtzite phase ZnS with characteristic peaks of $(100)_w$ and $(101)_w$. Additionally, the ratio of the peaks $(100)_w$ / $(002)_w$ (as indicated in Figure 5.3) as a function of the H_2S flow rate in the Spray-CVD process, as well as the corresponding ratio in the Spray-ILGAR process are demonstrated in Figure 5.4. It can be seen that this ratio decreases as the H_2S concentration goes up from 5 to 30 min/min in the Spray-CVD process and reaches the lowest value in the Spray-ILGAR process, where the H_2S concentration is the highest. It indicates that the sulfurization of the nanodots changes the preferential growth orientation. With the low H_2S concentration, the nanodots grow preferentially along (100) parallel to the substrate, whereas they prefer to grow oriented along (002) planes perpendicular to the substrate with the high H_2S concentration. This could be probably explained by the self-limiting growth model in section 4.3.2.1. In the Spray-CVD process the precursor molecules prefer to nucleate on the formed nanodots, which lead to the growth parallel to the substrate, while in the Spray-ILGAR process the precursor molecules nucleate at a new area and preferentially grow perpendicularly to the substrate. The more concentrated the H_2S, the less ZnO sites for nucleation while the more formation of new nuclei. Hence, as the H_2S concentration increases the nanodot growth prefers from (100) parallel to the substrate gradually to (002) perpendicular to the substrate.

However, it is interesting to note that no signals from crystalline ZnO can be detected. It could be that the amount of crystalline ZnO is too small to be detected (see Figure 4.12) or the ZnO in the Spray-CVD nanodots are amorphous or the ZnO particles are too small.

In section 5.2, the morphology and structure of the Spray-ILGAR and Spray-CVD nanodots are studied by TEM.

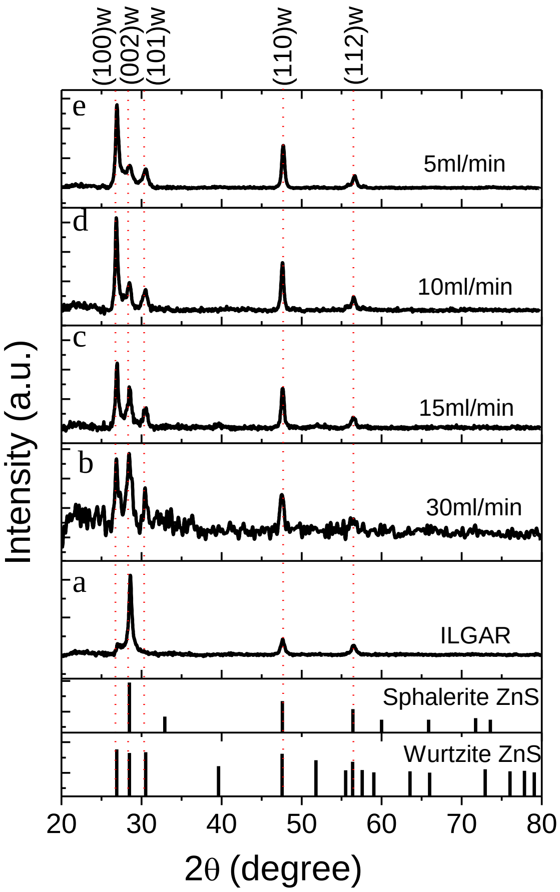

Figure 5.3: X-ray diffraction patterns of the nanodots obtained by Spray-ILGAR (a) and Spray-CVD at 225°C with different H_2S flow rates: (b) 5ml/min, (c) 10ml/min, (d) 15ml/min and (e) 30ml/min. The flow rate of the carrier gas N2 is 2.5 L/min. (Vertical bars: randomly oriented wurtzite ZnS, JCPDS card No.36-1450 and sphalerite ZnS, JCPDS card No. 05-0566).

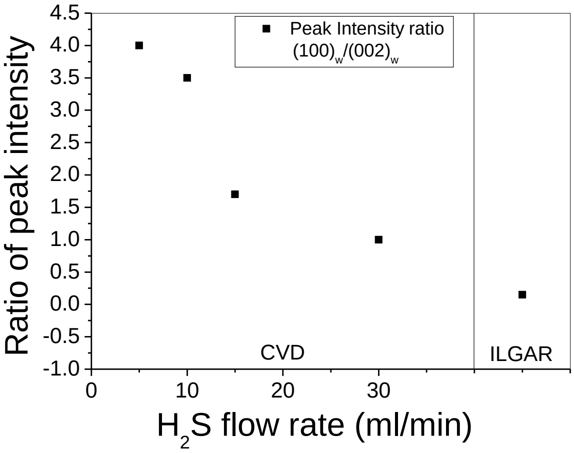

Figure 5.4: Intensity ratio of peak $(100)_w/(002)_w$ (indicated in Figure 5.3) as a function of H_2S flow rate in the Spray-CVD process. The flow rate of the

carrier gas N_2 is 2.5 L/min. This ratio in the Spray-ILGAR process is also shown for comparison (which is separated from the values of the Spray-CVD process by a vertical line).

5.2 Transmission electron microscopy

Transmission electron microscopy (TEM) and high resolution transmission electron microscopy (HRTEM) are carried out in order to image the structures of the obtained nanodots in the Spray-ILGAR and Spray-CVD processes.

Both the cross-section of the nanodots deposited on p-Si (100), and the plane view of the nanodots on Cu / Au / C grid are investigated. The nanodots were obtained at 200 °C on both substrates after 20 process cycles. See more details about TEM and the sample preparation in Appendix A.1.

5.2.1 TEM study on the cross-section of the Spray-ILGAR nanodots

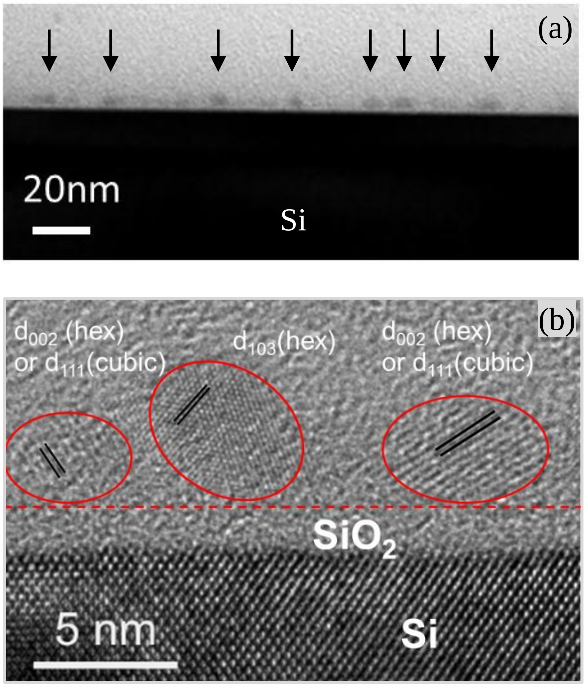

Figure 5.5: TEM (a) and HRTEM (b) images of the cross section of ZnS nanodots / Si deposited by Spray-ILGAR process.

In order to check if the nanodots directly deposited on the grid own the same morphology and structure as the ones deposited on the Si wafer, the cross section of the nanodots / Si is firstly studied in this section and then compared to the plan view of the nanodots/grid by TEM in the next section 5.2.2. Hence, both the cross section and the plan view of the nanodots are investigated.

Figure 5.5[3] shows the cross-sectional TEM and HRTEM images of the nanodots / Si. A few sub 10nm ZnS nanodots are distributed on the Si substrate surface with similar size

---

[3] The cross section TEM measurement has been done by Christel Dieker, Prof. Dr.Wolfgang Jäger in Christian-Albrechts-Universität zu Kiel.

and density as observed from the SEM image (Figure 3.2 in chapter 3). The nanodots are quasi-spheres slightly pressed along the direction perpendicular to the substrate surface (Figure 5.5 (a)). A layer of 2 nm SiO_2 is found in Figure 5.5 (b) inbetween the nanodots and the Si surface, which is due to the oxidation of the Si wafer. It is also obvious that the nanodots are polycrystalline. By measuring the distance between the lattice planes of the nanodots in Figure 5.5 (b), two of them are ascribed to either hexagonal ZnS (002) or to cubic ZnS (111) and the last one corresponds to the hexagonal ZnS (103). This observation is in agreement with the XRD measurement. In the next section, the plan views of the nanodots from the two processes are investigated.

5.2.2 Comparison of the Spray-ILGAR and Spray-CVD nanodots by TEM

This section focuses on the TEM study of the morphology and structure of the Spray-ILGAR and Spray-CVD nanodots, which are directly deposited on Cu/Au/C grids.

Figure 5.6 (a-b) and Figure 5.7 (a-c) illustrate the TEM and HRTEM images of the nanodots obtained by these two methods. Firstly, the comparison between the plain view of ZnS/grid (Figure 5.6) and the cross section of ZnS/Si (Figure 5.5) is described. It is obvious that, the nanodots are polycrystalline particles at around 3-8 nm, no matter what kind of substrate they are deposited onto. In addition, the nanodots can be obtained at any kinds of substrate, which is thermally stable at T ≥175 °C. This opens exciting opportunities for the incorporation of semiconductor nanoparticles in a variety of new applications.

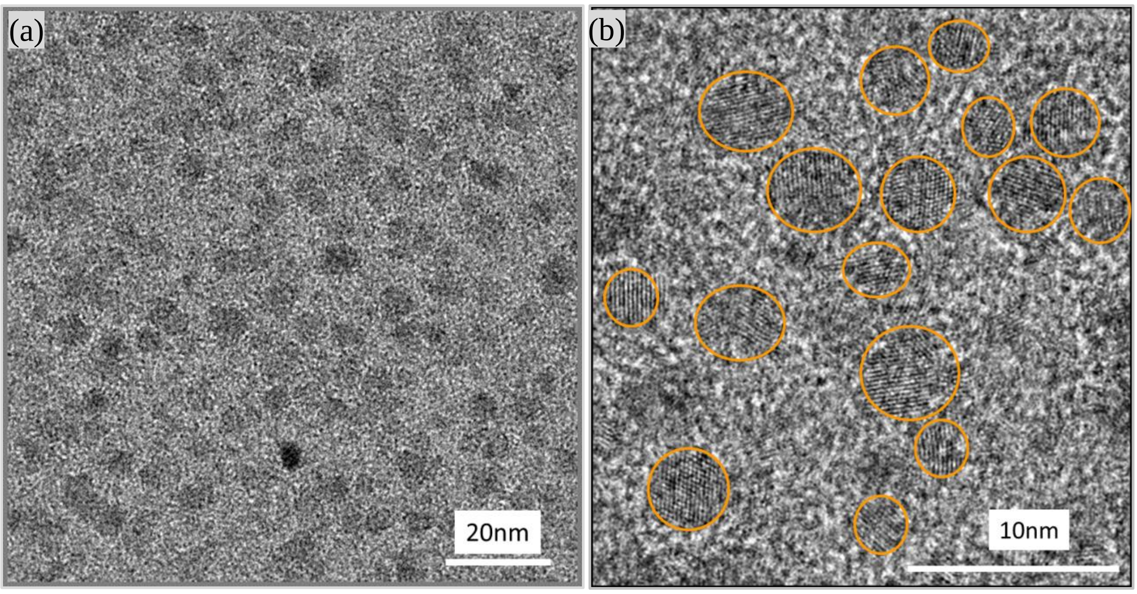

Figure 5.6: TEM (a) and HRTEM (b) images of the plan view of ZnS nanodots deposited on Cu/Au/C grid by the Spray-ILGAR process.

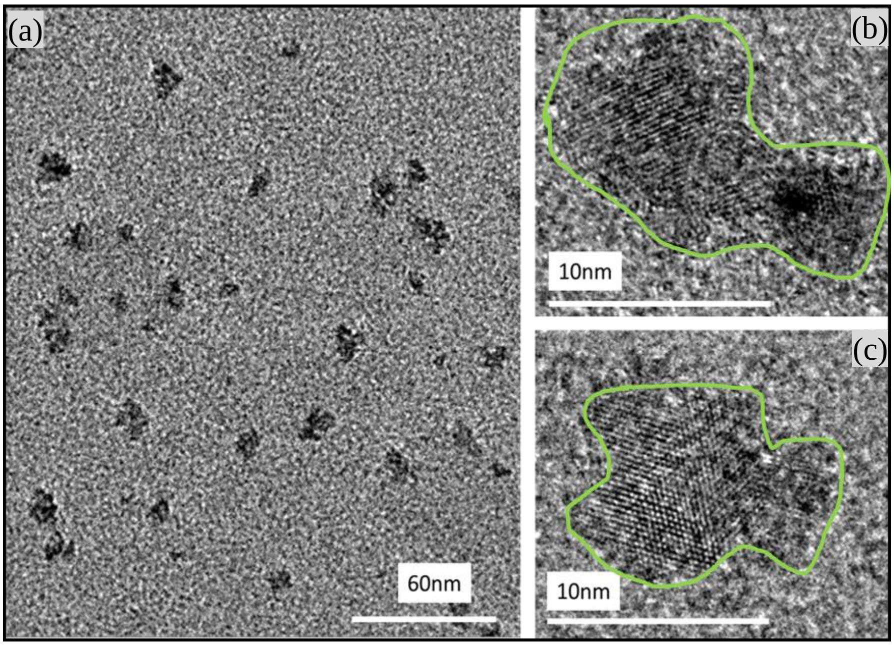

Figure 5.7: TEM (a) and HRTEM (b-c) images of the plan view of Zn(S,O) nanodots deposited on Cu/Au/C grid by the Spray-CVD process.

On the other hand, the Spray-CVD nanodots are also polycrystalline, but more irregular when compared to the Spray-ILGAR nanodots. Additionally, the Spray-CVD particles are larger, around 13-20 nm, which agrees well with the SEM observation. The irregular shape of the Spray-CVD nanodots is the result of the corresponding growth mechanism, which was mentioned in section 4.3.2. The detailed explanation will be given in the following. As displayed in Figure 4.4, the Spray-CVD nanodots consist of Zn(S,O), where the O rich places act as effective decomposition sites for the subsequent adsorption and nucleation of the precursor molecules. When the subsequent decomposition product ZnO “attaches” to these effective decomposition sites of the existing nanodots, it will make these originally quasi-sphere nanodot irregular. On the other hand, in the Spray-ILGAR process, the nanodots prefer to grow as a new individual particle instead of growing onto the exiting nanodots. Due to minimizing surface area as a result of the surface tension, the nanodots appear to be quasi-spheres.

5.3 Optical spectroscopy

For the determination of the band gap, transmission / reflection spectra of the nanodots deposited on quartz glass substrate are measured with an optical Cary 500 spectrometer with an integration sphere (for details, see Appendix A.4). The spectrometer is capable of measuring from the ultraviolet to the near infrared wavelength region. The absorption coefficient and optical band gap are calculated following Appendix A.4. An analysis of the optical band gap following Appendix A.4 agrees best for a coefficient n = 1/2 as given for a direct band gap (Eq. A.5).

5.3.1 Spray-ILGAR

The samples for the optical characterization were deposited by Spray-ILGAR at 175, 225, 300 and 400 °C for 100 cycles. Since ZnS is assumed to be a typical direct semiconductor, the value of optical gap is calculated by extrapolating the straight line portion of $(\alpha h\upsilon)^2$ vs $h\upsilon$ graph to $h\upsilon$ axis.

Figure.5.8 shows the Tauc plots of $(\alpha h\upsilon)^2$ vs $h\upsilon$ for the nanodot films obtained at the mentioned deposition temperatures. All the films display two distinct absorption energies, which are also reported by Bakke [107]. The extracted band gap values from Figure 5.8 are plotted in Figure 5.9. For the first absorption edge, similar values 3.7, 3.66, 3.65 and 3.65 eV are found for the four films deposited at 175, 225, 300 and 400 °C respectively, which is the commonly cited band gap value for ZnS [8]. On the other hand, the second absorption edge gradually red shifts from 3.98 to 3.88, 3.77 and finally to 3.71 eV as the deposition temperature increases from 175 °C to 400 °C. This shift could be explained by the increase of the particle size with increasing temperature, which was discussed in section 3.1.3.4 (see Figure 3.7).

There are two possibilities to account for this dual band gap (i) two populations of the particles size, (ii) the presence of both sphalerite and wurtzite phases of ZnS.

(i) Two populations of particles sizes: It is known that the enhancement of the semiconductor band gap due to quantum size effect can be achieved when the semiconductor particle size is comparable to the exciton Bohr radius, ca. 5 nm for ZnS. The sizes of the Spray-ILGAR ZnS nanodots obtained at 175 and 225 °C are around 3-8 nm observed by SEM and TEM (see Figure 3.7 and 5.6). On the other hand, the nanodots at 300 and 400 °C have a variety of sizes from a few nm to several tens of nm. It is proposed that the first absorption energy edge arises from the ZnS nanodots with particle sizes > 5nm, whilst the second absorption edge is attributed to the quantum size effect of the extremely small ZnS nanoparticles < 5nm.

The nanodots which are larger than the exciton Bohr radius own the bulk property. Hence, the first absorption energy edge of the larger particles (> 5nm), is independent on the particles size and therefore independent on the deposition temperature although the temperature could have influence on the size of the obtained particles. On the other hand, the smaller nanodots (< 5nm) show the quantum size effect, i.e. the absorption edge depends on the particle size. As the deposition temperature increases, the nanodots get larger in size. Therefore, the second absorption energy, which is attributed to the band gap of the smaller nanodots, shifts with the increasing process temperature to a lower value.

(ii) The presence of both sphalerite and wurtzite phases of ZnS: The contributions from both phases of ZnS is another possible reason for these two absorption energies. Most reports remark that for the band gap of cubic ZnS is 3.68 eV and for hexagonal ZnS it is 3.74-3.87 eV [110], which match well with the two observed band gap values 3.65-3.7 and 3.71-3.98 eV respectively in Figure 5.8. This dual band gap was reported for ALD ZnS film by Bakke [107], who attributed this phenomenon to the coexistence of cubic and hexagonal phases. This assumption also agrees with a previous report by Lantinen et al. who used electroreflectance to show that both cubic and hexagonal phases are present in ZnS films grown by ALD [8]. However, these two absorption energies are not observed for the nanodots obtained by Spray-CVD, which will be discussed in the next section.

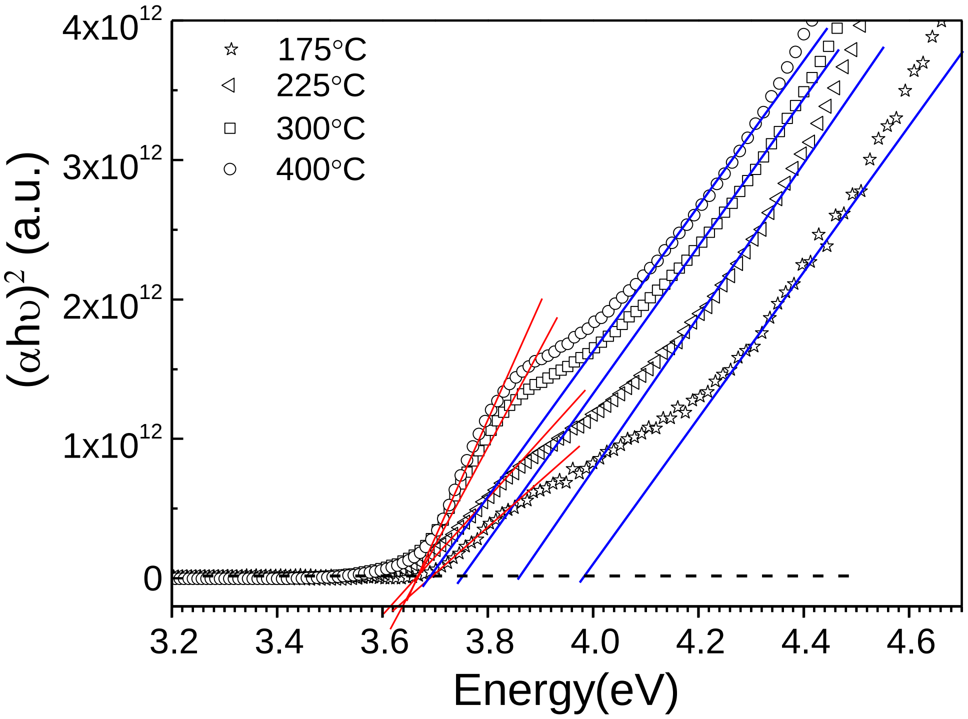

Figure 5.8: Tauc plot for Spray-ILGAR nanodots obtained at different temperatures: 175 °C, 225 °C, 300 °C and 400 °C. The linear extrapolations for the determination of the band gaps are also shown.

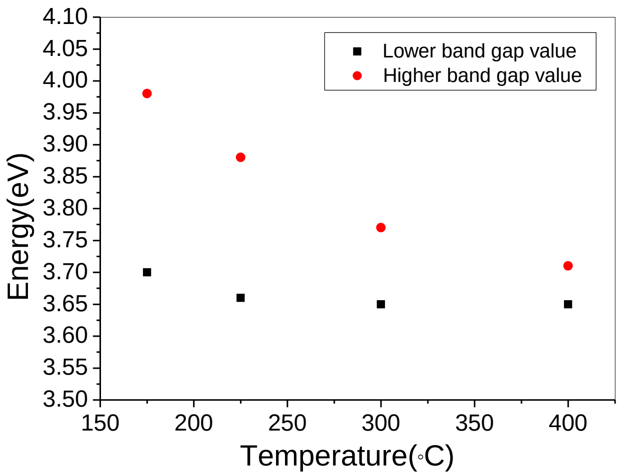

Figure 5.9: The extracted optical band gap values for the Spray-ILGAR nanodots obtained at different temperatures, which are calculated from the Figure 5.8. Bottom (black rectangular) and top (red circle) band gap values correspond to the two absorption energies at each temperature in Figure 5.8.

5.3.2 Spray-CVD

The samples were deposited by Spray-CVD with different H_2S flow rates 5, 10 and 15 ml/min at 225 °C for 100 cycles. Fig. 5.10 shows the Tauc plots of $(\alpha h\upsilon)^2$ vs hυ for these nanodot films deposited by Spray-CVD with different H_2S flow rate. As remark, the flow rate of the carrier gas N_2 is 2.5 L/min. The corresponding optical band gap values are displayed in Figure 5.11, which is 3.46, 3.49 and 3.58 eV respectively. For comparison, the band gap value of the nanodots obtained at the same temperature by the Spray-ILGAR process is shown as well. It is obvious that the band gap values by the Spray-CVD process increase with the increasing H_2S flow rate. These values , lower than the one of Spray-ILGAR ZnS nanodots (E_g=3.65 eV), are between the energy gaps reported for ZnO (E_g=3.2 eV) and ZnS (Eg=3.6 eV) [140].

A large bowing parameter in Zn(S,O) alloy is predicted due to the large difference in the electron negativity between O and S [141]. In addition, as reported by Meyer et al. [140], the band gap of $ZnO_xS_{(1-x)}$ ($0<x<1$) decreases from both end members of the solution series and go through a pronounced minimum at about x=0.5. Hence, the O content in an alloy might have an influence in the absorption edge measured. However, the Spray-CVD nanodots, as seen in Figure 4.12, are mixture of ZnS and ZnO rather than the Zn(S,O) alloy. Therefore, the measured band gap should not be induced by the band gap bowing, but could be attributed to the property of either ZnS or ZnO. This absorption edge below the reported ZnS band gap is not affected by ZnS and could be assigned to the absorption edge of quantum confined ZnO inclusions (about 1-2 nm as observed in Figure 4.12) within the Spray-CVD nanodots. As the H_2S flow rate increases, the quantum confined ZnO particles within the Spray-CVD nanodots will be gradually sulfurized, which leads to the decrease in the size. Therefore, a blue shift of the absorption peak is observed with increasing H_2S flow rate.

The corresponding composition of the nanodots achieved by these two processes will be discussed in the next section.

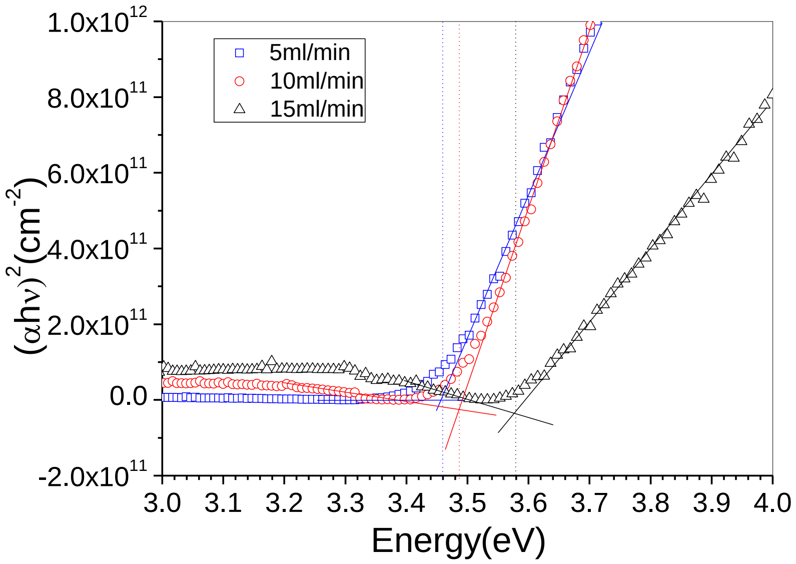

Figure 5.10: Tauc plot for the Spray-CVD nanodots obtained with different H_2S flow rates at 225 °C. The linear extrapolations for the determination of the band gaps are also shown.

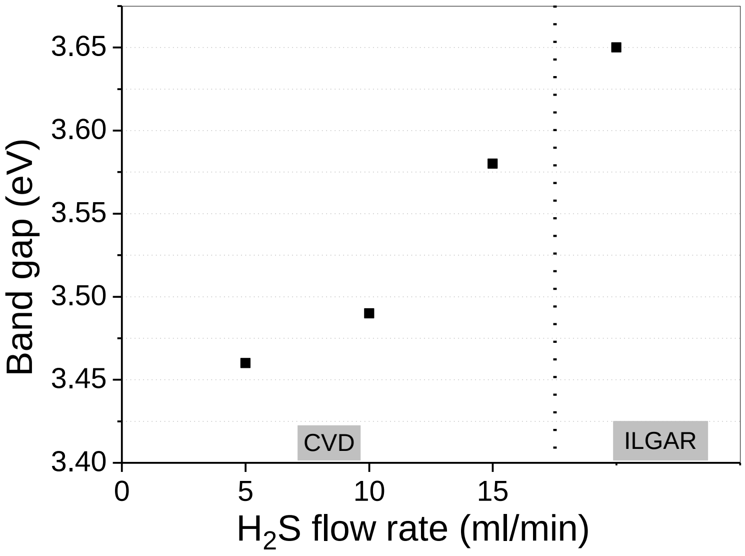

Figure 5.11: The extracted optical band gap values for the Spray-CVD nanodots with different H_2S flow rate 5, 10 and 15 ml/min, which are calculated from the Figure 5.10. The flow rate of the carrier gas N_2 is kept at 2.5 L/min. For comparison, the band gap value of the nanodots obtained by the Spray-ILGAR process is shown as well.

5.4 Surface analysis of the Spray-ILGAR and Spray-CVD nanodots

XPS and AES are used to study the compositions of the nanodots obtained by Spray-ILGAR and Spray-CVD. The nanodots were deposited onto glass substrates coated with Mo at 225 °C for 60 cycles in the Spray-ILGAR process and 60 min in the Spray-CVD process with 5ml/min 5% H_2S/Ar. In addition, reference ZnO was also prepared with the same precursor solution as the above two processes using spray pyrolysis method, which is actually the first step of the Spray-ILGAR process. To minimize contamination from ambient air, the samples were sealed in a polyethylene bag filled with N_2 immediately after the deposition. The samples were then transferred to the analysis chamber of a combined ultrahigh vacuum preparation and spectroscopy system (“CISSY-UHV” [142]), which is equipped with a CLAM4 (Thermo VG Scientific) concentric semi-hemispherical analyzer and an Al Kα / Mg Kα X-ray tube. The electron spectrometer is calibrated using XPS and Auger line positions of different metals (Cu 3p, Au $4f_{7/2}$, Cu L_3MM, and Cu $2p_{3/2}$) according to references [143]. A more detailed description of the XPS measurements can be found in Appendix A.5. In the following, the XPS and AES results obtained of three samples by means of will be discussed.

For each sample, a set of XPS spectra was recorded: overview and detail spectra of the Zn 2p, Zn LMM, Zn 3s, S 2p, Mo 3d, O 1s, O KLL, C 1s and valence band. Excitation source was an Mg Ka (energy: 1253.6) x-ray tube operating at a power of 250W. Prior and after each set, the Au 4f peak of a sputter-cleaned gold foil was recorded for energy calibration. A linear background was subtracted from the detail spectra.

The measured survey spectra of the Spray-ILGAR, Spray-CVD nanodots and spray pyrolysis ZnO can be seen in Figure 5.12. The presence of C 1s peak is mainly from the atmospheric contamination. The remaining Mo-attributed signals are observed, which means that the nanodots don't completely cover the Mo substrate or the thickness of the nanodots layer doesn't exceed the XPS information depth.

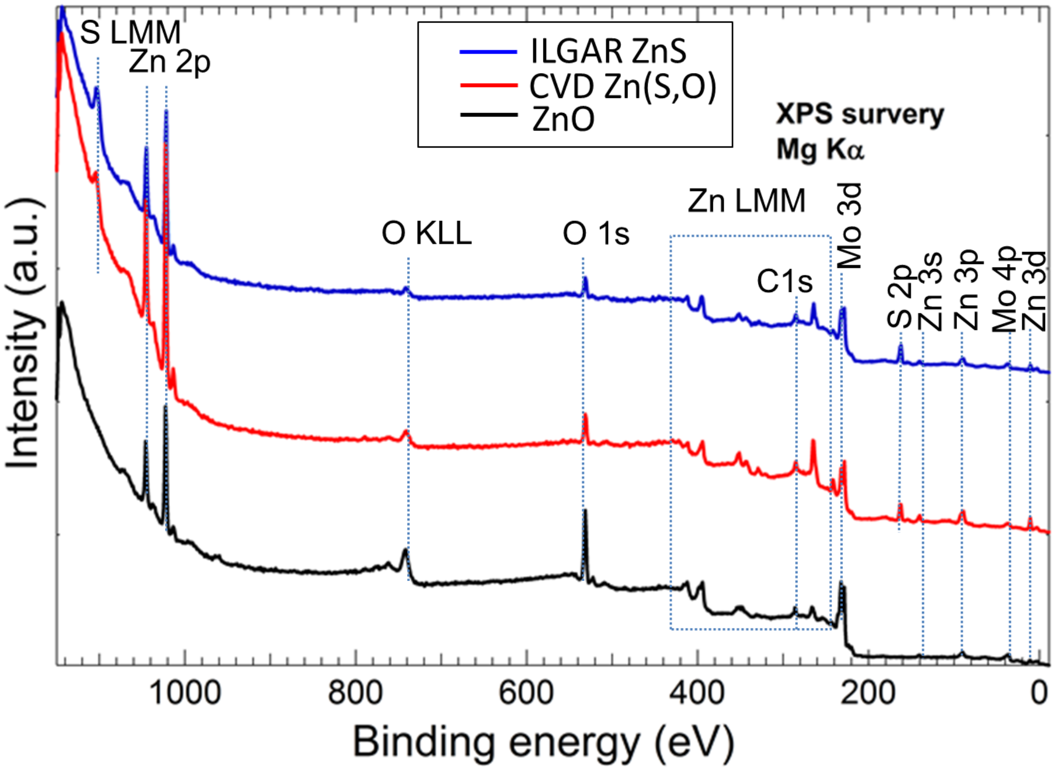

Figure 5.12: XPS survey spectra of the Spray-ILGAR, Spray-CVD nanodots and spray pyrolysis ZnO reference. Spectra have been shifted vertically for a better comparison.

In order to have more accurate information about the different compositions of the deposited nanodots layer, the Zn $L_3M_{45}M_{45}$ AES spectrum can be evaluated. This particular signal is more sensitive with respect to chemical composition than the most Zn photoemission lines [144]. The detailed Zn $L_3M_{45}M_{45}$ AES spectra of the three samples are shown in Figure 5.13. A pronounced shift of the Zn $L_3M_{45}M_{45}$ Auger peak can be observed, from a kinetic energy E_{kin} of 987.7±0.1 eV for spray pyrolysis ZnO, to 988.9±0.1 eV for Spray-CVD nanodots, further to 989.3±0.1 eV for Spray-ILGAR ZnS nanodots. Additionally, in order to exclude the influence from the band bending on the analysis of the energetic positions of the AES and XPS signals, the modified Auger parameters [145] are computed using the Zn $2p_{3/2}$ core level and the Zn $L_3M_{45}M_{45}$ Auger signal, $\alpha=E_{kin}[\text{Zn } L_3M_{45}M_{45}(^1G)]+E_B[\text{Zn } 2p_{3/2}]$ (Table 5.3), which also increase from spray pyrolysis ZnO to Spray-CVD nanodots, then to Spray-ILGAR ZnS. From this fact, it can be concluded that the shift of the Zn $L_3M_{45}M_{45}$ indicates a change in the chemical environment of Zn. When going from ZnS towards Zn(S,O), the Auger structure Zn LMM shifts to the lower energetic position [38, 146]. The comparison of the positions of the Zn $L_3M_{45}M_{45}$ Auger lines of these three samples suggests that a Zn(S,O) like composition is probable for the Spray-CVD nanodots, since the energetic position of the Zn $L_3M_{45}M_{45}$ (988.9±0.1 eV) Auger peak of Spray-CVD nanodots is found between that of spray pyrolysis ZnO (987.7±0.1 eV) and Spray-ILGAR ZnS (989.3±0.1 eV).

Although the Zn $2p_{3/2}$ core level signal is not as sensitive to chemical changes as the corresponding Zn $L_3M_{45}M_{45}$ Auger peak, the Zn $2p_{3/2}$ core level lines show a similar behavior to that observed for the Zn $L_3M_{45}M_{45}$ Auger signal (as shown in Figure 5.14). This shift in the Zn $2p_{3/2}$ support the conclusion of Zn(S,O) like composition for Spray-CVD nanodots. Therefore, it is considered that the Zn$2p_{3/2}$ spectra of the Spray-CVD samples are composed of two contributions, namely ZnS and ZnO. In consequence, the measured Zn$2p_{3/2}$ spectrum can be in principle fitted using two Voigt functions[4], as shown in Figure 5.15. For this fitting process, the full width at half maximum (FWHM) values of the photoemission signals of ZnS and ZnO (1.7 and 1.9eV respectively of the Zn$2p_{3/2}$ signal) are kept constant during the fit of the Zn$2p_{3/2}$ of the Spray-CVD nanodots. As remark, these FWHM values, which are in good agreement with the FWHM value reported by Bär et al. [146], are calculated by fitting the $Zn_{3/2}$ spectra of the Spray-ILGAR ZnS and spray pyrolysis ZnO (Figure 5.15). Taking the error bars into account, the determined energetic positions of both contribution (ZnS and ZnO), 1022.2 and 1022.5 eV respectively, agree with the energetic positions of the Spray-ILGAR ZnS and spray pyrolysis ZnO as well as the corresponding literature data (Table 5.3).

By using the areas below the Voigt profiles, which describe both contributions (ZnS and ZnO) to the Zn$2p_{3/2}$ spectra of the Spray-CVD nanodots, the ZnS / (ZnS+ZnO) ratio can be estimated to be 0.42. The Spray-CVD nanodots here were deposited with 5% H_2S/Ar at a flow rate of 5 ml/min. As mentioned in Chapter 3, the nanodots density drops off as the H_2S concentration increases in the Spray-CVD process. In the following, the compositions of the Spray-CVD nanodots as a function of the H_2S concentration will be discussed.

Table 5.4 gives the ratios of the integrated peak intensities of S 2p / Zn 3d (Figure 5.16), which are proportional to the S concentrations if the Zn concentrations are considered constant. Three different flow rates of 5% H_2S, which is transported by the carrier gas N_2 at 2.5 L/min to the spray chamber, are chosen at 5 ml/min, 10 ml/min, and 15 ml/min. This peak intensity ratio of the Spray-ILGAR nanodots is depicted as well for comparison. The peak intensity ratios can be further evaluated in terms of an absolute S concentration. Following the analysis outline in Appendix A.5, the concentration ratio of S / Zn, i.e. C_{ZnS} / $C_{(ZnS+ZnO)}$ can be calculated by Eq A.9, since the Mg Kα excited S 2p and Zn 3d lines indeed have a close E_{kin}, where $E_{kin,Zn}$=1.14 $E_{kin,Zn}$.

$$\frac{C_S}{C_{Zn}} = \frac{I_S}{I_{Zn}} \frac{\sigma_{Zn}}{\sigma_S} \frac{\lambda_{Zn}}{\lambda_S}$$

where C_i are the elemental concentrations, I_i are the measured intensities of the considered XPS emission lines, σ_i are the photoionization cross sections, λ_i is the inelastic mean free path (IMFP) and the index (i= Zn, S) refers to the element Zn and S respectively. The photoionization cross sections depend on the chemical bond, so in principle, the cross section of the ZnO and the ZnS contributions would be dissimilar. In practice, in a first approximation, these values are considered equal. Furthermore, in the literature data [147] available only values for the core level are given, regardless of the chemical environment. The photoionization cross sections given in reference show an inaccuracy around 25% [148]. IMFP λ is calculated by the TPP-2 formula [149] using the QUASES code written by Tougaard [150], which provides values with an absolute uncertainty of ~20% [150].

---

[4] Without loss of generality, if only centered profiles peaked at zero are considered, the Voigt profile is a convolution of a Lorentz profile and a Gaussian profile.

The values used for this evaluation are tabulated in Table 5.4. With these data the absolute ZnS concentrations of this series of samples can be estimated, which are listed in Table 5.5. Taking the error bars into account, the Spray-ILGAR nanodots with the highest S / Zn concentration ratio of 1.16, can be determined as pure ZnS. The Spray-CVD nanodots are considered to be Zn(S,O), which change from ZnO rich to ZnS rich composite with the increase of H_2S concentration. The estimated ZnS / (ZnS+ZnO) ratio of 0.42 for the Spray-CVD nanodots with 5ml/min H_2S is in good agreement with the calculation from two Voigt functions in Figure 5.15. These results support the conclusion stated earlier from the band gap calculation in section 5.2 and from the sulfur map of EF-TEM image in chapter 4, that the Spray-CVD nanodots are Zn(S,O) instead of pure ZnS.

Table 5.3 Energetic positions of Zn $2p_{3/2}$ photoemission line and Zn $L_3M_{45}M_{45}$ Auger line as found for the spray pyrolysis ZnO, Spray-CVD nanodots and Spray-ILGAR ZnS nanodots. In addition the corresponding values of the Auger parameter $\alpha = E_{kin}[\text{Zn } L_3M_{45}M_{45}(^1G)] + E_B[\text{Zn } 2p_{3/2}]$ are calculated using the values presented in table 5.3. For comparison the literature data for ZnS and ZnO are also given. All the values have an error of ±0.1 eV.

Sample	Zn $L_3M_{45}M_{45}$ (eV)	Zn $2p_{3/2}$ (eV)	Auger parameter (α) (eV)
Spray pyrolysis ZnO	987.7	1022.5	2010.2
Spray-CVD nanodots	988.9	1022.3	2011.2
Spray-ILGAR ZnS	989.3	1022.1	2011.4
ZnO (literature)	987.4-988.9	1021.2-1022.5	2009.5-2011.0
ZnS (literature)	988.2-989.9	1021.7-1022.0	2010.3-2011.9

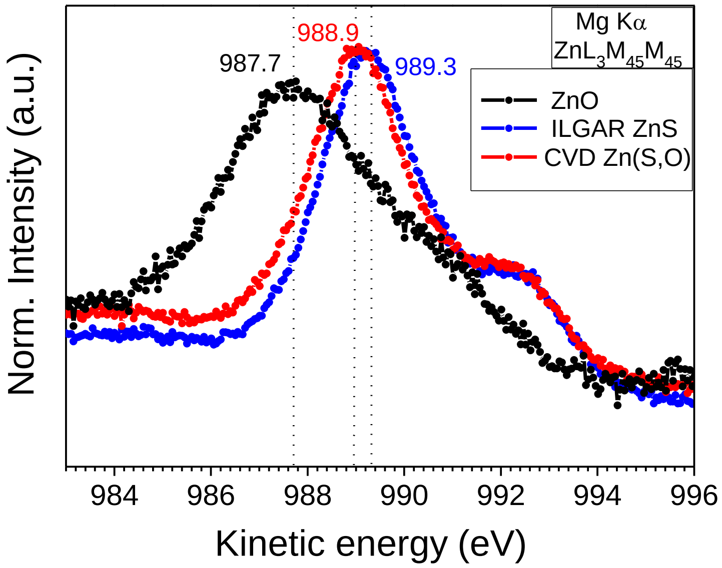

Figure 5.13: Zn $L_3M_{45}M_{45}$ AES detailed spectra of the Spray-ILGAR, Spray-CVD nanodots and spray pyrolysis ZnO reference. The values have an error of ±0.1 eV.

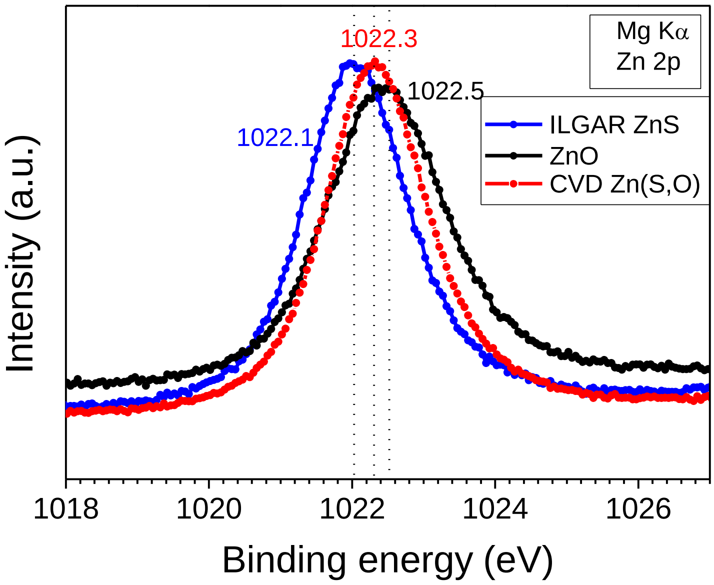

Figure 5.14: Zn 2p$_{3/2}$ detailed core level spectra of the Spray-ILGAR ZnS, Spray-CVD nanodots and spray pyrolysis ZnO reference. The values have an error of ±0.1 eV.

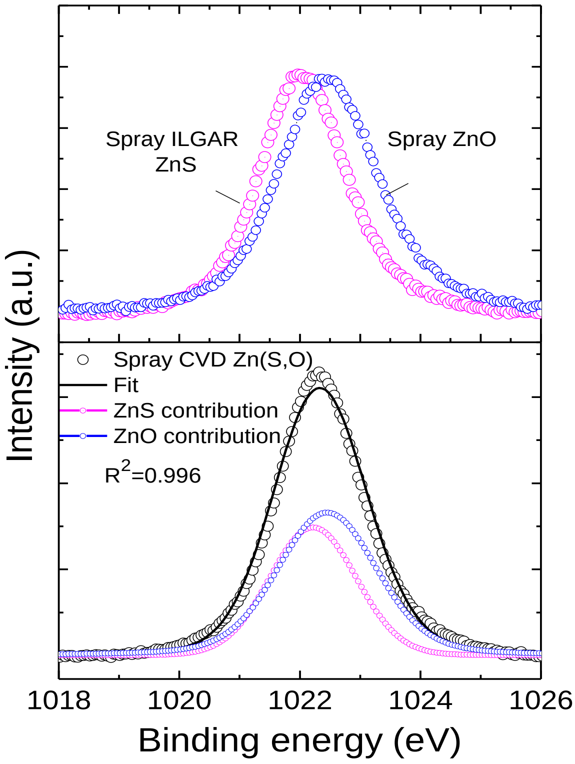

Figure 5.15: Bottom: XPS spectrum of the Zn2p$_{3/2}$ photoemission signal of the Spray-CVD nanodots (black open circles). The Voigt profiles accounting for the contributions of ZnS (magenta) and ZnO (blue), as well as the addition of these contributions are also presented (black solid line). Top: XPS detail spectra

of the Zn $2p_{3/2}$ photoemission signals of spray pyrolysis ZnO and Spray-ILGAR ZnS as reference are shown for comparison.

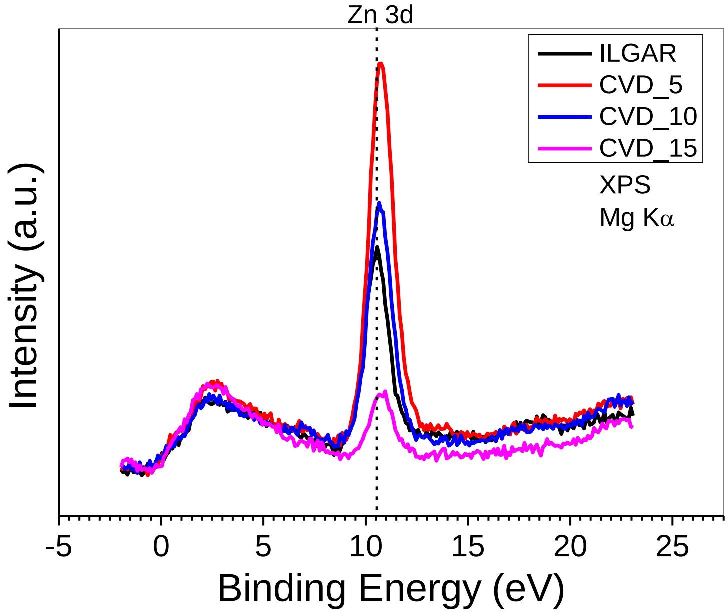

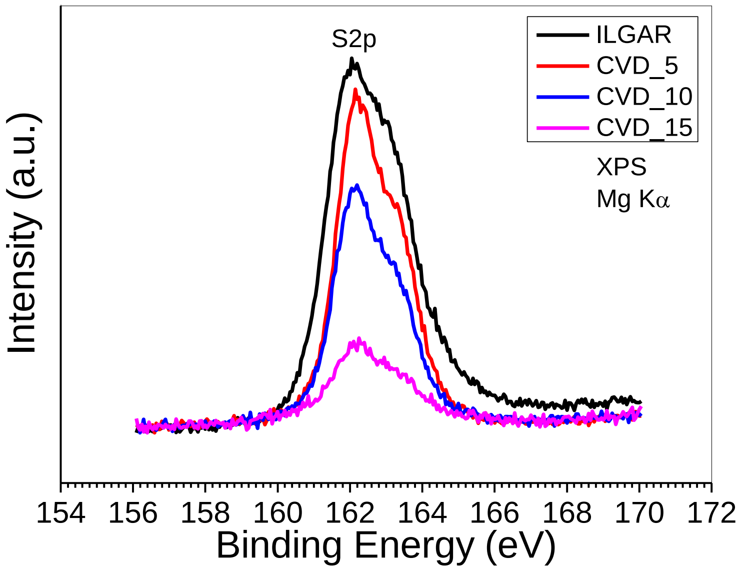

Figure 5.16: Detailed Zn 3s (top) and S 2p (bottom) core levels spectra of the Spray-ILGAR nanodots and the Spray-CVD nanodots with different H_2S flow rates, including 5, 10 and 15 ml/min. These Spray-CVD nanodots are indicated as CVD_5, CVD_10 and CVD_15 respectively in the figure. The values have an error of ±0.1 eV.

Table 5.4: Photoionization cross section σ and inelastic mean free path (IMFP) used for the evaluation of XPS data directly from Eq. A.9.

Line	σ (Mbarns) [147]	IMFP λ (nm) [149, 150]	
		ZnO	ZnS
S 2p	0.38	2.17	2.29
Zn 3d	0.21	2.38	2.52

Table 5.5: The ratios of the integrated peak intensities $I_{S\ 2p}$ / $I_{Zn\ 3d}$ and the S concentration, which is corresponding to C_{ZnS} / $C_{(ZnS+ZnO)}$ ratio, as calculated from Eq. A.9.

Process	ILGAR	CVD_15	CVD_10	CVD_5
$I_{S\ 2p}$ / $I_{Zn\ 3d}$	2	1.2	0.85	0.72
C_{ZnS} / $C_{(ZnS+ZnO)}$	1.16	0.69	0.49	0.42

5.5 Summary

In this chapter, the nanodots prepared by Spray-ILGAR and Spray-CVD are examined for their structure, morphology, chemical and optical properties.

The nanodots in both processes are polycrystalline investigated by means of XRD and TEM. These nanodots exist either in pure hexagonal structure alone or with the inclusion of some cubic phase. However, no crystalline ZnO is found for both processes. The achievement of the metastable hexagonal ZnS phase at such a low temperature (175~400 °C) could be explained by maintaining the structure during the conversion from the intermediate ZnO to the ZnS nanodots.

For the same spraying time, the sizes of Spray-CVD nanodots are found to be around 2 times larger than those of Spray-ILGAR nanodots by TEM. However, the Spray-CVD nanodots are more irregular, which is because that the precursor molecules are adsorbed and then decompose to nuclei on the randomly distributed O-rich regions of the primary Zn(S,O) nanodots.

The spray ILGAR nanodots are pure ZnS with a dual band gap. The estimated lower band gap is around 3.65~3.7 eV while the second one decreases with the deposition temperature from 3.98 eV to 3.71 eV. On the contrary, the Spray-CVD nanodots are Zn(S,O) compounds changing from ZnO rich to ZnS rich composite when they are deposited with the increasing H_2S flow rate. The band gap of the nanodots shifts from the lower value of 3.46 eV to the higher one of 3.58 eV with the increasing H_2S concentration.

Chapter 6

Chalcopyrite thin film solar cell with ZnS nanodots / In_2S_3 bilayer buffer

A bilayer buffer, named passivation / point contact buffer, which is composed of the Spray-ILGAR ZnS nanodots covered by a homogenous Spray-ILGAR In_2S_3 layer is applied in Cu(In,Ga)(S,Se)$_2$ (CIGSSe) thin film solar cells. To start with, the concept of the passivation / point contact buffer layer is described in section 6.1. Later, the preparation and characterization of the bilayer buffer and the complete solar cell are described in section 6.2. Afterwards, in section 6.3, the solar cells with this bilayer buffer are compared to the ones without buffer layer and with different single buffer layers, i.e. ZnS nanodots, In_2S_3 and CdS. The optimal ZnS dot density, In_2S_3 thickness and process temperature are discussed. Additionally, the In precursor salt solutions, indium chloride ($InCl_3$) and indium acetylacetonate (In(acac)$_3$) are changed for the deposition of In_2S_3, and the solar cells with the Spray-CVD Zn(S,O) as passivation buffer layer are compared to the ones with the Spray-ILGAR ZnS nanodots.

The interface formation, i.e. the potential diffusion processes at the buffer / absorber interface, is investigated by means of X-ray photoelectron (XPS) in section 6.4. In order to make the deeply buried absorber side of the buffer/absorber heterointerface accessible for characterization, the buffer layer is etched away by dilute HCl aqueous solution.

In section 6.5, the electronic properties and charge separation in single, double and triple layer systems based on Cu(In,Ga)(S,Se)$_2$, ZnS nanodots and In_2S_3 layers are investigated by surface photovoltage (SPV) spectroscopy in the Kelvin probe arrangement and compared with the open circuit voltage (V_{OC}) of solar cells.

6.1 Concept of the passivation / point contact buffer layer

Surface passivation of absorbers is important for achieving high conversion efficiency of solar cells. Passivation layers have to reduce the recombination of charge carriers at the heterointerface. Furthermore, the defect concentration at interfaces between absorber and passivation layer should be low enough to avoid the creation of additional recombination sites. A usual concept for passivation of conventional Si solar cells, for example, is based on the decrease of the charge carrier recombination with a perforated passivation layer while the distance between neighbored contact dots should be less than half of the diffusion length. The diffusion lengths are much shorter in chalcopyrite (Cu(In,Ga)(S,Se)$_2$)

based than in crystalline silicon solar cells, so that a structured passivation on a scale of tens to hundreds of nm is needed. Recently, a novel point contact buffer layer concept based on 3D simulations has been performed to proof the concept of local surface passivation for a CdS / chalcopyrite interface by introducing a hypothetic perforated passivation layer [151]. A first test by our group with such a buffer, had improved the cell performance as compared to a single In_2S_3 buffer layer [74].

As of today, for Cd-free buffer only chemical bath deposition (CBD)-Zn(S,O), CBD-In_2S_3, and ILGAR- In_2S_3 have been implemented in an industrial base-line production [44]. Cells with Spray-ILGAR In_2S_3 buffer (depositing using $InCl_3$ solution) show comparable efficiencies and stabilities as reference cells with CdS buffer [73, 79]. These buffers produce cells with a higher short circuit current and an equal or better fill factor compared to the CdS. However, the open circuit voltage is always slightly reduced which indicates that there is still room for improvement. In order to reduce the interface recombination at the CIGSSe / buffer interface, the as-prepared ZnS nanodots are applied as passivation layers in buffers of thin film solar cells. The pure In_2S_3 buffer layer is replaced by a combination of a ZnS nanodot film covered by the standard ILGAR In_2S_3 buffer layer. A Spray-ILGAR process is developed to produce this bilayer buffer (schematic of a solar cell shown in Figure 6.1). The ZnS should reduce the detrimental charge carrier recombination at the p-n junction which is one important position for performance loss in chalcopyrite solar cells. The In_2S_3 in-between and on top of the ZnS dots is needed for the charge carrier transport because of the large conduction band offset to ZnS as well as the low conductivity of ZnS. The complete deposition process for ZnS dots/ In_2S_3 film structure buffer layers for $Cu(Ga,In)(S,Se)_2$ solar cells is described in the following section.

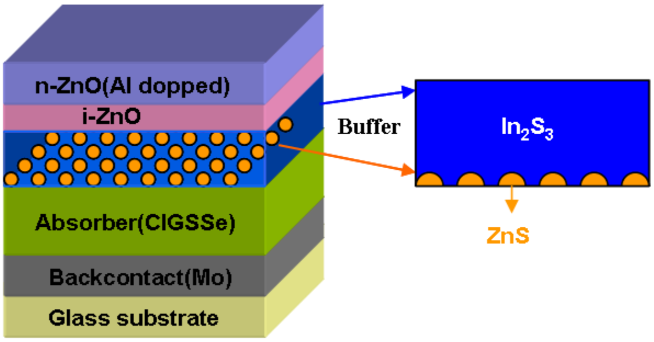

Figure 6.1: Schematic diagram of the passivation layer / point contact buffer layer for CIGSSe thin film solar cells.

6.2 ZnS nanodots / In_2S_3 bilayer buffer and the device preparation and characterization

Standard ZnS nanodots and In_2S_3 *layer deposition in thin film CIGSSe solar cells*

Both In_2S_3 and ZnS nanodot layers are performed by the two-step cyclical Spray-ILGAR technique.

To produce ZnS nanodots, an aqueous precursor solution of 25 mM zinc acetylacetonate ($Zn(acac)_2$) is used, which is mixed with acetic acid to adjust the pH value of the solution at 3. Standard ZnS nanodot films as passivation layer are deposited at 225 °C onto the CIGSSe absorber rather than 200 °C as deposited on Si substrate. The reason for the choice of the temperature at 225 °C is to keep the same temperature as the In_2S_3

deposition. Furthermore, since the given is the substrate holder temperature, the thicker glass substrate will lead to a lower surface temperature than Si wafer.

A 25 mM $InCl_3$ in ethanol is used for the In_2S_3 layer deposition. The standard In_2S_3 buffer is produced with 6 process cycles at 225 °C giving the thickness of approximately 12-15 nm.

Morphology of different buffers on CIGSSe absorber

Figure 6.2 (a) shows a SEM micrograph of the top view of the bare CIGSSe absorber. After being buffed with 6 standard process cycles of In_2S_3 (Figure 6.2 (b)), this absorber/buffer system surface looks completely different from the bare absorber surface. It is covered by a close film and becomes rough. When a ZnS nanodot film is prepared at 225 °C for 10 cycles by the Spray-ILGAR method, the nanodots are well distributed over the facets. The diameters of the nanodots are about 10 nm while the average distance between the nanodots is below 5 nm. As remark, the achieved nanodots on the absorber surface seem slightly different from the ones on the Si wafer (Chapter 3), larger and denser. This could be partially explained by the different substrate surface temperatures during deposition, which is described in the above paragraph. The detailed influence of the substrate on the morphology of nanodots is the topic for further study. For the buffer application, it is important that the distance is less than half of the minority carrier diffusion lengths. It should be on a scale of tens to hundreds of nm. The nanodots in our case are obviously within this range. Hence, the obtained nanodots, without insulating surfactant ligands, can serve as a passivation layer, still enabling lateral diffusion of charge carriers to the In_2S_3 contact bridge, which forms the point contact structure at the heterointerface.

ZnS can be tuned from a distributed nanodot films to a compact film by the parameters, such as the precursor concentration, the pH value of precursor solution, the solvent, the substrate temperature and the number of process cycles as discussed in Chapter 3.

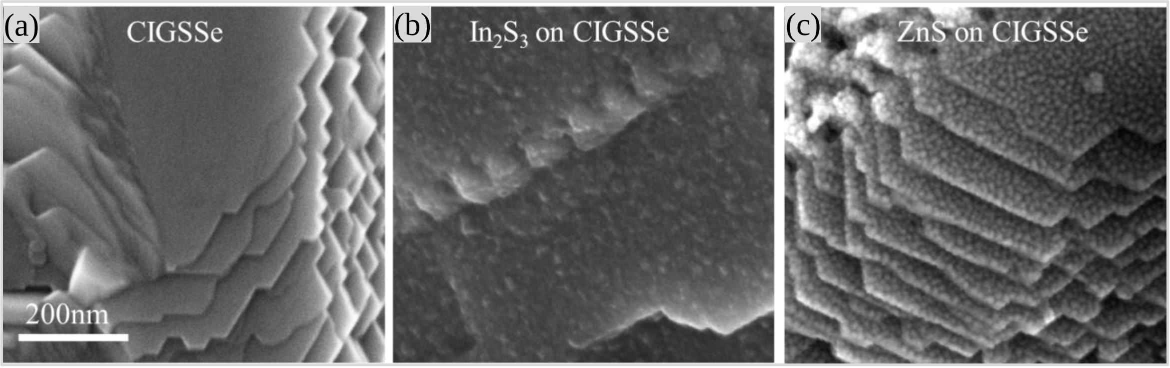

Figure 6.2: SEM images of a bared CIGSSe absorber (a), 6 process cycles of standard In_2S_3 on CIGSSe absorber (b), and 10 process cycles of ZnS nanodots on CIGSSe absorber.

Solar cell preparation and characterization

The solar cells are prepared on the base of $Cu(In, Ga)(S,Se)_2$ absorber layers provided by AVANCIS GmbH & Co. KG [35]. The structure of the full cell consists of a multilayer stack of Mo / $Cu(In,Ga)(S,Se)_2$ / buffer layer / i-ZnO / ZnO:Al / with Ni–Al contact grids. The performance of a solar cell is measured by current-voltage, J-V, measurements under illumination. To obtain world-wide comparable results, the measurements should be performed under standard test conditions: (i) the temperature of the cells at 25 °C, (ii) an illumination power density of 100 mW/cm^2 and (iii) a light with spectra distribution as close as possible to the sun at AM 1.5G^5 spectrum. Two samples of 25x25 mm^2 were prepared for each recipe. Each 25x25 mm^2 device was cut into eight 0.5 cm^2 cells, and six (or four) were taken out of eight in order to exclude cells with shunt or scribing defects. The average and the best cell were taken from the twelve (or eight) selected cells. The data of different series of experiment can't be compared as each experiment uses materials from different batches of 100 x 100 mm^2 absorber plate. Solar cells were characterized in-house with simulated AM1.5G light under standard conditions.

6.3 Photovoltaic properties with bilayer buffer

It has been shown that the ZnS nanodots and the In_2S_3 forms a point contact structure with the CIGSSe surface. How successfully they can be employed as buffer layers in a CIGSSe thin film solar cell device is discussed in the following section. This section starts with the comparison of the cell performance with ZnS nanodots / In_2S_3 bilayer buffer to the one with different single buffer layers, i.e. ZnS nanodots, In_2S_3, CdS, in section 6.3.1. Further optimization in the ZnS dot density, In_2S_3 thickness, process termperature are described in section 6.3.2, 6.3.3 and 6.3.4 respectively. Finally, the cells with the bialyer buffer from different In precursor solutions and the different prepartion techniques for the deposition of ZnS nanodots are compared in section 6.3.5 and 6.3.6 respectively.

6.3.1 $Cu(In, Ga)(S,Se)_2$ solar cells with different buffer layers

In order to examine the passivation effect of the deposited ZnS nanodots, CIGSSe cells with ZnS nanodots, In_2S_3 layer and ZnS nanodots / In_2S_3 bilayers are compared. After deposition of the buffer layer, solar cells are completed by sputtering the window layer and evaporating Ni/Al contact grids for better current collection. In addition, one sample without any buffer layer is also processed for comparison. Due to the process-batch dependent quality of the CIGSSe absorber layers, the performance of the Cd-free buffer layers will generally be judged in reference to a CdS buffer on an abosorber stemming from the same process batch. The PV parameters of these cells are presented in Figure 6.3.

The cells with no buffer layer show very low values in all PV parameters, which indicates the important role of the buffer layer. In the case of ZnS nanodots buffered solar cells, they do not result in good efficiencies. This is most probably due to an incompletele coverage of the absorber surface by the ZnS nanodots. The area covered directly by ZnO can lead to short circuit. It could be observed that the Spray-ILGAR In_2S_3 buffer works as well as the CdS buffer layer. However, the open circuit voltage is around 20 mV lower. This result agrees well with a previous report [73]. The best cell efficiencies are observed for the cells buffered with ZnS nanodots/ In_2S_3 bilayer, which results in improving cell efficiencies up to about 1% absolute as compared to the cells with a pure In_2S_3 buffer layer. The open circuit voltage of the ZnS nanodots/In_2S_3bilayer buffered cells can be clearly seen to approach that of the open circuit voltage of the CdS reference. The fill factor is also higher than that of CdS reference. The characterizaiton of the solar cells show that the addtion of this passivation / point contact layer results in a clear improvement of the cell performance (especially Voc and FF) and a favorable alternative to CdS as buffer layer material. Further investigation would be necessary in order to optimize its performance.

The ZnS dot density, In_2S_3 thickness and process temperature are varied and presented in the following section.

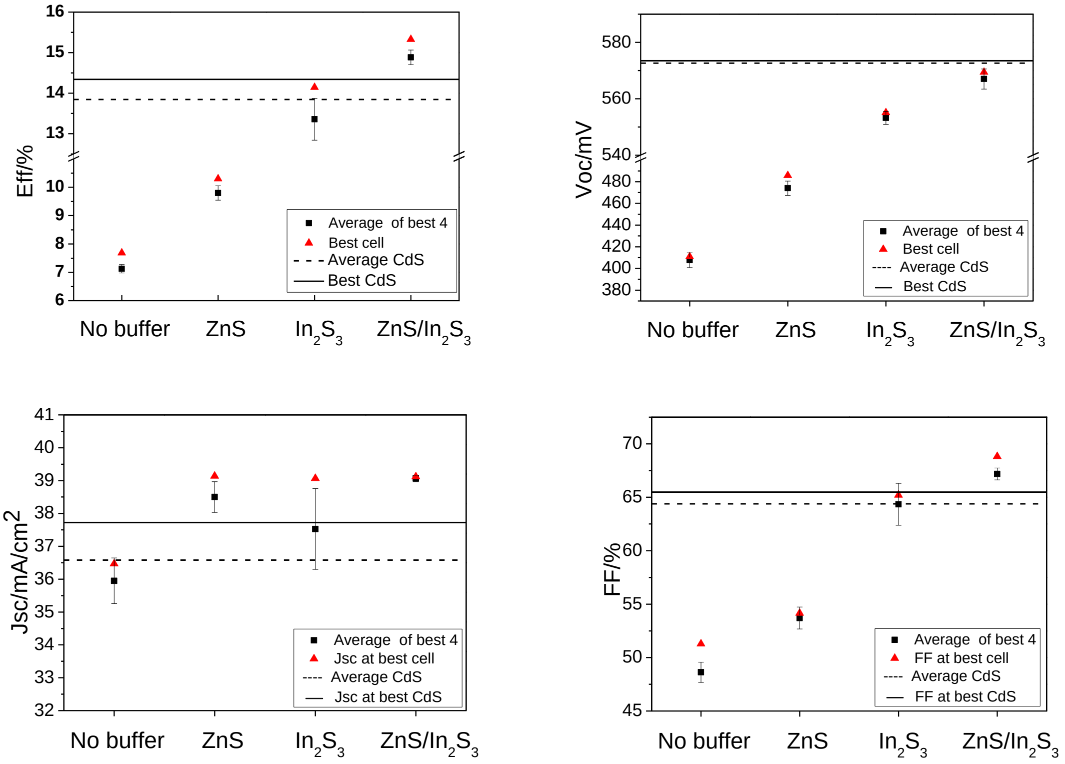

Figure 6.3: PV parameters, efficiency (Eff), open circuit voltage (V_{OC}), short circuit current (J_{SC}) and fill factor (FF), of the solar cells without buffer layer and with different kinds of buffer layers, i.e. ZnS nanodots, In_2S_3 and ZnS nanodots/ In_2S_3.

6.3.2 ZnS nanodot density variation

To investigate the influence of different ZnS nanodot densities on the solar cell performance, an increasing number of process cycles from 0 to 60 have been utilized for the ZnS deposition, whereas 6 cycles of In_2S_3 are kept constant for this series of experiments. The resulting solar cell performances are presented in Figure 6.4. With a deposition of 10 cycles of ZnS nanodots and the standard In_2S_3 buffer, the cell efficiency increases to 15.0% (best cell) and 14% (averaged) as compared to 14.1% (best cell) and 13.4% (averaged) for pure In_2S_3 layer. But the coverage of this ZnS nanodot film on the CIGSSe absorber surface may be still not enough. More absorber surfaces need to be passivated to decrease te performance loss. A deposition of 20 cycles of ZnS nanodots is observed to have the best result with the efficency value of 15.3% (best cell) and 14.8% (averaged), which is 1.2% absolute (best cell) and 1.4% absolute (averaged) higher than with a pure In_2S_3 buffer.

The cell efficency reaches a maximum value with 20 cycles of ZnS nanodots then drops off again by further increasing the deposition cycles of ZnS nanodots. The device charateristics with 40 and 60 cyles of ZnS nanodots are deteriorated as compared to a solar cell with a pure In_2S_3 layer. The same trend is clearly seen in the fill factor. The short circuit current density shows no significant dependence on the number of cycles, indicating that the ZnS nanodot film do not absorb much light. Interestingly, the open circuit voltage first increases with the addition of 10 to 20 cycles of ZnS nanodots, then no further obvious increase is observed for 30~60 cycles deposition. As it can be seen from the SEM micorgraphs of the nanodots deposited on the CIGSSe absorber (Figure 6.5), with increasing deposition cycles of ZnS nanodots, the density gradually increases and then reaches the maximum value at 20 cycles. In the following cycles, the nanodots grow larger with a neliglibe increase in the dot density and aggregate with each other. The ZnS nanodot films become so dense that there is no space for In_2S_3 contact area. Moreover, the thicker ZnS nanodot films increase the series cell resistance. Hence, it is easier to understand the behavior of the open circuit voltage and the cell efficiency as a function of the number of cycles of ZnS. More and more of the absorber surface is passivated by the deposition of ZnS within 20 spraying cycles. This can reduce the detrimental charge carrier recombination at the p-n junction which is one important position for performance loss in chalcopyrite solar cells. Consequently, the open circuit voltage will increase as well as the cell efficiency. Afterwards, all the absorber surface is passivated. Therefore, it results in no further increase in the voltage. However, the total cell resistances increases as a result of no In_2S_3 contact bridge and thicker and thicker closed ZnS layer. For these reasons, cell efficiency starts to go down in spite of the high open circuit. On the other hand, according to the Eq.2.6, as the series resistance increases, the fill factor decreases, which agrees well the observed result. Clearly, too dense ZnS nanodots have an adverse effect on the solar cell device.

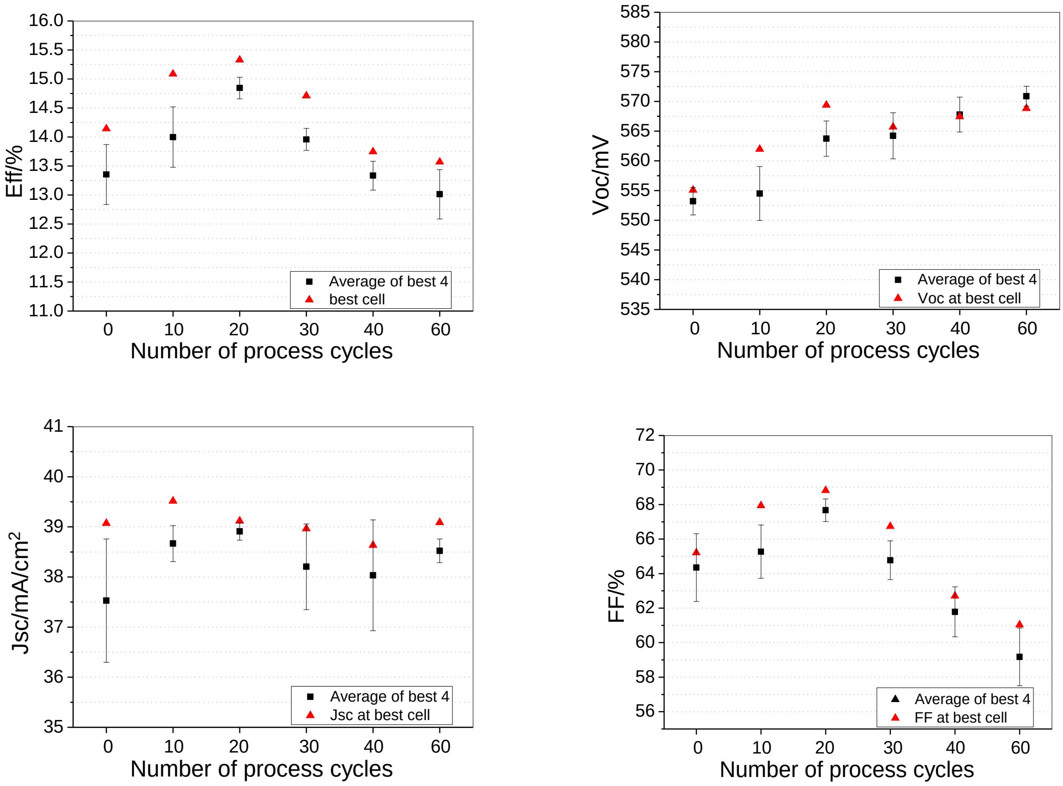

Figure 6.4: PV parameters, efficiency (Eff), open circuit voltage (V_{OC}), short circuit current (J_{SC}) and fill factor (FF), of the solar cells with increasing cycles of ZnS nanodots and standard In_2S_3 buffer. Cells are prepared with 0-60 cyles of ZnS nanodots and 6 cycles of In_2S_3.

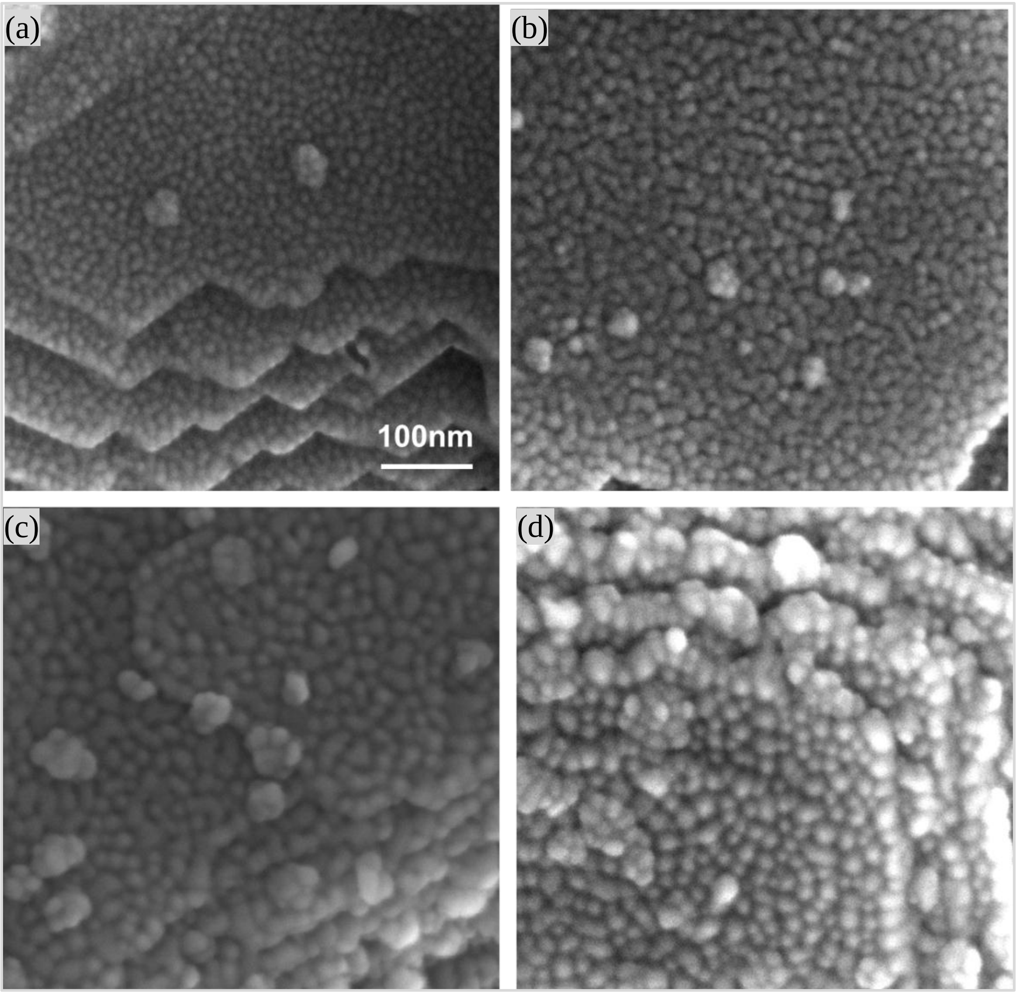

Figure 6.5: SEM images of ZnS nanodots obtained on CIGSSe substrates by Spray-ILGAR after different number of process cycles: a) 10, b) 20, c) 30 and (d) 40.

6.3.3 In_2S_3 thickness variation

The thickness of the In_2S_3 layer can be simply adjusted by varying the number of proces cycles due to the cyclical nature of the Spray-ILGAR process. The typical deposition rate is 2.5 nm/cycle. As reported previously[73], the cell efficiency shows rather a broad plateau than a pronounced maximum within 2-10 process cycles. In the case of this ZnS nanodots / In_2S_3 bilayer buffer, the performance of the solar cells are monitored as different process cycles of In_2S_3 are deposited on top of the ZnS nanodot film. For these series, the optimal density of ZnS, 20 process cycles are chosen.

The cell performance is greatly improved with the deposition of 2 cycles of In_2S_3 compared to ZnS nanodots alone as buffer layer. However, once the bridge is established, the thickness of In_2S_3 layer shows no obvious influence to the cell performance in this thickeness range. The PV parameters tend to be stable with varied thickness of In_2S_3 layers, which is same as with the pure In_2S_3 buffer. Therefore, it is clear that the In_2S_3 contact bridge is essential to the establish a good buffer layer, which is observed in both open circuit voltage and fill factor.

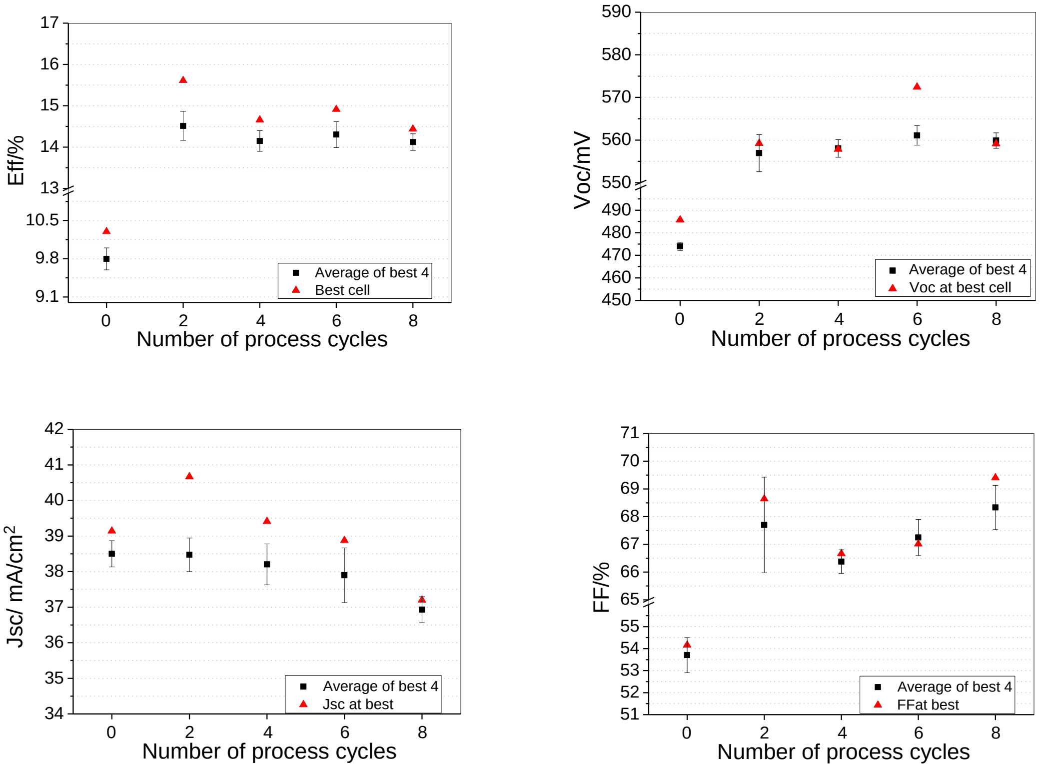

Fiugre 6.6: PV parameters, cell efficiency (Eff), open circuit voltage (V_{OC}), short circuit current (J_{SC}) and fill factor (FF), of the solar cells with increasing process cycles of In_2S_3 layer after the standard ZnS nanodots passivation buffer. Cells are prepared with 20 cyles of ZnS nanodots and 0-8 cylcs of In_2S_3.

6.3.4 Impact of the deposition temperature

High efficiency is obtained in devices with pure ILGAR In_2S_3 buffer for a wide temperature range [73]. However, for the ZnS nanodots/ In_2S_3 bilayer buffered cell the diffusion of zinc into the absorber is a possible mechanism for the improved efficiency. Therefore, the device performance may show an increased temperature dependence. In order to determine the optimum temperature for the bilayer buffer, a series of solar cells is made using 20 process cycles of ZnS nanodots and 6 cycles of In_2S_3 and the temperatures for ZnS nanodots deposition are varied between 175 and 275 °C. Given is always the substrate holder temperature. The temperature values given in this work are therefore comparable, however, care must be taken when the values are compared with the surface temperatures of the samples.

Figure 6.7 shows the efficiency and open circuit voltage of the cells as a function of temperature. The current density and fill factor are not shown since no change with temperature is observed. The cell efficiency gradually increases with temperature between 175 and 225 °C, mainly due to the an increase in the open circuit voltage. This could be partially explained by the lower dot density of ZnS nanodots at the lower temperature, due to the temerature dependence of the deposition rate of the nanodots. It can be seen that the highest cell efficiency exists at 225 °C. Afterwards it drops off slightly. However, the variation is weak, which is similar to the one observed with the pure In_2S_3 buffer layer. As the temperature increases, further copper and sodium out-diffusion from the absorber will be taking place and the chemical changes at the bilayer interface could happen as well. All these factors could influence the overall cell performance. Although the cell performance doesn't show an increased temperature dependence, the diffusion of Zn into the absorber could not be excluded. This topic will be further investigated in Section 6.4.

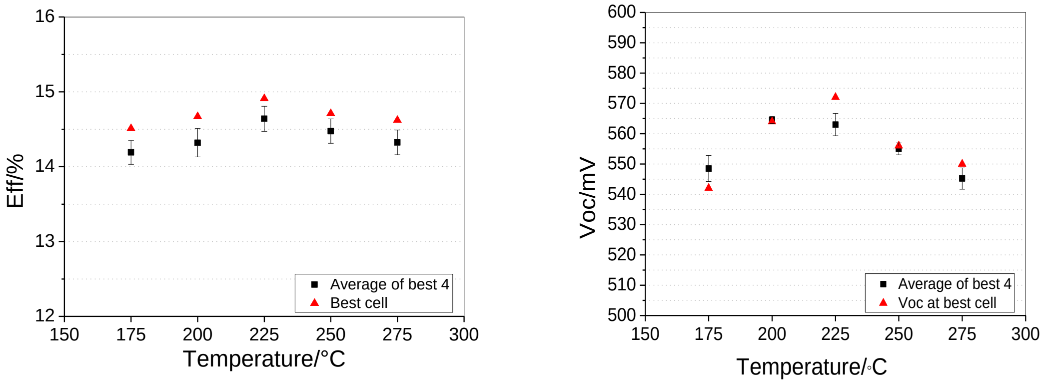

Figure 6.7: Cell efficiency (Eff) and open circuit voltage (V_{OC}) of the solar cells with ZnS nanodots/ In_2S_3 bilayer buffer as a function of temperature.

6.3.5 Influence of the In precursor solution

The ILGAR In_2S_3 films, grown using an $InCl_3$ precursor, characteristically have a chlorine content of 10-12 % atomic percent. The chlorine comes from the chloride precursor and can be avoided by using, for example, $In(acac)_3$ (indium acetylacetonate). The effect of Cl to the bilayer buffer is studied in this section. After the deposition of 20 process cycles of ZnS nanodots, In precursor salt solutions (chloride or acac) are changed for the Spray-ILGAR deposition of In_2S_3. The process cycles for both In_2S_3 deposition are 6 and indicated as In_2S_3 (Cl) (deposition using $InCl_3$ precursor solution) and In_2S_3 (acac) (deposition using $In(acac)_3$ precursor solution).

The deposition conditions for the In_2S_3 (Cl) and ZnS nanodots are the same as described in section 6.2, but the data cannot be directly compared as each series of experiment uses absorber material from different batches. The conclusion is further confirmed that the addition of ZnS nanodots increases the cell efficiency and open circuit voltage compared to the pure In_2S_3(Cl) buffer layer, which is reproducible in different bathes of absorber. On the other hand, the addition of ZnS nanodots has much less influence to the Cl-free In_2S_3 (acac) buffer layer, especially in the open circuit voltage (Figure 6.8).

The lowest values of Voc (554 and 552 mV for the best cell and averaged value, respectively) are obtained for the single buffer layer of In_2S_3 (Cl). The value of V_{OC} is increased to 570 (best cell) and 569 mV (averaged) for the combined ZnS nanodots / In_2S_3 (Cl) buffer layer. The value of V_{OC} is further increased to 581 mV (best cell) and 575 mV (averaged) if replacing In_2S_3 (Cl) by In_2S_3 (acac). The value of the averaged V_{OC} increased slightly to 577 mV for the ZnS nanodots / In_2S_3 (acac) buffer while the value of the best cell dropped to 576 mV.

Further discussion about the influence of the Spray-ILGAR In_2S_3 deposition from different precursor solutions on the open circuit voltage, the surface defects of ZnS nanodots and on the $Cu(In,Ga)(S,Se)_2$ absorber is shown in section 6.5.

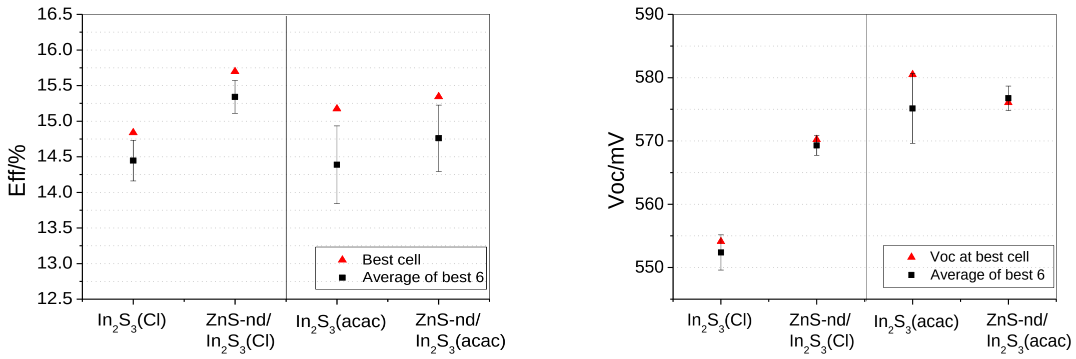

Figure 6.8: Dependence of cell efficiency and open circuit voltage for the best $Cu(In,Ga)(S,Se)_2$ solar cell (triangles) and for the averaged over all cells values (circles) on the buffer layer preparation (In_2S_3(Cl), ZnS nanodots / In_2S_3(Cl), In_2S_3(acac) and ZnS nanodots / In_2S_3(acac)). Cells were prepared with 20 cycles of ZnS nanodots and 6 cycles of In_2S_3.

6.3.6 Spray-CVD ZnS nanodot as passivation layer

The Spray-ILGAR ZnS nanodots work well as a passivation layer to reduce the recombination at the p-n junction and therefore increase the open circuit voltage and cell efficiency. In the following section, the application of Spray-CVD Zn(S,O) as passivation buffer layer is estimated, although it has different composition and optical band gap compared to the Spray-ILGAR ZnS nanodots. The cells are made with different spraying time of Spray-CVD Zn(S,O) (different dot density) plus 6 cycles of standard In_2S_3 (growing from $InCl_3$ precursor). For comparison, the data of the cells with the pure ILGAR In_2S_3 buffer and with the bilayer buffer of 20 process cycles of Spray-ILGAR ZnS nanodots combined with standard In_2S_3 are shown as well in Figure 6.9. It can be seen that the open circuit voltages with addition of 5-20min Spray-CVD Zn(S,O) nanodots are in the same range as the one with Spray-ILGAR ZnS nanodots, which is around 20mV higher than the voltage with the pure In_2S_3. This indicates that the Spray-CVD Zn(S,O) can work as a passivation layer as well. The cell efficiency rises to the maximum after 10-15 min then drops down again after 20 min deposition of CVD Zn(S,O), which could be too thick. However, it seems that the cell efficiencies with Spray-CVD Zn(S,O) nanodots have a larger variation than Spray-ILGAR ZnS nanodots.

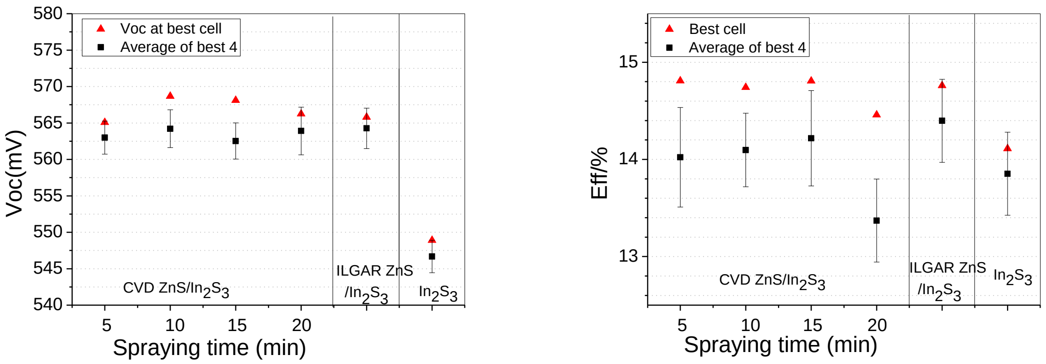

Figure 6.9: Open circuit voltage (V_{OC}) and cell efficiency (Eff) of the solar cells with different spraying time of Spray-CVD Zn(S,O) plus 6 cycles of standard

In_2S_3 buffer. For comparison, the data of the cells with the pure ILGAR In_2S_3 buffer and with bilayer buffer of 20 process cycles of Spray-ILGAR ZnS nanodots combined with standard In_2S_3 are shown as well.

6.4 Zn diffusion: XPS investigation

The information depth in XPS analysis is in the order of a few nanometers. In order to make the deeply buried absorber side of the ZnS nanodots/ CIGSSe heterointerface accessible for characterization, the nanodots are removed by etching the sample in 50 ml 2% aqueous HCl solution. Beginning with a short etching time of 1 min, the ZnS is incrementally removed from the CIGSSe absorber via various steps. When taken out of the HCl solution, the etched samples are rinsed in 100 ml fresh de-ionized water for three times and then under running deionized water. Finally they are dried in N_2 flow. After each ecthing step (1min, 5min, 15min, 1h and 20h), the samples are measured with XPS to follow the removal process in detail. It should be noted that 60 process cycles of ZnS nanodots are deposited in this series of experiment to ensure that a volume of CIGSSe containing Zn is not completely removed before it could be measured. Research has confirmed that chalcopyrite absorber are not attacked by the acid [152, 153].

Figure 6.10 shows the overview spectra of the incremental HCl etching experiment. For comparison, the as prepared ZnS nanodots / CIGSSe and bare CIGSSe samples are shown as reference. The removal of the ZnS layer is very clear in the measurements, which is indicated by the gradual attenuation of the Zn signals. The signals of the CIGSSe surface are immediately observed after 1min etching in HCl solution. The Na 1s peak remained unchanged for the bare CIGSSe absorber and ZnS nanodots/CIGSSe sample, but disappear after dipping in HCl solution, which can be explained by washing out.

The most prominent XPS feature of the ZnS nanodots, the Zn 2p photoemission line is shown in Figure 6.11. It can be observed that the intensity of the Zn 2p photoemission line for the ZnS nanodots/CIGSSe samples is gradually reduced after 1 and 5min HCl etching. The most noticeable feature is the big change after 15min HCl etching, where the Zn 2p signal is drastically reduced. Note that the etched samples at 15min, 1h and 20h are magnified by a factor of 11. HCl removes the ZnS quickly as expected. But it leaves behind a small amount of Zn whose concentration diminishes slowly further with each successive etching step. However, the Zn signal is not completely removed from the CIGSSe surfaces and is detectable even after 20 hours etching time. Interestingly, it was observed that ZnS on Mo is completely removed after 15 min etching in 5% HCl solution [154], which is indicative for the removal of ZnS also from the CIGSSe absorber. Therefore, it could be concluded that the remaining Zn on CIGSSe is not present as a constituent of ZnS. Otherwise it would be etched away as observed on Mo substrate due to the good solubility of ZnS in HCl [155]. It is extremely unlikely that Zn signals come from residual solution contamination, because the samples are rinsed very carefully after the etching step and no Cl is detectable by XPS. In consequence, this result could be interpreted as a Zn diffusion into the CIGSSe absorber. This could lead to an electronic improvement of the absorber surface, which will be discussed in the next paragraph. Similar behavior was observed for CdS by Johnson [156] .A pronounced shift of the energetic position of the photoemission lines Zn $2p_{3/2}$ and Zn $L_3M_{45}M_{45}$ can be observed as compared to the as prepared ZnS and the one after 1 min etching. In order to check if the shift is due to the change of chemical environment or due to the band bending, the modified Auger parameters [145] are computed using the Zn $2p_{3/2}$ core level and the Zn $L_3M_{45}M_{45}$ Auger signal, $\alpha=E_{kin}[\text{Zn } L_3M_{45}M_{45}(^1G)]+E_B[\text{Zn } 2p_{3/2}]$. The calculated result is listed in Table 6.1, in which no change in the modified Auger parameters is observed. This fact indicates that the shift in the energetic position of the photoemission lines Zn $2p_{3/2}$ and Zn $L_3M_{45}M_{45}$ can be attributed to the band bending. The Zn XPS peak position suggests that the Zn is bound to S or Se. The further decreased intensity of the Zn 2p XPS signal is probably due to the increasingly leaching out of the incorporated Zn with extensively increased exposure time to the HCl solution [154].

The diffusion of Zn into the uppermost region of the absorber can have a beneficial effect on the open circuit voltage and efficiency, which is observed with ZnS / In_2S_3bilayer buffer (Figure 6.3). The introduction of the bivalent Zn on the surface of the p type CIGSSe absorber, which is like the injection of acceptor state, brings the conduction band of the p type absorber down. This could lead to a type inversion and the photogenerated electrons in the p type absorber (minority charge carriers) reach the buffer/absorber interface as majority charge carriers [154]. The recombination rate is then effectively reduced due to the low concentration of recombination parters (holes) for the electrons and therefore the overall performance of the final solar cell device is improved.

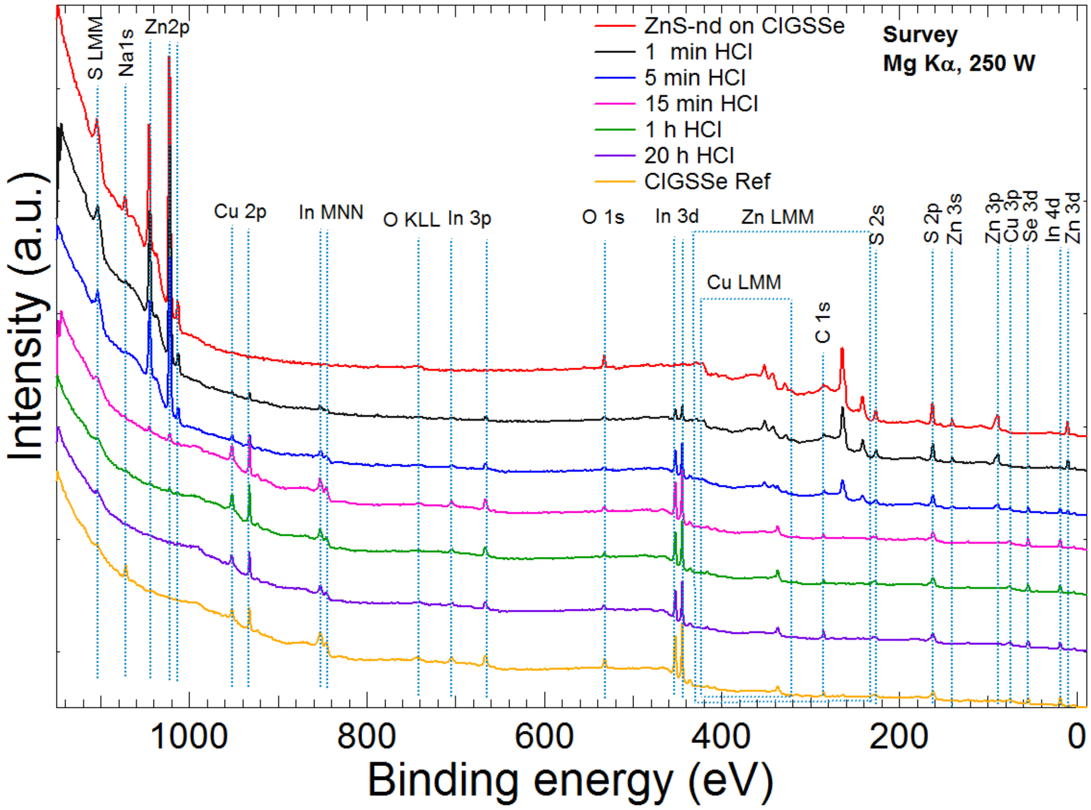

Figure 6.10: XPS survey spectra of the as-prepared ZnS nanodots (ZnS-nd) on a CIGSSe absorber (top), the bare CIGSSe absorber (bottom) and the incrementally etched ZnS nanodots on a CIGSSe absorber with aqueous HCl solution (middle). The corresponding etching times are 1min, 5min, 15min, 1h and 20h respectively.

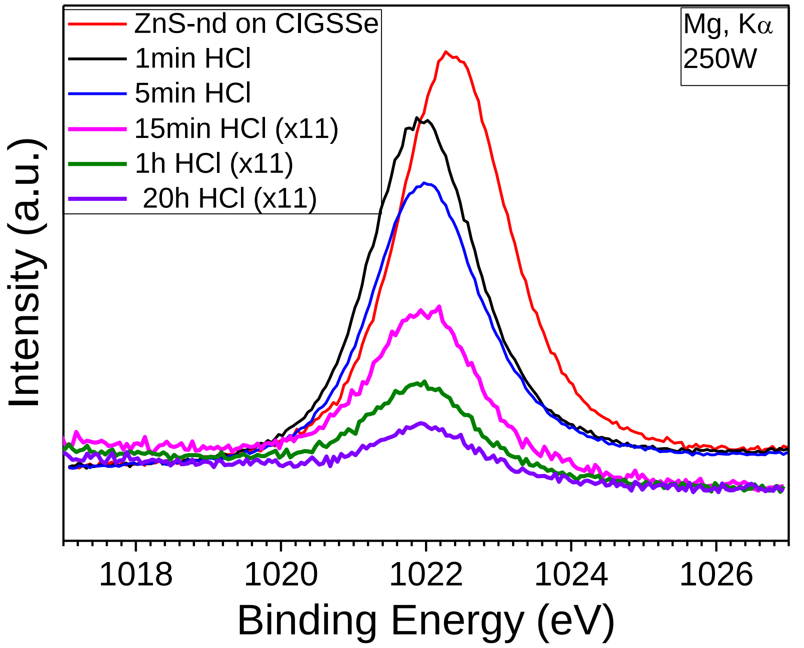

Figure 6.11: Zn $2p_{3/2}$ photoemission lines of as-prepared ZnS nanodots on a CIGSSe absorber (top), and the incrementally etched ZnS nanodots on a CIGSSe absorber with aqueous HCl solution. The corresponding etching times are 1min, 5min, 15min, 1h and 20h respectively. The values have an error of ±0.1 eV.

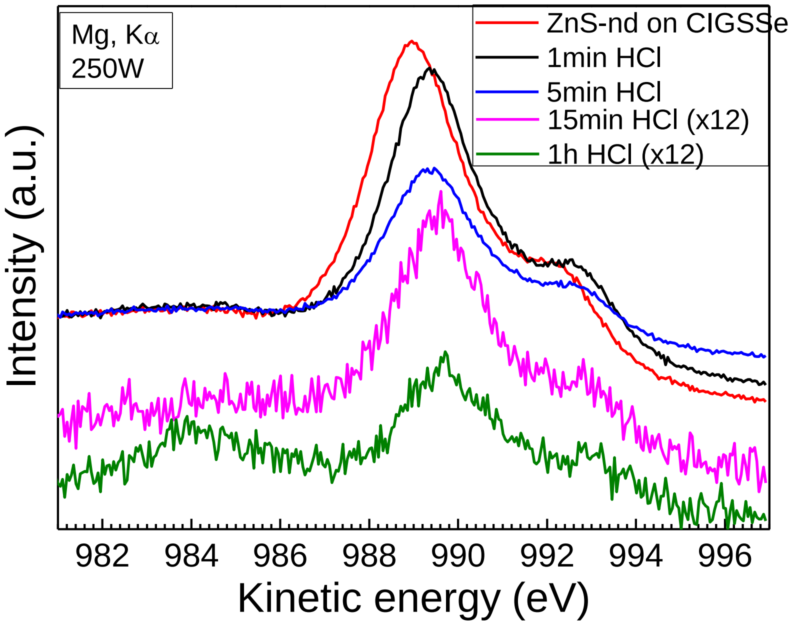

Figure 6.12: Zn $L_3M_{45}M_{45}$ Auger lines of as-prepared ZnS nanodots on a CIGSSe absorber (top), and the incrementally etched ZnS nanodots on a CIGSSe absorber with aqueous HCl solution. The corresponding etching times

are 1min, 5min, 15min and 1h respectively. The values have an error of ±0.1 eV.

Table 6.1: Energetic positions of Zn $2p_{3/2}$ photoemission line and Zn $L_3M_{45}M_{45}$ Auger line as found for the as-prepared ZnS nanodots on a CIGSSe absorber and the 1 min-etched ZnS nanodots on a CIGSSe absorber with aqueous HCl solution. In addition the corresponding values of the Auger parameter $\alpha=E_{kin}[\mathrm{Zn}\ L_3M_{45}M_{45}(^1G)]+E_B[\mathrm{Zn}\ 2p_{3/2}]$ are calculated using the values presented in table 6.1. All the values have an error of ±0.1 eV.

Sample	Zn $L_3M_{45}M_{45}$ (eV)	Zn $2p_{3/2}$ (eV)	Auger parameter (α) (eV)
As-prepared Zn-nd	989	1022.3	2011.3
After etching 1min	989.4	1021.9	2011.3

6.5 Surface photovoltage

This section is based on the following paper:

Y. P. Fu, T. Rada, C.-H. Fischer, M. Lux-Steiner, Th. Dittrich, Surface photovoltage spectroscopy on $Cu(In,Ga)(S,Se)_2$ / ZnS-nanodot / In_2S_3 systems, submitted to *Progress in Photovoltaics: Research and Applications*.

In this section, single and combined layer systems of $Cu(In,Ga)(S,Se)_2$, ZnS nanodots and In_2S_3 layers are investigated by surface photovoltage (SPV) spectroscopy in the Kelvin-probe arrangement [157], which provides information about electronic transitions from which charge separation is possible. Besides the combinations of $Cu(In,Ga)(S,Se)_2$, ZnS nanodots and In_2S_3 layers the In_2S_3 layer thickness (2 and 12 nm) and the In precursor salt solutions, indium chloride ($InCl_3$) and indium acetylacetonate ($In(acac)_3$) are changed and SPV measurements are performed in different ambience. Details on the fundamentals of SPV that was used can be found in Appendix A.6 and [157].

6.5.1 Surface photovoltage of single layer and combined layers

Single layers

Figure 6.13 depicts the surface photovoltage spectra of In_2S_3 (Cl, 12 nm) and ZnS nanodots measured in air, vacuum and nitrogen atmosphere. The slit of the monochromator is opened at 0.7 eV as mentioned above. The SPV signal of In_2S_3 (Cl, 12 nm) is positive over the whole spectrum, i.e. photo-generated holes are preferentially separated towards the external surface of In_2S_3. The SPV signal of In_2S_3 (Cl, 12 nm) set on when opening the slit of the monochromator, i.e. excitation from deep defect states lead to charge separation. Further the SPV signal of In_2S_3 (Cl, 12 nm) increase exponentially between 1.5 and 2.1-2.2 eV with a characteristic energy of 0.17 eV independent of ambience. For comparison, the optical band gap of In_2S_3 (Cl) layers is of the order of 2.2 eV [69]. The spectral feature around 2.6-2.7 eV is related to a peak in the intensity of the Xe lamp. The SPV signals increase in vacuum by about three times for excitation from deep defect states and by about 30% in the UV range. After filling in nitrogen atmosphere the SPV signal decrease by about 30 and 10% for excitation from deep defect states or in the UV range.

For ZnS nanodots in air a SPV signal with positive sign set on at about 3.2 eV and the SPV starts to decrease at about 3.6 eV with a change of the sign at about 3.8 eV and reaches SPV signal of -7 mV at 4 eV. For comparison, the band gap was 3.65 eV for a 150 nm thick ZnS layer deposited by ILGAR with the same precursors [74]. Therefore electrons are excited from occupied surface states at photon energies below the band gap and electrons photo-generated in the bulk of ZnS nanodots are preferentially separated towards the surface of the ZnS nanodots. Charge separation due to excitation from deep defect states occurred in vacuum and nitrogen atmosphere. A similar behavior is observed for TiO_2 nanoparticles [158]. It is suspected that the disappearance of water molecules physisorbed at the surface of ZnS nanodots lead to depassivation of surface defects.

The SPV spectra of In_2S_3 (Cl, 2 nm) and CIGSSe measured in air are plotted in figure 6.14 (a). The SPV signal of In_2S_3 (Cl, 2 nm) is positive and had a very low amplitude (about 2.5 mV at 3 eV). For comparison, the SPV signal amounts to 87 mV at 3 eV for In_2S_3 (Cl, 12 nm) in air. SPV signals are proportional to the charge separation length, i.e. the difference of the centers of mass of positive and negative charge carriers, and to the amount of charge carriers separated in space. For extremely thin layers, the charge separation length and the concentration of photo-generated charge carriers are proportional to the layer thickness. Therefore the SPV signal is proportional to the squared layer thickness for extremely thin layers if the dominating recombination mechanism remains unchanged what fits very well with the observed difference of SPV signal for 12 and 2 nm thick In_2S_3 (Cl) layers. The SPV signals of the bare CIGSSe layer set on at about 1 eV corresponding to the band gap of CIGSSe and are negative as expected for a p-type semiconductor in depletion.

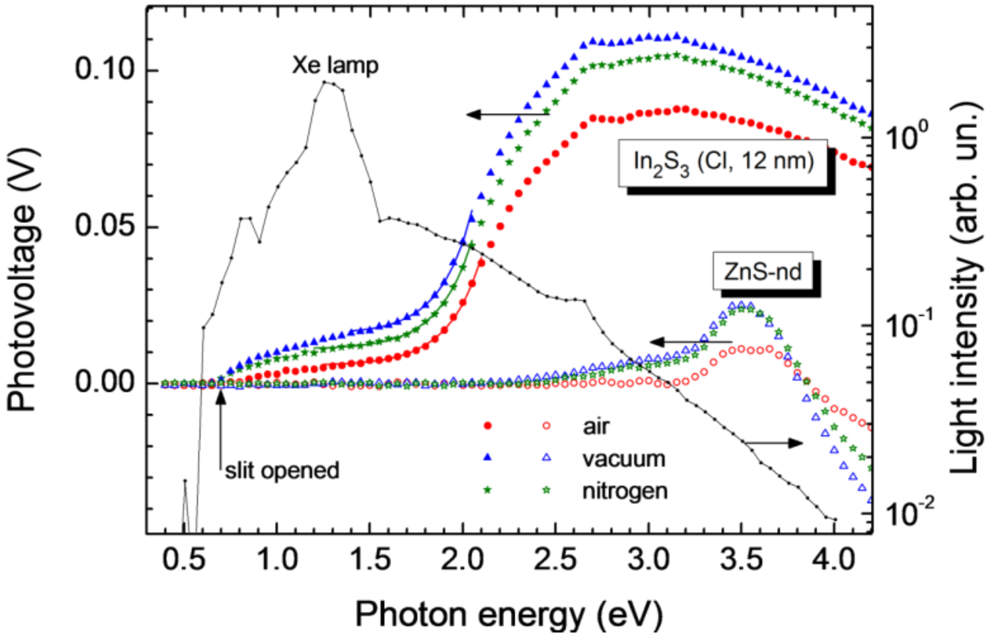

Figure 6.13: SPV spectra of In_2S_3 (Cl, 12 nm) (filled symbols) and ZnS nanodots (open symbols) measured in air, vacuum and nitrogen atmosphere (circles, triangles and stars, respectively). The intensity spectrum of the Xe lamp is shown for comparison on a logarithmic scale.

Double layers

The SPV spectrum of ZnS nanodots change strongly after deposition of In_2S_3 (Cl, 2 nm), In_2S_3 (Cl, 12 nm) and In_2S_3 (acac, 3 nm) as shown in figure 6.14 (b) for measurement in air. At lower photon energies the SPV spectra are positive for In_2S_3 (Cl, 12 nm) due to the influence of In_2S_3. However, the SPV signals started to decrease towards negative sign at 3.1 and 2.8 eV for ZnS nanodots / In_2S_3 (Cl, 2 nm) and ZnS nanodots / In_2S_3 (Cl, 12 nm) and at 3.2 eV for In_2S_3 (acac, 3 nm), respectively, what is not the case for the bare layers. This means that electrons excited from defect states below the band gap of ZnS nanodots are preferentially separated towards the external surface similarly to electrons photo-generated in the bulk of ZnS nanodots. Further, the SPV amplitudes at 4 eV increase strongly from -21 mV before to -73, -135 and -175 mV after deposition of In_2S_3 (Cl, 2 nm), In_2S_3 (Cl, 12 nm) and In_2S_3 (acac, 3 nm), respectively, what can be explained by additional charge transfer from ZnS nanodots into In_2S_3.

The nature of charge separation from defect states at ZnS nanodots change after deposition of In_2S_3 and deposition of the thicker In_2S_3 (Cl) layer lead to larger generation of new defect states. An extremely thin layer of In_2S_3 on top of ZnS nanodots increase very much the amount of electrons separated from ZnS nanodots towards the external surface. This can be explained by a reduction of the recombination rate at the ZnS nanodots / In_2S_3 interface due to a band-offset for which the conduction band edge of In_2S_3 is below the conduction band edge of ZnS nanodots. It is important to point out that the lowest SPV signal related to charge separation from defect states below the band gap of ZnS nanodots and the highest SPV signal related to separation of charge carriers excited by band-band transitions are observed after deposition of In_2S_3 (acac), i.e. the lowest defect concentration and recombination rate at the ZnS nanodots / In_2S_3 are achieved with In_2S_3 (acac).

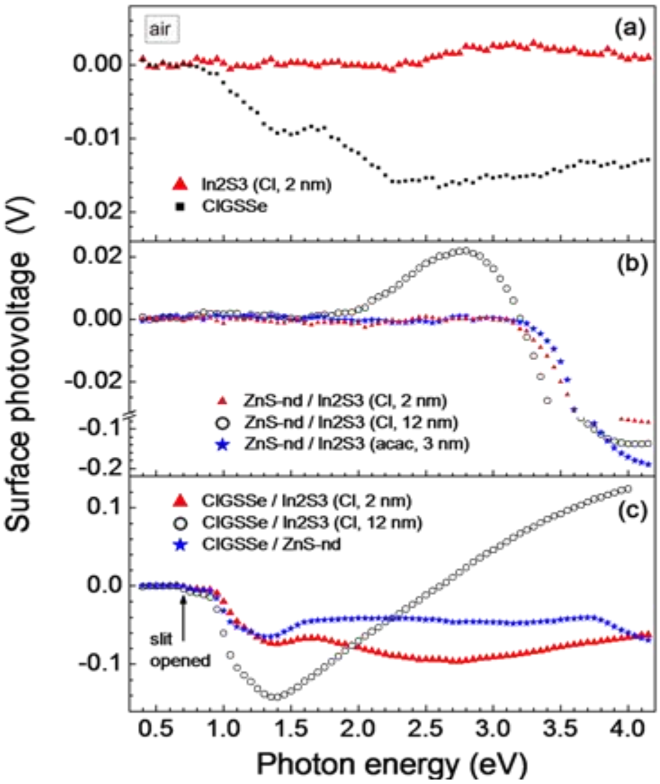

Figure 6.14 SPV: spectra of In_2S_3 (Cl, 2 nm), In_2S_3 (Cl, 12 nm), ZnS nanodots and CIGSSe (a), ZnS nanodots / In_2S_3 (Cl, 2 nm) and ZnS nanodots / In_2S_3 (Cl, 12 nm) (b) and of CIGSSe / In_2S_3 (Cl, 2 nm), CIGSSe / In_2S_3 (Cl, 12 nm) and CIGSSe / ZnS nanodots (c) measured in air.

SPV spectra measure in air for CIGSSe coated with ZnS nanodots, In_2S_3 (Cl, 2 nm) and In_2S_3 (Cl, 12 nm) are presented in figure 6.14 (c). The SPV signals at 1.3 eV increase strongly from -8 mV before to -65, -74 and -135 mV after deposition of ZnS nanodots, In_2S_3 (Cl, 2 nm) and In_2S_3 (Cl, 12 nm), respectively. Therefore, positive charge carriers are preferentially accumulated at the formed interfaces so that separation of electrons photo-generated in CIGSSe towards the CIGSSe surface increased very much. The peak in the SPV spectrum around 1.3-1.4 eV is caused by the intensity spectrum of the Xe-lamp. The features of the ZnS nanodots layer can be clearly seen between 3.2 eV (SPV became more positive) and 3.7 eV (SPV became more negative) in the spectrum of CIGGSe / ZnS nanodots. The spectrum of CIGSSe / In_2S_3 (Cl, 12 nm) start to become more positive at photon energies above 1.4 eV while a striking increase of the positive SPV component by more than 250 mV over the whole following spectral range has been observed. The means that the formation of the CIGSSe / In_2S_3 (Cl) interface have also a tremendous influence on separation of charge carriers photo-generated in the In_2S_3 (Cl) layer. This is not surprising if assuming an In_2S_3 surface with preferentially occupied acceptor states, i.e. negative surface charge, and a CIGSSe / In_2S_3 (Cl) interface with preferentially un-occupied donor states, positive interface charge.

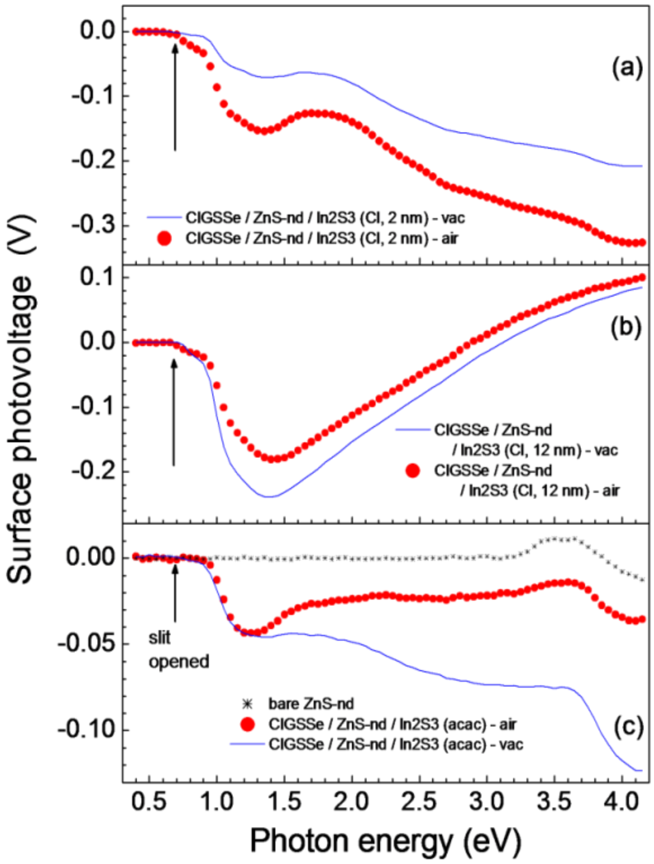

Figure 6.15: SPV spectra of CIGSSe / ZnS nanodots / In_2S_3 (Cl, 2 nm) (a), of CIGSSe / ZnS nanodots / In_2S_3 (Cl, 12 nm) (b) and of CIGSSe / ZnS nanodots / In_2S_3 (acac) (c) measured in air and vacuum. The spectrum of bare ZnS nanodots is shown for comparison (c).

Triple layers

For triple CIGSSe / ZnS nanodots / In_2S_3 (Cl, 2 nm) and CIGSSe / ZnS nanodots / In_2S_3 (Cl, 12 nm), see figure 6.15, the SPV signal at 1.3 eV (measured in air) increases further to

-150 and -170 mV, respectively. Charge separation from defect states below the band gap of CIGSSe is pronounced for both samples. A feature related to absorption in ZnS nanodots has been observed in the CIGSSe / ZnS nanodots / In_2S_3 (Cl, 2 nm) sample and the striking change towards positive SPV signals remain in the spectrum of CIGSSe / ZnS nanodots / In_2S_3 (Cl, 12 nm). Surprisingly the SPV signals at 1.3 eV decreased to -70 mV but increased to -235 mV for CIGSSe / ZnS nanodots / In_2S_3 (Cl, 2 nm) and CIGSSe / ZnS nanodots / In_2S_3 (Cl, 12 nm), respectively. This demonstrates the importance of exchange of charge between the different materials and interfaces for establishing equilibrium.

For CIGSSe / ZnS nanodots / In_2S_3 (acac) the SPV signal at 1.3 eV increased only to -45 mV but independent of ambience (figure 6.15 (c)). Further, pronounced charge separation from defect states below the band gap of CIGSSe has not been observed and the features in the spectral range of ZnS nanodots are practically identical for the bare ZnS nanodots layer and the triple layer system. The SPV signals at higher photon energies increase in vacuum while the spectral features remain practically unchanged. Therefore, deposition of In_2S_3 from $In(acac)_3$ precursor solution do not lead to defect generation at surface of ZnS nanodots and accumulation at positive charge at the CIGSSe surface is less pronounced, also due to reduced defect generation.

6.5.2 Formation of interface defects by etching with HCl byproduct

Electronic differences of the ZnS nanodots / In_2S_3 and $Cu(In,Ga)(S,Se)_2$ / In_2S_3 interfaces between films deposited from $InCl_3$ and from $In(acac)_3$ can be understood in view of the different chemical reactions taking place during layer formation. During the spray step of the ILGAR process HCl gas is formed as a by-product when a metal chloride is used as a precursor. This theoretically evident product could also be proven by mass spectrometry analysis[72]. The reactive HCl gas can attack Ga, Zn or In sulfides and oxides (oxides are present especially on aged absorber surfaces). The basic chemical reactions are expressed in the following equations:

$$Ga_2O_3 + 6\,HCl \rightleftarrows 2\,GaCl_3 + 3\,H_2O \qquad \text{Eq.6.1}$$

$$In_2O_3 + 6\,HCl \rightleftarrows 2\,InCl_3 + 3\,H_2O \qquad \text{Eq.6.2}$$

$$In_2S_3 + 6\,HCl \rightleftarrows 2\,InCl_3 + 3\,H_2S \qquad \text{Eq.6.3}$$

$$ZnS + 2\,HCl \rightleftarrows ZnCl_2 + H_2S \qquad \text{Eq.6.4}$$

Reaction (6.1) and (6.2) can take place during the initial deposition of In_2S_3 from the $InCl_3$ solution on $Cu(In,Ga)(S,Se)_2$ absorber covered with Ga and In oxides whereas reaction (6.4) becomes important for In_2S_3 deposition from $InCl_3$ solution on ZnS nanodots. Also the surface of the buffer In_2S_3 just formed in the foregoing sulfurization step may be partially etched (reaction (6.3)). All these etching processes might lead to a rougher surface of the absorber and/or rougher buffer structures with probably more defects as compared to the preparation route from chlorine free $In(acac)_3$. It is believed that increased surface roughness and generation of interface defects by etching with HCl byproduct causes lower V_{OC} of solar cells with bare In_2S_3 buffers deposited from $InCl_3$ solution.

6.6 Summary

The application of buffer layers, consisting of Spray-ILGAR ZnS nanodots and In_2S_3 film, in $Cu(In,Ga)(S,Se)_2$ thin film solar cells are investigated in this chapter. As yet, this ZnS / In_2S_3 bilayer buffer results in improving cell efficiencies by up to about 1% absolute compared to reference cells with a pure In_2S_3 buffer. The effect is explained as a passivation/point contact buffer: The ZnS reduces the recombination at the absorber/buffer heterointerface which is one important position for performance loss in chalcopyrite solar cells. The In_2S_3 in-between and on top of the ZnS dots is necessary for the charge carrier transport as ZnS has a poor conductivity.

However, excess ZnS nanodots have an adverse effect due to the increased resistance and the blockage of the carrier transport way. An In_2S_3 contact bridge is essential for these cells, but its thickness is not critical to the cell performance as long as the bridge is established. High efficiency is obtained in devices for a wide temperature range for this bilayer buffer. The optimum deposition temperature for this bilayer buffer onto the absorber is found to be around 225 °C. The addition of ZnS nanodots has much less influence to the pure In_2S_3 (acac) (deposition from $In(acac)_3$ precursor solution) buffer layer, especially in the open circuit voltage, compared to In_2S_3 (Cl) (deposition from $InCl_3$ precursor solution) buffer layer. Spray-CVD Zn(S,O) nanodots have a similar passivation effect as the Spray-ILGAR ZnS nanodots.

The diffusion of Zn into the near surface region of the absorber is observed by XPS, which could explain the improvement of the solar cell performance. This could be one reason why the open circuit voltage and efficiency of the cell with ZnS nanodots/ In_2S_3 bilayer is better than with the pure In_2S_3 buffer.

It is shown by SPV that ambience, layer combinations and side reactions during ILGAR deposition can have a tremendous influence on the SPV and that SPV measurements can be applied to investigate related phenomena, respectively. ZnS nanodots deposited by ILGAR improve significantly the passivation of CIGSSe absorbers while defect generation during subsequent ILGAR deposition of In_2S_3 is limited to the small area of direct interface to the absorber. This can be achieved if using chlorine free precursor salt solutions such as $In(acac)_3$. It has been demonstrated by the example of ZnS nanodots that the open circuit voltage of chalcopyrite solar cells and therefore also the energy conversion efficiency can be significantly increased by sophisticated interface engineering with structured passivation on a nanometer scale.

Chapter 7

Summary

The Spray-ILGAR technique produces high quality metal chalcogenide layers. They have successfully been used for buffer layers in thin film solar cells with excellent efficiency. So far only homogenous layers could be produced. It was a great challenge to elaborate a spray-based method to produce nanoparticles at the requisite temperature. In this thesis, the process has developed to enable the deposition of nanodots. High quality, uncoated and sub 10nm ZnS nanodot films have been obtained at the sufficiently low temperatures (< 250°C) by this sequential, cyclic and low cost method which can be scaled up for industrial in-line production. In this form, the process could be used for the deposition of nanodots for the first time. This is done by choosing an appropriate zinc containing compound ($Zn(acac)_2$) and solvent (H_2O). The deposition of ZnS nanodots proceeds in the following two steps:

1. Deposition of a precursor ZnO layer by spraying of an aqueous $Zn(acac)_2$ solution
2. Sulfurization of the precursor ZnO layer to ZnS nanodots by H_2S

These two steps are repeated till the desired dot density is obtained. These nanodots are homogeneous in size, shape and composition, and tend to keep maximum distance from each other. Moreover the obtained nanodots, lacking terminating and stabilizing organic ligands which can be detrimental for certain applications, are desirable for the later employ as passivation layer in solar cells. The deposition temperature for the nanodots is within the limit to avoid deterioration of the solar device (<250 °C). The dot density and to some extent also the size are controllable by varying the process parameters such as precursor concentration, precursor pH value, number of process cycles, substrate temperature, solvent, zinc-containing compound, and reagent gas. Additionally, other nanomaterials, such as In and Cu chalcogenide, have been successfully prepared by the Spray-ILGAR technique, which indicates that it is general method to prepare the nanodot film.

Moreover, with the same zinc containing compound and solvent, nanodots have also been successfully obtained by the Spray-CVD process. Different from the Spray-ILGAR process, in which H_2S comes on sequentially after the aerosol is switched off, in the Spray-CVD process, the nebulized aerosol and H_2S gas are simultaneously introduced into the chamber.

The obtained nanodot films are characterized chemically, crystallographically, morphologically and optically before their application as passivation buffer layers in the thin film solar cells. The difference and similarities of the nanodots achieved in these two processes are compared in the following:

- Compared to the **sub 10 nm Spray-ILGAR** nanodots, the nanodots obtained by **Spray-CVD** are also homogeneous in size, but **larger** in size at the same spraying time.
- **Deposition temperature <300 ºC**: In the Spray-ILGAR process, the nanodots get denser with increasing the number of process cycles (<50 cycles), while keep constant in size. Above 50 process cycles, the nanodots grow from sparse scattering to a dense arrangement, and finally to a compact film with a variety of different particle sizes. On the other hand, in the Spray-CVD process, the nanodots get larger in size even before forming a compact layer as the number of process cycles increases.
- **Deposition temperature >300 ºC**: In both processes, the nanodots are inhomogeneous in size, where large and small particles coexist. In the Spray-ILGAR process, some of the homogeneous monodisperse nanodots cluster into dimers and trimers with the size from a few nanometers to several tens of nanometer. The variety of the different sizes in both processes indicates a different nucleation behavior to the one at temperature < 300 ºC.
- **H_2S plays an important role in both processes.** In the Spray-ILGAR process, the residual H_2S from the last cycle is essential for the achievement of the homogeneous nanodots. Otherwise, only microparticles are obtained without H_2S in the first spraying step. While in the Spray-CVD process, the deposition rate decreases remarkably as the H_2S concentration increases.
- The studies of energy-filtered TEM images (EF-TEM) and corresponding sulfur maps reveal that the nanodots obtained by **Spray-ILGAR** are **quasi sphere particles**, which are **completely sulfurized**. In contrast, the ones in the **Spray-CVD** process are more **irregular** than Spray-ILGAR, and are **incompletely sulfurized**. The irregular shape of the Spray-CVD nanodots, which is in agreement with the standard TEM observation, is the result of the corresponding growth mechanism.
- The information about the chemical composition of the nanodots is acquired by means of XPS and AES. In the case of the **Spray-ILGAR** process, the nanodots are **pure ZnS**. Whilst in case of the **Spray-CVD** process, the chemical compositions of the nanodots shifts to a **Zn(S,O)** like compound, with a ZnS / (ZnS+ZnO) ratio of approximately 0.42 when deposited with 5 ml/min 5% H2S/Ar. This is in good agreement with the observation from EF-TEM and the corresponding sulfur map, where the Spray-CVD nanodots are not completely sulfurized.
- Resulting **Spray-ILGAR ZnS** has a dual band gap at about **3.65~3.7 and 3.71~3.98 eV**. On the other hand, the band gap of the **Spray-CVD Zn(S,O)** nanodots is about **3.46 to 3.58eV**.

Moreover, the resulting nanodots in both processes are crystalline, which exist either in hexagonal structure alone or with the inclusion of some cubic ZnS. No crystalline ZnO is found for both processes. The achievement of the metastable hexagonal ZnS phase at the low temperature could be explained by maintaining the structure during the conversion from the intermediate hexagonal ZnO in the 1st spray step to the ZnS nanodots in the 2nd sulfurization step. Last but not least, the Spray-CVD process is much faster than the Spray-ILGAR process since it saves half of the process time by omitting the sulfurization and two purge steps in the Spray-ILGAR process.

The investigation on the two processes and the fundamental properties of the obtained nanodots give hints for the thermal decomposition mechanism of $Zn(acac)_2$ on the hot substrate surface and allow for the deduction of a self-limiting growth model for ZnS nanodot deposition. In-situ mass spectrometry is applied to study the decomposition process in detail. It is found that with the help of H_2S, the decomposition of $Zn(acac)_2$ occurs together with evaporation of the specimen because evolution of acetylacetone and $Zn(acac)_2$ are simultaneously detected, which proves that the first step of the Spray-ILGAR nanodots deposition is a AACVD process. On the contrary, in the absence of H_2S, $Zn(acac)_2$ decompose directly on the substrate from submicron aerosol liquid droplet to solid with a negligible amount of evaporation. This is in good agreement with the observed influence of H_2S to the morphology of the achieved nanodots. Additionally, H_2O is found to promote the decomposition of $Zn(acac)_2$ by supporting hydrolysis of $Zn(acac)_2$.

Based on these studies, a decomposition route of $Zn(acac)_2$ on the hot surface could be suggested. The molecules adsorbed on the surface, firstly, open the chelate cycles and hydrolyze with the crystal H_2O. Afterwards, they could rearrange by migrating the intramolecular H or react with the extramolecular H stemmed from H_2O, H_2S and acid. The reaction with the extramolecular H gives an additional chance to yield ZnO. Therefore the existence of the extramolecular H donator, i.e. H_2O, H_2S and acid accelerates the $Zn(acac)_2$ decomposition.

The self-limiting growth of the nanodots in these two processes is understood by taking into account both the mechanism of the two temperature regimes of the conventional CVD process and the sulfurization of the nanodots.

In the low temperature region <300 ºC, the surface reaction kinetics controls this regime, where the precursor molecules have a finite time to diffuse and find the preferential nucleation site before decomposition.

- In the Spray-ILGAR process, the growth follows the Volmer-Weber mode in the 1st process cycle. The nuclei form on expense of the adsorbed precursor molecules on the substrate, grow into stable ZnO particles (3-8 nm) with a Gibbs free energy at minimum and are subsequently converted to ZnS particles. In the following cycles, nucleation occurs mostly onto the uncovered gaps among the existing nanodots. One possibility is that the gaps among the existing ZnS nanodots are too large for the adsorbed precursor to find an already formed dot before decomposition at the very beginning. The other main possibility is that the existing ZnS nanodots work as barrier layer for the subsequent ZnO nucleation on themselves due to the different composition and lattice distance between ZnS and ZnO. This leads to an increase of the dot density with a negligible increase of the dot size (chapter 3). When the dots are too dense to have uncovered substrate surface, they start touching each other and aggregate to larger nanodots. Hence, it results in the formation of nanodots with a variety of size.

- In the Spray-CVD process, the nucleation of ZnO occurs on the formed Zn(S,O) nanodots due to oxygen rich sites on the surface act as effective nucleation sites for the precursor molecules, which follows actually the Volmer-Weber growth model. Hence, this results in an increase of the size of the existing nanodots at the same rate with increasing spray time (chapter 3).

In the high temperature region >300 ºC, it is a regime dominated by the limit of the mass transfer, where the decomposition rate is very fast. In both processes, nucleation occurs both onto the uncovered gaps and the existing nanodots due to the instantaneous decomposition of absorbed precursor molecules. Therefore, the old existing nanodots continue to grow while new nanodots form as well, which results in a polydisperse size distribution.

By the Spray-ILGAR technique, a **structured buffer layer**, composed of ZnS nanodots covered by a closed In_2S_3 film, has been introduced in $Cu(In,Ga)(S,Se)_2$ thin film solar cells. The improvement of the cell performance is explained by a **controlled passivation/point contact effec**t: appropriate density of ZnS nanodots passivate defects and reduce the recombination at the absorber/buffer heterointerface which is one important position for performance loss in chalcopyrite solar cells. The In_2S_3 in-between and on top of the ZnS dots work as contact bridge, which is essential for the charge carrier transport as ZnS has a poor conductivity. The addition of ZnS nanodots helps to increase the open circuit voltage and fill factor of the solar cell and further raise the efficiency of the cell. As yet, this ZnS/In_2S_3 bilayer buffer results in improving cell efficiencies up to about 1% absolute compared to reference cells with a pure In_2S_3 buffer. This is considerable since the efficiency lies in the order of 15%. Additionally, the diffusion of Zn from the ZnS nanodots into the near surface region of the absorber is observed by XPS, which can partially explain the improved open circuit voltage and efficiency of the solar cells. Last but not least, the passivation of CIGSSe absorbers by the ZnS nanodots deposited by Spray-ILGAR is studied and proved by mean of SPV. From these measurements, it is found that the In_2S_3 deposition from $InCl_3$ is accompanied by defect generation at the interface due to the aggressive HCl formed during the sulfurization. This can be avoided by In_2S_3 deposited from $In(acac)_3$ as shown by SPV.

From ongoing studies, the extension of this sequential, cyclic and low cost methodology to the synthesis of nanostructure semiconductor materials seems widely applicable and can be scaled-up for industrial in-line production on a commercially available machine. This work brings a proof of concept for point contact / passivation buffer layer for chalcopyrite thin film solar cells. The open circuit voltage of chalcopyrite solar cells and therefore also the energy conversion efficiency can be significantly increased by sophisticated interface engineering with structured passivation on a nanometer scale.

In conclusion, this work has elaborated a novel, easy, flexible, widely applicable method for the deposition of nanodot film. One application in solar cells with clear improved efficiency has been shown. In future, more materials and also completely different application should be realized.

Appendix A

Analysis Techniques

A.1 Theoretical aspects of the electron microscope

Electron Microscopes are scientific instruments that use a beam of highly energetic electrons to examine objects on a very fine scale. This examination can yield information about the topography, morphology, composition and crystallographic information. When an electron hits onto a material, different interactions can occur, as summarized in Figure A.1.

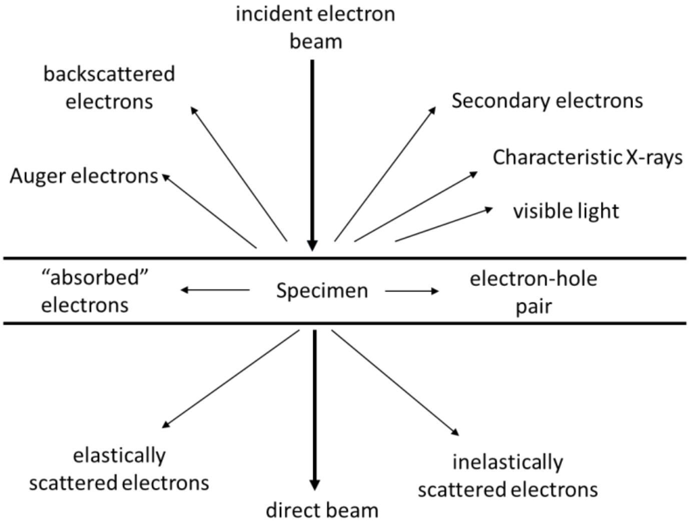

Figure A.1: Scheme of electron-matter interactions arising from the impact of an electron beam onto a specimen. Adapted and modified from the reference [159]. A signal below the specimen is only observable if the thickness is small enough to allow some electrons to pass through.

Scanning electron microscope

Scanning electron microscope (SEM) is an extremely useful tool for studying of the surface of the sample. It uses a focused beam of high-energy electrons to generate a variety of signals at the surface of solid specimens (Figure A.1). Secondary electrons and backscattered electrons are commonly used for imaging samples: secondary electrons are most valuable for showing morphology and topography on samples and backscattered electrons are most valuable for illustrating contrasts in composition in multiphase samples. The X-ray photons which have high energy are used for the compositional analysis of the sample. This technique is known as energy dispersive analysis of X-ray spectroscopy (EDS or EDX) and is used extensively to study the elemental composition of the sample.

The SEM images of the obtained nanodotsrs were obtained with a Leo 1530 SEM operated at accelerating voltage between 3 and 5 kV.

Transmission electron microscopy

Transmission electron microscopy (TEM) is a microscopy technique where a focused beam of electrons is transmitted through an ultra-thin specimen, interacting with it as they pass through. The transmitted electron beam strikes the fluorescent screen and generates an image with varying contrast. The darker areas of the image represent the thicker or denser region of the specimen (fewer electrons are transmitted) and the lighter areas of the image represent those areas which are thinner or less dense (more electrons are transmitted).

Electrons interact with the specimen elastically (where no energy is lost to the interaction) and inelastically (where some amount of energy is lost), with significantly more inelastic events than elastic events. If an "energy filter" is placed between the specimen and the plane where the final image is recorded, allowing those electrons that have not lost any energy, that have lost only a small amount of energy or that have lost discrete amounts of energy defined by the atoms in the specimen to form the image or diffraction pattern, this technique is called Energy-filtered transmission electron microscopy (EF-TEM). This prevents inelastic scattering from contributing to the image, and produces an enhanced contrast image. The Zero Loss EF-TEM is a technique, in which only unscattered or elastically scattered electrons are used.

Both the cross-section of the nanodots deposited on p-Si (100), and the plane view of the nanodots on Cu /Au/C grid were investigated. Since Cu reacts with H2S, the Cu grids were firstly covered with a thin Au film, and then coated with a carbon film. For the case of the plan view TEM analysis, the nanodots were deposited directly at 200° C onto Cu /Au / C grid, which were placed on top of the Si wafer in order to keep the temperature the same as the Si wafer. While for the preparation of the cross-section sample, the sample nanodots /Si were cut into two pieces and glued face to face with conductive epoxy. In the following, these pieces were cut into pieces perpendicular to the interface plane with around 0.5 mm thickness. The slices were then thinned with polishing discs and then ion-milled with Ar+ ions. The samples for cross-section investigations using Ar+ ion beam milling / Gatan PIPS parameters are 3.0 kV Ar 7° / 0.2 kV Ar 9°.

The microscopes used for analysis are a commercial Philips CM12 transmission electron microscope with an operating voltage of 120 kV and a LaB6 cathode (HZB) and a FEI Tecnai F30 G2 transmission electron microscope, which is also equipped with a LaB6 filament that provides a 300 kV electron beam (Kiel University).

A.2 Mass Spectrometry

The mass spectrometer can be regarded as a kind of chemistry laboratory, especially designed to study ions in the gas phases [118, 119]. The basic principle of mass spectrometry (MS) is to generate ions from either inorganic or organic compounds by any suitable method, to evaporate these ions by their mass-to-charge ratio (m/z) and to detect them qualitatively and quantitatively by their respective m/z and abundance. The analyte maybe ionized thermally, by electric fields or by impacting energetic electrons, ions or photons [160].

In a typical MS procedure:

- sample introduction and vaporization
- ionization
- ion separation according to their m/z ratio in an analyzer by electromagnetic fields
- ions detection
- ion signal conversion into mass spectra

A mass spectrometer consists of three modules:

- An ion source, which can create ions from gas phase sample molecules (or, in the case of electrospray ionization, convert ions that exist in solution into the gas phase)
- A mass analyzer, which separates the ions by their masses by applying electromagnetic fields
- A detector, which measures the value of an indicator quantity and thus provides data for calculating the abundances of each ion present

In our case, the ILGAR spray chamber fitted with a mass spectrometer was custom built by Hiden Analytical. The system is a HPR-60 molecular beam sampling system with an integrated multi-stage pumping system and HAL quadrupole mass spectrometer.

A. 3 X-ray Diffraction (XRD)

X-ray Diffraction (XRD) is a powerful nondestructive analytical technique for characterizing crystalline materials. The wavelength of x-ray is comparable to the size of atoms, so they can be effectively used to measure the structural arrangement of atoms in the solids. If the atoms are arranged in a periodic fashion, as in the case of crystals, the peaks in the interference pattern will correspond to the distribution of atoms. The peaks in an x-ray diffraction pattern are directly related to the atomic distances by Bragg's law [161]

$$2d \sin\theta = n\lambda \qquad \text{Eq. A.1}$$

Here, λ is the x-ray wavelength, d is the distance between two lattice planes, θ is the angle between incoming (outgoing) X-ray beam and lattice plane, and n is a natural number representing the order of the diffraction peak, as shown in Figure A.2.

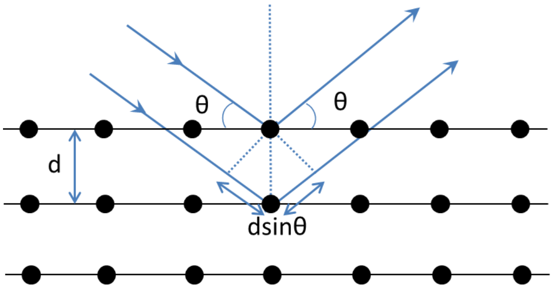

Figure A.2: Schematic representation of the geometry considered for the derivation of the Bragg condition.

The peak position, intensity, and shape provide important information about the structure of the material. The peaks are characteristic for a certain material and the crystalline orientation of the grains in a polycrystalline layer. The average grain size of the crystals in a polycrystalline thin layer can be quantitatively calculated by the Debye-Scherrer formula [162, 163]

$$d = \frac{0.89\lambda}{B\cos\theta} \qquad \text{Eq. A.2}$$

where 0.89 is the shape factor, λ is the x-ray wavelength (0.154nm), B is the line broadening at half the maximum intensity (FWHM) in radians, θ is the Bragg angle, and d is the mean crystal size. A general introduction to X-ray diffraction is given in Ref. [1, 162].

All XRD-measurements were performed in a Bruker D8 diffractometer in grazing incidence mode. In this setup a copper filament emits Cu Kα radiation with characteristic wavelength of 1.5406 Å. For the accomplished measurements the acceleration voltage is set to 40 kV and the filament current to 30 mA. The measurements were recorded in grazing incidence mode with a fixed angle of incidence in the range of 0.5-2° due to the limited thickness of the investigated nanodot films. In grazing incidence mode, the X-ray source is fixed, whilst the detector is moved in a range of 10-80° during the measurements.

A.4 Optical Characterization

Optical properties of the obtained nanodot films have been analyzed by reflection / transmission measurements with an optical spectrometer (Cary 500 Scan UV-Vis-NR Spectrophotometer). The data evaluation has been carried out following Pankove [164]. If only simple reflections are considered, the optical absorption coefficients (α) can be calculated using the following equation

$$T \approx (1-R)\exp(-\alpha x) \qquad \text{Eq. A.3}$$

Where, T is transmission, R is reflection, and x is the film thickness. Therefore the absorption coefficient follows from:

$$\alpha \approx -\frac{1}{x}\ln\left(\frac{T}{1-R}\right) \qquad \text{Eq. A.4}$$

The absorption coefficient is related to the incident photon energy (hυ) as follows [164]:

$$\alpha(h\nu) = A\frac{(E_g - h\nu)^n}{h\nu} \qquad \text{Eq. A.5}$$

where A is a constant, E_g is the energy band gap, and n is a constant equal to ½ for direct band gap semiconductors and 2 for indirect band gap materials.

A.5 X-ray Photoelectron Spectroscopy (XPS)

XPS is a widely used surface analysis technique to investigate the surface of materials (< 100 Å), which is based on the photoelectron effect. The principle of the photoelectric effect was described first by Einstein [165] through the following equation, shown in modern form:

$$E_{kin} = h\upsilon - E_{bin} - \Phi \qquad \text{Eq. A.6}$$

When the sample surface is exposed to an incident X-ray photon of energy *hv*, energy is thus imparted to a bound electron and the core level electron could be removed from the atom (Figure A.3 (a)). If the photon energy *hυ* exceeds the sum of the binding energy E_{bin} of the electron and of the work function Φ of the electron analyzer, a so called emitted photoelectron leaves the atom with a kinetic energy E_{kin}, from which E_{bin} could be calculated in the Eq.A.6.

Once the electron has been emitted from the atom, an electron vacancy remains on its original energy level. This vacancy can be filled by an electron from an upper shell, the energy difference being released by the emission of an electron from upper shell (Auger emission, A.3 (b)) or in the form of characteristic X-ray emission (Figure A.3 (c)). The two processes give rise to other spectroscopic methods: X-ray fluorescence (XRF) and Auger electron spectroscopy (AES), respectively.

In XPS or AES experiments, the photoelectrons or Auger electrons are detected respectively. They do not only provide information about the elemental composition of a surface but also the chemical environment of the elements present in the sample. The characteristic binding energies of photoelectrons depend on the specific element as well as the chemical state of the corresponding atom. Therefore, changes in the chemical environment of the elements can give rise to small shifts in the peak positions in the spectrum, so-called chemical shifts. Chemical shifts are recorded as a displacement in binding energies of photoelectrons excited from atoms in a compound compared to the energies of the corresponding pure substance. More detailed information could be found in dedicated books [166, 167].

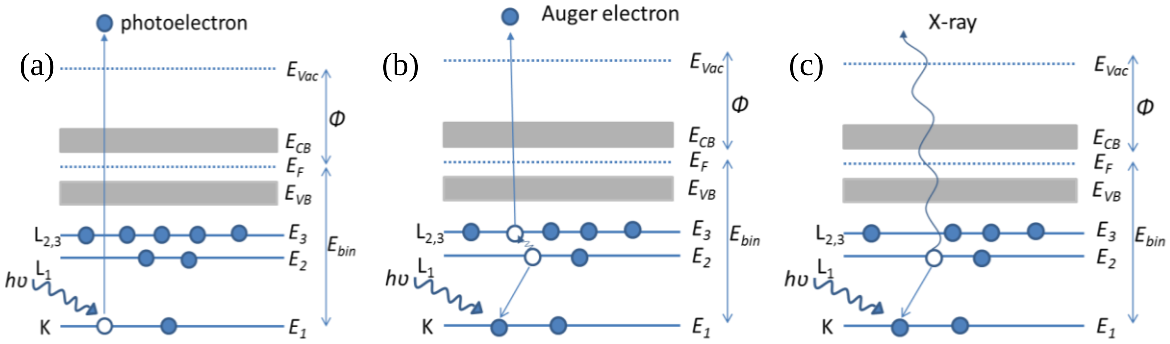

Figure A.3: Schematic representations showing the photoelectric effect (a), the subsequent Auger process (b) and X-ray fluorescence process. The blue circles represent occupied states, and white circles correspond to unoccupied states.

The position of an XPS lines provides the information necessary to identify the corresponding element and its chemical state. The line intensity, i.e. peak area, reflects the amount of the given element present in the surface near region of the samples. More precisely, the intensity of an XPS lines is described as follows [166]:

$$I \propto \sigma(h\nu)\cdot J \cdot L_A(\gamma)\cdot T(E_{kin})\cdot c_A \cdot \lambda_A(E_{kin})\cdot \cos(\theta) \qquad \text{Eq.A.7}$$

Here, σ(hν) is the photoionization cross section for the emission line, which depends on the element (Z), the core level and the exciting energy (hν). J is the x-ray flux, $L_A(\gamma)$ is the angular asymmetry parameter of the photoelectron line concerned, γ is the angle between incident X-ray photons and outgoing photoelectrons, c_A is the concentration of the element, $\lambda_A(E_{kin})$ is the inelastic mean free path (IMFP) of the electrons, which is a function of E_{kin}, and θ is the angle between emission of photoelectrons and the sample normal. $T(E_{kin})$ is the analyzer transmission function which depends on the kinetic energy of the electrons. For the used analyzer, T is approximately proportional to $E_{kin}^{-1/2}$ [168, 169]. X-ray tube axis and spectrometer axis are arranged under approximately 55°. Under this so called magic angle of XPS [170] the angular asymmetry parameter L is a constant and can be omitted in the quantification of XPS data. Hence by comparing the emission intensity of the emission lines from two elements, it is easy to determine the elemental ratio:

$$\frac{C_A}{C_B} = \frac{I_A}{I_B} \frac{\sqrt{E_{kin,A}}}{\sqrt{E_{kin,B}}} \frac{\sigma_B}{\sigma_A} \frac{\lambda_B}{\lambda_A} \qquad \text{Eq.A.8}$$

Eq A.8 can be simplified if the chosen lines of the two elements have a similar kinetic energy as follows:

$$\frac{C_A}{C_B} = \frac{I_A}{I_B} \frac{\sigma_B}{\sigma_A} \frac{\lambda_B}{\lambda_A} \qquad \text{Eq. A.9}$$

A.6 Surface photovoltage (SPV) technique

Contact Potential Difference (CPD)

Surface photovoltage (SPV) techniques have been widely used for non-destructive and high sensitive contactless characterisation, which has been successfully used to study the electronic properties of a wide range of semiconductor bulk materials, multilayers nanostructures and actual device structures [157, 171]. The surface photovoltage (SPV) is defined as the illumination-induced change in the surface potential [157], which can be caused, for example, by a built-in potential, and / or by surface dipoles rather than an external potential. Therefore, the SPV cannot be measured simply with some form of voltmeter. One of the traditional methods for this measurement is Kelvin Probe.

The Kelvin Probe Method is based on the measurement of the work function difference between a sample and a reference, which is Contact Potential Difference (CPD). The work function is the minimum energy needed to move an electron from the Fermi level into vacuum. The change of the CPD with illumination is the negative SPV signal.

A scheme of the measurement principle of the Kelvin Probe Method is shown in Figure A.4, which can be understood regarding two metal plates, e.g. from a parallel plate capacitor[157].

Figure A.4 (a) shows the schematic band diagram of two metal electrodes, investigated sample and reference, which have the same vacuum level, but characterized with different work function. When both electrodes are brought in contact, electrons move from the one with the lower work function to the one with higher work function until the Fermi levels are aligned (Figure A.4 (b)). The local vacuum energies are shifted and therefore, not at the same level anymore. The potential drop between the two materials is called Contact Potential Difference (CPD), which is defined as the difference in work function of two different materials

$$CPD = \frac{W_S - W_{ref}}{q} \qquad \text{Eq.A.10}$$

Theoretically, if the stored charge Q and the capacitance C were known, the CPD is given by the relation:

$$CPD = \frac{Q}{C} \qquad \text{Eq.A.11}$$

However, it is difficult to measure the storage charge precisely. An external dc bias [172], equal and opposite to the CPD is applied in Figure A.4 (c) to prevent charge flowing from one electrode to the other. In order to determine the applied bias V_b, the spacing is varied periodically till the capacitor is discharged, where the current is ac zero. This bias V_b then corresponds to the Contact Potential Difference (CPD).

Usually, a known metal, e.g. gold, the work function of which doesn't change under illumination, works as a reference electrode under ultra-high vacuum condition. It is assumed that the work funtion of the reference electrode is not affected by illumination.

Surface Photovoltage (SPV)

When a semiconductor specimen is illuminated with a photon energy bigger than the band gap energy of the semiconductor, the photogenerated electron–hole pairs can be seperated and caused by this a change in the CPD. A charge separation can be driven by different processes such as drift in built-in elcetrical fields or asymmetric trapping of electrons and holes at surface states. Chemical surface treatments greatly affect the concentration and distribution of surface states which can be monitored by SPV.

The difference in surface potential of the illuminated sample and the sample in the dark defines the Surface Photovoltage (SPV).

The surface potential can be measured with the Kelvin Probe Method explained in the above section. The Change of the CPD between the metal reference and the sample with illumination defines $\Delta CPD = CPD_{ill}-CPD_{dark}$. The relation between SPV and the Change of CPD is shown followingly:

$$SPV = -\Delta CPD \qquad \text{Eq.A.12}$$

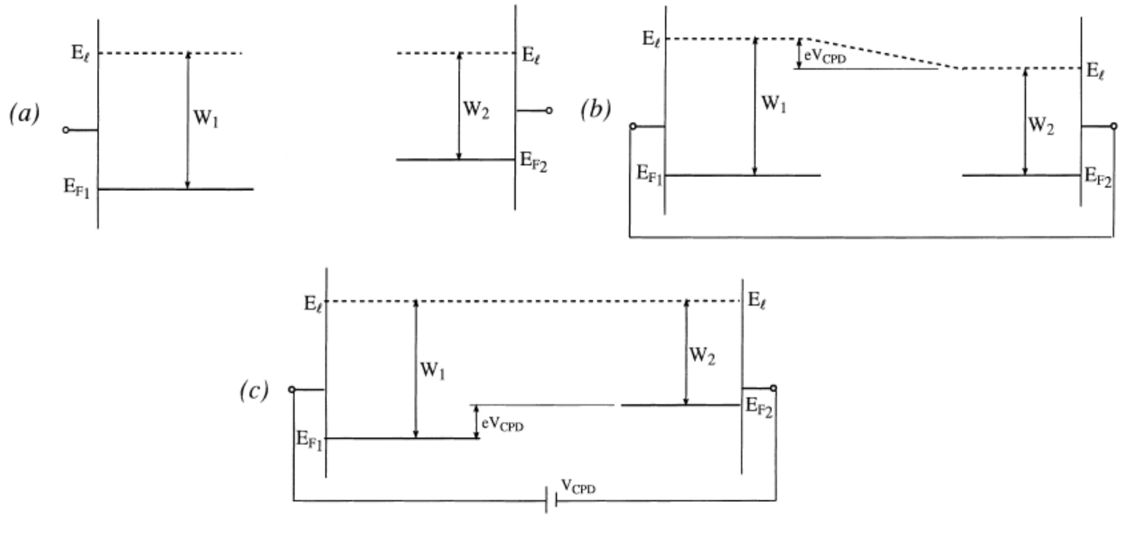

Figure A.4 Schematic band diagram of a prallel plate capacitor formed from two different metals: (a) the plates isolated, (b) the plates short-circuited and (c) the plates connected through a DC bias. The DC bias is equal and opposite to the Contact Potential Difference [157].

SPV characterization

SPV measurements are performed in the Kelvin-probe (Delta PHI, Besocke) arrangement in a home made set-up allowing investigations in air, vacuum ($4\cdot10^{-2}$ mbar, rotary pump) and N_2 (measurements at 600 mbar) atmospheres. The Kelvin-probe consists of a swinging gold mesh with diameter of 3 mm. A bias voltage of 5 V corresponding to the work function of gold in ultrahigh vacuum is set at the control unit. The sample surface is illuminated with monochromatic light from a halogen lamp with a quartz prism monochromator through the swinging gold mesh. The SPV spectra are measured from lower to higher photon energy. Before starting the measurement the ΔCPD is stabilized. The stabilization of the ΔCPD signal in the dark is controlled with a monitor measuring ΔCPD after each second. The SPV measurements are started in the dark and the slit of the monochromator is opened at 0.7 eV.

Appendix B

List of Abbreviation & Symbols

Table B.1: Abbreviations

AACVD	Aerosol Assisted Chemical Vapor Deposition
ALD	Atomic Layer Deposition
AES	X-ray Auger electron spectroscopy
AM1.5G	Air Mass 1.5 Global
CBD	Chemical Bath deposition
CIGSSe	Copper indium-gallium sulphur-selenide($Cu(In,Ga)(S,Se)_2$)
CdS	Cadmium sulfide
CVD	Chemical Vapor Deposition
DSC	Dye-sensitized solar cells
EF-TEM	Energy-filtered transmission electron microscopy
EDX	Energy-dispersive X-ray spectroscopy
FWHM	Full width at half maximum
HAc	Acetic acid
Hacac	acetylacetone
HRTEM	High-resolution transmission electron microscopy
H_2S	Hydrogen sulfide
IFMP	Inelastic free mean path
ILGAR	Ion Layer Gas Reaction
$In(acac)_3$	Indium acetylacetonate
$InCl_3$	Indium chloride
In_2S_3	Indium sulfide
I(V)	Current-voltage characteristic
JCPDS	Joint Committee on Powder Diffraction Standards
MS	Mass spectrometry
nd	nanodots
PES	Photoelectron spectroscopy
PV	Photovoltaics
PVD	Physical vapor deposition
SEM	Scanning electron microscopy
SLG	Soda Lime glass
SPV	Surface photovoltage
TCO	Transparent conductive oxide
TEM	Transmission electron microscopy
USP	Ultrasonic spray pyrolysis

UHV	Ultra high vacuum
UV-Vis	Ultraviolet-visible
XPS	X-ray photoelectron spectroscopy
XRD	X-ray diffraction
$Zn(ac)_2$	Zinc acetate
$Zn(acac)_2$	Zinc acetylacetonate
ZnO	Zinc oxide
ZnS	Zinc sulfide

Table B.2: Symbols

A	Diode quality factor
C_i	Elemental concentration
d	Mean diameter of aerosol droplets
D	Diffusion coefficient
D_0	Diffusion coefficient at reference conditions
E	Energy level
E_A	Activation energy
E_{bin}	Binding energy
E_{CB}	Energy of the conduction band
E_F	Fermi level
E_g	Band gap energy
E_{kin}	Kinetic energy
E_{VB}	Energy of the valence band
FF	Fill factor
f	Frequency of ultrasonic source
h	Planck constant $6.626 \cdot 10^{-34}$ J·s
hkl	Miller index
I	Current
I_i	Intensity of the considered XPS emission line
I_{ilu}	Illumination intensity
I_{MPP}	Current at maximum power point
I_0	Initial light intensity
I_{sc}	Short circuit current
J	Current density
J_D	Diode current density
J_L	Photogenerated current density
J_0	Saturation current density
J_{sc}	Short circuit current density
k	Boltzmann constant $1.381 \cdot 10^{-23}$ J/K
K_0	Pre-exponential constant
L	The thickness of the concentration boundary layer
m/z	Mass over charge
p	Saturated vapor pressure
P	Total pressure

P_0	Total pressure at reference conditions
P_r	Reaction partial pressure outside the concentration boundary
P_{in}	Power input
P_{out}	Power output
P_{MPP}	Maximum power
q	Elementary charge $1.602 \cdot 10^{-19}$ C
r	Ratio: $p / (\sigma \cdot \eta_{vis})$
R	Gas constant 8.314 J/mol·K
R_p	Parallel resistance
R_s	Series resistance
SPV	Surface photovoltage
T	Temperature
T_0	Reference temperature
v	Volume of deposition precursor atom
V_{MPP}	Voltage at maximum power point
V_{OC}	Open circuit voltage
x	Film thickness
α	Absorption coefficient
$\alpha_{1,2}$	Auger parameters
η_{vis}	Dynamic viscosity
η	Energy conversion efficiency
θ	Angle
λ	Wavelength, inelastic free mean path
ρ	Density
σ	Surface tension
σ_i	Photoionization cross section of considered clement
ν	Frequency
Φ	Work function

References

[1] Kittel C. Introduction to solid state physics. 6th ed. New York: Wiley; 1986.

[2] Fahrenbruch AL, Bube RH. Fundamentals of solar cells : photovoltaic solar energy conversion. New York: Academic Press; 1983.

[3] Poortmans J, Arkhipov V. Thin film solar cells : fabrication, characterization and applications. Chichester, England ; Hoboken, NJ: Wiley; 2007.

[4] Luque A, Hegedus S. Handbook of photovoltaic science and engineering. Hoboken, NJ: Wiley; 2003.

[5] Davidson WL. X-Ray Diffraction Evidence for Zns Formation in Zinc Activated Rubber Vulcanizates. Phys Rev. 1948;74:116-7.

[6] Scott SD, Barnes HL. Sphalerite-Wurtzite Equilibria and Stoichiometry. Geochim Cosmochim Ac. 1972;36:1275.

[7] Oikkonen M, Tammenmaa M, Asplund M. Comparison of Zns Thin-Films Grown by Atomic Layer Epitaxy from Zinc Acetate and Zinc-Chloride - an X-Ray-Diffraction and Spectroscopic Ellipsometric Study. Mater Res Bull. 1988;23:133-42.

[8] Lahtinen JA, Lu A, Tuomi T, Tammenmaa M. Effect of Growth Temperature on the Electronic-Energy Band and Crystal-Structure of Zns Thin-Films Grown Using Atomic Layer Epitaxy. J Appl Phys. 1985;58:1851-3.

[9] Xin ZJ, Peaty RJ, Rutt HN, Eason RW. Epitaxial growth of high-quality ZnS films on sapphire and silicon by pulsed laser deposition. Semicond Sci Tech. 1999;14:695-8.

[10] Yeh CY, Lu ZW, Froyen S, Zunger A. Zinc-Blende-Wurtzite Polytypism in Semiconductors. Phys Rev B. 1992;46:10086-97.

[11] Nakada T, Mizutani M, Hagiwara Y, Kunioka A. High-efficiency Cu(In,Ga)Se-2 thin-film solar cells with a CBD-ZnS buffer layer. Sol Energ Mat Sol C. 2001;67:255-60.

[12] Shao LX, Chang KH, Hwang HL. Zinc sulfide thin films deposited by RF reactive sputtering for photovoltaic applications. Appl Surf Sci. 2003;212:305-10.

[13] Blackmore JM, Cullis AG. The Structure of Zns Thin-Films Deposited by Rf-Sputtering. Thin Solid Films. 1991;199:321-34.

[14] Bayer A, Boyle DS, O'Brien P. In situ kinetic studies of the chemical bath deposition of zinc sulfide from acidic solutions. J Mater Chem. 2002;12:2940-4.

[15] URL:http://enwikipediaorg/wiki/Zinc_sulfide.

[16] Fang XS, Bando Y, Shen GZ, Ye CH, Gautam UK, Costa PMFJ, et al. Ultrarine ZnS nanobelts as field emitters. Adv Mater. 2007;19:2593.

[17] Fang XS, Bando Y, Ye CH, Golberg D. Crystal orientation-ordered ZnS nanobelt quasi-arrays and their enhanced field-emission. Chem Commun. 2007:3048-50.

[18] Fang XS, Gautam UK, Bando Y, Dierre B, Sekiguchi T, Golberg D. Multiangular branched ZnS nanostructures with needle-shaped tips: Potential luminescent and field-emitter nanomaterial. J Phys Chem C. 2008;112:4735-42.

[19] He JH, Zhang YY, Liu J, Moore D, Bao G, Wang ZL. ZnS/Silica nanocable field effect transistors as biological and chemical nanosensors. J Phys Chem C. 2007;111:12152-6.

[20] Fang XS, Bando Y, Liao MY, Gautam UK, Zhi CY, Dierre B, et al. Single-Crystalline ZnS Nanobelts as Ultraviolet-Light Sensors. Adv Mater. 2009;21:2034-9.

[21] Fang XS, Bando Y, Liao MY, Zhai TY, Gautam UK, Li L, et al. An Efficient Way to Assemble ZnS Nanobelts as Ultraviolet-Light Sensors with Enhanced Photocurrent and Stability. Adv Funct Mater. 2010;20:500-8.

[22] Chen ZG, Zou J, Liu G, Lu HF, Li F, Lu GQ, et al. Silicon-induced oriented ZnS nanobelts for hydrogen sensitivity. Nanotechnology. 2008;19.

[23] Uematsu T, Taniguchi S, Torimoto T, Kuwabata S. Emission quench of water-soluble ZnS-AgInS(2) solid solution nanocrystals and its application to chemosensors. Chem Commun. 2009:7485-7.

[24] Pratap S, Prasad J, Kumar R, Murari K, Singh SS. Preparation & characterisation of IR window grade zinc sulphide powder. Defence Sci J. 1996;46:215-21.

[25] Page RH, Schaffers KI, DeLoach LD, Wilke GD, Patel FD, Tassano JB, et al. Cr2+-doped zinc chalcogenides as efficient, widely tunable mid-infrared lasers. Ieee J Quantum Elect. 1997;33:609-19.

[26] Fang XS, Bando Y, Gautam UK, Zhai TY, Zeng HB, Xu XJ, et al. ZnO and ZnS Nanostructures: Ultraviolet-Light Emitters, Lasers, and Sensors. Crit Rev Solid State. 2009;34:190-223.

[27] O'Hare IP, Govender K, O'Brien P, Smyth-Boyle D. Chemical bath deposition of zinc sulfide from acidic solutions. Materials Research Society Symposium Proceedings 668: Warrendale, PA. 2001:p. H 8.15.1–H.8..6.

[28] Bhattacharya RN, Ramanathan K. Cu(In,Ga)Se-2 thin film solar cells with buffer layer alternative to CdS. Sol Energy. 2004;77:679-83.

[29] Contreras MA, Nakada T, Hongo M, Pudov AO, Sites JR. Proceedings 3rd World Conference of Photovoltaic Energy Conversion. 2003;Osaka, Japan:570.

[30] Green MA. Solar cells : operating principles, technology, and system applications. Englewood Cliffs, NJ: Prentice-Hall; 1982.

[31] Jackson P, Hariskos D, Lotter E, Paetel S, Wuerz R, Menner R, et al. New world record efficiency for Cu(In,Ga)Se(2) thin-film solar cells beyond 20%. Prog Photovoltaics. 2011;19:894-7.

[32] Kaufmann CA, Klenk R, Lux-Steiner MC, Neisser A, Korber P, Scheer R, et al. Proceedings of the 20th European Photovoltaic Solar Energy Conference,Barcelona, Spain. 2005.

[33] Caballero R, Kaufmann CA, Eisenbarth T, Cancela M, Hesse R, Unold T, et al. The influence of Na on low temperature growth of CIGS thin film solar cells on polyimide substrates. Thin Solid Films. 2009;517:2187-90.

[34] Maeda T, Takeichi T, Wada T. Systematic studies on electronic structures of CuInSe2 and the other chalcopyrite related compounds by first principles calculations. Physica Status Solidi a-Applications and Materials Science. 2006;203:2634-8.

[35] AVANCIS GmbH & Co KG URL: http://wwwavancisde.

[36] Palm J, Probst V, Stetter W, Toelle R, Visbeck S, Calwer H, et al. CIGSSe thin film PV modules: from fundamental investigations to advanced performance and stability. Thin Solid Films. 2004;451:544-51.

[37] Rau U, Schmidt M, Jasenek A, Hanna G, Schock HW. Electrical characterization of Cu(In,Ga)Se-2 thin-film solar cells and the role of defects for the device performance. Sol Energ Mat Sol C. 2001;67:137-43.

[38] Sáez-Araoz R. Chemical bath deposition of Zn(S,O) buffer layers and application in Cd-free chalcopyrite-based thin-film solar cells and modules. Berlin: Freien Universität Berlin; 2009.

[39] Shafarman WN, Klenk R, McCandless BE. Device and material characterization of Cu(InGa)Se-2 solar cells with increasing band gap. J Appl Phys. 1996;79:7324-8.

[40] Rau U, Schock H. Cu(In,Ga)Se_2 solar cells, in Clean electricity from photovoltaics. London: Imperial College Press; 2001.

[41] Buecheler SF. Investigation of compound semiconductors as buffer-layer in thin film solar cells Switzerland: ETH ZURICH; 2010.

[42] Mccandless BE, Hegedus SS. Influence of Cds Window Layers on Thin-Film Cds/Cdte Solar-Cell Performance. Conference Record of the Twenty Second Iee Photovoltaic Specialists Conference - 1991, Vols 1 and 2. 1991:967-72.

[43] Sterner J. ALD Buffer Layer Growth and Interface Formation on Cu(In,Ga)Se2 Solar Cell Absorbers: Uppsala University; 2004.

[44] Naghavi N, Abou-Ras D, Allsop N, Barreau N, Bucheler S, Ennaoui A, et al. Buffer layers and transparent conducting oxides for chalcopyrite Cu(In,Ga)(S,Se)(2) based thin film photovoltaics: present status and current developments. Prog Photovoltaics. 2010;18:411-33.

[45] Saez-Araoz R, Krammer J, Harndt S, Koehler T, Krueger M, Pistor P, et al. ILGAR-In2S3 buffer layers for Cd-FREE Cu(In,Ga)(S,Se)2 solar cells with certified efficiencies above 16%. Submitted. 2012.

[46] Sze SM. Physics of semiconductor devices. 2nd ed. New York: Wiley; 1981.

[47] Klenk R. Characterisation and modelling of chalcopyrite solar cells. Thin Solid Films. 2001;387:135-40.

[48] Klein A, Sauberlich F, Spath B, Schulmeyer T, Kraft D. Non-stoichiometry and electronic properties of interfaces. J Mater Sci. 2007;42:1890-900.

[49] Siebentritt S. Alternative buffers for chalcopyrite solar cells. Sol Energy. 2004;77:767-75.

[50] Hariskos D, Spiering S, Powalla M. Buffer layers in Cu(In,Ga)Se-2 solar cells and modules. Thin Solid Films. 2005;480:99-109.

[51] Hariskos D, Ruckh M, Ruhle U, Walter T, Schock HW, Hedstrom J, et al. A novel cadmium free buffer layer for Cu(In,Ga)Se-2 based solar cells. Sol Energ Mat Sol C. 1996;41-2:345-53.

[52] Kessler J, Velthaus KO, Ruckh M, Laichinger R, Schock HW, Lincot D, et al. Chemical Bath Deposition of CdS on CIS, etching effects and growth kinetics. Photovoltaic Science and Engineering Conference. 1992.

[53] Rau U, Braunger D, Herberholz R, Schock HW, Guillemoles JF, Kronik L, et al. Oxygenation and air-annealing effects on the electronic properties of Cu(In,Ga)Se2 films and devices. J Appl Phys. 1999;86:497-505.

[54] Ritala M, Leskela M. Handbook of thin film materials. San Diego: Academic Press; 2001.

[55] Zimmermann U, Ruth M, Edoff M. Cadmium-free CIGS mini-modules with ALD-grown Zn(O,S)-based buffer layers. Proceedings of the 21st European Photovoltaic Solar Energy Conference. 2006:1831–4.

[56] Hultqvist A, Platzer-Björkman C, Törndahl T, Ruth M, Edoff M. Optimization of i-ZnO window layers for Cu(In,Ga)Se2 solar cells with ALD buffers. Proceedings of the 22nd European Photovoltaic Solar Energy Conference. 2007:2381–4.

[57] Naghavi N, Spiering S, Powalla M, Cavana B, Lincot D. High-efficiency copper indium gallium diselenide (CIGS) solar cells with indium sulfide buffer layers deposited by atomic layer chemical vapor deposition (ALCVD). Prog Photovoltaics. 2003;11:437-43.

[58] Pistor P, Caballero R, Hariskos D, Izquierdo-Roca V, Wachter R, Schorr S, et al. Quality and stability of compound indium sulphide as source material for buffer layers in Cu(In,Ga)Se(2) solar cells. Sol Energ Mat Sol C. 2009;93:148-52.

[59] Negami T, Aoyagi T, Satoh T, Shimakawa S, Hayashi S, Hashimoto Y. Cd free CIGS solar cells fabricated by dry processes. Conference Record of the Twenty-Ninth Ieee Photovoltaic Specialists Conference 2002. 2002:656-9.

[60] Chamberl.Rr, Skarman JS. Chemical Spray Deposition Process for Inorganic Films. J Electrochem Soc. 1966;113:86.

[61] Mooney JB, Radding SB. Spray Pyrolysis Processing. Annu Rev Mater Sci. 1982;12:81-101.

[62] Buecheler S, Corica D, Guettler D, Chirila A, Verma R, Muller U, et al. Ultrasonically sprayed indium sulfide buffer layers for Cu(In,Ga)(S,Se)(2) thin-film solar cells. Thin Solid Films. 2009;517:2312-5.

[63] Fischer C-H, Lux-Steiner, M.C., Möller, J. ,Könenkamp, R. , Siebentritt, S. . Verfahren und Anordnung zur Herstellung dünner Metallchalkogenid-Schichten. Germany.

[64] Fischer CH, Muffler HJ, Bar M, Fiechter S, Leupolt B, Lux-Steiner MC. Ion layer gas reaction (ILGAR) - conversion, thermodynamic considerations and related FTIR analyses. J Cryst Growth. 2002;241:151-8.

[65] Bar M, Muffler HJ, Fischer CH, Lux-Steiner MC. ILGAR technology IV: ILGAR thin film technology extended to metal oxides. Sol Energ Mat Sol C. 2001;67:113-20.

[66] Bar M, Fischer CH, Muffler H, Zweigart S, Karg F, Lux-Steiner MC. Replacement of the CBD-CdS buffer and the sputtered i-ZnO layer by an ILGAR-ZnO WEL: optimization of the WEL deposition. Sol Energ Mat Sol C. 2003;75:101-7.

[67] Christian C. Spray ILGAR growth and Raman spectroscopy of CuInS2 thin films [PhD]. Berlin: Free university; 2008.

[68] http://wwwresearch-in-germanyde/main/campaigns-activities/ghtc-award/ghtc-award-2011-photovoltaics/69796/rodrigo-saez-araoz,currentTab=reiter2html.

[69] Allsop NA, Schonmann A, Belaidi A, Muffler HJ, Mertesacker B, Bohne W, et al. Indium sulfide thin films deposited by the spray ion layer gas reaction technique. Thin Solid Films. 2006;513:52-6.

[70] Fischer CH, Allsop NA, Gledhill SE, Kohler T, Kruger M, Saez-Araoz R, et al. The spray-ILGAR (R) (ion layer gas reaction) method for the deposition of thin semiconductor layers: Process and applications for thin film solar cells. Sol Energ Mat Sol C. 2011;95:1518-26.

[71] Allsop NA, Niesen TP, Gledhill SE, Kruger M, Kohler T, Lux-Steiner MC, et al. Up-scaling ILGAR In2S3 buffer layers production for chalcopyrite solar modules. Proceedings of the 34th IEEE Photovoltaic Specialists Conference1–3. 2009:2212–6.

[72] Gledhill S, Allison R, Allsop N, Fu YP, Kanaki E, Saez-Araoz R, et al. The reaction mechanism of the spray Ion Layer Gas Reaction process to deposit In(2)S(3) thin films. Thin Solid Films. 2011;519:6413-9.

[73] Allsop NA, Schonmann A, Muffler HJ, Bar M, Lux-Steiner MC, Fischer CH. Spray-ILGAR indium sulfide buffers for Cu(In, Ga)(S, Se)(2) solar cells. Prog Photovoltaics. 2005;13:607-16.

[74] Allsop NA, Camus C, Hansel A, Gledhill SE, Lauermann I, Lux-Steiner MC, et al. Indium sulfide buffer/CIGSSe interface engineering: Improved cell performance by the addition of zinc sulfide. Thin Solid Films. 2007;515:6068-72.

[75] Camus C, Allsop NA, Gledhill SE, Bohne W, Rohrich J, Lauermann I, et al. Properties of Spray ILGAR CuInS2 thin films. Thin Solid Films. 2008;516:7026-30.

[76] Gledhill S, Grimm A, Allsop N, Koehler T, Camus C, Lux-Steiner M, et al. A spray pyrolysis route to the undoped ZnO layer of Cu(In,Ga)(S,Se)(2) solar cells. Thin Solid Films. 2009;517:2309-11.

[77] Gledhill S, Zykov A, Allsop N, Rissom T, Schniebs J, Kaufmann CA, et al. Spray pyrolysis of barrier layers for flexible thin film solar cells on steel. Sol Energ Mat Sol C. 2011;95:504-9.

[78] Gledhill SE, Allsop N, Nier P, Camus C, Lux-Steiner M, Fischer CH. Towards lower deposition temperatures of spray deposited ZnO films. Mater Res Soc Symp P. 2007;1012:81-6.

[79] Fischer CH, Allsop NA, Hansel A, Visbeck S, Niesen TP, Lux-Steiner MC. The dry and damp heat stability of chalcopyrite solar cells prepared with an indium sulfide buffer deposited by the spray-ILGAR technique. Thin Solid Films. 2006;511:55-9.

[80] Allsop N, Nurnberg R, Lux-Steiner MC, Schedel-Niedrig T. Three-dimensional simulations of a thin film heterojunction solar cell with a point contact/defect passivation structure at the heterointerface. Appl Phys Lett. 2009;95.

[81] Yu JH, Joo J, Park HM, Baik SI, Kim YW, Kim SC, et al. Synthesis of quantum-sized cubic ZnS nanorods by the oriented attachment mechanism. J Am Chem Soc. 2005;127:5662-70.

[82] Khitrov GA, Strouse GF. ZnS nanomaterial characterization by MALDI-TOF mass spectrometry. J Am Chem Soc. 2003;125:10465-9.

[83] Ma C, Moore D, Li J, Wang ZL. Nanobelts, nanocombs, and nanowindmills of wurtzite ZnS. Adv Mater. 2003;15:228.

[84] Zhao YW, Zhang Y, Zhu H, Hadjipianayis GC, Xiao JQ. Low-temperature synthesis of hexagonal (wurtzite) ZnS nanocrystals. J Am Chem Soc. 2004;126:6874-5.

[85] Zhu YC, Bando Y, Xue DF, Golberg D. Nanocable-aligned ZnS tetrapod nanocrystals. J Am Chem Soc. 2003;125:16196-7.

[86] Didenko YT, Suslick KS. Chemical aerosol flow synthesis of semiconductor nanoparticles. J Am Chem Soc. 2005;127:12196-7.

[87] Bang JH, Hehnich RJ, Suslick KS. Nanostructured ZnS : Ni2+ photocatalysts prepared by ultrasonic spray pyrolysis. Adv Mater. 2008;20:2599.

[88] Tamaki S, Tohge N, Tagami K, Okuyama K. Preparation of fine particles of ZnS-CdS solid solution by the spray-pyrolysis. J Ceram Soc Jpn. 1996;104:137-9.

[89] Xia B, Lenggoro IW, Okuyama K. Novel route to nanoparticle synthesis by salt-assisted aerosol decomposition. Adv Mater. 2001;13:1579.

[90] Lenggoro IW, Itoh Y, Iida N, Okuyama K. Control of size and morphology in NiO particles prepared by a low-pressure spray pyrolysis. Mater Res Bull. 2003;38:1819-27.

[91] Fauteux C, Longtin R, Pegna J, Therriault D. Fast synthesis of ZnO nanostructures by laser-induced decomposition of zinc acetylacetonate. Inorg Chem. 2007;46:11036-47.

[92] Brahma S, Shivashankar SA. Microwave irradiation-assisted method for the deposition of adherent oxide films on semiconducting and dielectric substrates. Thin Solid Films. 2010;518:5905-11.

[93] Kodas TT, Hampden-Smith MJ. Aerosol processing of materials. New York: Wiley-VCH; 1999.

[94] Zhang SC, Messing GL. Solid Particle Formation during Spray Pyrolysis. Ceramic Powder Science Iii. 1990;12:49-57.

[95] Messing GL, Zhang SC, Jayanthi GV. Ceramic Powder Synthesis by Spray-Pyrolysis. J Am Ceram Soc. 1993;76:2707-26.

[96] Zhang SC, Messing GL, Huebner W. Yba2cu3o7-X Superconductor Powder Synthesis by Spray Pyrolysis of Organic-Acid Solutions. J Aerosol Sci. 1991;22:585-99.

[97] Cabanas MV, Valletregi M, Labeau M, Gonzalezcalbet JM. Spherical Iron-Oxide Particles Synthesized by an Aerosol Technique. J Mater Res. 1993;8:2694-701.

[98] Allsop NA, Camus C, Gledhill S, Unold T, Lux-Steiner M, Niesen T, et al. Nanostructured ZnS : In(2)S(3) buffer layers on Cu(In,Ga)(S,Se)(2): Can voltage and efficiency be improved through interface inhomogeneities on a scale below the minority carrier diffusion length? Mater Res Soc Symp P. 2007;1012:43-9.

[99] Arii T, Kishi A. Humidity controlled thermal analysis - The effect of humidity on thermal decomposition of zinc acetylacetonate monohydrate. J Therm Anal Calorim. 2006;83:253-60.

[100] Fiddes AJC, Durose K, Brinkman AW, Woods J, Coates PD, Banister AJ. Preparation of ZnO films by spray pyrolysis. J Cryst Growth. 1996;159:210-3.

[101] Lang RJ. Ultrasonic Atomization of Liquids. J Acoust Soc Am. 1962;34:6.

[102] Vacassy R, Scholz SM, Dutta J, Plummer CJG, Houriet R, Hofmann H. Synthesis of controlled spherical zinc sulfide particles by precipitation from homogeneous solutions. J Am Ceram Soc. 1998;81:2699-705.

[103] Tammenmaa M, Antson H, Asplund M, Hiltunen L, Leskela M, Niinisto L, et al. Alkaline-Earth Sulfide Thin-Films Grown by Atomic Layer Epitaxy. J Cryst Growth. 1987;84:151-4.

[104] Tadokoro T, Ohta S, Ishiguro T, Ichinose Y, Kobayashi S, Yamamoto N. Growth and Characterization of (Cds)4/(ZnS)16 Superlattices. J Cryst Growth. 1993;130:21-8.

[105] Leskela M, Niinisto L, Niemela P, Nykanen E, Soininen P, Tiitta M, et al. Preparation of Lead Sulfide Thin-Films by the Atomic Layer Epitaxy Process. Vacuum. 1990;41:1457-9.

[106] Venables JA, Spiller GDT, Hanbucken M. Nucleation and Growth of Thin-Films. Rep Prog Phys. 1984;47:399-459.

[107] Bent SF, Bakke JR, King JS, Jung HJ, Sinclair R. Atomic layer deposition of ZnS via in situ production of H(2)S. Thin Solid Films. 2010;518:5400-8.

[108] Irgens RL. Thioacetamide as a Source of Hydrogen-Sulfide for Colony Growth of Purple Sulfur Bacteria. Curr Microbiol. 1983;8:183-6.

[109] Makhova LV, Konovalov I, Szargan R, Aschkenov N, Schubert M, Chasse T. Composition and properties of ZnS thin films prepared by chemical bath deposition from acidic and basic solutions. Phys Status Solidi C. 2005;2:1206-11.

[110] Arenas OL, Nair MTS, Nair PK. Chemical bath deposition of ZnS thin films and modification by air annealing. Semicond Sci Tech. 1997;12:1323-30.

[111] Celikkaya A, Akinc M. Morphology of Zinc-Sulfide Particles Produced from Various Zinc Salts by Homogeneous Precipitation. J Am Ceram Soc. 1990;73:245-50.

[112] Butler EA, Peters DG, Swift EH. Hydrolysis Reactions of Thioacetamide in Aqueous Solutions. Anal Chem. 1958;30:1379-83.

[113] Sawyer WE, Mann, A. US Patent. 1880;229:335.

[114] Kodas T, Hampden-Smith MJ. The chemistry of Metal CVD: VCH; 1994.

[115] Mount E. Principles of Chemical Vapor Deposition (Book). Sci-Tech News. 2003;57:80.

[116] Hampdensmith MJ, Kodas TT. Chemical-Vapor-Deposition of Metals .1. An Overview of Cvd Processes. Chem Vapor Depos. 1995;1:8-23.

[117] Gurav A, Kodas T, Pluym T, Xiong Y. Aerosol Processing of Materials. Aerosol Sci Tech. 1993;19:411-52.

[118] Porter CJ, Beynon JH, Ast T. The Modern Mass-Spectrometer - a Complete Chemical Laboratory. Org Mass Spectrom. 1981;16:101-14.

[119] Schwarz H. Chemistry of Naked Molecules - Mass-Spectrometer as Laboratory. Chem Unserer Zeit. 1991;25:268-78.

[120] Bykov AF, Turgambaeva AE, Igumenov IK, Semyannikov PP. Mass-Spectrometric Study of Thermolysis Mechanism of Metal Acetylacetonates Vapor. J Phys Iv. 1995;5:191-7.

[121] Turgambaeva AE, Bykov AF, Igumenov IK. Mass-Spectrometric Study of Copper(Ii) Beta-Diketonates Vapor Thermolysis Mechanism and Kinetics. J Phys Iv. 1995;5:221-8.

[122] Krisyuk VV, Turgambaeva AE, Igumenov IK. Volatile lead beta-diketonates as CVD precursors. Chem Vapor Depos. 1998;4:43.

[123] Ismail HM. A Thermoanalytical Study of Metal Acetylacetonates. J Anal Appl Pyrol. 1991;21:315-26.

[124] Entry No. 12767, NIST 107 (zinc acetylacetonate, $C_{10}H_{14}O_4Zn$).

[125] Entry No. 19843, NIST 107 (acetylacetone, $C_5H_8O_2$).

[126] Gledhill SE, Niesen TP, Allsop NA, Gimpl G, Kruger M, Kohler T, et al. Improvement in Spray Deposition of the Intrinsic Zno Window Layer for Chalcopyrite Solar Cells. 2009 34th Ieee Photovoltaic Specialists Conference, Vols 1-3. 2009:65-9.

[127] Kamata K, Hosono H, Maeda Y, Miyokawa K. Synthesis of Zinc-Oxide Powder by Hydrolysis of Bis(Acetylacetonato)Zinc(Ii) in Aqueous-Solution. Chem Lett. 1984:2021-2.

[128] Macdonal.Cg, Shannon JS. Mass Spectrometry and Structures of Metal Acetylacetonate Vapours. Aust J Chem. 1966;19:1545.

[129] Marshall GL. Electron-Impact Mass-Spectrometry of the Acetates of Zinc, Magnesium, Cobalt and Manganese. Org Mass Spectrom. 1983;18:168-72.

[130] Vogelsberger W, Schmidt J. A Nanoparticle in a Nanoscale Volume of Solvent: Thermodynamic and Kinetic Considerations. J Phys Chem C. 2008;112:16240-7.

[131] Hadgiivanova R, Diamant H, Andelman D. Kinetics of Surfactant Micellization: A Free Energy Approach. J Phys Chem B. 2011;115:7268-80.

[132] Jensen KF. Chemical Vapor-Deposition. Adv Chem Ser. 1989:199-263.

[133] Peng ZM, Yang H. Designer platinum nanoparticles: Control of shape, composition in alloy, nanostructure and electrocatalytic property. Nano Today. 2009;4:143-64.

[134] Banfield JF, Zhang HZ, Gilbert B, Huang F. Water-driven structure transformation in nanoparticles at room temperature. Nature. 2003;424:1025-9.

[135] Huang F, Zhang HZ, Banfield JF. The role of oriented attachment crystal growth in hydrothermal coarsening of nanocrystalline ZnS. J Phys Chem B. 2003;107:10470-5.

[136] De Stasio G, Chan CS, Welch SA, Girasole M, Frazer BH, Nesterova MV, et al. Microbial polysaccharides template assembly of nanocrystal fibers. Science. 2004;303:1656-8.

[137] Chen CC, Herhold AB, Johnson CS, Alivisatos AP. Size dependence of structural metastability in semiconductor nanocrystals. Science. 1997;276:398-401.

[138] Zhang HZ, Banfield JF. Identification and Growth Mechanism of ZnS Nanoparticles with Mixed Cubic and Hexagonal Stacking. J Phys Chem C. 2009;113:9681-7.

[139] Suslick KS, Bang JH, Hehnich RJ. Nanostructured ZnS : Ni2+ photocatalysts prepared by ultrasonic spray pyrolysis. Adv Mater. 2008;20:2599.

[140] Meyer BK, Polity A, Farangis B, He Y, Hasselkamp D, Kramer T, et al. Structural properties and bandgap bowing of ZnO1-xSx thin films deposited by reactive sputtering. Appl Phys Lett. 2004;85:4929-31.

[141] Iwata K, Fons P, Yamada A, Shibata H, Matsubara K, Nakahara K, et al. Bandgap engineering of ZnO using Se. Phys Status Solidi B. 2002;229:887-90.

[142] Lauermann I, Bar M, Ennaoui A, Fiedeler U, Fischer CH, Grimm A, et al. Analysis of zinc compound buffer layers in Cu(in,Ga)(S,Se)(2) thin film solar cells by synchrotron-based soft x-ray spectroscopy. Compound Semiconductor Photovoltaics. 2003;763:175-80.

[143] Briggs D, Seah MP. Practical surface analysis. 2nd ed. Chichester ; New York: Wiley; 1990.

[144] C. D. Wagner WMR, L. E. Davis, and J. F. Moulder. Handbook of X-ray Photoelectron Spectroscopy. USA: Perkin-Elmer Corporation (Physical Electronics); 1979.

[145] Wagner CD. Chemical-Shifts of Auger Lines, and Auger Parameter. Faraday Discuss. 1975;60:291-300.

[146] Bar M, Ennaoui A, Klaer J, Kropp T, Saez-Araoz R, Allsop N, et al. Formation of a ZnS/Zn(S,O) bilayer buffer on CuInS2 thin film solar cell absorbers by chemical bath deposition. J Appl Phys. 2006;99.

[147] Yeh JJ, Lindau I. Atomic Subshell Photoionization Cross-Sections and Asymmetry Parameters - 1 Less-Than-or-Equal-to Z Less-Than-or-Equal-to 103. Atom Data Nucl Data. 1985;32:1-155.

[148] Bär M. Neuartige Cd-freien Fensterstruktur für Chalkopyrit-Dünnschichtsolarzellen. Berlin: Technische Universität Berlin; 2003.

[149] Tanuma S, Powell CJ, Penn DR. Calculations of Electron Inelastic Mean Free Paths (Imfps) .4. Evaluation of Calculated Imfps and of the Predictive Imfp Formula Tpp-2 for Electron Energies between 50 and 2000 Ev. Surf Interface Anal. 1993;20:77-89.

[150] Tougaard S. QUASES-IMP-TPP2M code for the calculation of the inelastic electron mean free path, Version 2.2. http://wwwquasescom/.

[151] Allsop N, Nurnberg R, Lux-Steiner MC, Schedel-Niedrig T. Three-dimensional simulations of a thin film heterojunction solar cell with a point contact/defect passivation structure at the heterointerface. Appl Phys Lett. 2009;95.

[152] Fukuzaki K, Kohiki S, Yoshikawa H, Fukushima S, Watanabe T, I K. Changes in the electronic structure of CuInS(2) thin films by Na incorporation. Appl Phys Lett. 1998;73:1385-7.

[153] Rockett A, Liao D, Heath JT, Cohen JD, Strzhemechny YM, Brillson LJ, et al. Near-surface defect distributions in Cu(In,Ga)Se-2. Thin Solid Films. 2003;431:301-6.

[154] Bar M, Ennaoui A, Klaer J, Kropp T, Saez-Araoz R, Lehmann S, et al. Intermixing at the heterointerface between ZnS/Zn(S,O) bilayer buffer and CuInS2 thin film solar cell absorber. J Appl Phys. 2006;100.

[155] Lide DR. CRC handbook of chemistry and physics. Boca Raton, FL: CRC Press; 2005.

[156] Johnson B, Klaer J, Fischer C-H, Lauermann I. Depth profiling of a CdS buffer layer on CuInS2 measured with XPS during removal by HCl etching. submitted.

[157] Kronik L, Shapira Y. Surface photovoltage phenomena: theory, experiment, and applications. Surf Sci Rep. 1999;37:1-206.

[158] Duzhko V, Timoshenko VY, Koch F, Dittrich T. Photovoltage in nanocrystalline porous TiO2. Phys Rev B. 2001;64.

[159] Williams DB, Carter CB. Transmission electron microscopy : a textbook for materials science. New York: Plenum Press; 1996.

[160] Kienitz H, Aulinger F. Massenspektrometrie. Weinheim/Bergstrasse,: Verlag Chemie; 1968.

[161] Bragg W. The diffraction of short electromagnetic waves by a crystal. Proceedings of the Cambridge Philosophical Society. 1913;17:43-57.

[162] Cullity BD. Elements of x-ray diffraction. 2d ed. Reading, Mass.: Addison-Wesley Pub. Co.; 1978.

[163] Jenkins R, Snyder RL. Introduction to X-ray powder diffractometry. New York: Wiley; 1996.

[164] Pankove JI. Optical processes in semiconductors. Englewood Cliffs, N.J.,: Prentice-Hall; 1971.

[165] Einstein A. Concerning an Heuristic Point of View Toward the Emission and Transformation of Light. Ann Phys. 1905;17:132.

[166] Moulder JF, Stickle WF, Sobol PE, Bomben KD. Handbook of X-Ray Photoelectron Spectroscopy. USA: Perkin-Elmer Corporation; 1992.

[167] Yu PY, Cardona M. Fundamentals of semiconductors : physics and materials properties. 3rd, rev. and enlarged ed. Berlin ; New York: Springer; 2001.

[168] Weinhardt L. Elektronische und chemische Eigenschaften von Grenzflächen und Oberflächen in optimierten Cu(In,Ga)(S,Se)2 Dünnschichtsolarzellen: Bayrische Julius-Maximilians-Universität Würzburg; 2005.

[169] Briggs D, Seah MP. Practical surface analysis : by auger and x-ray photoelectron spectroscopy. Chichester ; New York: Wiley; 1983.

[170] Smith GC. Surface analysis by electron spectroscopy : measurement and interpretation. New York: Plenum Press; 1994.

[171] Schroder DK. Surface voltage and surface photovoltage: history, theory and applications. Meas Sci Technol. 2001;12:R16-R31.

[172] Patai IF, Pomerantz, M.A.. Contact potential differences. Journal of the Franklin Institute. 1951;252:239.

List of publications

Journal Publications

- *ZnS nano dot film as defect passivation layer for Cu(In,Ga)(S,Se)$_2$ thin film solar cells deposited by Spray-ILGAR® (ion layer gas reaction)*
  Fu, Y.P.; Allsop, N.A.; Gledhill, S.E.; Köhler, T.; Krüger, M.; Sáez-Araoz, R.; Blöck, U.; Lux-Steiner, M.Ch.; Fischer, Ch.-H.
  Advanced Energy Materials 1 (2011), p. 561-564

- *Surface photovoltage spectroscopy on Cu(In,Ga)(S,Se)$_2$ / ZnS-nanodot / In$_2$S$_3$ systems*
  Fu, Y.P.; Rada,T.; Fischer, Ch.-H.; Lux-Steiner, M.Ch.; Dittrich,T.
  Submit to Progress in Photovoltaics: Research and Applications

- *The reaction mechanism of the spray Ion Layer Gas Reaction process to deposit In(2)S(3) thin films*
  Gledhill, S.; Allison, R.; Allsop, N.; Fu, Y.P.; Kanaki, E.; Sáez-Araoz, R.; Lux-Steiner, M.; Fischer, Ch.-H.
  Thin Solid Films 519 (2011), p. 6413-6419

- *The spray-ILGAR ® (ion layer gas reaction) method for the deposition of thin semiconductor layers: Process and applications for thin film solar cells*
  Fischer, Ch.-H.; Allsop, N.A.; Gledhill, S.E.; Köhler, T.; Krüger, M.; Sáez-Araoz, R.; Fu, Y.P.; Schwieger, R.; Richter, J.; Wohlfahrt, P.; Bartsch, P.; Lichtenberg, N.; Lux-Steiner, M.Ch.
  Solar Energy Materials and Solar Cells 95 (2011), p. 1518-1526

Oral Conference presentation

- *Controlled Spray-ILGAR deposition of ZnS nano dots covered by In$_2$S$_3$: An Improved buffer layer for Cu(In,Ga)(S,Se)$_2$ thin film solar cells*
  Fu, Y.P.; Allsop, N.A.; Gledhill, S.E.; Köhler, T.; Krüger, M.; Sáez-Araoz R.; Lux-Steiner, M.Ch.; Fischer, Ch.-H.
  2011 Material Research Society Spring Meeting. San Francisco, USA, April 25th-29th 2011.

- *Improved efficiency of thin film solar cells using Spray-ILGAR ZnS nano-dot films*
  Fischer, Ch.-H.; Fu, Y.P.; Gledhill, S.E.; Köhler, T.; Krüger, M.; Sáez-Araoz R.; Allsop, N.A.; Lux-Steiner, M.Ch.
  2011 European Materials Research Society, Nice, France, May 10th-12th, 2011.

Curriculum Vitae

For reasons of data protection, the Curriculum vitae is not included in the online version.

Statement

I hereby declare that this submission is my own work and that, to the best of my knowledge and belief, it contains no material previously published or written by another person, except where due acknowledgement is made in the text. I also declare that the intellectual content of this thesis is the product of my own work, even though I may have received assistance from others on style, presentation and language expression.

Berlin…...…………………………..   Signed……………………………..